

A quest for ferroelectricity
in the intercalated compounds $\text{Lu}_2\text{Fe}_3\text{O}_7$ and
 $\text{Lu}_3\text{Fe}_4\text{O}_{10}$

Von der Fakultät für Mathematik, Informatik und Naturwissenschaften der RWTH
Aachen University zur Erlangung des akademischen Grades einer Doktorin der
Naturwissenschaften genehmigte Dissertation

von

Master of Science

Sabreen Saleh Said Hammouda

aus Jerusalem, Palestine

Berichter: Juniorprofessor Dr. Manuel Angst
Universitätsprofessor Dr. Uwe Klemradt

Tag der mündlichen Prüfung: 23. Juli 2021

Diese Dissertation ist auf den Internetseiten der Universitätsbibliothek verfügbar.

This thesis is dedicated to the elucidation of the charge order (CO) realized in the intercalated rare earth ferrites $R\text{Fe}_2\text{O}_4(\text{RFeO}_3)_n$. Rare earth ferrites have attracted a lot of attention as proposed multiferroics. In particular, LuFe_2O_4 was considered a clear example of ferroelectricity from CO of Fe^{2+} and Fe^{3+} in the Fe-O bilayers, though recently this was contradicted. YbFe_2O_4 was found by structural refinement and bond-valance-sum (BVS) analysis to contain polar bilayers, though with anti-polar stacking. In order to modify the CO, one can focus on the interactions between different bilayers. These can be tuned by inserting single Fe-O layers, increasing the distance between the bilayers. The CO within individual bilayers of intercalated rare earth ferrites is expected to be very similar as in YbFe_2O_4 , with the intercalation possibly rendering the anti-polar stacking to a polar. Deducing the CO pattern realized in the intercalated compounds requires the growth of single crystals. These should be of high quality with the proper oxygen stoichiometry, which is critical for the establishment of 3D CO as already noted for not intercalated rare earth ferrites. However, the more complex crystal structure makes the synthesis of high quality single crystals more difficult. With the controlled growth using mixed gas flow of $\text{CO}_2:\text{CO}$, single crystals of intercalated layered $\text{R}_{1+n}\text{Fe}_{2+n}\text{O}_{4+3n-\delta}$ ($n=1,2$) with different oxygen stoichiometries δ are fabricated. For the first time crystals sufficiently stoichiometric to exhibit superstructure reflections in X-ray diffraction attributable to charge ordering were obtained. The estimated correlation lengths tend to be smaller in $\text{Lu}_2\text{Fe}_3\text{O}_7$ and larger in $\text{Lu}_3\text{Fe}_4\text{O}_{10}$ compared to the not intercalated LuFe_2O_4 . For both compounds, two different superstructures were observed in different crystals, one an incommensurate zigzag pattern, the other an apparently commensurate pattern with $(\frac{1}{3}\frac{1}{3}0)$ -propagation. This propagation vector is similar to what was found in LuFe_2O_4 and in YbFe_2O_4 , however, without doubling of the cell in c-direction.

The magnetic properties of both compounds were studied using macroscopic magnetization measurements and X-ray magnetic circular dichroism (XMCD). Additionally, polarized neutron scattering and ac-susceptibility measurements were performed on $\text{Lu}_2\text{Fe}_3\text{O}_7$. Macroscopic magnetization measurements performed on the most stoichiometric $\text{Lu}_2\text{Fe}_3\text{O}_7$ crystal show no sharp features attributable to phase transitions, suggesting reduced magnetic correlations with the presence of the ferrimagnetic state and the absence of an antiferromagnetic state like those observed in LuFe_2O_4 and YbFe_2O_4 . In contrast to this, similar measurements performed on $\text{Lu}_3\text{Fe}_4\text{O}_{10}$ suggested a first order meta-magnetic transition between a high-field ferrimagnetic and a low-field antiferromagnetic state similar to LuFe_2O_4 . Polarized neutron scattering on $\text{Lu}_2\text{Fe}_3\text{O}_7$ reveals diffuse magnetic scattering along $(\frac{1}{3}\frac{1}{3}\ell)$ and frequency-dependence is observed in the ac-susceptibility, consistent with glassy freezing rather than long-range spin order (SO). The appearance of 3D CO but not 3D SO in a $\text{Lu}_2\text{Fe}_3\text{O}_7$ crystal indicates that the SO is more fragile with respect to oxygen off-stoichiometry. All magnetic properties are consistent with the SO within individual bilayers of $\text{Lu}_2\text{Fe}_3\text{O}_7$ essentially being the same as in LuFe_2O_4 , though with a less well-established order. This is indicated in particular by XMCD measurements, which support the same SO in the individual bilayer of $\text{Lu}_3\text{Fe}_4\text{O}_{10}$ as well. Moreover, XMCD confirms also the same CO in the individual bilayers. In the additional Fe-O

single layers, a magnetic moment seems induced by the application of a magnetic field, i.e. the single layers act as a paramagnetic-like additional contribution.

The availability of stoichiometric crystals with commensurate CO facilitates the refinement of CO. For $\text{Lu}_2\text{Fe}_3\text{O}_7$, symmetry analysis based on the $(\frac{1}{3}\frac{1}{3}0)$ -propagation vector led to the same likely CO configurations as discussed for LuFe_2O_4 : either charged bilayers or polar bilayers stacked with the same or alternating polarizations. For $\text{Lu}_3\text{Fe}_4\text{O}_{10}$, only polar bilayers stacked with the same polarizations can be realized. The refinement of the average structure disregarding the modulation for the data collected from a commensurate CO $\text{Lu}_2\text{Fe}_3\text{O}_7$ crystal by single crystal synchrotron X-ray diffraction at 100 K, manifests symptoms of the CO represented in the splitting of some of the Lu-atom positions. This splitting seems to result from the positional modulation of the Lu that accompanies the CO as observed in LuFe_2O_4 . Surprisingly, the refinement of the superstructure in all symmetries still exhibits the Lu-splitting. The best results are achieved for the polar $\text{Cmc}2_1$ structure. However, the performed BVS analysis reveals an intermediate valance on 8 Fe-sites indicating an incomplete CO in the bilayer. These sites correlate with the Lu-position splitting. This is very likely due to a superposition of CO configurations of different symmetries. The formation of these structure polytypes can be understood as resulting from the inter-bilayer interactions being much weaker due to the intercalation, which makes CO with different stacking closer in energy. In conclusion, the results obtained within this study indicate strongly that both compounds are polar, validating the intercalation approach to producing ferroelectricity from CO in the rare earth ferrites.

Zusammenfassung

Diese Arbeit befasst sich mit der Bestimmung der Ladungsordnung (LO), welche in den interkalierten seltene Erd-Ferrite $R\text{Fe}_2\text{O}_4(\text{RFeO}_3)_n$ realisiert wird. Seltene Erd-Ferrite haben viel Aufmerksamkeit gefunden als vorgeschlagene Multiferroika. Insbesondere LuFe_2O_4 wurde als klares Beispiel für Ferroelektrizität hervorgerufen durch Ladungsordnung, hier von Fe^{2+} und Fe^{3+} in den Fe-O Doppelschichten, betrachtet – wobei dieses Szenarium vor kurzem widerlegt wurde. In YbFe_2O_4 zeigten Strukturverfeinerung und Bond-Valenz-Summen (BVS) Analyse, daß polare Doppelschichten existieren, wobei diese allerdings antipolar gestapelt sind. Um die LO zu modifizieren kann der Fokus auf die Interaktionen zwischen verschiedenen Doppelschichten gelegt werden. Diese Interaktionen können verändert werden durch das Einfügen von Fe-O Einzelschichten, was den Abstand zwischen benachbarten Doppelschichten vergrößert. Es wird erwartet, daß die LO in den individuellen Doppelschichten ähnlich ist wie in YbFe_2O_4 , die Interkalation jedoch möglicherweise zu einer polaren statt antipolaren Stapelung führt. Die Bestimmung des in den interkalierten Verbindungen realisierten LO Musters erfordert die Zucht von Einkristallen. Diese sollten außerdem von hoher Qualität sein mit der richtigen Sauerstoff-Stöchiometrie – dies ist entscheidend für die Bildung von dreidimensionaler LO, wie für nicht interkalierte seltene Erd-Ferrite gefunden wurde. Die durch die Interkalierung verursachte komplexere Kristallstruktur erschwert die Synthese von Einkristallen hoher Qualität zusätzlich. Mit durch einen gemischten $\text{CO}_2:\text{CO}$ Gasfluss kontrollierten Synthese wurden Einkristalle der interkalierten geschichteten Verbindungen $\text{R}_{1+n}\text{Fe}_{2+n}\text{O}_{4+3n-\delta}$ ($n=1,2$) mit verschiedenen Sauerstoff-Stöchiometrien δ hergestellt. Zum ersten Mal wurden Einkristalle erhalten, die eine genügend gute Stöchiometrie haben, um Ladungsordnungs-Überstruktureffekte in Röntgenbeugung zu sehen. Die geschätzten Korrelationslängen tendieren dazu kleiner zu sein in $\text{Lu}_2\text{Fe}_3\text{O}_7$ und größer in $\text{Lu}_3\text{Fe}_4\text{O}_{10}$, verglichen mit dem nicht interkalierten LuFe_2O_4 . Für beide Verbindungen wurden in verschiedenen Kristallen zwei verschiedene Überstrukturen beobachtet, eine davon ein inkommensurables Zickzack-Muster, die andere ein anscheinend kommensurables Muster mit Ausbreitungsvektor $(\frac{1}{3}\frac{1}{3}0)$. Dieser Ausbreitungsvektor ist ähnlich zu dem in LuFe_2O_4 und YbFe_2O_4 gefundenen, allerdings ohne Verdopplung der Einheitszelle in c Richtung.

Die magnetischen Eigenschaften beider Verbindungen wurden durch makroskopische Magnetisierungsmessungen und zirkularem Röntgendifferenzismus ("XMCD") untersucht. Überdies wurden für $\text{Lu}_2\text{Fe}_3\text{O}_7$ polarisierte Neutronenstreuung und ac-Suszeptibilitätsmessungen durchgeführt. Makroskopische Magnetisierungsmessungen durchgeführt am $\text{Lu}_2\text{Fe}_3\text{O}_7$ Einkristall mit der besten Stöchiometrie zeigten keine scharfen Merkmale die auf Phasenübergänge hindeuten. Die Messungen deuten auf reduzierte magnetische Korrelationen hin, sowie auf das Vorhandensein eines ferrimagnetischen Zustands und das Fehlen eines antiferromagnetischen Zustands wie in LuFe_2O_4 and YbFe_2O_4 beobachtet. Im Gegensatz dazu suggerieren Magnetisierungsmessungen an $\text{Lu}_3\text{Fe}_4\text{O}_{10}$ einen Übergang erster Ordnung zwischen einem ferrimagnetischen Zustand in hohen Feldern und einem antiferromagnetischen Zustand in tiefen Feldern, ähnlich wie in LuFe_2O_4 . Polarisierte Neutronenstreuung an $\text{Lu}_2\text{Fe}_3\text{O}_7$ offenbart diffus-magnetische Streuung entlang $(\frac{1}{3}\frac{1}{3}\ell)$ und Frequenzabhängigkeit wird in ac-Suszeptibili-

tät gefunden, beides konsistent mit einem glasartigen Gefrieren der Spins anstelle einer langreichweitigen Spinordnung (SO). Das Auftreten von dreidimensionaler LO, nicht jedoch von dreidimensionaler SO in einem $\text{Lu}_2\text{Fe}_3\text{O}_7$ Kristall deutet darauf hin, daß in dieser Verbindung SO fragiler ist gegenüber Abweichungen von der idealen Sauerstoff-Stöchiometrie. Alle magnetischen Eigenschaften sind vereinbar mit einer SO in den individuellen Doppelschichten von $\text{Lu}_2\text{Fe}_3\text{O}_7$, die im Wesentlichen dieselbe ist wie in LuFe_2O_4 , allerdings weniger gut geordnet. Dies wird insbesondere durch die XMCD Messungen aufgezeigt, welche überdies auch in $\text{Lu}_3\text{Fe}_4\text{O}_{10}$ dieselbe SO in den individuellen Doppelschichten suggerieren. Außerdem bestätigt XMCD auch dieselbe LO in den individuellen Doppelschichten. In den zusätzlichen Fe-O Einzelschichten scheint ein magnetisches Moment durch das anlegen eines magnetischen Feldes induziert zu werden, d.h. die Einzelschichten agieren als ein "paramagnetischer" Zusatzbeitrag.

Das Vorhandensein stöchiometrischer Einkristalle mit kommensurabler LO ermöglicht die Verfeinerung der LO. Im Fall von $\text{Lu}_2\text{Fe}_3\text{O}_7$ führt eine Symmetrieanalyse basierend auf dem Ausbreitungsvektor $(\frac{1}{3}\frac{1}{3}0)$ zu denselben möglichen LO Anordnungen wie für LuFe_2O_4 diskutiert: entweder geladene Doppelschichten oder polare Doppelschichten mit einer Stapelung von identischen oder alternierenden Polarisierungen. Im Fall von $\text{Lu}_3\text{Fe}_4\text{O}_{10}$ können nur polare Doppelschichten mit identischer Polarisationsrichtung realisiert werden. Die Verfeinerung der unter Außerbetrachtung der Modulation erhaltenen "Durchschnittsstruktur", erfolgt mit Synchrotron-Röntgenbeugungsdaten gemessen bei 100 K enthüllt Symptome der LO in Form von gespalteten Lu Atompositionen. Diese Spaltung resultiert höchstwahrscheinlich von der Modulation der Lu Positionen, die mit der LO einhergeht, wie in LuFe_2O_4 beobachtet. Erstaunlicherweise bleibt diese Spaltung jedoch im Fall von $\text{Lu}_2\text{Fe}_3\text{O}_7$ bestehen wenn die Überstruktur verfeinert wird, unabhängig von der angenommenen Symmetrie. Die besten Verfeinerungsergebnisse werden für die polare Raumgruppe $\text{Cmc}2_1$ erhalten. Allerdings indiziert die BVS-Analyse eine mittlere Valenz an 8 Fe Positionen und damit eine unvollständige Ladungsordnung in der Doppelschicht. Diese Positionen korrelieren mit den Lu Positionen die gespalten sind. Diese Resultate lassen sich erklären durch die Superposition von LO Konfigurationen unterschiedlicher Symmetrie. Die Formierung solcher struktureller Polytypen kann verstanden werden als verursacht von den durch die Interkalierung abgeschwächten Interaktionen zwischen verschiedenen Doppelschichten, welche den Energiegewinn von LO mit unterschiedlicher Stapelung sehr ähnlich macht. Abschließend kann festgestellt werden, daß die im Rahmen dieser Arbeit erhaltenen Resultate stark darauf hindeuten, daß beide Verbindungen polar sind, was den Ansatz der Interkalation zur Erzeugung von "Ferroelektrizität aus LO" in seltene Erd-Ferriten validiert.

Dedicated wholeheartedly to
my beloved mother and my father who could not see this...

1	Introduction	1
1.1	Multiferroics	1
1.2	The proposed polar compound: LuFe_2O_4	3
1.2.1	Polar/ non-polar CO in LuFe_2O_4 ?	3
1.2.2	Magnetic properties and Spin order in LuFe_2O_4	6
1.3	Motivation and a glance into the history of intercalated rare earth ferrites	8
2	Experimental Techniques & Theory	15
2.1	Synthesis	15
2.1.1	Powder synthesis	15
2.1.2	Single crystal growth	16
2.2	Magnetometry	17
2.2.1	SQUID at MPMS	17
2.2.2	VSM at PPMS/dynacool	19
2.2.3	AC Magnetometry	19
2.3	Scattering Theory and Experiments	19
2.3.1	Scattering Theory	19
2.3.2	Scattering from crystalline structures	21
2.3.3	X-ray scattering	22
2.3.4	Powder X-ray diffraction-Huber Guinier D670	23
2.3.5	Laue diffraction-MWL 120	23
2.3.6	Single crystal X-ray diffraction-Supernova	23
2.3.7	P24-beam-line : single crystal X-ray diffraction	25
2.3.8	Neutron Scattering	26
2.3.9	Nuclear scattering	26
2.3.10	Magnetic scattering	27
2.3.11	DNS instrument	29
2.4	Processing of X-ray diffraction data	30
2.4.1	Data reduction and absorption correction	30
2.4.2	Space group determination and structure solution	31
2.4.3	Structural Refinement in least square	32
2.4.4	Bond Valence Sum (BVS) analysis	33
2.5	X-ray magnetic circular dichroism	34
2.5.1	High field chamber	36
3	Synthesis and optimization of the intercalated compound	39
3.1	Optimization of polycrystalline $\text{Lu}_2\text{Fe}_3\text{O}_7$ synthesis	39
3.2	Effect of stoichiometry on magnetic behavior of polycrystalline $\text{Lu}_2\text{Fe}_3\text{O}_7$	40
3.3	Optimization of single crystal growth of $\text{Lu}_2\text{Fe}_3\text{O}_7$ and $\text{Lu}_3\text{Fe}_4\text{O}_{10}$	42
3.4	Magnetization affected by stoichiometry	44

3.4.1	Variation of magnetic properties in $\text{Lu}_2\text{Fe}_3\text{O}_7$	44
3.4.2	Variation of magnetic properties in $\text{Lu}_3\text{Fe}_4\text{O}_{10}$	47
3.5	Charge order and oxygen stoichiometry	48
3.5.1	Charge ordering in $\text{Lu}_2\text{Fe}_3\text{O}_7$	48
3.5.2	Charge ordering in $\text{Lu}_3\text{Fe}_4\text{O}_{10}$	49
3.6	Discussion	49
4	Magnetic properties of $\text{Lu}_2\text{Fe}_3\text{O}_7$ and $\text{Lu}_3\text{Fe}_4\text{O}_{10}$	51
4.1	Macroscopic magnetic properties of stoichiometric $\text{Lu}_2\text{Fe}_3\text{O}_7$	51
4.1.1	Low field studies of $\text{Lu}_2\text{Fe}_3\text{O}_7$	51
4.1.2	High field studies of $\text{Lu}_2\text{Fe}_3\text{O}_7$	52
4.1.2.1	Isofield magnetization of $\text{Lu}_2\text{Fe}_3\text{O}_7$	52
4.1.2.2	Isothermal magnetization in $\text{Lu}_2\text{Fe}_3\text{O}_7$	54
4.1.2.3	Thermo-remanent magnetization in $\text{Lu}_2\text{Fe}_3\text{O}_7$	55
4.1.3	Magnetic phase diagram of $\text{Lu}_2\text{Fe}_3\text{O}_7$	57
4.2	Macroscopic magnetic properties of stoichiometric $\text{Lu}_3\text{Fe}_4\text{O}_{10}$	58
4.2.1	Low field studies of $\text{Lu}_3\text{Fe}_4\text{O}_{10}$	58
4.2.2	High field studies of $\text{Lu}_3\text{Fe}_4\text{O}_{10}$	59
4.2.2.1	Isofield magnetization of $\text{Lu}_3\text{Fe}_4\text{O}_{10}$	59
4.2.2.2	Isothermal magnetization of $\text{Lu}_3\text{Fe}_4\text{O}_{10}$	60
4.3	Diffuse magnetic scattering	62
4.4	X-ray magnetic circular dichroism	66
4.4.1	X-ray magnetic circular dichroism on $\text{Lu}_2\text{Fe}_3\text{O}_7$	67
4.4.2	X-ray magnetic circular dichroism on $\text{Lu}_3\text{Fe}_4\text{O}_{10}$	71
4.5	Discussion and conclusion	72
5	Charge order studies and crystallographic refinement of $\text{Lu}_2\text{Fe}_3\text{O}_7$ and $\text{Lu}_3\text{Fe}_4\text{O}_{10}$	75
5.1	Commensurate and incommensurate charge ordering in $\text{Lu}_2\text{Fe}_3\text{O}_7$	75
5.2	$\text{Lu}_2\text{Fe}_3\text{O}_7$ CO crystal structure at 100 K	78
5.2.1	Indexing the pattern	79
5.2.2	$\text{Lu}_2\text{Fe}_3\text{O}_7$ representation analysis	80
5.2.3	Refinement of the average structure	86
5.2.4	Super-cell refinement	92
5.3	Commensurate and incommensurate charge ordering in $\text{Lu}_3\text{Fe}_4\text{O}_{10}$	100
5.3.1	$\text{Lu}_3\text{Fe}_4\text{O}_{10}$ representation analysis	101
5.3.2	$\text{Lu}_3\text{Fe}_4\text{O}_{10}$ average structure at room temperature	102
5.4	Discussion	105
6	Summary and outlook	107
	Bibliography	110
	A Appendix	123

List of figures	124
List of tables	136
Acknowledgments	139

1

Introduction

Many functionalities have been discovered such as the high-T superconductivity [1], the magnetocalorics [2], colossal magnetoresistance effect CMR [3–5], negative thermal expansion [6], metal-insulator-transitions [7], and finally what interests us here is multiferroicity [8–10]. Functionality is what ultimately of most interest in materials, which hopefully one day will be applicable for example in information technology applications. These functionalities can be realized in transition metal oxides, which are strongly correlated electron systems with a complex interplay of many active degrees of freedom: charge, spin, orbital and lattice.

1.1 Multiferroics

Multiferroics refer to materials having simultaneously more than one ferroic order [12], for example ferroelectricity and ferromagnetism. The mutual influence of having these two orderings involved in the interaction between charge and spin degrees of freedom with the possibility of switching the order parameter with its conjugate field (i.e. switching the magnetization with electric field and the polarization by magnetic field) demonstrated in Fig. 1.1. This is very promising for practical applications, such as magnetoelectric memory [13], providing an opportunity to write the information with the use of electric field rather than an electric current. Hence, gaining the benefits of overcoming the heat problem, the power consumption and reducing the size as well.

The number of compounds in which magnetism and ferroelectricity coexist is limited [14], due to decisive conditions regarding the symmetry that must be achieved in these materials: both time and spatial inversion symmetries should be broken [8]. Moreover, the conventional mechanisms driving the ferroelectricity and magnetism are contraindicated. Consider for example the classical ferroelectric BaTiO_3 . In this compound, the polarization occurs due to off-centering of the Ti^{4+} cation. This off-centering is stabilized by establishing a covalent bond between the oxygen 2p orbitals and the empty d shell of Ti^{4+} . However, this tendency for off-center ferroelectric distortion is reduced by the d electrons essential for magnetism in transition metals Ti^{4+} [14, 15]. For the mentioned reasons, the researchers started extensively looking for new origins of ferroelectricity that are compatible with magnetism.

The key to understand the ferroelectricity is the concept of electric polarization in which

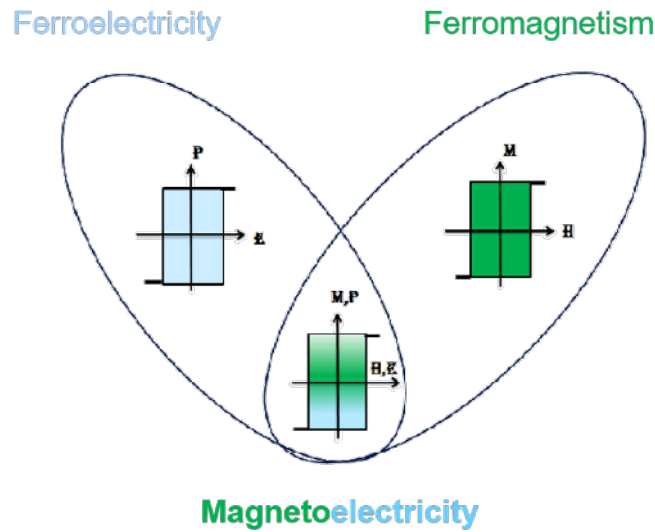


Figure 1.1: Diagram of overlapped two ferroic orders. The ferroelectricity (left) with the polarization P is switchable with the application of electric field E and the ferromagnetism (right) with the magnetisation M is switchable with the application of magnetic field H . In the overlapped area (Magnetoelectric multiferroics), switching process is reversed i.e. H for the electric polarization and E for magnetisation. Concept from [11] and adapted.

an array of electric dipoles are aligned to the same direction. However, to consider system as a ferroelectric, the system should have two or more states with “spontaneous” polarization i.e. nonzero electric polarization in zero applied electric field with the possibility of switching between the states upon the application of electric field. According to the driving force, the ferroelectric materials are categorized into two types: improper and proper ferroelectrics. In the **improper type**, the classification stem from non-conventional ferroelectric induction in which electron pairing is the main driving force of the transition. The ferroelectricity in this case are induced from some complex structural change or magnetic ordering such as a collinear magnetic ordering in $YMnO_5$ [16] which originates from highly frustrated Ising spins for ions with up-up-down-down spins alternatively [17] or from a spin-spiral magnetic ordering in the perovskite $RMnO_3$ series [17] that caused by Dzyaloshinskii-Moriya (DM) interaction [18]. In the **proper type**, the primary order parameter is ferroelectric distortion. Examples of this type are: i) the ferroelectricity is driven by hybridization and covalency such as in the conventional example $BaTiO_3$. ii) the ferroelectricity by Lone-pair in $BiFeO_3$ where the electric polarization stems from the $6s$ lone pair of electrons present in the Bi^{3+} . These electrons are free to move since they don’t participate in any chemical bond. But rather they modify the hybridization to break the inversion symmetry, thus an associated dipole moments is created [9]. iii) the ferroelectricity from geometric frustration as occurs in the hexagonal-type $YMnO_3$ compound [19, 20], which consists of a trigonal bipyramids of MnO_5 separated by a monolayers of Y , these MnO_5 trigonal bipyramids are formed in a different closed-backing structure for energy favorable state i.e. a structural distortion takes place and affects the dipole-dipole interaction in which the oxygen rotation can create a ferroelectric state. iv) finally, the ferroelectricity from

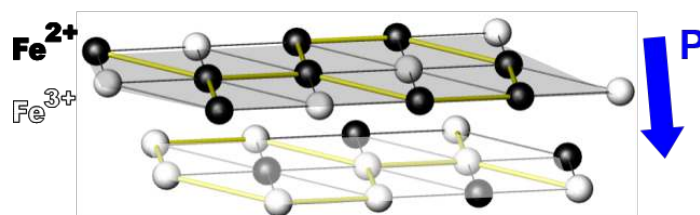


Figure 1.2: Charge order model for single Fe-bilayer as proposed by [25, 26] with polarization direction indicated by arrow.

electronic origin, which is the main focus of thesis, basically occurs via charge ordering of different electron valences which is prevalent in transition metal compounds with ions, that have a mixed valence i.e. the average valence of an ion is not an integer for example in the rare earth ferrite family RFe₂O₄ with R being a 3⁺ ion (Y, Ho, Er, Tm, Yb, Lu, or In). This family crystallizes in a rhombohedral structure, with alternate triangular lattices of Fe₂O_{2.5} bilayers separated by RO_{1.5} monolayers. The Fe ion in RFe₂O₄ has an average valence of 2.5 as result to have an overall neutral compound, meaning a mixed valences Fe³⁺ and Fe²⁺ coexists. The polarization occurs when electric dipoles are formed breaking the spatial inversion symmetry i.e. charge ordering (CO) is non-centrosymmetric. This happens in RFe₂O₄ compounds below the charge ordering temperature when an equal amount of Fe³⁺ and Fe²⁺ are distributed in the Fe₂O_{2.5} bilayers, leading to a disproportionation and a super-lattice due to symmetry lowering. The presence of different Fe-valences implying the first active degree of freedom: the charge. A second degree of freedom is present as well, which is the spin of the mixed Fe-valency. As both the spin and charge degrees of the freedom occurs at the same site, therefore, the same electrons/sites involved, a strong magnetoelectric coupling between them is likely [21].

There are not many examples of materials of multiferroicity of electronic origin (CO). One example is Magnetite (Fe₃O₄), which is a complex charge-ordered crystal structure that was recently understood [22] and found to be polar. In addition, the performed macroscopic measurements by [23] indicated a switchable polarization. The structural switching was recently demonstrated [24]. Another proposed example is LuFe₂O₄ which has attracted a lot of attention as proposed multiferroics due to charge ordering [25]. However, in recent experiments, different results were obtained. These will be discussed in the next section.

1.2 The proposed polar compound: LuFe₂O₄

1.2.1 Polar/ non-polar CO in LuFe₂O₄ ?

LuFe₂O₄ has been extensively studied for its proposed ferroelectricity from charge ordering (CO) of Fe²⁺ and Fe³⁺ in the Fe-O bilayers [25]. This was concluded from pyroelectric current measurements performed by [25], where an apparent remnant electric polarization was observed even larger than in the traditional ferroelectric BaTiO₃, and from dielectric spectroscopy [25, 26], which suggests a freezing of polar domains with antiphase boundaries of short range

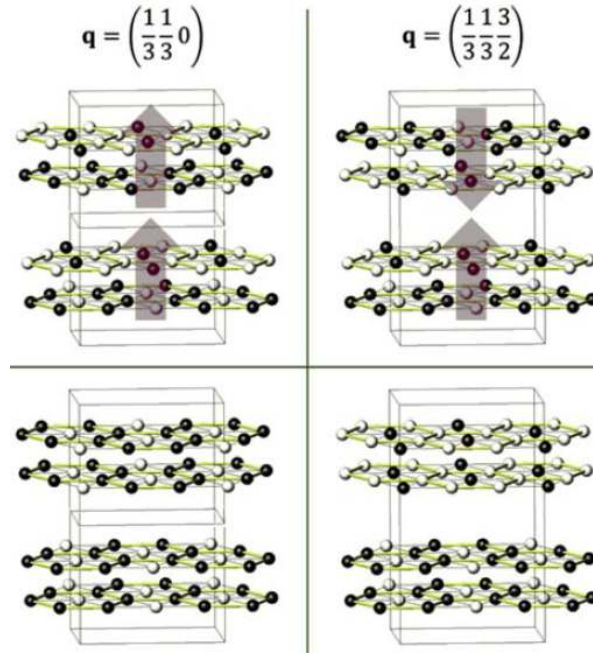


Figure 1.3: Structural solution representation obtained from the representation analysis for two different propagation vectors. Arrows indicated the bilayer polarization direction. Taken from [21].

charge order batches consistent with the presence of ferroelectric polarization. Microscopically, the presence of Fe^{2+} and Fe^{3+} valances in LuFe_2O_4 was clarified by resonant X-ray diffraction [25, 27], and an evidence for the superstructure reflections appearance was reported by [28, 29] below $T_{\text{CO}} \sim 320$ K revealing a three dimensional CO. The observed superstructure reflections were indexed with the incommensurate propagation vector $(\frac{1}{3} + \tau, \frac{1}{3} + \tau, \frac{3}{2})$ and symmetry-equivalent charge order domains with a 120° twining described by $(\frac{-2}{3} - 2\tau, \frac{1}{3} + \tau, \frac{3}{2})$ and $(\frac{1}{3} + \tau, \frac{-2}{3} - 2\tau, \frac{3}{2})$ as reported in [29, 30], with an incommensuration value $\tau \sim 0.0028$ [28, 29]. This led [25] to propose a likely CO model that is polar as shown in Fig. 1.2. In this model one layer of the Fe-bilayer is rich mostly in Fe^{2+} and the other in Fe^{3+} exhibiting an inherent charge imbalance, implying a polar bilayer. The combination of macroscopic indications of ferroelectricity with the proposed polar model was taken as proof of ferroelectricity from CO in LuFe_2O_4 , i.e. the first observation of ferroelectricity of an electronic origin. However, there was no definite proof due to the still lacking details about the actual charge configuration and the stacking of the polarization in different bilayers.

The same type of incommensurately modulated superstructure reflections was observed later [31] below T_{CO} by X-ray scattering, moreover a diffuse scattering consisting of strongly overlapping reflections above T_{CO} with $(\frac{1}{3}\frac{1}{3}0)$ propagation. These studies allow the discussion of potentially CO phases. The found propagation vector suggests an incommensurate modulation of the iron valances indicating a wide distribution of Fe^{2+} and Fe^{3+} in contradiction to what was previously found by spectroscopic measurements [32–34]. Likely, locally a commensurate state is interspersed with discommensurations or antiphase boundaries [21]. Consequently, the representation analysis for $(\frac{1}{3}\frac{1}{3}\frac{3}{2})$ propagation results in two charge order

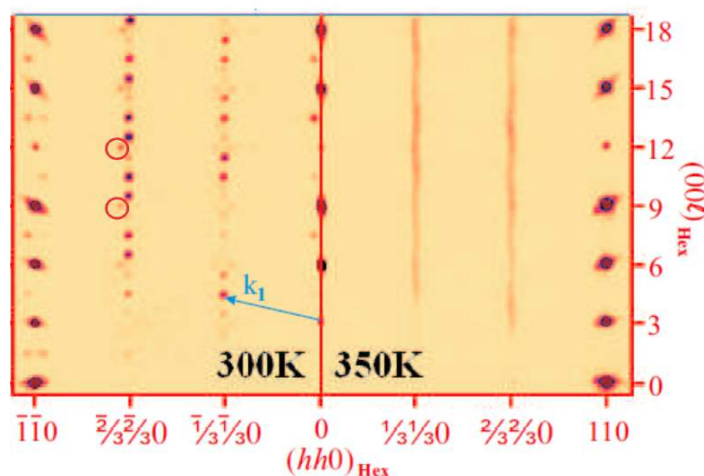


Figure 1.4: Composite image of the hhl -plane of highly stoichiometric LuFe₂O₄ crystal. Left: incommensurate CO at room temperature with circles surrounded the reflections type neglected in the refinement. Right: diffuse scattering replacing the 3D-CO above T_{co} . Taken from [11] and adapted by [35].

configurations: (1) polar bilayers with an antiferroelectric (AFE) stacking but no net polarization (Figure 1.3 upper right), (2) charged bilayers with alternating charge stacking (Figure 1.3 lower right). Configuration (2) was excluded as being unreasonable physically due to the implied transfer of charge between the neighboring bilayers separated by 6 Å [31].

However, representation analysis for $(\frac{1}{3}\frac{1}{3}0)$ propagation also results in two charge order configurations: (1) charged bilayers with net charge (Figure 1.3 lower left), indeed this configuration can be excluded as the whole structure would be charged, (2) polar bilayers with ferroelectric (FE) stacking (Figure 1.3 upper left) which corresponds to what [25] proposed. Given that the observed reflections corresponds to $(\frac{1}{3}\frac{1}{3}\frac{3}{2})$, an antiferroelectric polarization stacking in the bilayers was deduced. This would support LuFe₂O₄ being able to become overall polar if the application of electric field upon cooling switches the antiferroelectric stacked polarization. No prove or disprove of intrinsic ferroelectricity by microscopic methods was given until 2012, in which [11, 36] performed a full structural refinement on the charge ordered crystal. The refinement was done for the two solutions previously proposed in [31] using the $(\frac{1}{3}\frac{1}{3}\frac{3}{2})$ propagation. These are shown in the right (upper, lower) panels of Fig. 1.3), both are monoclinic with space group $C2/m$ but with different inversion center positions. For one, the inversion center is located between the bilayers at Lu positions corresponds to antiferroelectrically (AFE) stacked polar bilayers. For the other, it is located between two Fe layers of a bilayer corresponds to charged bilayers with a net charge. However, the refinement was based on the assumption of commensurate charge order on incommensurate modulated CO, considering the observed incommensurate reflections at $(\frac{1}{3}, \frac{1}{3}, 0)$ and $(0, 0, \frac{3}{2})$ as discommensuration. Performing the refinement commensurately led to poor integration for $(\frac{N}{3} \pm \tau, \frac{N}{3} \pm \tau, 0)$ and $(\pm \tau, \pm \tau, \frac{3}{2})$ indexed reflections (marked by circles in Fig. 1.4) and made the model which has inversion center between two Fe layers statistically more favorable. This indicated the non-polar CO in the bilayers precluding the ferroelectricity. The absence of

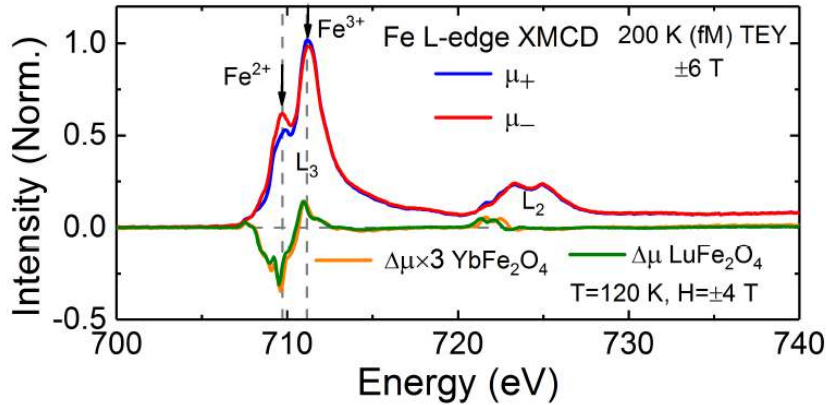


Figure 1.5: XMCD spectra for both LuFe_2O_4 at 4 T and YbFe_2O_4 at 6 T across the Fe $L_{2/3}$ with total electron yield. Taken from [35].

polarity is confirmed by dielectric measurements and polarization hysteresis loops measured by [37, 38] and later by [39]. The possible explanation for the results of the pyroelectric current measurements and the dielectric spectroscopy is that the remanent polarization originates from the charge carrier localized at surfaces. Up to date, no commensurate CO phase in LuFe_2O_4 was found under any conditions. However, a transition from a very similar incommensurate CO phase to a commensurate one was discovered recently in the isostructural YbFe_2O_4 [35, 40]. The structural refinement of the commensurate CO phase in YbFe_2O_4 incorporating all the observed superstructure reflections unexpectedly was achieved in $P\bar{1}$, resulting in polar bilayers with anti-polar stacking [35], which was earlier proposed by Angst for LuFe_2O_4 [31], but with a lower symmetry ($P\bar{1}$ rather than $C2/m$). The lower symmetry $P\bar{1}$ solution corresponds to a superposition of the two configurations shown in the right panel of Fig. 1.3. This result is representative for LuFe_2O_4 , since the Yb is quite close in size to Lu. However, oxygen stoichiometry plays an important role in the intrinsic properties of the system, because it controls the Fe^{2+} and Fe^{3+} ratio in the compound [41, 42]. The availability of the stoichiometric LuFe_2O_4 crystals was the key for the establishment of 3D CO, however, the effect is not limited to the CO but also extended to the magnetic properties and the spin order as will be discussed in the next section.

1.2.2 Magnetic properties and Spin order in LuFe_2O_4

The extensive investigations by different techniques showed a very rich magnetic behaviour for LuFe_2O_4 , which however varies with the oxygen content. The oxygen stoichiometry of different sample was characterized by magnetization vs temperature measurements in low magnetic fields. The criteria is the sharpness of field cooling (FC) curve in low field at T_N , but also the variation in the transition temperature (T_N) i.e. the higher T_N is the more stoichiometric [11]. The Fe spins have a strong preference to be aligned $\parallel c_{\text{hex}}$ (Ising) below T_N [33, 43, 44]. For off-stoichiometric samples, the macroscopic magnetic properties reveal a growing 2D-ferrimagnetic phase characterized by a smearing and broadening in the FC curve

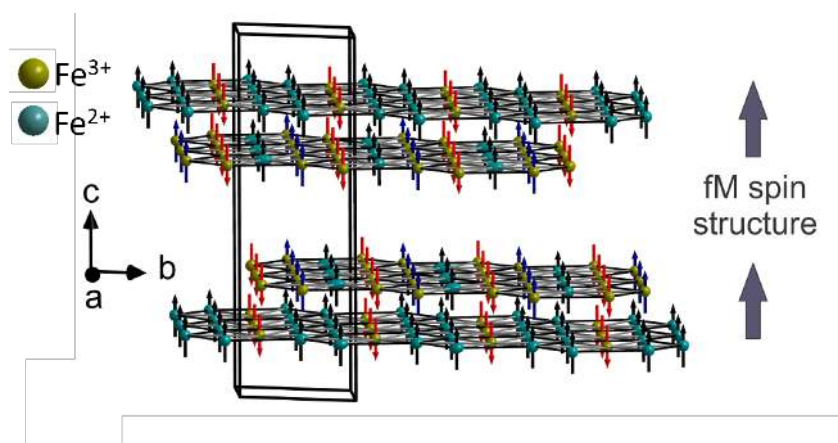


Figure 1.6: The combined CO with SO $P\bar{1}$ superstructure cell for the ferrimagnetic phase in YbFe₂O₄. Taken from [35].

[11]. Moreover, Mössbauer spectroscopy in combination with neutron diffraction [45, 46] show the formation of a ferrimagnetic cluster state with Ising spin behaviour along the c -direction, but not 3D long range magnetic order, indicated for example by diffuse magnetic scattering along $(\frac{1}{3}\frac{1}{3}\ell)$ below T_N . The observation of spin glass state is indicated by a strong frequency dependence in AC magnetization measurements [47]. In samples of different quality, high coercive fields are observed at low temperatures [34, 47–50]. The potential explanation was by [34] in terms of kinetic arrest between two different magnetic phases, and by [50, 51] due to the formation of the packing configuration of irregular Ising pancakes in which the enhancement of coercivity is linked to collective freezing of these Ising pancakes for lower temperatures. In contrast, for the stoichiometric samples, in macroscopic magnetic measurements a sharp-FC feature was seen, revealing long-range spin order at $T_N \sim 240$ K accompanied at $T_{LT} \sim 170$ K by a low temperature phase transition into a phase with glassy magnetic dynamics. Additionally, in neutron diffraction, sharp magnetic Bragg peaks along the $(\frac{1}{3}\frac{1}{3}\ell)$ diffraction line were observed [43, 52, 53], in particular at $(\frac{1}{3}\frac{1}{3}\frac{3}{2})$ positions suggesting the existence of long-range magnetic spin order. However, above T_N , the measurements performed by [11, 53] show a random stacking of the bilayer net moment of still medium-range ordered bilayers, i.e. a 2D order, with additional indication seen in the deviation of magnetization from Curie-Weiss behaviour up to ~ 400 K. The established magnetic phase diagram [53] reveals a competition between the two nearly degenerate AFM and fM phases at T_N . This competition between the fully ordered spin alignments was attributed to geometrical frustration [11, 53].

The observed magnetic unit cell [53] was found to be identical to the CO supercell $C2/m$. However, as the refinement of the CO for the commensurate case in YbFe₂O₄ was achieved in a lower symmetry ($P\bar{1}$) as mentioned in the previous section, it is likely that the magnetic space group is also $P\bar{1}$ [35]. The performed XMCD measurements on YbFe₂O₄ and also LuFe₂O₄ are presented in Fig. 1.5. In these measurements, but also in [11, 33, 44], the downward peak was assigned to Fe²⁺, which is larger than the upward peak (assigned to Fe³⁺). Regardless of the stoichiometry, XMCD spectra can be explained by: all the Fe²⁺ and $\frac{1}{3}$ of the Fe³⁺ spins

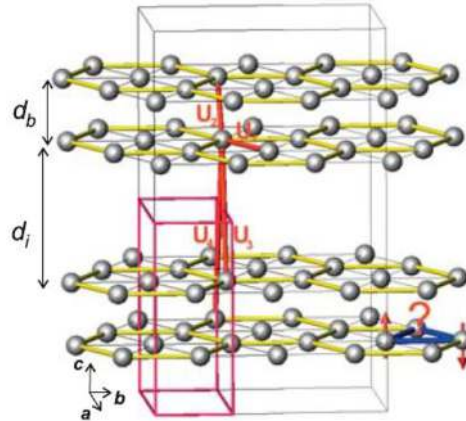


Figure 1.7: Minimum set of interactions $U_1 \dots U_4$ leading to 3D charge ordering. Geometrical frustration is indicated by blue triangle. Taken from [21].

pointing in the field direction, and the remaining Fe^{3+} ($\frac{2}{3}$) spins pointing opposite to the field. The final combined CO and SO supercell is shown in Fig. 1.6. As can be seen, two bilayers are present in the unit cell, each containing 6 Fe sites, the bond valance-sum analysis [35] revealed that in each bilayer, 3 Fe sites are of 2+ valance and 3 Fe sites of 3+ valance as distributed, with the help of the XMCD, the 3 Fe^{2+} are determined to be all up and 2:1 Fe^{3+} down, up respectively.

1.3 Motivation and a glance into the history of intercalated rare earth ferrites

For the stacked layers RFe_2O_4 that contain mixed Fe valance, a repulsive force between the extra-electrons on Fe^{2+} sites, drives Fe^{2+} and Fe^{3+} to be ordered with electrostatic energy being minimized. The appearance of 3D charge orders can be explained using the model by Yamada et al. [30] in which at least four different screened coulomb interactions are required $U_1 \dots U_4$, shown in Fig. 1.7. For magnetic ordering, similar consideration holds, and an equivalent minimal set of super-exchange interactions [54, 55] is needed.

To explain the stabilized CO in the bilayer, two interactions should be taken into account, U_1 and U_2 . With only U_1 considered, whole CO configurations are degenerate, simply due the fact the Fe ions are arranged in a triangular geometry leading to what called "geometrical frustration" for both CO and SO. However, considering U_2 broke the degeneracy leading to a preferred CO. The realized CO pattern theoretically [56] for example in YFe_2O_4 is different than the found experimentally [57] indicted the contribution of other factors in stabilizing the CO, such as lattice in which the relaxation lowering the energy of the CO further [58] and magnetism [55] in the light of the strong spin-charge coupling. Despite these additional factors, CO can be stabilized in one bilayer by controlling U_1 and U_2 interactions. For example, the rare earth substitutions (changing the rare earth ion size) led to a significant distortion in the bilayer and therefore, tuning the relevant interactions [21] resulting in a similar CO

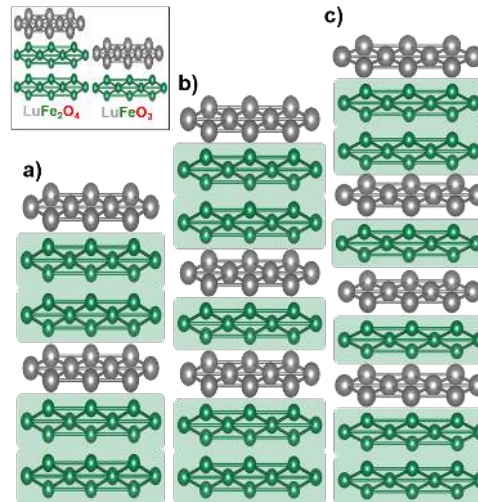


Figure 1.8: Sketch of the layer stacking of a) LuFe₂O₄, b) Lu₂Fe₃O₇ containing one LuFeO₃ block, c) Lu₃Fe₄O₁₀ containing two LuFeO₃ blocks (Oxygen ions are omitted). Taken from [64].

for R = Yb, which has almost the same ion size as Lu [35, 59] but a dramatically different CO for the larger Y [57, 60]. Another way to tune the CO is to focus on the interactions between different bilayers. This can be achieved by intercalating single Fe-O layers, increasing the distance between the bilayers, therefore, inter-bilayer couplings can be expected to become weaker, possibly rendering the anti-polar stacking to a polar.

In intercalated rare earth ferrites RFe₂O₄(RFeO₃)_n, nRFeO₃ blocks are inserted between the Fe-O bilayers (see Fig. 1.8), forming (as a function of n) a series of compounds that crystallize alternately in rhombohedral (R $\bar{3}$ m, n even) and hexagonal (P6₃/mmc, n odd) space groups as found for the Yb-compound in [61–63]. Each RFeO₃ block contains a mono-layer of Fe-O and a mono-layer of R-O.

The fact that intercalations of rare earth ferrites exist has been known since the 1970s. The initial synthesis of intercalated RFe₂O₄ (R= Lu, Yb) was achieved in 1974 by Kimizuka et al. [65]. They were successful in growing single crystals of Yb₂Fe₃O₇, but not Lu₂Fe₃O₇, in a hexagonal structure, surprisingly with the use of CO₂/H₂ atmosphere to control the oxygen stoichiometry. The use of CO₂/H₂ atmosphere for crystal growth normally would lead to the formation of water and disturb the nucleation process [66]. Soon afterward, the synthesis and optimization of the oxygen content were performed for both Yb₂Fe₃O₇ [67] and Lu₂Fe₃O₇ [42]. The established phase diagram of the Fe-Fe₂O₃-Lu₂O₃ ternary system at 1200 C° is shown in Fig. 1.9. No systematic change of lattice parameters for samples with different oxygen stoichiometry was noticeable in [42] as can be seen in Fig. 1.10. These changes are very small, with no minima in c lattice parameter of the stoichiometric sample in contrast to LuFe₂O₄. The stoichiometry range for Lu₂Fe₃O_{7- δ} is wider than for LuFe₂O_{4- δ} , with δ ranging from 0 to 0.104 (0 to 0.065 and surplus of 0.015) for Lu₂Fe₃O_{7- δ} (LuFe₂O_{4- δ}) according to [42]. In particular, no region of surplus oxygen ($\delta < 0$) was reported in [42], suggesting that the most stoichiometric compound will be near the upper phase stability range with respect to the equilibrium oxygen partial pressure, which is 10^{-7.53} atm at 1200 C°. At the upper stability

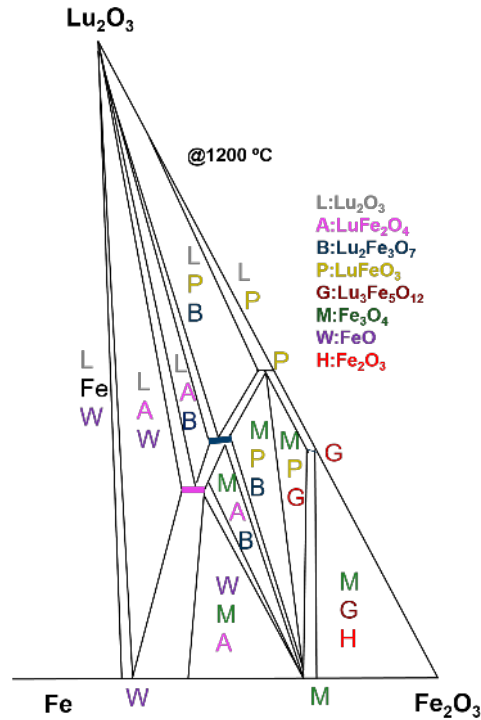


Figure 1.9: Phase diagram of the Fe-Fe₂O₃-Lu₂O₃ at 1200 C° with the use of different CO₂/H₂. The regions where Lu₂Fe₃O₇ are stable are marked in blue and LuFe₂O₄ in pink. Lu₃Fe₄O₁₀ and higher intercalated compounds are not present in this phase diagram, which may be only stable at higher temperatures. Redrawn from [42].

limit, the stoichiometric sample Lu₂Fe₃O₇ is in equilibrium with Fe₃O₄ and LuFeO₃. This is different for stoichiometric Yb₂Fe₃O₇, which is in equilibrium with YbFe₂O₄ and YbFeO₃ [67].

Parameter	[65]	[68]
Spacegroup	P6 ₃ /mmc	P6 ₃ /mmc
a (Å)	3.4523(3)	3.4551(1)
c (Å)	28.416(5)	28.4347(9)
V (Å ³)	283.29(7)	293.962(17)

Table 1.1: Published Lu₂Fe₃O₇ Lattice parameters

The crystal structure of Yb₂Fe₃O₇ at room temperature was determined by [69, 70] and is presented in Fig. 1.11. It crystallizes in P6₃/mmc space group. The unit cell contains two Fe-bilayers of triangular arrangements alternating along the c-direction sandwiched by single Fe-layer and two Yb-layers. In the single Fe-layer, Fe ions are coordinates by five O²⁻ ions forming a trigonal bipyramid. The arrangement of bi- and trivalent Fe ions on the triangular lattice leads to both spin and charge frustration. The lattice parameters refinement of polycrystalline Lu₂Fe₃O₇ by [65, 68] led to the results summarized in table 1.1.

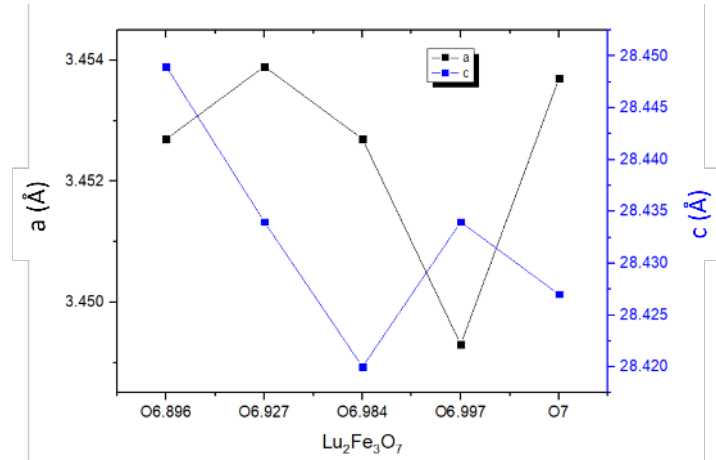


Figure 1.10: The change of lattice parameters of polycrystalline $\text{Lu}_2\text{Fe}_3\text{O}_{7-\delta}$ for different oxygen stoichiometry. Figure plotted based on data from [42].

Several magnetic measurements, neutron diffraction and Mössbauer spectroscopy studies [46, 71, 72] performed on off-stoichiometric polycrystalline $\text{Lu}_2\text{Fe}_3\text{O}_7$, indicate that the Fe-O mono-layer in LuFeO_3 block contains only Fe^{3+} ions, while the bi-layer contains $\text{Fe}^{2.5+}$ as in LuFe_2O_4 . 2D magnetic ordering was concluded from neutron diffraction and suggested by Mössbauer spectroscopy in [46, 71, 72] in which the Fe ions in the bilayer ordered ferrimagnetically along c-direction around 260 K/ 230 K (265-270 K was found later by [68]), i.e. behave similar as in LuFe_2O_4 , while Fe^{3+} ions in the single layer are paramagnetic down to ~ 100 -80 K behave as Heisenberg-like spins in a two-dimensional antiferromagnet on a triangular lattice. However, below 50 K, the latter lie on c-plane i.e. making an angle with c-axis that is changing with temperature and equal to 20° at 4.2 K. Moreover, hysteresis measurements [73] show a large coercive field of about 5 T at 77 K. A large coercivity has been observed before in LuFe_2O_4 and claimed to be originating from the collective freezing of nanoscale pancake-like ferrimagnetic domains with large uniaxial anisotropy (named Ising pancake) [51]. Furthermore, the magnetic susceptibility per Fe at low-T and the thermoremanent magnetization (TRM) per formula unit are similar to LuFe_2O_4 [73]. The only study of $\text{Lu}_2\text{Fe}_3\text{O}_7$ [74]

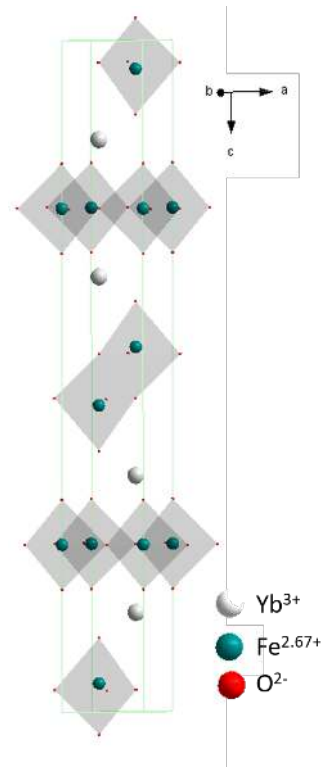


Figure 1.11: The hexagonal crystal structure of $\text{Yb}_2\text{Fe}_3\text{O}_7$ at room temperature drawn based on [69, 70].

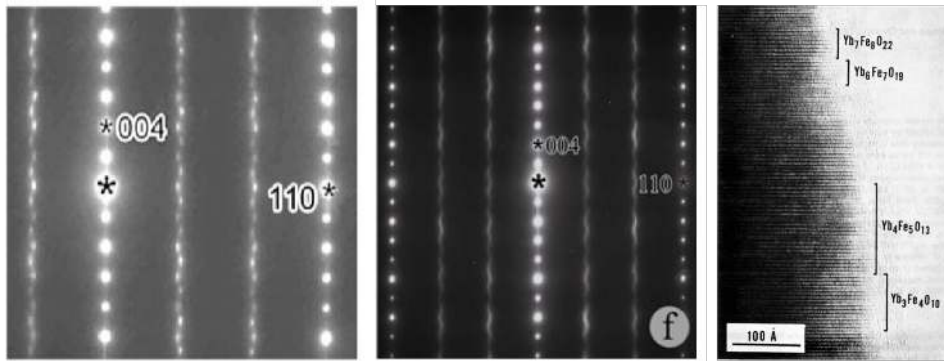


Figure 1.12: Electron diffraction image shows the (left) incommensurate superstructure reflections of $\text{Lu}_2\text{Fe}_3\text{O}_7$, taken from [75] (middle) diffuse scattering of $\text{Yb}_2\text{Fe}_3\text{O}_7$, taken from [76] (right) intergrowth of different Yb-intercalated compounds, taken from [61].

by neutron single-crystal diffraction reports the observation of a diffuse magnetic rod along $(\frac{1}{3} \frac{1}{3} \ell)$, which corresponds to typical observations in off-stoichiometric RFe_2O_4 [21]. The diffuse rod indicates the presence of two dimensional spin order, meaning at least short to medium range correlations within the bilayers while little correlation between different layers. Since the distance of iron ions in different (bi)layers is much larger than the in-plane nearest neighbour distance (c.f. Fig. 1.11), in-plane correlations are much stronger than out-of-plane correlations.

The observation of superstructure spots has been reported only from electron diffraction on small grains of polycrystalline $\text{Lu}_2\text{Fe}_3\text{O}_7$ [75, 77]. These spots form an incommensurate zig-zag pattern around the $(\frac{1}{3} \frac{1}{3} \ell)$ line (see Fig. 1.12left), which is consistent with a similar CO as in LuFe_2O_4 but rather up to higher temperatures than LuFe_2O_4 . However, electron diffraction is generally not suited to deduce the concrete CO pattern in real space since the electron diffraction can only probe a small area of the sample and intensities are heavily influenced by multiple scattering. For $\text{Yb}_2\text{Fe}_3\text{O}_{7-\delta}$, electron diffraction on small off-stoichiometric crystals with oxygen deficiency $\delta = 0.12$ by [63] and on polycrystalline samples by [76] showed only two-dimensional charge order (see Fig. 1.12 middle).

Polarization hysteresis loop (P-E) was observed for $\text{Lu}_2\text{Fe}_3\text{O}_7$ by [77] (see Fig. 1.13a), nevertheless, it was unstable due to the charge fluctuations and did not exhibit the ideal square shape due to the current leakage as reported by [78]. However, with slight (29%) Mn for Fe substitution, the current leakage is suppressed resulting in the only believable polarization hysteresis loop in the rare earth ferrite literature [77] (see Fig. 1.13b). Although a very small polarization was found, still it indicates ferroelectricity being realized in the compound. In contrast, LuFe_2O_4 exhibits linear P vs E curves without hysteresis saturation [37–39] (see Fig. 1.13c). Later measurements performed on the Mn-doped $\text{Lu}_2\text{Fe}_3\text{O}_7$ indicated the occurrence of at least piezoelectricity confirmed by piezoresponse force microscopy [79]. Partial substitution on the iron site with Mg^{2+} in the intercalated $\text{Lu}_2\text{Fe}_3\text{O}_7$, generally leads to a suppression of long-range charge and magnetic ordering greater than for LuFe_2O_4 [80]. A recent study [81] of intercalated Lu-compounds grown in artificial heterostructures, indicates that ferroelectricity is not realized in thin film $\text{Lu}_2\text{Fe}_3\text{O}_7$.

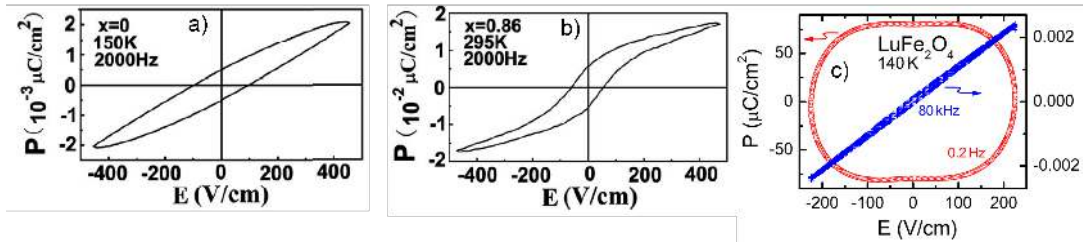


Figure 1.13: The P-E hysteresis loops of (a) $\text{Lu}_2\text{Fe}_3\text{O}_7$ [38] (b) $\text{Lu}_2\text{Fe}_2\text{Fe}_{0.14}\text{Mn}_{0.86}\text{O}_7$ [38] and (c) LuFe_2O_4 [77].

For the intercalated rare earth ferrites $\text{RFe}_2\text{O}_4(\text{RFeO}_3)_n$ with $n > 1$, small crystals particularly of $\text{Yb}_3\text{Fe}_4\text{O}_{10}$ and $\text{Yb}_4\text{Fe}_5\text{O}_{13}$ were synthesized by Kimizuka et al. in 1976 [61]. However, in these crystals, an intergrowth of other intercalated Yb-compounds was observed by electron diffraction. The intergrown compounds extend over large regions in the crystals as shown in the right panel of Fig. 1.12, which led to a difficulty in the crystal structural refinement. The grown [61] off-stoichiometric $\text{Yb}_3\text{Fe}_4\text{O}_{10}$ crystals were studied using electron diffraction by [63], showing diffuse scattering, i.e. 2D CO.

The CO within the individual bilayers of intercalated rare earth ferrites may be expected to be very similar as the CO in not intercalated ones because the very similar local atomic arrangement (see Fig. 1.14) implies very similar intralayer interactions, with the intercalation serving as another knob to tune the concrete 3D arrangement involving many bilayers. However, the more complex crystal structure makes the synthesis of high quality single crystals more difficult. This complication is added to the problem of ensuring the proper oxygen stoichiometry already noted for not intercalated rare earth ferrites, where it was found to be critical to the elucidation of the CO that is established [35, 36, 57, 59, 60]. The hope is that the ferroelectricity will be realized in the intercalated $\text{Lu}_2\text{Fe}_3\text{O}_7$, however, unconventionally, the motivation for the investigation.

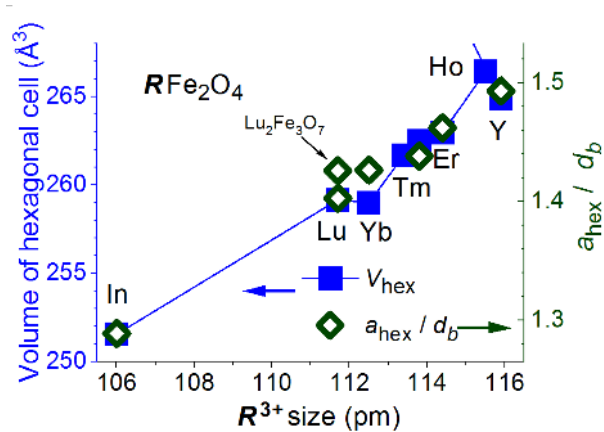


Figure 1.14: The rare-earth ion radius R^{3+} effect on the cell volume from and the ratio of the intralayer Fe-Fe distance a_{hex} to bilayer thickness d_b . Figure from [21] and adapted, data based on [44, 45, 47, 65, 82–85].

2

Experimental Techniques & Theory

2.1 Synthesis

2.1.1 Powder synthesis

Achieving the aim of the elucidating the CO of $\text{Lu}_2\text{Fe}_3\text{O}_7$ requires the fabrication of samples in form of single crystals. For this, polycrystalline samples need to be synthesized at first. Following the same method used in preparing many of the rare earth ferrites (e.g. [59, 60]), powdered Lu_2O_3 (99.9%) and Fe_2O_3 (99.99%) were mixed in stoichiometric quantities with respect to the metal ions. With significant grinding of the mixture by ball milling using an addition of isopropanol, a homogeneous fine mixture is produced, which is necessary to maximize the surface contact area between particles thus reducing the diffusion path length according to Fick's 1st law (eq. 1.1) and enhancing the reaction rate.

$$J = -D \left(\frac{\partial c}{\partial X} \right) \quad (2.1)$$

Here, D is the diffusion coefficient, J is the flux of diffusing species and $\left(\frac{\partial c}{\partial X} \right)$ represents the concentration gradient.

Pelleting the powder was essential to ensure the reaction to be completed and avoid the appearance of white color identified as due to an impurity of Lu_2O_3 , see Fig. 2.1 left. Afterward, the pellet was calcined in a tube furnace (shown in Fig. 2.1 right) under controlled oxygen partial pressure using varying mixtures of flows of CO_2 and $\text{Ar}(96\%):\text{H}_2(4\%)$ at 1250°C , for 40 hours. At first, gas is passed for a period of time to expel all air from the furnace, and then continues to flow during the heating and cooling cycle. Gas flow was surely maintained during the reaction by monitoring the bubbler. The oxygen partial pressure resulting from using different gas ratios determines phase stability and oxygen stoichiometry [42]. The raw ground powder was compressed using a hydraulic press to form rods of 5-6 cm (feed rod) and 1-2 cm (seed rod) in length for single crystal growth then sintered to improve the mechanical strength using the same temperature and time used for the pellet in a flow of 27 ml/min. CO_2 and 30 ml/min. $\text{Ar}(96%):\text{H}_2(4\%)$ to maintain the phase purity.

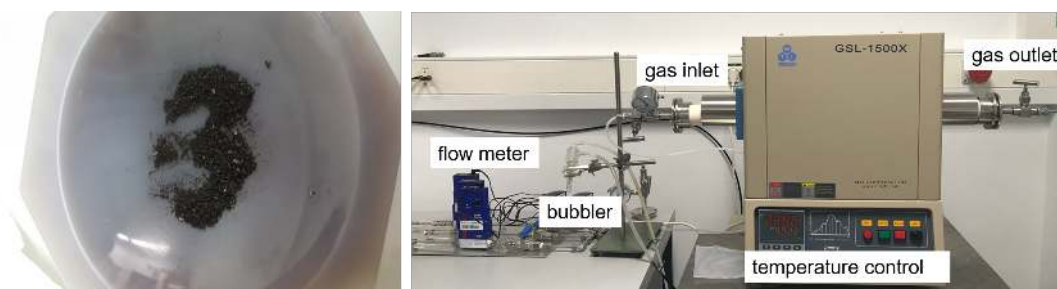


Figure 2.1: $\text{Lu}_2\text{Fe}_3\text{O}_7$ prepared as loose powder, white color indicated impurities of Lu_2O_3 and the used tube furnace.

2.1.2 Single crystal growth

The floating zone method was used for crystal growth employing a four-mirror furnace FZ-T-10000-H-VI-VP0 (see Fig. 2.2). This method had been used successfully by [74] to prepare $\text{Lu}_2\text{Fe}_3\text{O}_7$ single crystals, but without optimization for the oxygen stoichiometry.

In the process of our crystal growth, I chose halogen lamps of 1KW power which are installed at the foci of the four mirrors to create a localized hot zone. At the first stage, the feed and seed rods are set separately in a vertical setup and adjusted to be in the hot zone, surrounded by quartz tube, and flushed with Argon gas, this enables the control of the atmosphere. We rotate both rods in opposite directions with rotation speed of 20 (16) rpm for the feed (seed) rod to achieve better mixing for the molten zone and better heat distribution. As the tips of both rods are melted, we brought them in contact and move them downward gradually away from the localized hot zone. Melting occurs at the upper solid-liquid interface and at the same time crystallization occurs at the lower solid-liquid interface, at the end the molten zone freezes out and set on the lower interface in a crystalline form which is energetically more favorable. However, to keep the stability of the molten zone, the proper amount of energy must be provided. If the energy exceeds the limit, the volume of the molten zone increases, causing it to eventually drop down because the surface tension is no longer balancing the pressure.

A growth speed of 1-1.1 mm/hr was used, since the lower the speed, the larger the chance is to get a bigger single crystal as found by [41]. A direct visual observation using a camera was possible. A gas flow of varying CO_2/CO ratio was used to tune the oxygen partial pressure during the growth. Fine tuning of the gas ratio was previously used to grow high-quality crystals of LuFe_2O_4 [43], YFe_2O_4 [60] and YbFe_2O_4 [59]. However, stabilizing the molten zone was more difficult compared to LuFe_2O_4 , which might be due to the complex layered structure and no stoichiometric single crystals that are large enough for e.g. neutron diffraction were obtained. The grown boule has a length of about 8 mm.

In analogy to LuFe_2O_4 [11], the obtained crystals tend to cleave along the layers. Facets are formed because of the anisotropic distribution of the growth velocities, here in particular (001) facets are formed [41, 86]. The grown boule of $\text{Lu}_2\text{Fe}_3\text{O}_7$ in a gas flow of $\text{CO}_2/\text{CO} = 33$ and a cleaved facet along the layer can be seen Fig. 2.2b. Based on trial-and-error, many attempts

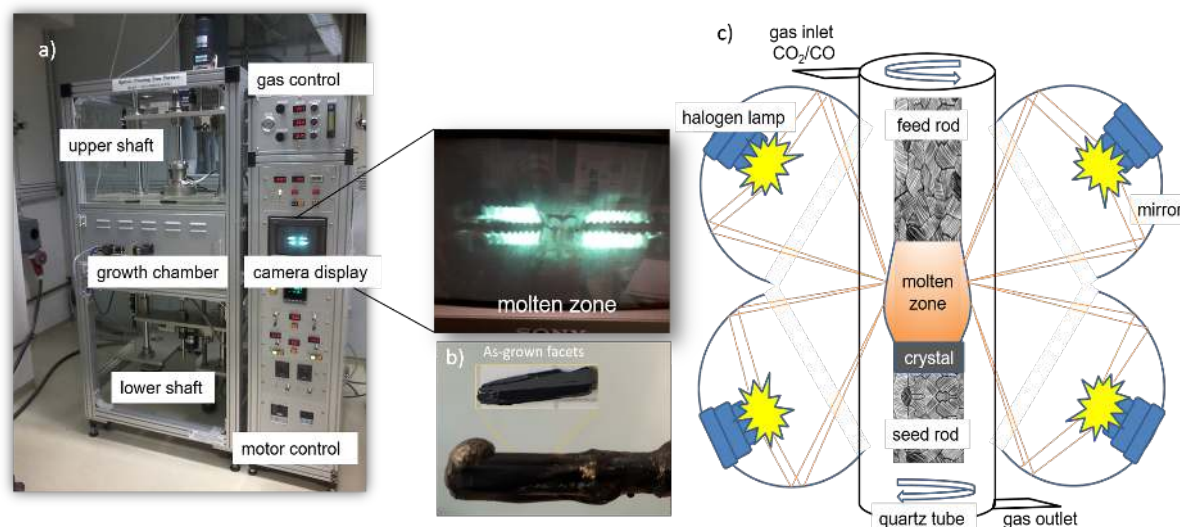


Figure 2.2: a) An image of the used optical mirror furnace with inset of a real molting zone b) Crystal boule grown in gas flow of $\text{CO}_2/\text{CO} = 33$ and (001) facets c) Sketch of the floating zone setup with four mirrors. b) taken from [64].

with different gas ratios had been made to optimize the stoichiometry. In order to analyze the grown rod for each attempt, it was crushed, and the desired crystals were isolated by hand under the microscope. No calculations were made for the oxygen off-stoichiometry δ neither for polycrystalline samples nor single crystals by Thermo-Gravimetric-Analysis, as for the needed accuracy in δ , TGA is at the limit of what is feasible (c.f. [87]).

2.2 Magnetometry

In order to understand the magnetic behavior of our compounds and investigate their response to the presence of magnetic field and temperature, either the Vibrating Sample Magnetometer (VSM) option of a Quantum Design PPMS/ DYNACOOOL [88] or the Reciprocating Sample Option (RSO) of a Quantum Design MPMS [89] were used. The change of the magnetization as a function of the temperature was examined using the ZFC (Zero Field Cooling) protocol, which was obtained when the sample is cooled in zero field and the magnetization is recorded while warming in the presence of a field. On the other hand, FC (FW) curves are measured, which are obtained as the sample is cooled and warmed in an applied field and the magnetization is measured during cooling (warming). Moreover, the magnetic hysteresis $M(H)$ was measured.

2.2.1 SQUID at MPMS

The Magnetic Property Measurements System (MPMS) is a Superconductor Quantum interface device (SQUID) detection system. It uses the combination of superconducting material and Josephson junction to measure the magnetic moment in temperature range of 4 to 400 K and magnetic field of 0 to 7 T. Liquid helium is used to cool the sample and keep the electromagnet

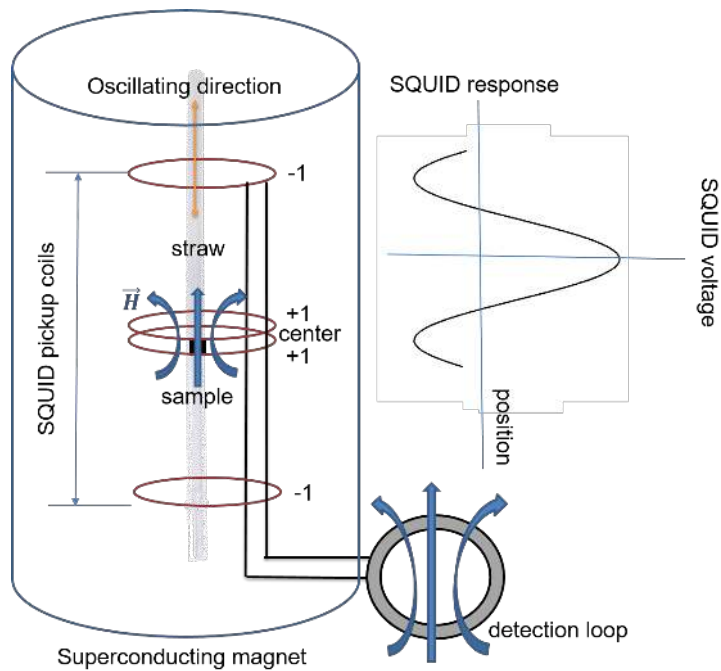


Figure 2.3: Illustration of the SQUID set up and it's response curve.

in a superconducting state. The big advantage of the MPMS is the high sensitivity ($5 \cdot 10^{-8}$ emu) especially at low fields, this was very critical for our measurements due to the very small size of the stoichiometric crystals and the use of low field of 100 Oe.

Our measurements were performed using the Reciprocating Sample Option (RSO). In contrast to the DC measurements, where the sample is moving in a discrete steps through the coils, RSO measures the sample by moving it rapidly and sinusoidally through the coils achieving faster measurements. An illustration of the SQUID setup is shown in Fig. 2.3. Samples are mounted on a Teflon strip with GE varnish, which is then it settled on top of a half straw. The whole set is then inserted inside a complete straw. Another half empty straw was added to get a homogeneous holder and reduce the background.

The principle is: the sample is oscillating through superconducting pickup coils linked to a superconducting detector loop with parallel Josephson junctions under an applied external magnetic field. A magnetic flux is produced by the oscillating sample and an applied bias current reestablishes in the superconducting loop indicating the magnetism of the sample. The changes of the voltage in the coils can be traced as a function of sample position in the so called response curve (shown in Fig. 2.3) and the moment is then obtained by fitting the response as resulting from a point-like dipole moment. The RSO option of the MPMS measures the sample while it is oscillating either at the center position or at the maximum slope position. At the center position, the sample is properly located and full response curve of sinusoidal shape is obtained due to configuration of the pickup coils as a second order gradiometer (shown in Fig. 2.3), while at the maximum slope position, the sample is oscillated over 2mm at the linear part

of response curve. Due to the low magnetic moment for our small crystals, a magnetized piece of a floppy disk was used to provide a sufficient signal in the centering process.

2.2.2 VSM at PPMS/dynacool

The Vibrating sample Magnetometer (VSM) option of a Quantum Design PPMS (Physical Property Measurement System) was used as a DC magnetometer for measuring the equilibrium value of the samples magnetization specially the large size samples. It provides a higher maximum magnetic field of 9T but lower sensitivity (10^{-6} emu) than the MPMS. It is based on Faraday's law, where the sample is oscillating near detection pickup coils, which detect the induced voltage corresponding to the flux change, therefore the magnetic moment in the sample. Dynacool [90] is the same as the PPMS but without the need for helium filling since it uses a closed cycle cryostat.

2.2.3 AC Magnetometry

AC magnetic susceptibility measurement was used to get information about the magnetization dynamics if present, in a region around the transition temperature. It was conducted for large-sized samples on the PPMS, where an alternating magnetic field of 10 Oe was applied with a frequency range between 30 to 9300 Hz. This alternating field generates moments oscillating with same frequency (time-dependent moments), allowing the measurements without the need to oscillate the sample. This yields in-phase real part susceptibility χ' and out-of-phase imaginary part susceptibility χ'' . More information are available in [91].

2.3 Scattering Theory and Experiments

Much of our understanding about the microscopic characteristics of materials was obtained by scattering. Scattering is a non-destructive unique tool, where a beam of particles hits a target and the particles emerging after the interaction with the sample are observed. Scattering forms a large portion of the experimental work performed in this thesis, therefore, the foundations of the scattering theory will be briefly reviewed at first, followed later on by the used methodologies and the related instruments for both X-ray and neutron scattering.

2.3.1 Scattering Theory

Here, we deal with quantum description of scattering neglecting the inelastic scattering involving creation or annihilation of phonons or similar collective excitations. The result of this description is applicable to both X-rays and neutrons. In scattering experiments, we aim to investigate the scattering potential $V(\mathbf{r}')$ describing the interaction of the studied sample with the incident particles. As a starting point, this interaction is described by the stationary Schrödinger equation. The wave nature is considered during the derivation of the scattering theory.

Before scattering, the incident particles are sufficiently far away from the scatterer, so the potential is zero, and the incident particles are considered to be free. Their state can be

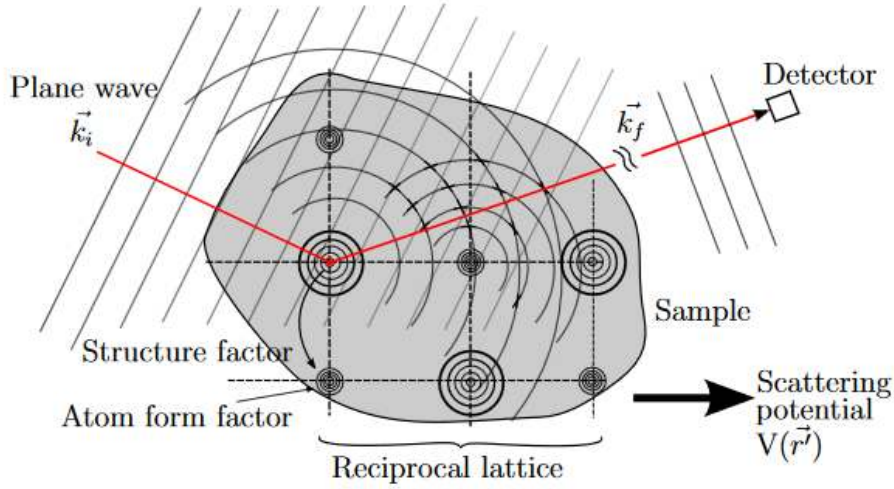


Figure 2.4: Illustrations of scattering geometry, taken from [92].

represented by a plane wave: $\Psi_{\mathbf{k}}(\mathbf{r}) = \Psi_0(\mathbf{r})e^{i\mathbf{k}\cdot\mathbf{r}}$ with the wave vector \mathbf{k} . When the scattering occurs, these plane waves interact with the scattering potential $V(\mathbf{r}')$ creating spherical waves $\Psi_{\mathbf{k}}(\mathbf{r}') = \Psi_0(\mathbf{r}')e^{i\mathbf{k}'\cdot\mathbf{r}'}/(4\pi|\mathbf{r} - \mathbf{r}'|)$ at all sample positions. Their amplitude and phase are of dependence on $V(\mathbf{r}')$. At the end, the scattered wave is the interference of all spherical waves, scattering geometry is shown in in Fig. 2.4.

In the following, I use an approximation, called the first Born Approximation, which is good provided that the potential is weak when calculating the amplitude of the scattered waves, it refers to the Kinematical theory of scattering where the multiple scattering events are neglected. In this approximation, the scattered waves can be described by:

$$\Psi^1(\mathbf{r}) = e^{i\mathbf{k}_i\cdot\mathbf{r}} + \Psi_0 \int \frac{e^{i\mathbf{k}|\mathbf{r}-\mathbf{r}'|}}{4\pi|\mathbf{r}-\mathbf{r}'|} V(\mathbf{r}') e^{i\mathbf{k}'\cdot\mathbf{r}'} d^3r' \quad (2.2)$$

with the scaling factor $\Psi^1(\mathbf{r})$ being 1 for X-rays and $(\frac{2m_n}{\hbar^2})$ for neutrons.

Taking into account the Fraunhofer approximation since the detector is far away from the sample, where $|\mathbf{r}-\mathbf{r}'| \gg |\mathbf{r}'|$, using the scattering vector $\mathbf{Q} := \mathbf{k}' - \mathbf{k}$ and $\mathbf{R} = \mathbf{r}-\mathbf{r}'$, yielding:

$$\Psi^1(\mathbf{R}) = e^{i\mathbf{k}_i\cdot\mathbf{R}} + \frac{e^{i\mathbf{k}\cdot\mathbf{R}}}{R} \frac{\Psi_0}{4\pi} \int V(\mathbf{r}') e^{i\mathbf{Q}\cdot\mathbf{r}'} d^3r' \quad (2.3)$$

With scattering amplitude $F(\mathbf{Q}) =$

$$F(\mathbf{Q}) = \frac{\Psi_0}{4\pi} \int V(\mathbf{r}') e^{i\mathbf{Q}\cdot\mathbf{r}'} d^3r' \quad (2.4)$$

it is nothing but the Fourier transformation of the scattering potential.

The square of the absolute value of the scattering amplitude is the intensity:

$$I(\mathbf{Q}) = |F(\mathbf{Q})|^2 \quad (2.5)$$

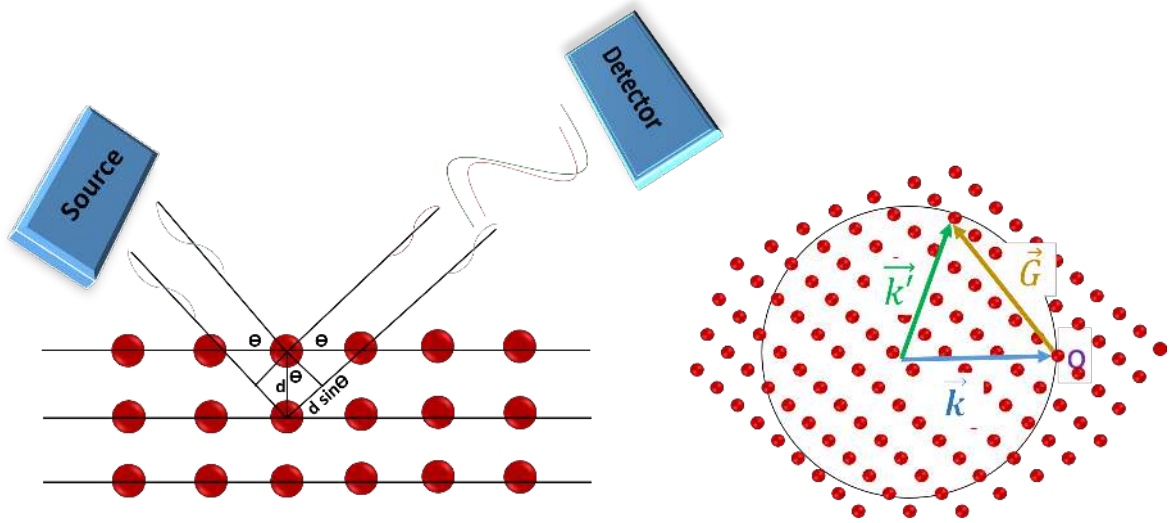


Figure 2.5: Illustration for Bragg's law and the Ewald sphere construction.

2.3.2 Scattering from crystalline structures

Diffraction in crystalline material leads to a destructive and constructive interference. The constructive interference occurs under a specific condition. This is Bragg condition translated in the followed mathematical equation and depicted in Fig. 2.5 (right):

$$2d_{(hkl)} \sin\theta = n\lambda \quad (2.6)$$

where n is integer and $d_{(hkl)}$ the spacing between adjacent (hkl) lattice planes, for hexagonal symmetry, is given by:

$$\frac{1}{d_{(hkl)}^2} = \frac{4}{3} \frac{h^2 + hk + k^2}{a^2} + \frac{\ell^2}{c^2} \quad (2.7)$$

In crystalline material [93], the periodicity is reflected in identical unit cell contents having an identical scattering density $\rho_u(\mathbf{r})$ as well and are connected by direct lattice vectors $\mathbf{R} = u\mathbf{a} + v\mathbf{b} + w\mathbf{c}$, being u, v, w integer numbers, the overall scattering density from the entire crystal is then the convolution of the scattering density in one unit cell with the lattice in real space, described by a sum of delta peaks.

$$\rho_t(\mathbf{r}) = \underbrace{\rho_u}_{\text{basis}} \otimes \underbrace{\sum_{uvw} \delta(\mathbf{r} - \mathbf{R}_{uvw})}_{\text{lattice}} \quad \text{where } \otimes \text{ denotes convolution.} \quad (2.8)$$

The scattering amplitude is the product of the Fourier transform of the scattering density of one unit cell refers to the what is known as structure factor in crystallography determines the observed intensities and the Fourier transform of the direct lattice giving the criteria for the observation of intensities, it is the scattering vector being the reciprocal lattice (Bragg condition) represented by construction called Ewald sphere (3D) and a circle in (2D), it is shown in Fig.

2.5 (left), with radius equal to the reciprocal of the wavelength of the incident X-ray ($1/\lambda$), and whenever the reciprocal lattice point of the plane concerned lies on the surface, Bragg scattering occurs.

$$F(\mathbf{Q}) = \underbrace{\mathcal{F}([\rho_{\mathbf{u}}])(\mathbf{Q})}_{\text{structure factor } F_{hkl}} \cdot \underbrace{\mathcal{F}\left([\sum_{uvw} \delta(\mathbf{r} - \mathbf{R}_{uvw})]\right)(\mathbf{Q})}_{\sum_{hkl} \delta(\mathbf{Q} - \mathbf{G}_{hkl})} \quad (2.9)$$

The reciprocal lattice vector \mathbf{G} :

$$\mathbf{G} = h\mathbf{a}^* + k\mathbf{b}^* + l\mathbf{c}^* \quad (2.10)$$

And the individual reciprocal lattice vectors can be written as:

$$\mathbf{a}^* = \frac{2\pi(\mathbf{b} \times \mathbf{c})}{\mathbf{a} \cdot (\mathbf{b} \times \mathbf{c})} \quad (2.11)$$

$$\mathbf{b}^* = \frac{2\pi(\mathbf{c} \times \mathbf{a})}{\mathbf{b} \cdot (\mathbf{c} \times \mathbf{a})} \quad (2.12)$$

$$\mathbf{c}^* = \frac{2\pi(\mathbf{a} \times \mathbf{b})}{\mathbf{c} \cdot (\mathbf{a} \times \mathbf{b})} \quad (2.13)$$

The width of Bragg peaks [93] is given by the average number of cells that are coherently ordered (CO cells in our compounds) expressed by the correlation length ξ . The higher number, the sharper corresponding Bragg reflections. Essentially the width of Bragg peaks is inversely proportional to the correlation length. The structure factor for N atoms in the unit cell can be written as:

$$F_{hkl} = \sum_{j=1}^N f_j(\mathbf{Q}_{hkl}) \exp(i\mathbf{Q}_{hkl} \cdot \mathbf{r}_j) \quad (2.14)$$

with f_j the atomic form factor and \mathbf{r}_j the position of the j -th atom in the unit cell.

2.3.3 X-ray scattering

In X-ray scattering, the interaction occurs between the incident photon and the electrons surrounding the nuclei of atoms. In a classical picture, the electrical component of the electromagnetic wave leads to the oscillation of the charged electrons, which in turn emits electromagnetic waves like in an antenna with same frequency as the incident one, i.e. this so-called Thomson scattering is elastic. The atomic form factor for X-ray scattering is the Fourier transform of the scattering potential (proportional to the electron density $\rho(\mathbf{r})$) associated with the atom:

$$F(\mathbf{Q}) = \int \rho(\mathbf{r}) e^{i\mathbf{Q}\mathbf{r}} d^3r \quad (2.15)$$

More information can be found in [94].

2.3.4 Powder X-ray diffraction-Huber Guinier D670

Powders are composed of randomly distributed crystallites. If one hits the powder with monochromatic X-ray, Bragg scattering occurs from the planes of crystallites with the right orientation to fulfill the Bragg condition producing a Debye-Scherrer diffraction cone. Then, the detector scans through an arc in which intersects each Debye cone at a single point, giving a diffraction peak forming diffraction pattern, more information can be found in [95, 96].

Powder X-ray diffraction using a Huber Guinier D670 diffractometer (Cu-K α radiation) was used to check the phase purity for each prepared pellet calcined at specific CO₂-H₂(4%) gas flow. Moreover, it was always used for optimizing the synthesis conditions based on the presence of foreign phases, in which regions of the grown boule containing several crystals and potentially polycrystalline material from each growth attempt were ground and checked at room temperature.

2.3.5 Laue diffraction-MWL 120

Laue diffraction is the use of a continuous band of X-ray wavelengths, usually employed to determine the orientations of single crystals of a known structure for various microscopic or macroscopic measurements based on their symmetry, and to ensure the single nature of the crystal. In this case, as the wavelength increases continuously, typically plenty of the reciprocal lattice points may lie on the surfaces of Ewald's spheres with varied radius and symmetrically arranged spots called Laue spots emerge. Usually the backreflection mode is used rather than transmission mode because the crystals tend to be too large for the X-rays to penetrate. State of the art Laue-cameras work in real-time with efficient area detectors, one to a few seconds integration time, with motorized goniometers that make orienting crystals very efficient. A translational scanning can be used to probe if it is really a single crystal or consisting of several grains.

A MWL120 real time Laue system from Multiwire Laboratories Ltd., which has a 30x30 cm proportional wire chamber area detector, was used in this thesis to orient crystals for polarized neutron scattering experiments.

2.3.6 Single crystal X-ray diffraction-Supernova

Monochromatic X-rays hit a periodically arranged atoms at different orientations, and the scattered intensity is collected by an area detector to determine the structure of specific compounds. For the course of this thesis, a Rigaku Supernova diffractometer employing Mo-K α radiation was used to investigate CO at different temperatures, as it was already used to determine the CO of LuFe₂O₄ [36], YbFe₂O₄ [35, 59] and YFe₂O₄ [57, 60]. It is a four-circle diffractometer (ω , κ , ϕ and θ) (A photo of the experimental set-up is shown in Fig. 2.6) with a kappa-goniometer allowing an easy crystal loading and orientation to successively bring as many of the reciprocal lattice points on the Ewald sphere as can be reached. It employs a charge-coupled device (CCD) area detector as a photon counter enabling a rapid data collection. It provides dual micro-focus wavelength sources molybdenum (Mo-K α) with $\lambda = 0.709\text{\AA}$ and

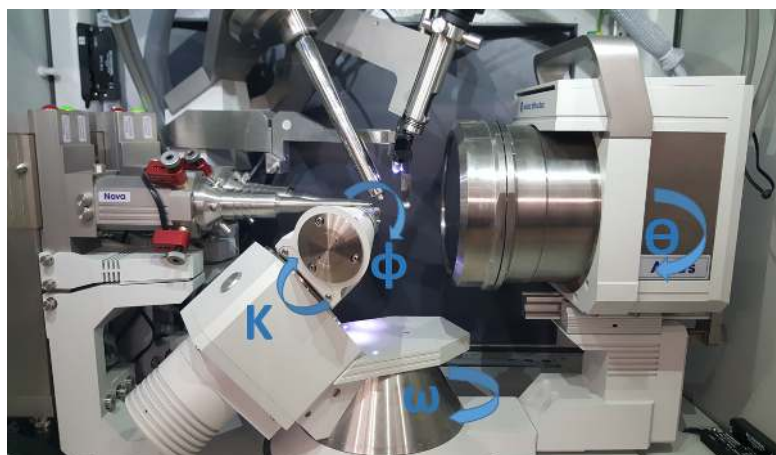


Figure 2.6: In-house supernova diffractometer.

copper (Cu-K α) with $\lambda = 1.540\text{\AA}$. The use of Mo X-source is useful to access a larger volume of the reciprocal space (more reflections) and to avoid stronger absorption, which is an issue for our compound and strong Fe-K α fluorescence because the Fe K-absorption edge is at 7.1 keV and the corresponding K α fluorescence line is at 6.4 keV and Cu-K α energy is 8 keV, slightly higher than the Fe K-edge. A Cryojet with Nitrogen gas flow on the sample and controlled via a Lakeshore temperature controller was used to set a sample temperature in the range from 100 K up to 400 K.

Picking a good quality crystal is the key toward a successful diffraction experiment, meaning a single grain crystal that is neither too thin or small to produce enough number of reflections, nor too large to avoid large absorption effects. The chosen crystal is mounted on a goniometer head with adjustable translations and rotations to position the crystal in the center of rotation of the diffractometer which corresponds also to the center of the incident monochromatic X-ray beam. The goniometer head is sitting at the top of goniometer to rotate the crystals in different angles to satisfy the Bragg condition. Finally, the scattered photons are counted by a detector. A short measurement (screening) is required to check the quality of the crystal, later on one can decide based on the obtained result for a long time measurements. The CrysAlisPro software package [97] was used for the pre-treatment of collected data including indexing, integration, and absorption correction. Many factors have to be considered during setting up a strategy for long time data collection: the high coverage up to the maximum 2θ available with the used wavelength since the more collected data is the better refinement, for example with Mo, typically $2\theta = 50^\circ$ is possible to be reached. In addition, the more unique reflections, in my work I used the Laue symmetry in which the full sphere containing all the unique reflections will be measured. Furthermore to collect the symmetry equivalent reflections that have the same intensity and therefore an average can be calculated for better statistics merged data and confirming the crystal symmetry.

Due to instrumental resolution and mosaicity of the crystal, the measured reflections are not infinitely sharp but rather have a finite width. In order to capture the full intensity, one has to scan through the reflection with axis of rotation either ω or ϕ in an incremental angular step



Figure 2.7: Kappa-diffractometer at EH1.

forming frames [98]. However, for one or more large unit cell parameters, the reflections would appear close to each other and sometimes overlapped, to overcome this problem, extending the detector to sample distance can be helpful with paying the price of reduced maximum 2θ [98] and long time experiment since more detector angle settings are available.

2.3.7 P24-beam-line : single crystal X-ray diffraction

To decide which of the possible CO configurations is actually realized in $\text{Lu}_2\text{Fe}_3\text{O}_7$ requires a collection of a full data set of integrated intensities and structural refinement, as previously done for the non-intercalated compounds [35, 36, 57]. Our data collection performed in-house using supernova indicates a significant peak overlap. We ameliorated this problem by improving the experimental resolution, and collecting a data set for CO superstructure refinement on the P24 beamline at the PETRA III synchrotron. It is a recent beam line operated since 2018 with a Kappa-diffractometer at the hatch 1 (EH1) that has a 60 deg Alpha-angle between the incoming beam direction and κ rather than 50 deg for the supernova. Moreover, it has different circle senses, as depicted in Fig. 2.7. At P24EH1, ω , ϕ turn clockwise, κ turns counter-clockwise viewed along the beam, in contrast to χ of an Eulerian diffractometers which turns clockwise.

The measurement was done on SC3 $\text{Lu}_2\text{Fe}_3\text{O}_7$, that was checked already by Supernova to exhibit a commensurate CO (as we will see later in Sec. 3.5.1). The measurements was first done briefly (~ 4 h) at 50 K, using a wavelength of 0.49 \AA with a MarCCD detector at a distance of 125 mm from the sample within the context of another beam time. Statistics was insufficient however, with many reflections unobserved. Moreover, the coverage, completeness and redundancy needs to be much better in light of previous CO determination on non-intercalated compounds [11, 35]. The intercalated compounds are even more complex in structure, and therefore extensive measurements are required. Therefore, the measurements

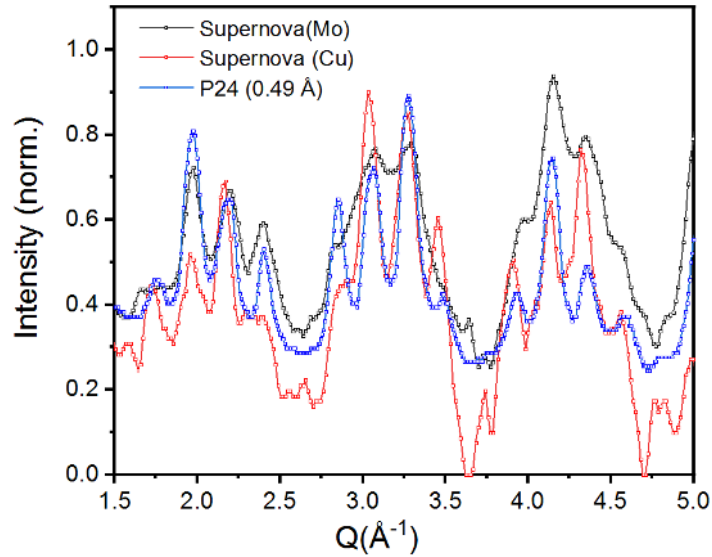


Figure 2.8: Line profile along ℓ for data measured at Supernova (Cu, Mo)- $K\alpha$ and at P24 (0.49 Å).

was done again at 100 K in a new beam time (50 K was not possible to reach due to technical problems). The first task was to optimize the conditions in term of energy and detector distance that sufficiently reduce the peaks overlap (c.f. Fig. 2.8) while allowing to access a large enough number of reflections. The optimal values were found to be as follows: $\lambda = 0.56$ Å and a detector distance of 120 mm. 22 different runs were measured, their protocol is summarized in Table. A.1. The measurement time is three seconds except for the first scan (1 sec) and the second scan (2 sec). Processing the X-ray diffraction data will be explained in details later on in Sec. 2.4.

2.3.8 Neutron Scattering

Neutrons are extremely useful for investigating condensed matter, especially for studying magnetic structures, because they have a magnetic moment (μ_n) resulting from the combined magnetic moments of the constitute quarks [99]. In a scattering experiment, the relevant quantity is the interaction potential. Neutrons are neutral particles, so there is no electric interaction with the electrons or nuclei. Instead, two interactions are possible: nuclear interaction with potential $V_N(\mathbf{r})$ and magnetic interaction with the magnetic field distribution in the sample, the potential $V_M(\mathbf{r})$, these further described in the following sections.

2.3.9 Nuclear scattering

The interaction of neutron with the nucleus of the atom by the strong force yields a nuclear scattering potential. The range of this interaction about 10^{-14} m, and the wavelength of the thermal neutrons is $\sim 10^{-10}$ m = 1 Å. Because the interaction range is small compared to

the wavelength, the nucleus can be considered as a point source. $V_N(\mathbf{r})$ can be modeled by delta-function potential which is called Fermi-pseudo potential given by:

$$V_N(\mathbf{r}) = \frac{2\pi\hbar^2}{m} b\delta(\mathbf{r} - \mathbf{r}_j) \quad (2.16)$$

where \mathbf{r}_j is the position of the nucleus and b is the scattering length describing the strength of the interaction potential, it is in general complex and energy dependent but Q -independent. It is different for different isotopes of an element and also depends on the nuclear spin state. Given the small nuclear radius (interaction range), therefore a small scattering probability, the first Born approximation can be applied for not too large samples. The scattering amplitude is the Fourier transform of interaction potential, a sum of contributions of the form of eq. 2.16 from the different nuclei instead of the charge density for X-ray scattering:

$$F(\mathbf{Q}) = \sum_j b_j \exp(i\mathbf{Q} \cdot \mathbf{r}_j). \quad (2.17)$$

The differential cross section for neutron scattering taking into account the random isotopes distribution and different nuclear spin states leads to two contributions: the first is the coherent scattering containing the phase information, with the possibility of interference. The second is the incoherent scattering containing no phase information leading to a uniform background proportional to the number of scatterers N [100]:

$$\frac{d\sigma(\mathbf{Q})}{d\Omega} = \underbrace{\langle b \rangle^2 \left| \sum_i \exp(i\mathbf{Q}\mathbf{r}_i) \right|^2}_{\text{coherent}} + \underbrace{N \langle (b - \langle b \rangle)^2 \rangle}_{\text{incoherent}}. \quad (2.18)$$

2.3.10 Magnetic scattering

The magnetic dipole moment μ of the neutron interacts with the dipole field distribution of the unpaired electrons in the sample including the interaction with both the spin ($\mathbf{B}_s = \nabla \times \frac{\mu_e \times \mathbf{r}}{r^3}$) and the orbital moment ($\mathbf{B}_L = -\frac{e \cdot v_e \times \mathbf{r}}{c \cdot r^3}$ Biot-Savart law) via Zeeman energy being the interaction potential $V_M(\mathbf{r}) = -\mu \cdot \mathbf{B}$ where $\mathbf{B} = \mathbf{B}_L + \mathbf{B}_s$.

For z -quantization axis defined by a small guide magnetic field, the differential cross section can be derived, (the calculation of the cross section is quite involved mathematically, and can be found in [100–102]):

$$\left(\frac{d\sigma}{d\Omega} \right)_{\text{mag}} = (\gamma_n r_0)^2 \left| \frac{1}{2\mu_B} \langle S'_z | \hat{\sigma} \cdot \mathbf{M}_{\perp \mathbf{Q}} | S_z \rangle \right|^2, \quad (2.19)$$

where γ_n is the neutron gyromagnetic ratio, r_0 the electron radius, S_z, S'_z express the spin of the neutron in its quantization axis z before and after scattering consequently and $\hat{\sigma}$ the neutron spin operator which is given by

$$\hat{\sigma} = (\hat{\sigma}_x, \hat{\sigma}_y, \hat{\sigma}_z), \quad (2.20)$$

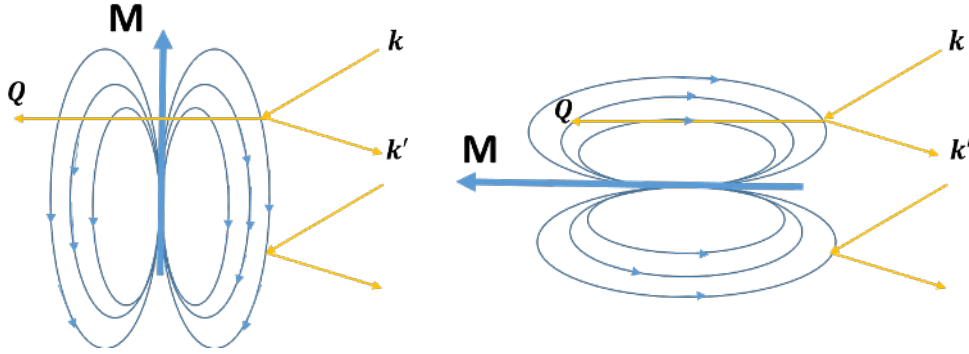


Figure 2.9: The magnetic field line configuration for M perpendicular (left) and parallel (right).

where x, y, z are the Cartesian axes and with the Pauli spin matrices

$$\hat{\sigma}_x = \begin{pmatrix} 0 & 1 \\ 1 & 0 \end{pmatrix} \quad \hat{\sigma}_y = \begin{pmatrix} 0 & -i \\ i & 0 \end{pmatrix} \quad \hat{\sigma}_z = \begin{pmatrix} 1 & 0 \\ 0 & -1 \end{pmatrix} \quad (2.21)$$

$\mathbf{M}(\mathbf{Q})$ is the density of magnetic moment in reciprocal space by the Fourier transform of the magnetization in real space:

$$\mathbf{M}(\mathbf{Q}) = \int_{-\infty}^{\infty} \mathbf{M}(\mathbf{r}) \exp(i\mathbf{Q} \cdot \mathbf{r}) d\mathbf{R}. \quad (2.22)$$

Only the magnetization component perpendicular to \mathbf{Q} gives rise to magnetic scattering and so is observable when we perform a neutron scattering experiment:

$$\mathbf{M}_{\perp \mathbf{Q}} = \hat{\mathbf{Q}} \times \mathbf{M}(\mathbf{Q}) \times \hat{\mathbf{Q}} = \mathbf{M} - (\hat{\mathbf{Q}} \cdot \mathbf{M})\hat{\mathbf{Q}} \quad \text{with } \hat{\mathbf{Q}} = \frac{\mathbf{Q}}{|\mathbf{Q}|} \quad (2.23)$$

This can be explained based on Fig. 2.9: when the moment is parallel to \mathbf{Q} , the Bragg planes are perpendicular to the moment and by the nature of the dipole field for each point on the Bragg plane with positive field, another point with negative field exists resulting in an average of zero, which is not the case for the magnetization component perpendicular to \mathbf{Q} where Bragg planes are parallel to the moment.

In contrast to nuclear scattering where the form factor is constant due to the point-like nucleus, the magnetic form factor for spin can be approximated with just the unpaired electron density, and it decreases faster than the X-ray form factor, because the latter is the Fourier transform of all electron density, while the former is the Fourier transform of the density of unpaired electrons – which e.g. for transition metal ions are in the 3d-shells. The 3d-electron density is further spread out in real space than the average electron density, which in Fourier space means we have more concentration around $Q=0$. Polarized neutron scattering was used in this thesis, to study diffuse magnetic scattering. The rules to be considered for polarization analysis are: Magnetic scattering inverts the spin (Spin flip) for the polarization of neutron $\mathbf{P} \perp \mathbf{M}_{\perp \mathbf{Q}}$ and does not invert it for $\mathbf{P} \parallel \mathbf{M}_{\perp \mathbf{Q}}$.

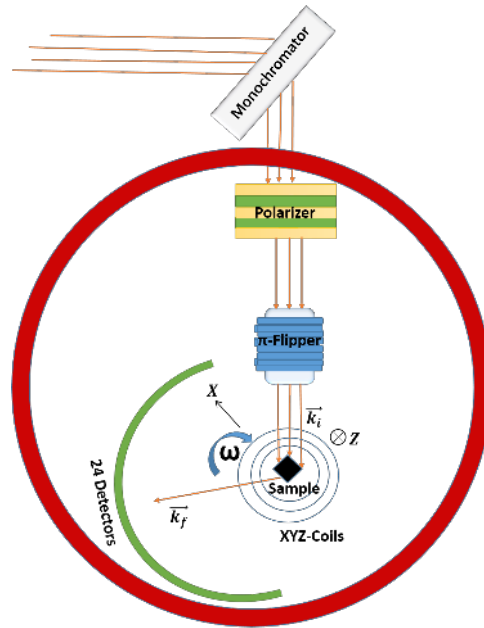


Figure 2.10: Schematic setup for DNS: Z-field means a field perpendicular to the horizontal scattering plane. The x-direction is facing the end of the detector array and is parallel to the average \mathbf{Q} . The y-axis is perpendicular to x and z.

2.3.11 DNS instrument

A neutron scattering experiment could only be performed on a non-stoichiometric large single crystals of $\text{Lu}_2\text{Fe}_3\text{O}_7$, due to the absence of a stoichiometric crystal large enough for neutron scattering. This experiment was done to study the diffuse magnetic scattering by polarized neutrons beam on the DNS instrument at the FRMII reactor in Garching. DNS is a cold neutron diffractometer with polarization analysis but also a capability of separation for different scattering contributions. A double monochromator of PG (002) provides a wavelength in the region $2.4\text{\AA} < \lambda < 6.0\text{\AA}$. DNS is equipped with XYZ Helmholtz coils to guide the polarization of the incoming polarized neutrons in to any desired direction. Furthermore, it has a π flipper to flip the neutron polarization. Finally, an efficient detection is achieved by 24 detectors filled with He^3 gas. These detectors contain a $m = 3$ super-mirror for the polarization analysis. The measurements were done at 5 detector-bank positions to ensure a hole-free mapping of the reciprocal space. Moreover, the measurements were corrected for deviating detector efficiency by the almost pure spin-incoherent scatterer vanadium. The setup is depicted in Fig. 2.10.

The experiment was conducted using neutrons of a wavelength 4.2\AA and two different polarization directions: X-direction which is facing the end of the detector array and parallel to the average scattering vector \mathbf{Q} and Z-direction which in vertical direction perpendicular to the horizontal scattering plane. For the measurements, the crystals were fixed on an Al-holder and oriented using Laue X-ray diffraction to obtain the $(hh\ell)$ -plane since all magnetic scattering in non-intercalated compounds were found to occur in this plane [11, 57, 59]), see Fig. 2.11.

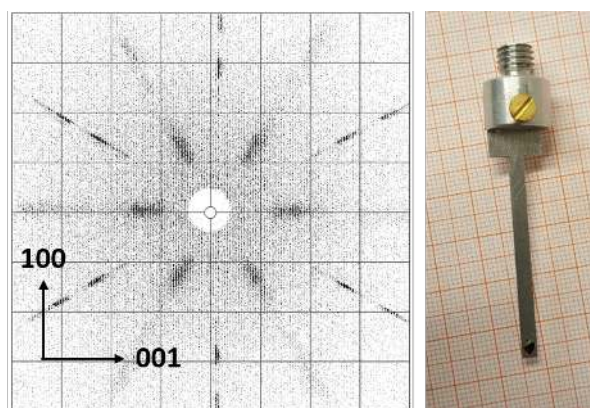


Figure 2.11: (left) Laue image along c-direction, (right) Single crystal of $\text{Lu}_2\text{Fe}_3\text{O}_7$ mounted on Al-holder in which $(1\bar{1}0)$ axis is perpendicular to the scattering plane.

2.4 Processing of X-ray diffraction data

2.4.1 Data reduction and absorption correction

In a diffraction experiment, the aim typically is to determine the crystal structure, which is achieved by calculating the electron density (for X-ray diffraction) from the diffraction pattern by inverse Fourier transform. However, the detector provides us an image in the reciprocal space including reflections that each have an intensity (the absolute square of structure factor), but no information about the phase of the structure factor which is crucial and contains most of the information (phase problem [103]). The position of these spots provides information about the unit cell and the intensity about the positions of the atoms within the unit cell (see Sec. 2.3.2).

The data used for CO crystal structure refinement was collected using the kappa diffractometer at the beamline P24 as mentioned before in Sec. 2.3.7, where different phi and theta scans were measured. This implies some additional work including collecting the different runs and entering them to the CrysAlis Pro software, taking into account the difference in geometry to the supernova (different motor angles have to be imported in Eulerian to CrysAlis Pro). Otherwise, the followed steps to process the data are the same for both diffractometers. However, after the diffraction takes place, we need to collect all the measured reflections from different frames by using the what called "peak hunting" in CrysAlis Pro software. With the use of the smart peak hunting option, one collects even reflections that are very weak in intensity. This is critical for our study, since we are looking for superstructure reflections which has weak intensity. Afterward, assigning the obtained reflections to unit cell comes, which is called indexing. Searching potential twin components is possible using the Ewald explorer option. Finally, the integration is done by harvesting the intensity with minimal value of background from 3D constructed image. However, the superstructure reflections are weak in intensity meaning they are quite difficult to integrate due to the high noise. Therefore, the integration is done twice, once for the strong reflections only with flagging the weak reflections, then the process is repeated for the weak reflections using the profile of the strong ones. This inte-

gration result in a hkl file which will be used later for the structure determination. However, before using the collected intensities for structure determination, a re-finalization is necessary implementing corrections to be applied, particularly the absorption correction for both the incident and the diffracted beam. This correction is needed due to the fact that the intensity is reduced by absorption when it passes through the crystal. It depends on the distance that each photon travels in a crystal. Thus, it depends on the shape of the crystal but also on the diffraction angle. Moreover, it is different for different reflections. Absorption contributes to a large effect for our crystals, since they contain the heavy element Lu. Absorption correction can be done analytically by calculating the transmittance from very small pieces of the crystal for each measured reflection. Two types of correction can be done: Numerical and empirical. Numerical absorption correction depends on the shape of the crystal, which can be determined by indexing crystal faces. Therefore, the use of well defined crystal faces is advantage in this case. This option can be easily done with the use of CryAlis Pro software which allows one to index the faces based on a recorded video taken for the measured crystal beforehand by camera impeded in the supernova. On other hand, the empirical correction depends on the measured reflections, specifically the equivalent reflections, therefore, a high multiplicity of observations (redundancy) is required. This correction is accomplished by comparing the intensities from the redundant measurements, and then the shape is approximated to spherical or cylindrical using a number of spherical harmonics in a least square procedure, then absorption for the sample is calculated. The P24 beam line is not provided with a camera to record video. However, the redundancy was high enough for the collected data allowing the use of the empirical absorption correction.

A first impression about the data before re-finalization can be obtained by looking at standard deviation i.e. the residual-R value:

$$R_{\sigma} = \frac{\sum_i \sigma(F_i)}{\sum F_i} \quad (2.24)$$

2.4.2 Space group determination and structure solution

Single crystal refinement was done with the use of JANA2006 [104]. First of all, the re-finalized data was imported to Jana, then based on the extinction rules, we limited the possible space groups [105]. The Laue group was determined later on depending on what called internal R-value (or $R_{\text{merg}}/R_{\text{sym}}$.) which forces identical intensities for certain group of reflections "equivalent reflections" defined as

$$R_{\text{int}} = \sum_i \sum_j \frac{F_j^2 - \langle F_i^2 \rangle}{\langle F_i^2 \rangle} \quad (2.25)$$

where i is running over all independent reflections and j over all equivalent reflections and for a specific i and $\langle F_i^2 \rangle = \sum_{j=1..n} \frac{F_j^2}{n}$. Moreover, the R_{int} value tells if the absorption correction is good.

Important to remember that the R for the refinement should be below the R_{int} . The higher the symmetry, the more reflections are merged. This is reflected in the so-called "Redundancy"

which is the average number of observed reflections merged into symmetry-unique ones. Redundancy can be increased by measuring reflections more than once, doing this helps with the identification of the outliers, moreover, with carrying out the empirical absorption correction as mentioned in the previous section, thus generally better quality of the model.

With these all in hand, we need to recover the missing phases by providing a close enough "starting structure", there are several methods that can be used for this structure solution step: direct methods [106] in SIR92 [107] or charge flipping method [108–110] in Superflip [111]. The basic assumption behind charge flipping is the electron density cannot be negative in any point \mathbf{r} : $\rho_t(\mathbf{r}) > 0$. It follows the following algorithm: We assign all the observed reflections with random phases, then we calculate the electron density with an inverse of the Fourier transform. We exchange the negative densities with a positive one and a modified electron density is produced. Afterward, we calculate a new structure factor from these modified intensities, and we combine the experimental amplitudes with the phases that we calculated later to get new structure factors, with this we start the process again till it converges.

2.4.3 Structural Refinement in least square

The outcome of the structure solution is approximate. Therefore, a further refinement of the parameters of the structural model is needed with the use of Least square method where we minimize the difference between the calculated F_c and the observed F_o structure factor amplitudes.

$$P = \sum \omega (|F_{\text{calc}}| - |F_{\text{obs}}|)^2 \quad (2.26)$$

With ω being the weighting factor including instability factor u which set to be 0.01:

$$\omega_{(hkl)} = \frac{1}{\sigma(|F_{\text{obs}}|) + (uF_{\text{obs}})^2} \quad (2.27)$$

Alternatively, refinement can be done also based on F^2 , with minimized function:

$$P_2 = \sum \omega' (F_{\text{calc}}^2 - F_{\text{obs}}^2)^2 \quad \text{with weights} \quad \omega' = \frac{\omega}{4F_{\text{obs}}^2} = \frac{1}{4F_{\text{obs}}^2 \cdot (\sigma(|F_{\text{obs}}|) + (uF_{\text{obs}})^2)} \quad (2.28)$$

Refinement based on F^2 was used during our refinement i) since we measure F^2 , ii) to avoid problems with very weak reflections or reflections with negative intensities, and iii) to resolve the difficulty of estimation $\sigma(F)$ from $\sigma(F^2)$ [112]. A further advantages are more easily refinement of twinned structures and lower chances of the refinement getting structure in a local minimum [113].

The structure solution often does not find all the atoms in the model, particularly the light ones e.g. Oxygen. To find the missing atoms, Fourier synthesis is used in which the potential atom sites can be guessed where a maxima is found by the interpolation between the grid points. The phases (mostly influenced by the heaviest atoms) will nevertheless be close to their real values, therefore, once the heaviest atoms are found, the Fourier synthesis works well.

During the refinement process, apart from the major interest to find the atom positions, many further parameters should be considered to get best model in which we settled them to a reasonable values and well-behaved ones. For example, the atomic displacement parameters (ADP) arises from the time average temperature movement of atoms around their mean position but also their random distribution from one unit to another. ADP for atoms can be isotropic or anisotropic (represented by ellipsoid), these values should not be negative, otherwise it would indicate real problem in the structural model. Refinements become unstable if correct relations are not set to be as constraints during refinement [98]. Twinning should be considered as well, occurring due to the lowering of crystal symmetry and breaking some of the symmetry elements in the modulated structure.

To quantify the matching between the calculated F_c and the observed F_o one uses various residuals R_1 (R_2) for refinement based on F (F^2):

$$R_1 = \frac{\sum_j ||F_{obs}| - |F_{calc}||}{\sum_j |F_{obs}|} \quad R_2 = \frac{\sum_j |F_{obs}^2 - F_{calc}^2|}{\sum_j F_{obs}^2} \quad (2.29)$$

These are associated with weighted functions ωR (ωR_2):

$$\omega R = \sqrt{\frac{\sum_j \omega (|F_{obs}| - |F_{calc}|)^2}{\sum_j \omega (F_{obs})^2}} \quad \omega R_2 = \sqrt{\frac{\sum_j \omega (F_{obs}^2 - F_{calc}^2)^2}{\sum_j \omega (F_{obs}^2)^2}} \quad (2.30)$$

Moreover, another helpful quantity is the goodness of fit $Goof$ ($Goof_2$) including the number of used reflections n and parameters p :

$$Goof = \sqrt{\frac{\sum_j \omega (F_{obs} - F_{calc})^2}{n - p}} \quad Goof_2 = \sqrt{\frac{\sum_j \omega (F_{obs}^2 - F_{calc}^2)^2}{n - p}} \quad (2.31)$$

Theoretically, the best value for $Goof$ should be close to 1 and the final R-value should be within the realms of 1 or 2 %. However, these values are difficult to be reach due to weak intensity superstructure reflections, a reasonable R-value in this case is around 5 % depending of course on number of parameters and variables, moreover on the complexity of the structure. Values less than one for $Goof$ means over-refinement which indicates either a failure to do proper absorption correction or a wrong space group [112].

The final step, is to check the validation of the used model, with acceptable overall agreement factor being lower than R_{int} . In addition, reasonable displacement parameter, the validation of anisotropic displacement parameter can be examined with the Hirshfeld test [114]. Moreover, no significant maxima should persist in the difference Fourier synthesis. Finally, bond angles and distances need to be reasonable.

2.4.4 Bond Valence Sum (BVS) analysis

X-ray diffraction experiment can not directly address the different valances of atoms in compounds since the X-ray form factor curves of Fe , Fe^{2+} and Fe^{3+} are identical beyond $\sin(\theta)/\lambda = 0.25$ (see Fig. 2.12). Therefore, Bond Valence Sum (BVS) analysis is used to determine the

valences of each atomic site of a properly refined crystal structure in which different valences are distinguishable by the fact the bond length varies with the electro-static interaction between a cation and an anion rather than for different cation valences.

Valences can be calculated considering all the neighboring ions via:

$$\text{Valence} = \sum_i \exp \frac{d_0 - d_i}{0.37} \quad (2.32)$$

where d_i is the experimental bond length to the neighboring ions and d_0 is a tabulated [115, 116] characteristic bond length between cation-anion pair.

	$d_{0i}(\text{Fe}^{2+})$	$d_{0i}(\text{Fe}^{3+})$
[115]	1.734(3)	1.759(3)
[117]	1.713	1.751
[118]	1.700	1.765
mean	1.716(10)	1.758(4)

Table 2.1: Characteristic bond lengths d_{0i} of Fe^{2+} , Fe^{3+} taken from published crystal data in [115, 117, 118].

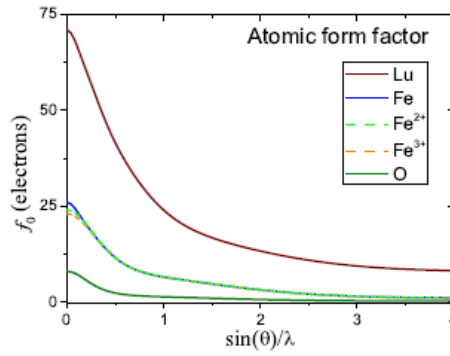


Figure 2.12: Atomic X-ray form factor for all elements in $\text{Lu}_2\text{Fe}_3\text{O}_7$ including the different valences of Fe ions, taken from [11].

2.5 X-ray magnetic circular dichroism

X-ray magnetic circular dichroism (XMCD) is an absorption spectroscopy technique in which the absorption process depends on the photon polarization \mathbf{P} and the sample magnetization \mathbf{M} . The XMCD originates from the difference in the absorption spectrum of the photon energy with left μ_+ and right μ_- circularly polarized X-ray for magnetized sample (\mathbf{M}) and the XMCD signal $\Delta\mu(\mathbf{B})$ (\mathbf{B} : applied magnetic field) is defined as [119, 120]:

$$\Delta\mu(\mathbf{B}) = \mu_+(\mathbf{B}) - \mu_-(\mathbf{B}) \quad (2.33)$$

For circularly polarized X-rays, the polarization \mathbf{P} is the incoming beam direction \mathbf{k} . Necessarily, for dichroism to take place, the \mathbf{M} must have a component parallel to \mathbf{P} ($\parallel \mathbf{k}$), to break the time-inversion symmetry and to achieve a proper degeneracy of the orbital states by the Zeeman effect. XMCD can be measured either by switching the photon polarization as it was done in this thesis, or by changing the magnetization direction [121].

An important characteristic of XMCD is that one can probe the desired element as the absorption edge energy is element specific. Moreover, it allows to distinguish between different valences [122] as the position of the edge also depends on the valence state. The reason is

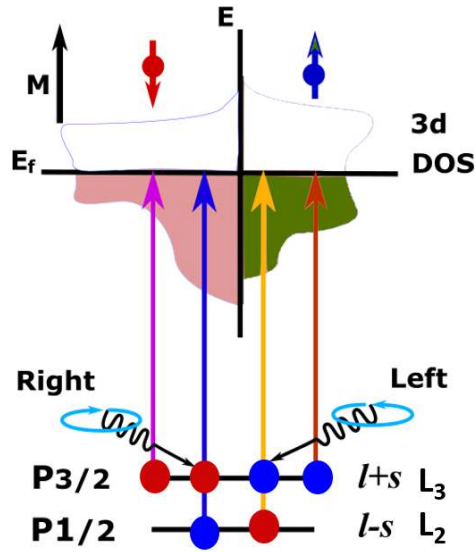


Figure 2.13: Schematic representation of absorption process in the case of $2P \rightarrow 3d$ transitions at the $L_{2/3}$ edges.

that the binding energy (energy of e.g. the 1s electrons) is affected by screening of the nuclear charge by all the other electrons present in the atom including the valence electrons.

The difference in the absorption process for different polarization direction can be explained as the following: initially, the absorption of the circularly polarized photon with an appropriate energy which leads to photoelectron excitation from 2p state and consequently the transition of the respective photoelectron to a higher empty energy levels, for the $L_{2/3}$ edge XMCD measured in this work that is the spin polarized 3d-states of the transition metal element (Fe ions in our intercalated compounds). Due to the spin-orbit coupling (SOC), the 2p state is split into states: $2p_{1/2}$ and $2p_{3/2}$. As a consequence, two edges in the X-ray absorption spectrum (XAS) are present: L_3 -edge (L_2 -edge) which is due to the transition from $2p_{3/2}$ ($2p_{1/2}$) into the 3d states [123]. The permitted transitions are those consist with the dipole selection rules :

$$\Delta l = \pm 1 \quad , \quad \Delta m_s = 0 \quad \text{and} \quad \Delta m_l = \begin{cases} -1 & \text{for right circularly polarization} \\ +1 & \text{for left circularly polarization} \end{cases} \quad (2.34)$$

The left (right) circularly polarized photon $m_l=1$ ($m_l=-1$) leads to a spin up (spin down) polarization of the photoelectron at L_3 -edge via SOC ($j = l + s$) because of the angular momentum conservation. This is reversed at L_2 edges since it exhibits an opposite SOC ($j = l - s$), therefore the direction of the XMCD signal for the two edges are reversed (see fig. 2.13). The imbalance of the spin up and the spin down in the 3d valance state reveals the spin-polarization of the photoelectron [124]. Therefore, with XMCD it is possible to probe the spin polarization of unoccupied 3d-states i.e. the magnetization of the sample as a high absorption occurs for matched spin polarization and a lower absorption upon reversing the photon polarization. The magnitude of XMCD relative to the XAS provides a net moment in the beam direction [125].

For information about the absorption probability for the L_3 and L_3 dipole transitions for 3d elements, see [121, 126].

One can use what so called "sum rules" [127, 128] on the integrated XMCD signal to separate the orbital moment $m_{\text{orb}} = -\langle L_z \rangle \frac{\mu_B}{\hbar}$ and spin magnetic moment $m_{\text{spin}} = -2 \langle S_z \rangle \frac{\mu_B}{\hbar}$:

$$\frac{m_{\text{orb}}}{m_{\text{spin}}} = \frac{2q}{9p - 6q} \quad (2.35)$$

With

$$p = \int_{L_3} (\mu_+ - \mu_-) d\omega \quad (2.36)$$

$$q = \int_{L_3+L_2} (\mu_+ - \mu_-) d\omega \quad (2.37)$$

2.5.1 High field chamber

The XMCD measurements at L_3 and L_2 -edges of $\text{Lu}_2\text{Fe}_3\text{O}_7$ and $\text{Lu}_3\text{Fe}_4\text{O}_{10}$ single crystals were carried out on the beamline UE46/PGM-1 at the end station high field chamber placed at BESSY, the synchrotron facility in Berlin. The beamline provides soft X-rays, with energy in the range of 120 eV to 2000 eV, of tunable polarization (linear and circular), giving access to the Fe $L_{2/3}$ -edges and the oxygen K-edge. At the high field chamber, magnetic fields up to 7 Tesla can be reached, and temperatures down to 4 K. The presence of superconducting coil that can rotate in vacuum independently from the sample allows XMCD experiments in various geometries. However, in our experiments, all absorption spectra were measured using one geometry with applied magnetic field \parallel c-axis \parallel \mathbf{k} as the Fe ions are Ising along this direction [74] and to achieve the maximum dichroic effect. The absorption signal can be measured using different ways: 1. Total transmission method (TMY) which requires a very thin sample to reduce the strong absorption in the soft x-ray regime (this is not applicable to our samples). However, it is the most reliable method as it probes the entire sample. 2. Total fluorescence method (TFY) in which the excited states decay via X-ray fluorescence (photon emission). This method has the advantage that is applicable to insulating materials. Moreover, it is a bulk sensitive with much large penetrating depth, however, this leads at the same time to a drawback of the self-absorption effect while penetrating through in the sample. 3. Total electron yield method (TEY) via the sample drain current through the electrically contacted sample which was used during our measurements. In TEY, the Auger effect occurs in which the excited state decays not by emitting a photon, but rather an electron in a higher shell to above the Fermi level. This is very surface sensitive because emitted electrons can penetrate only up to 25 to 50 Å of the sample [129] due to the strong interaction of electrons with matter. X-ray absorption spectrum (XAS) was found to be affected by surface oxidization in LuFe_2O_4 but no significant influence on the XMCD was found [11, 33, 44]. TEY works only for not too insulating samples because otherwise the electrons then cannot be sucked off from the sample and transferred to the detector. However, one of the drawbacks of the TEY is the charging effect that can occur for too insulating sample and distort the spectra, this was avoided in our

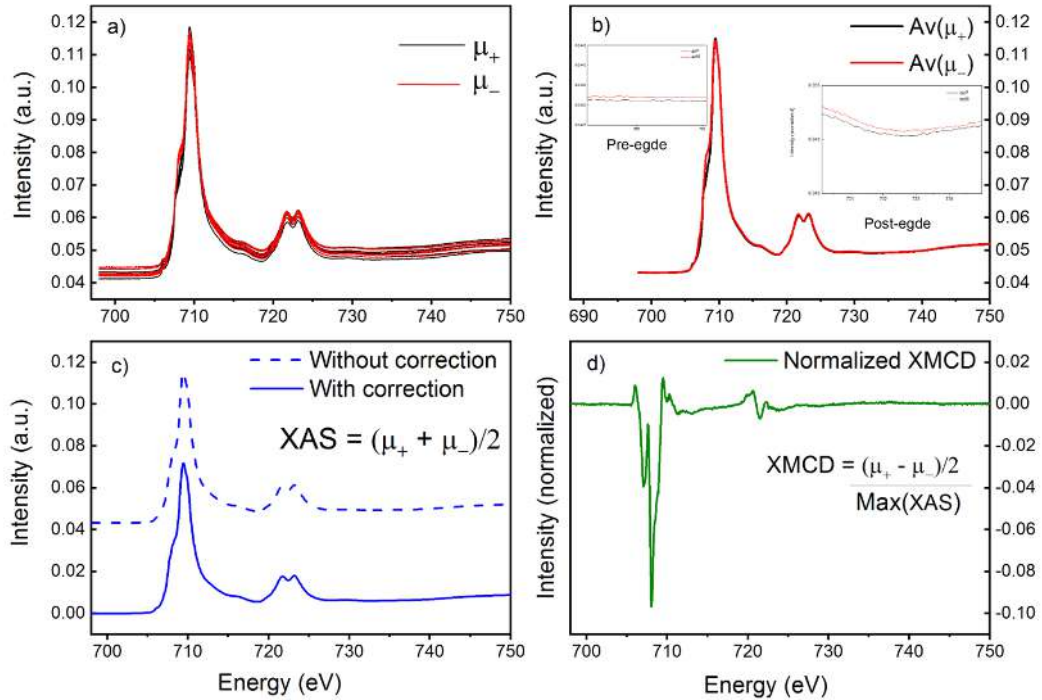


Figure 2.14: Figure illustrates the steps used to analysis the data: a) Twelve raw absorption spectra: six μ_+ for left and six μ_- right circularly polarized X-ray. b) Averaged absorption spectra of μ_+ and μ_- (the inset shows the offset in the pre- and post-edges). c) Constant background subtraction for XAS. d) Normalized XMCD signal.

measurements by measuring at 120 K in which the sample was conductive enough for TEY. At the beamline, depending on the sample, a noise-to-signal ratios as low as 10^{-4} can be achieved by measurement of the total electron yield. Relatively quick recording of the pairs of the XMCD signals (about 10 min.) using the implemented continuous-mode scanning can be achieved. Many artifacts could potentially lead to a misinterpretation of the XMCD signal, such as the energy shift due to helicity switching which can include a first derivative structure in their XMCD. Moreover, the background may vary as a result of the time-drift and the dependence on the direction of energy change in part likely due to the variation of the beam position relative to sample. However, these artifacts were more pronounced for smaller crystal size, which may be due to the smaller surface area more affected by drifts of the beam position.

To reduce the effect of individual artifacts, a series of the absorption spectrum (μ_+ μ_- μ_- μ_+) was measured multiple times, an example is shown Fig. 2.14a. For the analysis, the following steps were carried out: 1. The average of μ_+ and average of μ_- were calculated (see Fig. 2.14b) 2. The offset present at the pre- and post-edge (insets of Fig. 2.14b) was eliminated through multiplication by scale factor. 3. The X-ray absorption spectrum was calculated by:

$$\text{XAS} = \mu_+(\mathbf{B}) + \mu_-(\mathbf{B}) \quad (2.38)$$

and a constant background was subtracted as shown in Fig. 2.14c. 4. The XMCD signal shown in Fig. 2.14d calculated using eq. 2.33 and normalized through division by the maximum of XAS spectrum. Technical information of the beamline and the used end-station are from [130], with further description of the beamline construction available.

3

Synthesis and optimization of the intercalated compound

This chapter will visit the synthesis and optimization of polycrystalline samples and single crystals of $\text{Lu}_2\text{Fe}_3\text{O}_7$ prepared with different gas ratios. The optimization is performed to get a single phase material, without impurities from other phases. The careful control of the oxygen partial pressure is needed to obtain stoichiometric crystals. It has been known that oxygen deficiency obscures the intrinsic properties [11, 35] i.e. for non-stoichiometric compounds neither 3D charge ordering nor 3D magnetic ordering can be observed. Thus, getting stoichiometric crystals are necessary to get long-range charge and spin order and determine the corresponding configurations. In the following part of the chapter, the macroscopic magnetic investigations of different oxygen stoichiometries crystals of $\text{Lu}_2\text{Fe}_3\text{O}_7$ and $\text{Lu}_3\text{Fe}_4\text{O}_{10}$ are presented. This is done to clarify the relation between the stoichiometry and magnetic properties in these compounds. At the end, the observed charge order types is introduced. Parts of the results described in this chapter have been published in Ref. [64].

3.1 Optimization of polycrystalline $\text{Lu}_2\text{Fe}_3\text{O}_7$ synthesis

Polycrystalline preparation of the target phase $\text{Lu}_2\text{Fe}_3\text{O}_7$ was needed to be used afterward to from the seed and feed rods for crystal growth, moreover, to have a clear idea about the magnetic behavior and their changes with oxygen stoichiometry. Therefore, pellets of $\text{Lu}_2\text{Fe}_3\text{O}_7$ were prepared via solid state reaction at 1250 °C as described in Sec. 2.1, with the use of mixtures of flows of CO_2 and $\text{Ar}(96\%):\text{H}_2(4\%)$ to control oxygen partial pressure. This is necessary for the determination of phase stability and oxygen stoichiometry as found by

Pellet	P1	P2	P3	P4	P5	P6	P7	P8	P9	P10
CO_2	18	21	24	27	30	33	39	42	45	50
$\text{Ar}(96%):\text{H}_2(4\%)$	30	30	30	30	30	30	30	30	30	30

Table 3.1: Overview of the whole prepared pellets with the use of different mixtures of CO_2 and $\text{Ar}(96%):\text{H}_2(4\%)$ flows.

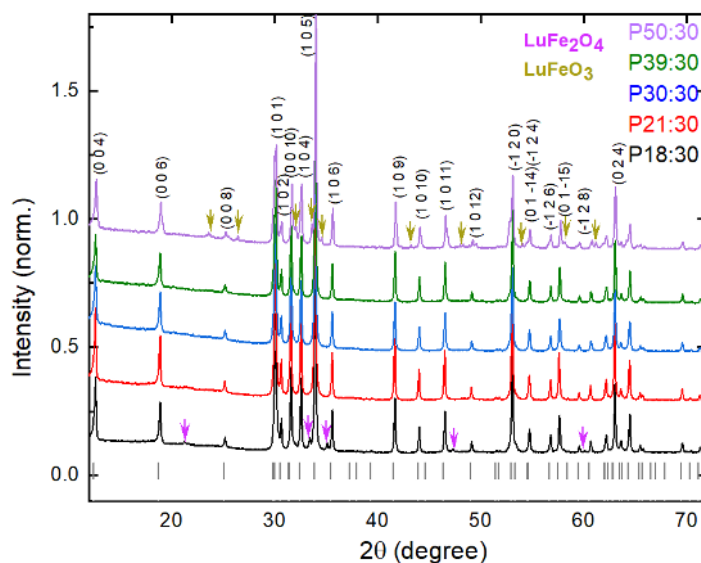


Figure 3.1: Powder X-ray diffractogram of polycrystalline pellets of $\text{Lu}_2\text{Fe}_3\text{O}_7$ calcined under different CO_2 and $\text{Ar}(96\%):\text{H}_2(4\%)$ ratios. The flow of $\text{Ar}(96%):\text{H}_2(4\%)$ is fixed to 30 ml/min and the flow of CO_2 varied. Impurities of LuFe_2O_4 & LuFeO_3 are indicated by arrows. Taken from own work [64] and adapted.

[42]. The optimization process was done as follows: 1) a pellet was synthesized with specific $\text{CO}_2\text{-H}_2(4\%)$ gas flow, 2) it was checked by powder X-ray diffraction c.f. Sec. 2.3.4) to verify the obtained phase or phases and the purity with the help of the established [42] phase diagram at $1200\text{ }^\circ\text{C}$, which is very close to the temperature ($1250\text{ }^\circ\text{C}$) used in our case, 3) finally, magnetization measurements was performed to check the quality of different pellets. The used gas ratios are summarized in table 3.1.

The corresponding diffractogram for some pellets of $\text{Lu}_2\text{Fe}_3\text{O}_7$ calcined under the flow of $\text{Ar}(96%):\text{H}_2(4\%)$ which is fixed to 30 ml/min and the varied flow of CO_2 is shown in Fig. 3.1. Starting with the lowest gas ratio $\text{CO}_2/\text{H}_2(4\%) = 18$ leads to the formation of $\text{Lu}_2\text{Fe}_3\text{O}_7$ as a main phase and some impurities of LuFe_2O_4 indicating the very low oxygen partial pressure following the phase diagram of [42] (see Fig. 1.9). In contrast, using a very high gas ratio of $\text{CO}_2/\text{H}_2(4\%) = 50$ leads to the formation of LuFeO_3 beside the main phase indicating the very high oxygen partial pressure as in [42]. $\text{Lu}_2\text{Fe}_3\text{O}_{7-\delta}$ is formed as stable pure phase in a region with gas flows varying between 21-39 ml/min. CO_2 and 30 ml/min. $\text{Ar}(96%):\text{H}_2(4\%)$. All the found phases are consistent with the phase diagram shown in Fig. 1.9 on P. 10 with no other phases observed.

3.2 Effect of stoichiometry on magnetic behavior of polycrystalline $\text{Lu}_2\text{Fe}_3\text{O}_7$

Based on the results found for LuFe_2O_4 [53], YFe_2O_4 [60] and YbFe_2O_4 [59], we expect a dependence of the magnetic properties on the oxygen content as well. A question rises here

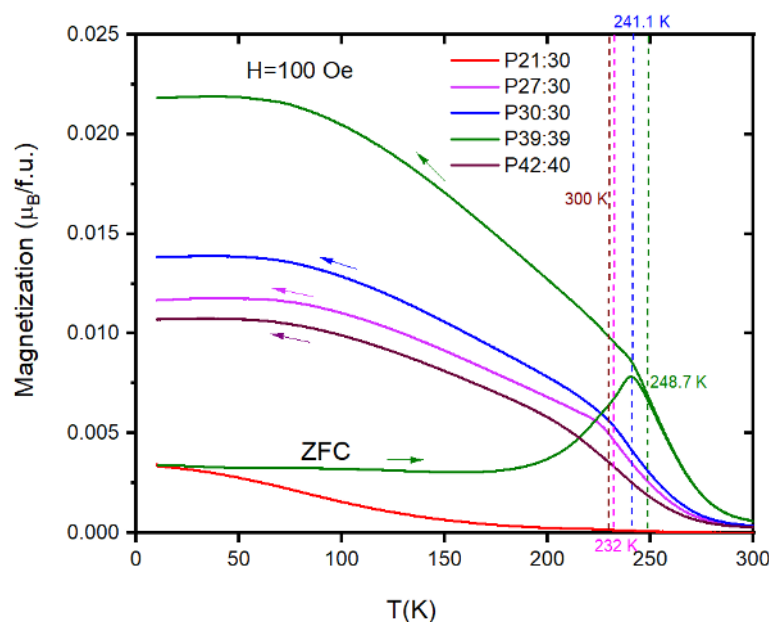


Figure 3.2: Field cooled magnetization measured in $H=100$ Oe on five different pellets synthesized in different CO_2 and $\text{Ar}(96\%):\text{H}_2(4\%)$ ratios. Zero field cooling curve for P39:30 is shown as well. Dashed lines indicate the freezing temperature for each pellet, and was determined by the steepest slope of FC curves.

how stoichiometry influences the occurrence and the temperatures of magnetic transitions? Magnetization measurements were performed on the whole prepared pellets to assess indirectly the stoichiometry in terms of some indications such as broadening (toward less oxygen content-off stoichiometric) or sharpening (toward more oxygen content-stoichiometric) in the transition features as was found for the non-intercalated compounds [53, 59, 60]. Another indication for better stoichiometry is the shift in those features to higher temperatures. The performed field cooling (FC) and Zero-field cooling (ZFC) measurements for some of the pellets are shown in Fig. 3.2. No sharpening in the field cooled curves is observed, which indicates that these pellets do not show a long range magnetic ordering down to 10 K. Instead, a glassy frozen state is developed with different freezing temperatures for pellets prepared with different stoichiometry, as shown in Fig. 3.2, which is ascribed to the formation of ferrimagnetic clusters. The divergence between FC and ZFC curve at low T is a signature of the spin freezing state [21, 131]. The nonzero ZFC magnetization at low temperature in this case is probably due to the small residual field in the magnetometer. This glassy behavior was observed before in the non-stoichiometric LuFe_2O_4 [45, 132], YbFe_2O_4 [35] and YFe_2O_4 [57]. For the pellet P39:30, the cooling in a field of 100 Oe is able to order the spins in the clusters more than other pellets as it exhibits the highest moment at low- T . In addition, a shift in the freezing temperature for higher values for pellets prepared with higher oxygen partial pressure is noticeable. These observations lead to the conclusion that the pellet prepared with 39 CO_2 and 30 $\text{Ar}(96%):\text{H}_2(4\%)$ ratio is the most stoichiometric one since it exhibits the highest freezing temperature in comparison with other pellets. As was observed for the non-intercalated ferrites,

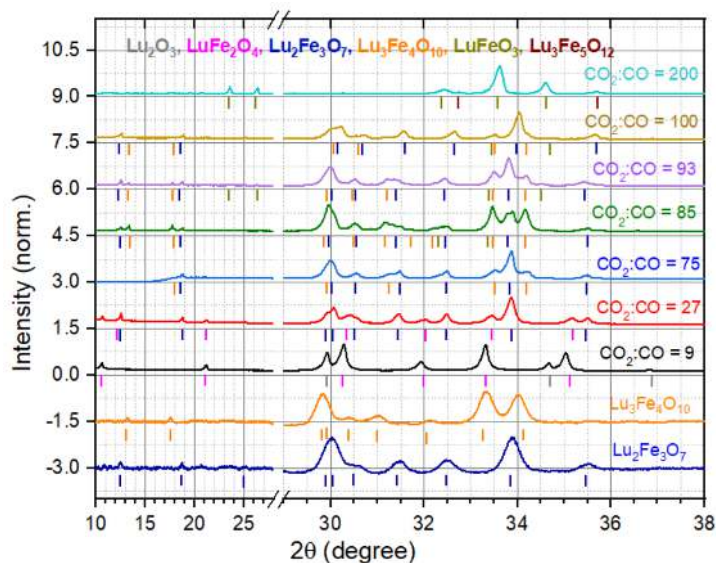


Figure 3.3: X-ray powder diffractograms of powdered parts of the grown boules (see text) grown with selected different gas flow of CO_2/CO , and of pure $\text{Lu}_2\text{Fe}_3\text{O}_7$ and $\text{Lu}_3\text{Fe}_4\text{O}_{10}$ crystals (extracted from single crystal X-ray diffraction). The present phases in each diffractogram marked with small lines. Taken from own work [64].

the higher the temperature is better in term of oxygen-stoichiometry [11, 21]. However, none of the prepared $\text{Lu}_2\text{Fe}_3\text{O}_7$ pellets exhibit sharp transition features indicating long-range magnetic order.

3.3 Optimization of single crystal growth of $\text{Lu}_2\text{Fe}_3\text{O}_7$ and $\text{Lu}_3\text{Fe}_4\text{O}_{10}$

After the determination of the range in which the polycrystalline $\text{Lu}_2\text{Fe}_3\text{O}_7$ is a pure phase, 27 CO_2 and 30 $\text{Ar}(96\%):\text{H}_2(4\%)$ was used in the preparation of needed rods for crystal growth. To investigate charge order in $\text{Lu}_2\text{Fe}_3\text{O}_7$, high quality stoichiometric crystals are required. These were grown via optical floating zone method under CO_2/CO ratios rather than CO_2 and $\text{Ar}(96\%):\text{H}_2(4\%)$ to avoid water formation [66] (Sec. 2.1.2). However, crystal growth of $\text{Lu}_2\text{Fe}_3\text{O}_7$ tends to be more difficult than for LuFe_2O_4 due to the more complex crystal structure [64]. Optimization of single crystals was done following the same procedure used for optimizing the polycrystalline material. The first order of businesses was to grow crystals as phase pure as possible and later on to fine-tune the oxygen stoichiometry. For optimizing the synthesis conditions based on the presence of foreign phases, regions of the grown boule containing several crystals and potentially polycrystalline material from each growth attempt were ground and checked by powder X-ray diffraction (c.f. Sec. 2.3.4) at room temperature. Fig. 3.3 shows the corresponding powder diffractograms of parts of the grown boules for a few selected CO_2/CO ratios.

Starting with the lowest gas ratio $\text{CO}_2/\text{CO} = 9$, this gas ratio leads to the formation of LuFe_2O_4 as the main phase but not the target $\text{Lu}_2\text{Fe}_3\text{O}_7$, and some impurity of Lu_2O_3 ,

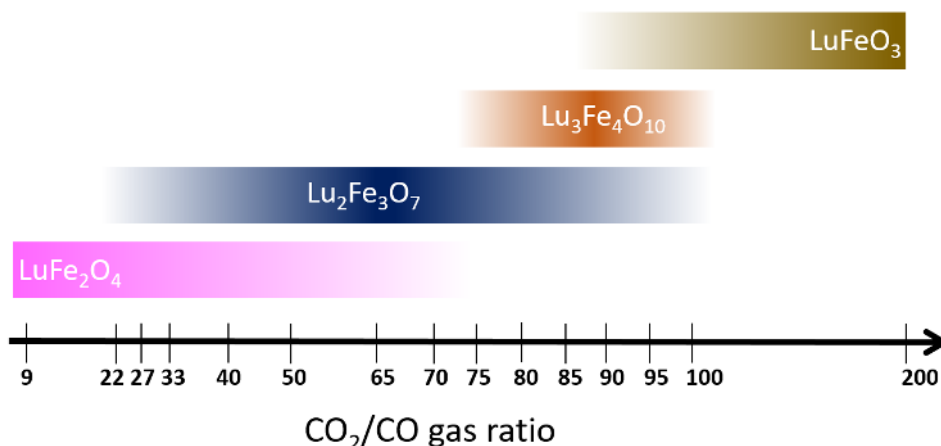


Figure 3.4: Main phases obtained for some of the crystal growth attempts at different gas flow of CO_2/CO . The ticks at the bottom indicate the concrete gas ratios used in the various crystal growths. Taken from own work [64].

indicating the very low oxygen partial pressure following the phase diagram see Fig. 1.9. In contrast, using a very high gas ratio of 200 leads to the growth of LuFeO_3 as main phase and some impurities of $\text{Lu}_3\text{Fe}_5\text{O}_{12}$ indicating the very high oxygen partial pressure as in Fig. 1.9. The observed phases of LuFe_2O_4 (LuFeO_3) at low (high) oxygen partial pressure is similar to what has been observed for the polycrystalline samples.

The target phase $\text{Lu}_2\text{Fe}_3\text{O}_7$ was observed in the range of CO_2/CO from 22 to 100, but it was never observed as the only phase, in contrast to our synthesized polycrystalline samples, see Fig. 3.4. For growths in the range $\text{CO}_2/\text{CO} = 75\text{--}80$, neither LuFe_2O_4 nor LuFeO_3 were present. However, new peaks which index to the second intercalation compound $\text{Lu}_3\text{Fe}_4\text{O}_{10}$ are present. Its structure was shown in Fig. 1.8 on p. 9. However, the $\text{Lu}_3\text{Fe}_4\text{O}_{10}$ phase was not observed during the synthesis of the polycrystalline samples, and was not observed in Sekine's phase diagram. Most likely, this is due to the much higher temperature used for crystal growth (higher than 1400 K), which changes the phase diagram and can stabilize new phases. This has been found before for the $\text{Fe-Fe}_2\text{O}_3\text{-Y}_2\text{O}_3$, [60], where YFe_2O_4 exists as a stable phase at 1200 °C [133], but not at 1100 °C [134]. Additional peaks indexing to LuFeO_3 are sometimes observed in the range of $\text{CO}_2/\text{CO} = 80\text{--}100$ besides those. Moreover, the powderized material was attracted by magnet suggesting the presence of a small phase fraction of Magnetite as well, which was not detectable in the diffractogram, likely because magnetite is very weakly diffracting. The presence of both LuFeO_3 and Fe_3O_4 is an indication that we are around the upper stability limit of the $\text{Lu}_2\text{Fe}_3\text{O}_7$, therefore in the region of most stoichiometric $\text{Lu}_2\text{Fe}_3\text{O}_7$ according to [42]. $\text{Lu}_3\text{Fe}_4\text{O}_{10}$ is also present at this upper stability limit. Despite the absence of single phase region, individual crystals are either $\text{Lu}_2\text{Fe}_3\text{O}_7$ or $\text{Lu}_3\text{Fe}_4\text{O}_{10}$, but (unlike reported in [63]), no instances of intergrowths of both phases in the same crystal were found.

3.4 Magnetization affected by stoichiometry

We have seen the influence of stoichiometry on magnetic behavior of the polycrystalline $\text{Lu}_2\text{Fe}_3\text{O}_7$ in Sec. 3.2. Consequently, we expect a dependence of the magnetic properties on oxygen content in crystals as well. So far, magnetization measurements on a non-stoichiometric $\text{Lu}_2\text{Fe}_3\text{O}_7$ single crystal exhibiting 2D magnetic ordering have been reported only, in [74]. Moreover, we expect sample-to-sample variation within one crystal growth as was noticed for LuFe_2O_4 [11, 53], YFe_2O_4 [60] and YbFe_2O_4 [59]. Therefore, after each crystal growth, many crystals were measured from different positions along the grown boule.

According to the only magnetization measurements performed on single crystalline $\text{Lu}_2\text{Fe}_3\text{O}_7$ [74], no magnetic response was observed under the application of 300 Oe perpendicular to c -axis, but observed for field applied parallel to the c -axis. Furthermore, the field cooled magnetization curves measured on SC1 (defined in next section 3.4.1) shown in Fig. 3.5 reveal significant differences in magnetization for the different orientations the parallel and the perpendicular to the field. This illustrates that the Fe spins behave as Ising on the triangular lattices along the c -axis similar to those in LuFe_2O_4 [11]. Therefore, the magnetic field was applied parallel to the c -direction in both DC and AC measurements for both compounds, as there is no reason to expect different behaviour for $\text{Lu}_3\text{Fe}_4\text{O}_{10}$. However, the alignment was relatively easy because the crystals cleave perpendicular to the c -direction. Low field magnetization measurements are used as a pre-characterization to assess the quality of samples in term of oxygen-stoichiometry, before doing detailed measurements as it was the best and the easiest indication for oxygen-stoichiometry in the non-intercalated compounds [11, 35, 57].

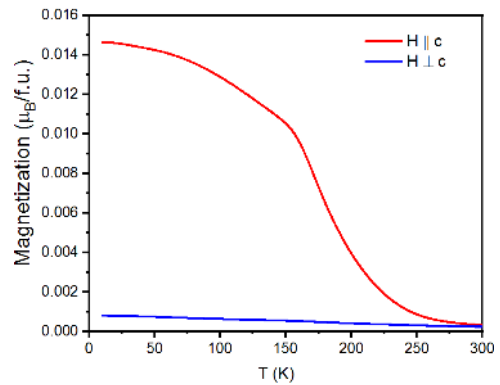


Figure 3.5: Field cooled magnetization measured on SC1 in a magnetic field of 100 Oe along two different orientations parallel and perpendicular to the field.

3.4.1 Variation of magnetic properties in $\text{Lu}_2\text{Fe}_3\text{O}_7$

A large number of crystals from each batch was analyzed for magnetic characterization. The results of the different characterized samples are represented by magnetization versus temperature from three single crystals (SC) in Fig. 3.6: SC1 obtained from the crystal growth using $\text{CO}:\text{CO}_2 = 50$ atmosphere, while SC2 and SC3 were both from a growth using $\text{CO}:\text{CO}_2 = 85$ atmosphere. Qualitatively, no variation in the magnetic behavior of different crystals is observable, i.e no sharpening in the FC feature with changing oxygen partial pressure in contrast to LuFe_2O_4 [11, 53], YbFe_2O_4 [35] and YFe_2O_4 [57]. The smeared upturn around ~ 263.6 K and ~ 213 K (the steepest slope temperature in the FC) in SC3 and SC2 respectively suggests the occurrence of short range ferrimagnetic spin order, with no indication for an antiferromagnetic phase as found in LuFe_2O_4 [53]. Moreover, the large difference between

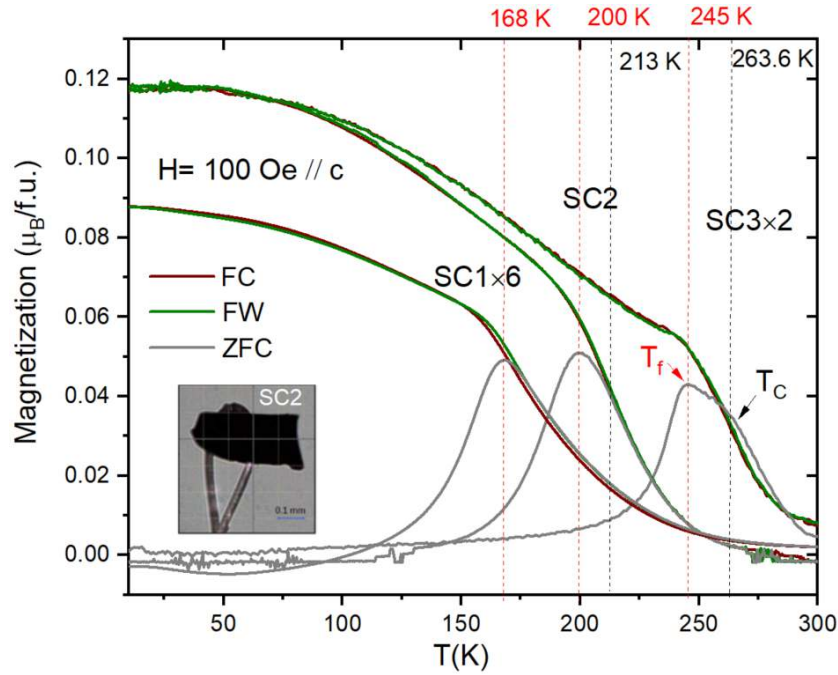


Figure 3.6: Temperature dependence magnetization measured with 100 Oe applied field parallel to c-direction for different $\text{Lu}_2\text{Fe}_3\text{O}_7$ single crystals, the inset shows the $(0.4 \times 0.2 \times 0.05) \text{ mm}^3$ measured SC2 mounted on holder for single crystal X-ray diffraction

FC and ZFC curves at low temperature indicates the formation of a spin glassy phase, or more likely clusters as found in LuFe_2O_4 [11], which is assigned by the maximum of ZFC curves in SC3 and SC2 (freezing temperature T_f : $\sim 245\text{K}$ and $\sim 200\text{K}$). This suggests that both crystals don't exhibit 3D spin order (SO). The observation of spin glass arises from the highly frustrated spin magnetic arrangements as in the LuFe_2O_4 [11]. For SC1, a broad transition can be observed around 168 K, meaning this crystal does not develop any long range order, but the system is glassy owing to the weakening of the magnetic correlations between the bilayers caused by the existence of the monolayer. The difference in magnetization for SC2 and SC3 in contrast to SC1 at low temperature suggests a considerable difference in the size of the ferrimagnetically ordered spins in the formed clusters.

The ac-susceptibility measurements with different driving frequencies are conducted to probe the magnetic correlations and to verify the spin (or cluster) glass state in SC1. Fig. 3.7 middle and lower panels show the real (χ') and imaginary (χ'') parts of the AC susceptibility as a function of temperature. Strong frequency dependence can be seen in the χ' of the AC susceptibility around T_C . The peaks in both χ' and χ'' shifts to higher temperature with increasing frequency. Such behavior is found for off-stoichiometric LuFe_2O_4 in various publications [45, 132]; and indicates that the crystal undergoes glass transition at this temperature, implying that crystal SC1 is definitely off-stoichiometric.

From the DC and AC magnetization results, and in combination with previously published results on the non-intercalated LuFe_2O_4 , it is concluded that SC1 is an off-stoichiometric crystal exhibiting short range magnetic order and frequency dependence in the AC susceptibility.

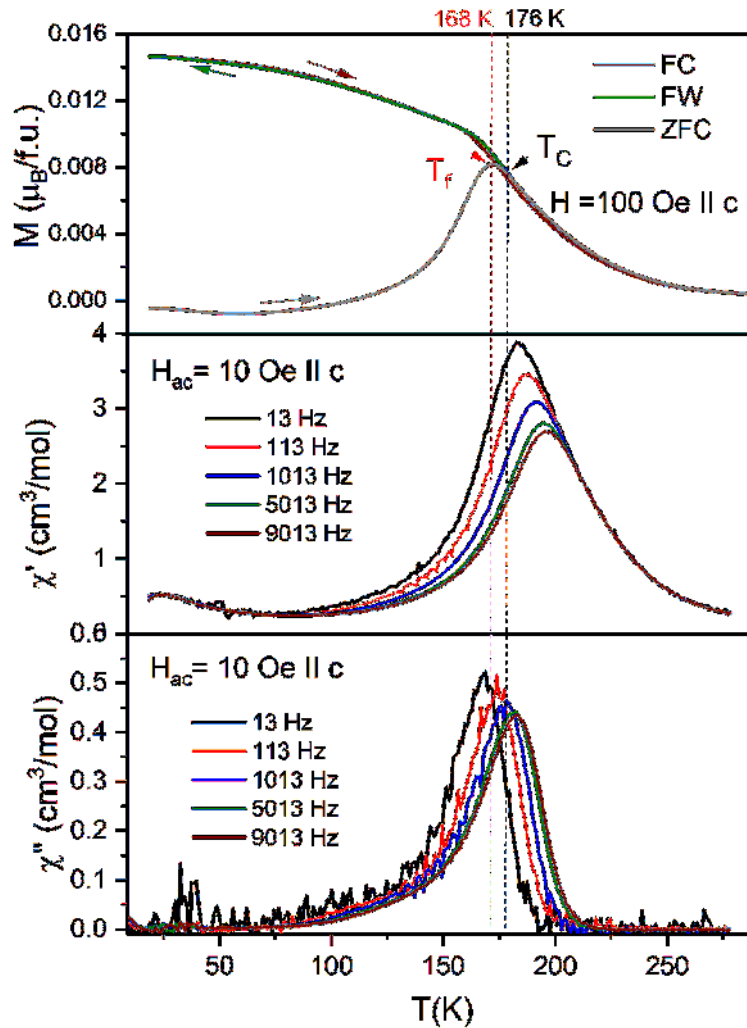


Figure 3.7: Temperature dependence of the magnetization (upper panel) and AC susceptibility obtained with different frequencies as labeled and 10 Oe applied Ac magnetic field. The real and imaginary parts of the susceptibility are shown in the middle and lower panels. All are performed using the non-stoichiometric $\text{Lu}_2\text{Fe}_3\text{O}_7$ SC1.

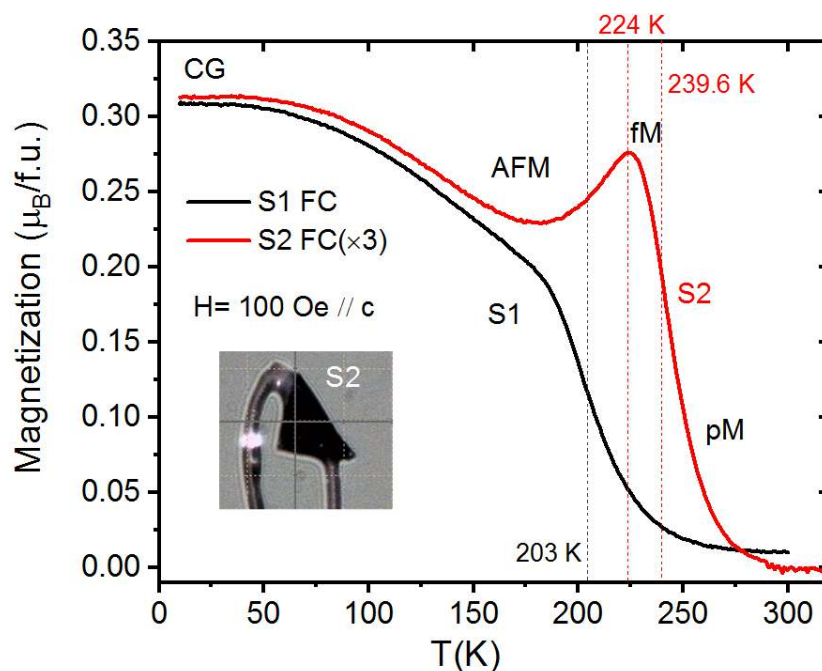


Figure 3.8: Field cooled magnetization measured in a magnetic field of 100 Oe on two $\text{Lu}_3\text{Fe}_4\text{O}_{10}$ crystals grown with gas ratio = 85, the inset shows the $(0.4 \times 0.2 \times 0.05) \text{ mm}^3$ measured S2 mounted on holder for single crystal X-ray diffraction.

While SC2 and SC3 are better in term of oxygen stoichiometry as the different features occur at higher temperatures (although still no long range spin order) and this is supported by the appearance of charge order superstructure reflections in X-ray diffraction. Based on these different indications, SC3 is the most stoichiometric one. Detailed discussion of the magnetization measurement of the most stoichiometric crystal SC3 will be presented in next chapter.

3.4.2 Variation of magnetic properties in $\text{Lu}_3\text{Fe}_4\text{O}_{10}$

No magnetization investigations had been published at all on $\text{Lu}_3\text{Fe}_4\text{O}_{10}$, therefore, no comparison can be made with our data. In analogy to $\text{Lu}_2\text{Fe}_3\text{O}_7$, $\text{Lu}_3\text{Fe}_4\text{O}_{10}$ crystals were measured in a field of 100 Oe parallel to the *c*-direction. Within the investigated crystals obtained from the crystal growth using $\text{CO}:\text{CO}_2 = 85$ atmosphere, a large variation in the magnetic properties is observed. Field cooling (FC) curves for are shown in Fig. 3.8. The first crystal (S1) shows behavior very similar to SC1 of $\text{Lu}_2\text{Fe}_3\text{O}_7$ suggesting that it is off-stoichiometric. Interestingly, the second crystal (S2) exhibits a completely different behavior, in which a sharp feature under cooling. This type of magnetic behavior could be classified to be in between type B and C of LuFe_2O_4 reported in [11]. Apparently, there are four distinctive regions of temperature in the FC curve, and correspondingly, magnetization curves for these three T regions, shows different character which are tentative and assigned based on LuFe_2O_4 in [11]: above 286 K, it is paramagnetic, between 286 K and 223 K, it is ferrimagnetic, antiferromagnetic phase at ~ 223 K, finally a glassy phase at low temperature. However, although a relatively sharp feature in

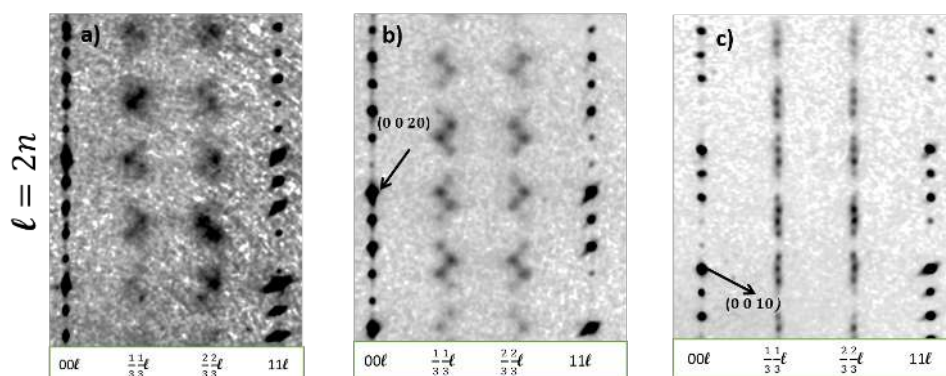


Figure 3.9: Precession images of the (hhl) reciprocal space plane of $\text{Lu}_2\text{Fe}_3\text{O}_7$ crystals grown with $\text{CO}_2/\text{CO} = 83$ for a and 85 for b (SC2) and c (SC3), measured at room temperature. From own work [64]

the FC is observed which indicates better stoichiometry than S1, still it does not show the best sharpness as type A LuFe_2O_4 in [11]. Detailed discussion of the magnetization measurement of the most stoichiometric S2 crystal will be presented in Sec. 4.2.

3.5 Charge order and oxygen stoichiometry

In the limited number of publications on intercalated rare earth ferrites either experimental or theoretical, the charge order has been rarely studied (See Sec. 1.3). 2D CO diffuse correlations have been observed by [63] using electron diffraction on a small grains of polycrystalline $\text{Yb}_2\text{Fe}_3\text{O}_7$ and $\text{Yb}_3\text{Fe}_4\text{O}_{10}$ [63], by [76] on polycrystalline $\text{Yb}_2\text{Fe}_3\text{O}_7$, and by [80] on Mg-doped $\text{Lu}_2\text{Fe}_3\text{O}_7$. The only observation of superstructure spots was by [75, 77] from electron diffraction on small grains of polycrystalline $\text{Lu}_2\text{Fe}_3\text{O}_7$ and $\text{Lu}_2\text{Fe}_2\text{Fe}_{0.2}\text{Mn}_{0.86}\text{O}_7$ samples.

The charge order CO in this work was investigated at room temperature using a Rigaku Supernova diffractometer employing Mo- $K\alpha$ radiation, as detailed in Sec. 2.3.6. Many crystals from different batches were checked with a focus on crystals grown with gas ratio 80-100, in which the most stoichiometric $\text{Lu}_2\text{Fe}_3\text{O}_7$ is expected.

3.5.1 Charge ordering in $\text{Lu}_2\text{Fe}_3\text{O}_7$

Regarding $\text{Lu}_2\text{Fe}_3\text{O}_7$, three different types of diffraction results were obtained: the first type with strong off-stoichiometry showing a zigzag diffuse scattering along $(\frac{1}{3} \frac{1}{3} \ell)$ in addition to Bragg reflections from the $P6_3/mmc$ basic crystal structure (c.f. Fig. 1.11 on P. 11), indicating short range charge order, (See Fig. 3.9 a). The second type of crystals of magnetic behaviour of SC2 exhibits superstructure reflections also with zigzag pattern but with stronger intensity and narrower peaks, as can be seen in the projection of the reciprocal hhl plane (Fig. 3.9 b). This indicates that the sample is more stoichiometric. This type of incommensurate pattern had been reported for small regions of polycrystalline $\text{Lu}_2\text{Fe}_3\text{O}_7$ using electron diffraction in [75]. Interestingly, the third type of magnetic behaviour, of SC3, is more stoichiometric and exhibits a commensurate ($\tau = 0$ within experimental resolution) superstructure (Fig. 3.9 c). Such a commensurate CO was not observed before in LuFe_2O_4 or $\text{Lu}_2\text{Fe}_3\text{O}_7$, but there is two

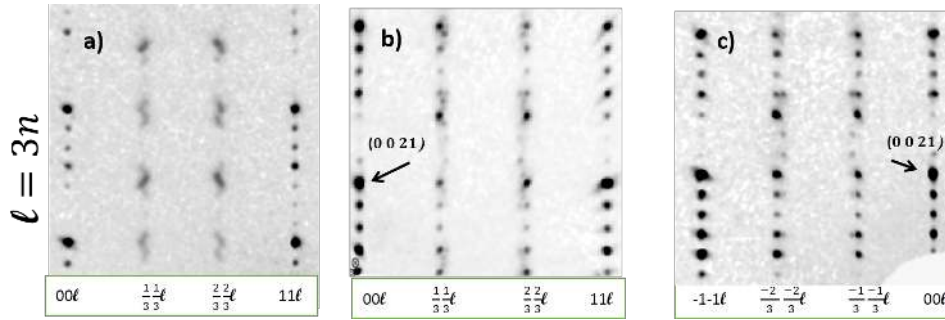


Figure 3.10: Precession images of the $(hh\ell)$ reciprocal space plane of a $\text{Lu}_3\text{Fe}_4\text{O}_{10}$ crystals grown with $\text{CO}_2/\text{CO} = 90$ for a and 85 for b (S1) and c (S2), measured at room temperature. Figure (a,b) from own work [64]

reports where such a commensurate pattern was found in YbFe_2O_4 below ~ 250 K [35, 40]. The detailed analysis of this type of CO will be presented in Chapter 5.

3.5.2 Charge ordering in $\text{Lu}_3\text{Fe}_4\text{O}_{10}$

Crystals of $\text{Lu}_3\text{Fe}_4\text{O}_{10}$ also exhibit three different types of diffraction results as well: the first type with strong off-stoichiometry showing a zigzag diffuse scattering along $(\frac{1}{3}\frac{1}{3}\ell)$ in addition to Bragg reflections from the $R\bar{3}m$ basic crystal structure (shown in Fig. 5.21 on P. 105), indicating a two dimensional charge order. See Fig. 3.10 a. This type has been observed before in [63] on $\text{Yb}_3\text{Fe}_4\text{O}_{10}$. Second type are crystals with magnetic behavior of S1 with superstructure reflections with a zigzag pattern indicate a better stoichiometry. For the final type, crystals of magnetic behavior of S2 exhibit a purely commensurate superstructure (Fig. 3.10 c). This type of 3D commensurate CO has never been observed before in LuFe_2O_4 , $\text{Lu}_3\text{Fe}_4\text{O}_{10}$. More in-depth studies of this type of CO is presented in Sec. 5.3.

3.6 Discussion

Based on our interest of investigating the CO in the intercalated compounds, we succeeded in growing single crystals of $\text{Lu}_2\text{Fe}_3\text{O}_7$, but also $\text{Lu}_3\text{Fe}_4\text{O}_{10}$, which are sufficiently stoichiometric to exhibit for the first time superstructure reflections indicating the long range charge order. The performed magnetic investigations led to the conclusion that no pronounced dependence of the magnetic property has been detected in $\text{Lu}_2\text{Fe}_3\text{O}_7$, in contrast to $\text{Lu}_3\text{Fe}_4\text{O}_{10}$ i.e. no changes in the features found in $\text{Lu}_2\text{Fe}_3\text{O}_7$ referring basically to the sharpness in the FC curve which mostly due to insufficient oxygen content. Moreover, a strong inhomogeneity of the crystals stoichiometry in samples from the same growth for both compounds was observed. The magnetization measurements performed on $\text{Lu}_2\text{Fe}_3\text{O}_7$ are correlated with charge ordering types, however, even for clearly long-range CO, there is no long range SO. This is in contrast to non-intercalated compounds [11, 35, 57]. It is likely that for more stoichiometric crystals, a long-range spin order could be established. In any case, the SO appears to be more fragile than CO in the system. A similar observation was made before for some crystals of YbFe_2O_4 [35].

In the following chapter 4, the magnetization behaviour of the most stoichiometric samples for both compounds with further in-depth studies will be discussed before heading into the analysis and the refinement of the CO crystal structure in chapter 5.

4

Magnetic properties of $\text{Lu}_2\text{Fe}_3\text{O}_7$ and $\text{Lu}_3\text{Fe}_4\text{O}_{10}$

In this chapter, extensive investigations of the magnetic behavior of $\text{Lu}_2\text{Fe}_3\text{O}_7$ and $\text{Lu}_3\text{Fe}_4\text{O}_{10}$ single crystals are presented. These were performed to study how intercalating additional single Fe-layers in LuFe_2O_4 affects the magnetic ordering in these compounds. A clear understanding of the magnetic ordering is missing due to the limited number of publications on $\text{Lu}_2\text{Fe}_3\text{O}_7$ [65, 68, 71–75] and the absence of any for $\text{Lu}_3\text{Fe}_4\text{O}_{10}$. As Lu^{+3} is nonmagnetic, the magnetism arises from contributions of Fe-ions in the single Fe layers and of Fe-ions in the bilayers (see Fig. 1.8 on p. 9). The magnetic field was applied parallel to the c-axis for both compounds due to the strong Ising behaviour as discussed in Sec. 3.4. In the first two sections, the macroscopic magnetization measurements on $\text{Lu}_2\text{Fe}_3\text{O}_7$ and $\text{Lu}_3\text{Fe}_4\text{O}_{10}$ are presented in detail. The following sections are devoted to the microscopic magnetization measurements with analysis including polarized neutron scattering and the X-ray magnetic circular dichroism measurements. At the end, the chapter closes with a discussion interconnecting the results from different measurements.

4.1 Macroscopic magnetic properties of stoichiometric $\text{Lu}_2\text{Fe}_3\text{O}_7$

This section is focused on a $\text{Lu}_2\text{Fe}_3\text{O}_7$ crystal (SC3) obtained from the crystal growth using $\text{CO}_2:\text{CO} = 85$ and judged to be the most stoichiometric since it exhibits commensurate superstructure reflections by single crystal X-ray diffraction (Fig. 3.9 c on p. 48).

4.1.1 Low field studies of $\text{Lu}_2\text{Fe}_3\text{O}_7$

Figure 4.1 shows the temperature-dependent magnetization of crystal SC3 measured in a field of 100 Oe during cooling (FC), warming (FW) and warming after zero-field-cooling (ZFC). The magnetization curves presented in this figure was shown before in Sec. 3.4.1 to compare it with the magnetic behaviour of other samples in term of stoichiometry and it was found to be the best. Magnetization under cooling in 100 Oe does not exhibit any sharp peak or other sharp feature. The non-sharpness of the upturn around 264 K (T_C) suggests the occurrence of short or medium-range ferrimagnetic spin order. Moreover, at the lower temperature side in the vicinity of T_C , a slight bump in the FC can be observed. The observed bump is very weak without any sharp drop which is likely due to the absence of long-range order on the high and

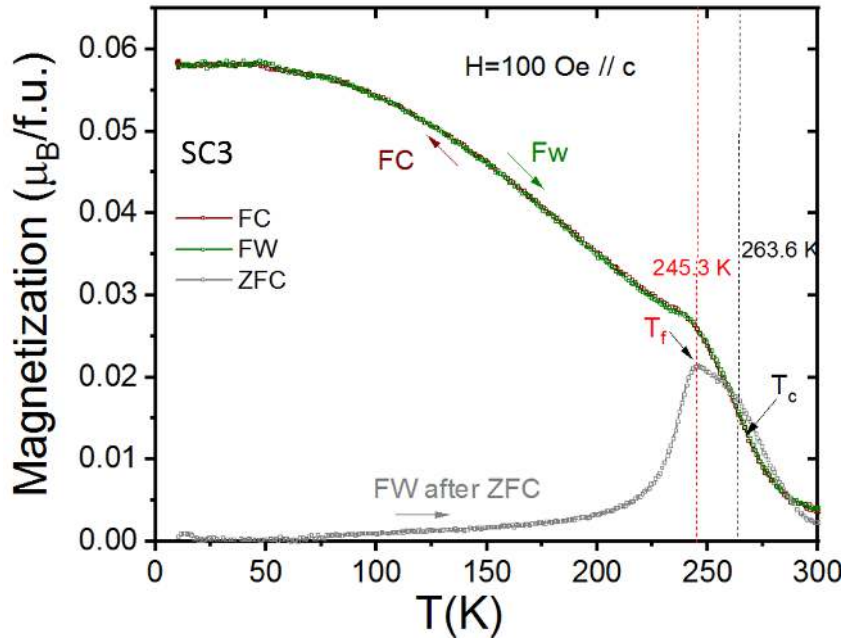


Figure 4.1: Magnetization on $\text{Lu}_2\text{Fe}_3\text{O}_7$ during field cooling, field warming and zero field cooling at 100 Oe. T_C assigned by the steepest slope in FC curve, while T_f by the maximum of ZFC curve.

low temperature sides. As can be seen, no change in the magnetic behaviour upon warming and cooling, meaning no thermal hysteresis between FC and FW curves is present, suggesting the absence of a first-order transition. On the other hand, the ZFC curve has a maximum at 245 K, to which we assign the freezing temperature T_f , and exhibits much lower magnetization at low temperature, which is a signature for spin glasses and other "glassy" like cluster glasses [131] preventing the system to develop a long-range magnetic order. A cluster glass is very likely to be formed since it was previously reported for LuFe_2O_4 [45, 47, 132], due to the magnetic frustration leading to a competition between ferrimagnetic and antiferromagnetic phases [50, 135]. In this glassy phase, the spins slow down their thermal fluctuations and build up in to locally correlated units exhibiting a cluster characteristic without long range magnetic order [131]. The ZFC curve seems to exhibit a higher magnetization than both the FC and FW curves directly above T_C , which may be related to the presence of small second grain observed by single crystal X-ray diffraction (this can be seen as an overlap of the ZFC of both crystals).

4.1.2 High field studies of $\text{Lu}_2\text{Fe}_3\text{O}_7$

4.1.2.1 Isofield magnetization of $\text{Lu}_2\text{Fe}_3\text{O}_7$

Magnetization vs. temperature measurements in higher fields were performed to map the magnetic phase diagram of $\text{Lu}_2\text{Fe}_3\text{O}_7$ and are shown in the left panel of Fig. 4.2. No differences in magnetization between warming and cooling were observed in all measured fields. As can be seen, with increasing the magnetic field, the feature assigned T_C starts to smear out and shift to higher temperatures as expected for a ferro- or ferrimagnetic transition, the shift was noticeable

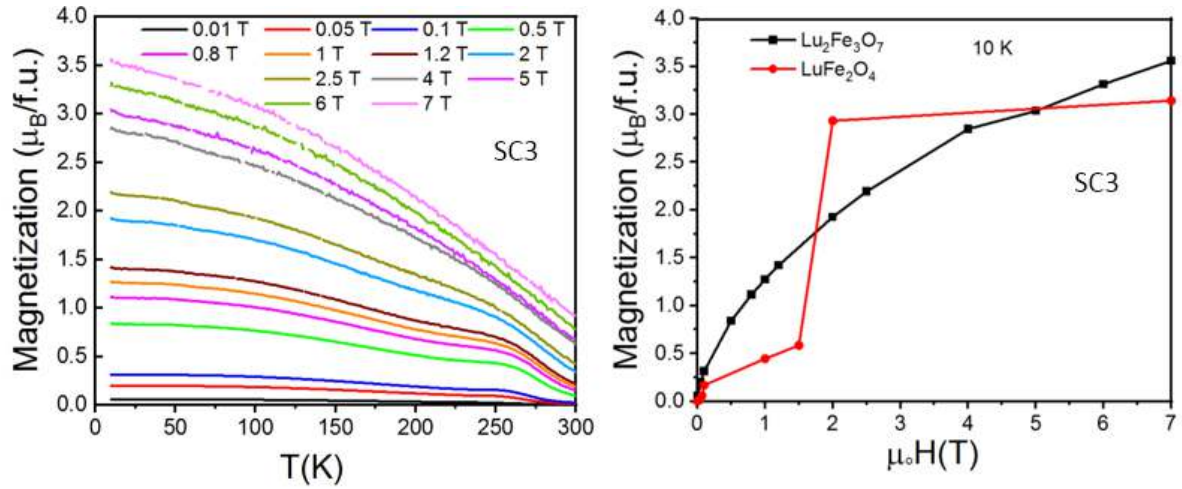


Figure 4.2: Left: Temperature dependent magnetization during field cooling and followed by field warming at different magnetic fields. FC and FW are perfectly overlapped for all used fields. Right: Field dependent low-temperature magnetic moment for $\text{Lu}_2\text{Fe}_3\text{O}_7$ (black curve) and for LuFe_2O_4 (red curve). LuFe_2O_4 data were extracted from Fig. 4 in [136].

as determined by the steepest slope criteria (see Fig. 4.7 on p. 58). For very high fields (higher than 2 T), the peak-like shape below T_C vanishes and a continual increase in the magnetization is observed. The net moment at low-temperature, extracted from the field-cooling curves, is inconsistent with a ferromagnetic order (for which $10 \mu_B/\text{f.u.}$ would be expected) and depends on the applied field as shown in the right panel of Fig. 4.2. For comparison, the low-T moment of LuFe_2O_4 is also shown. As can be seen, LuFe_2O_4 containing only the Fe bilayers exhibits a constant $2.9 \mu_B/\text{f.u.}$ moment at 2 T (in lower fields it is no longer in the ferrimagnetic phase [see e.g. [11]]) and higher fields. In contrast, $\text{Lu}_2\text{Fe}_3\text{O}_7$ exhibits a comparable value only at 5 T and interestingly continues to increase afterward with an approximately linear behaviour in the moment-field dependence, which might indicate a paramagnetic behaviour in the single layer. However, for the assumption of paramagnetic behaviour to hold, the slope (magnetic susceptibility) should be inversely proportional to the temperature. At 200 K, the slope is $0.09 (\mu_B/\text{f.u.})/(\mu_0\text{H(T)})$. Therefore, a slope of $1.8 (\mu_B/\text{f.u.})/(\mu_0\text{H(T)})$ is expected at 10 K which is not the case (a slope of $0.13 (\mu_B/\text{f.u.})/(\mu_0\text{H(T)})$ is obtained from Fig. 4.6c). This clearly indicates that normal paramagnetic behaviour does not apply. However, a Curie-Weiss-like paramagnetic behaviour can not be excluded. Unfortunately, there is not sufficient data to conclusively confirm or reject this hypothesis. The contributions of the bilayer and the single layer to the overall moment at low-T will be elucidated later in Sec. 4.1.2.3 based on the thermomnant measurements.

Fig. 4.3 shows the zero-field-cooling and field-cooling measurements for both the most stoichiometric single crystal SC3 and the off-stoichiometric crystal SC1 (as discussed in Sec. 3.4.1 and Sec. 3.5.1). For SC3, ZFC curves exhibit a small feature at low temperature. The FC and ZFC curves of SC1 are shown because this crystal was used in polarized neutron scattering experiment (see Sec. 4.3).

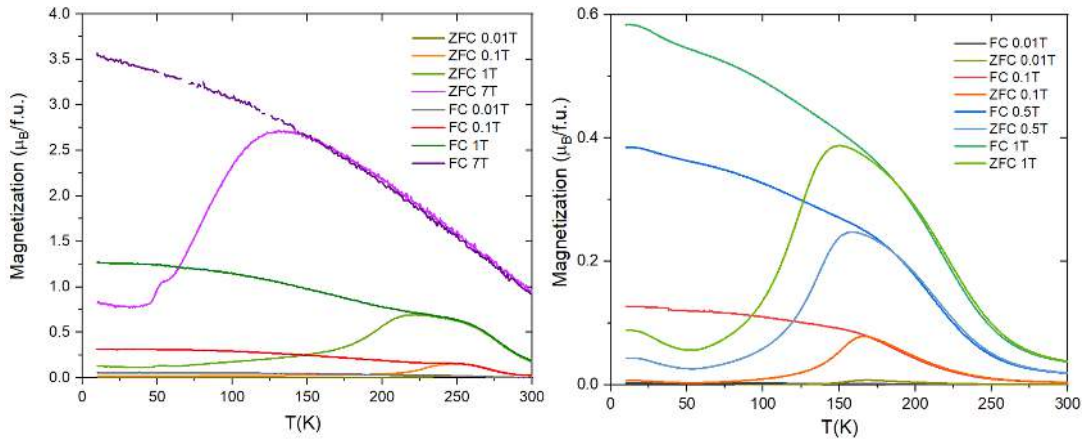


Figure 4.3: Left: Zero-field-cooling and field-cooling measurements for SC3. Right: Zero-field-cooling and field-cooling measurements for SC1.

4.1.2.2 Isothermal magnetization in $\text{Lu}_2\text{Fe}_3\text{O}_7$

Hysteresis ($M(H)$) loops measured at different temperatures are shown in Fig. 4.4a. The shape of $M(H)$ -loops below T_C correspond to the behaviour expected for ferro- or ferrimagnetic spin order without any indications for meta-magnetic phase transitions as $M(H)$ -loops carry a net moment at both low-field and high-field regions. Moreover, the virgin curve of $M(H)$ -loop measured after cooling in zero field is (within error bars) inside the loop, an example measured at 160 K is shown in the inset (b) of Fig. 4.4. All these provide no indication for the presence of first order metamagnetic transition. In contrast, a butterfly-like shape $M(H)$ -loops are observed in LuFe_2O_4 [11] with the virgin curve being outside the loop indicating the presence of AFM-fM metamagnetic transitions [11].

The linear behaviour at 320 K reveals a pure paramagnetic phase for the whole system. However, at 290 K which is still higher than the T_C extracted from the $M(T)$ curve, $M(H)$ exhibits nonlinear behaviour with bending in low-field (S-like shape). This deviation from the pure paramagnetic behaviour was previously observed in LuFe_2O_4 [11, 53] in $M(H)$ in a wide T -range above the transition temperature, up to ~ 400 K. It was explained based on the polarized neutron scattering evidence as due to the alignment of randomly stacking of the net moment of still short-range ordered bilayers (2D magnetic order) [11]. Below 220 K, $M(H)$ exhibits hysteresis resembling a ferrimagnetic phase with remanent magnetization. All the measured loops do not reveal a saturation in fields up to 7 T, in agreement with FC measurements at high fields shown in the right panel of Fig. 4.2.

$M(H)$ -loops exhibit roughly linear behaviour in the range 5-7 T. These were fitted and the temperature dependence of the slopes and the corresponding intercepts are shown in 4.4c. The slope might be taken to represent the behaviour of the spins in the single layer if we assume that their contribution behaves like a paramagnetic and in this field range the bilayers contribution is saturated as discussed in the previous Sec. 4.1.2.1, while the intercept then gives the magnetic moment in the bilayers. The focus is on $M(H)$ -loops below T_C , as the bilayers are assumed to be saturated by 5 T. Below T_C , the magnetic moment in the bilayers increases as the

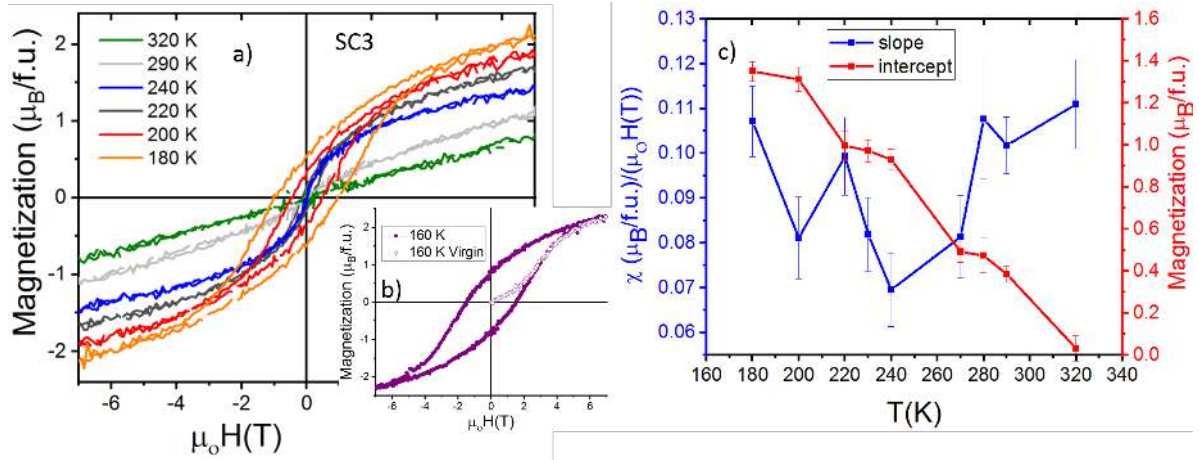


Figure 4.4: a) Magnetization M vs. $H \parallel$ to c loops measured on $\text{Lu}_2\text{Fe}_3\text{O}_7$ at different temperatures. b): hysteresis loop including the virgin curve which was measured after cooling in zero field at 160 K. c) The slopes and the intercepts of the fitted hysteresis in field region of 5-7 T. The dotted line indicated the expected behaviour.

temperature decreases. Tentatively, the induced magnetic moment in the single layer decreases with increasing T below T_C as well. Note that a small temperature region was investigated, since the $M(H)$ -loops at 7 T do not reach the magnetization obtained after FC. In addition, large error bars are present. Figure 4.5 shows the $M(H)$ -loops started after zero-field-cooling for temperatures below T_f (symbols) and the part after cooling in a field of 7 T (lines). The loops are less sharp and not saturated. A discrepancy can be seen in the magnetization values at 7 T for $M(H)$ loops measured after cooling in zero field and $M(H)$ measured after cooling and it is getting increased for lower temperatures. This leads to the conclusion that 7 T is not sufficient to obtain a full loop and higher fields are definitely needed. This is not unique to $\text{Lu}_2\text{Fe}_3\text{O}_7$, but is also the case in LuFe_2O_4 [11], in which a magnetic field of 22 T was needed to obtain full $M(H)$ -loop at 4 K. Therefore, the shown $M(H)$ curves are not representative of full loops. Therefore, the obtained " H_c " below 120 K shown in the right panel of Fig. 4.5 are not the coercive fields. The expected behaviour for full loops are indicated by dotted line. An enhancement in the coercivity can be clearly seen in the right panel of Fig. 4.5 below the freezing temperature i.e. in the cluster glass state similar to what observed in LuFe_2O_4 [47, 50]. According to [47, 50], the collective freezing of ferrimagnetic clusters below the freezing temperature leads to the onset of increase in coercivity.

4.1.2.3 Thermo-remnant magnetization in $\text{Lu}_2\text{Fe}_3\text{O}_7$

Thermoremanent magnetization (TRM) measurements were carried out by measuring upon warming the sample from 10 K to 400 K in zero field after the sample had been cooled to 10 K in either 7 T or 1 T and are shown together with the corresponding FC curves in Fig. 4.6a. Large TRM values are noticeable at low- T , which is unusual. However, such large values have been observed previously in LuFe_2O_4 with almost no difference to the FC value at the base temperature, attributed to the system being trapped in the fM-phase. For temperatures below

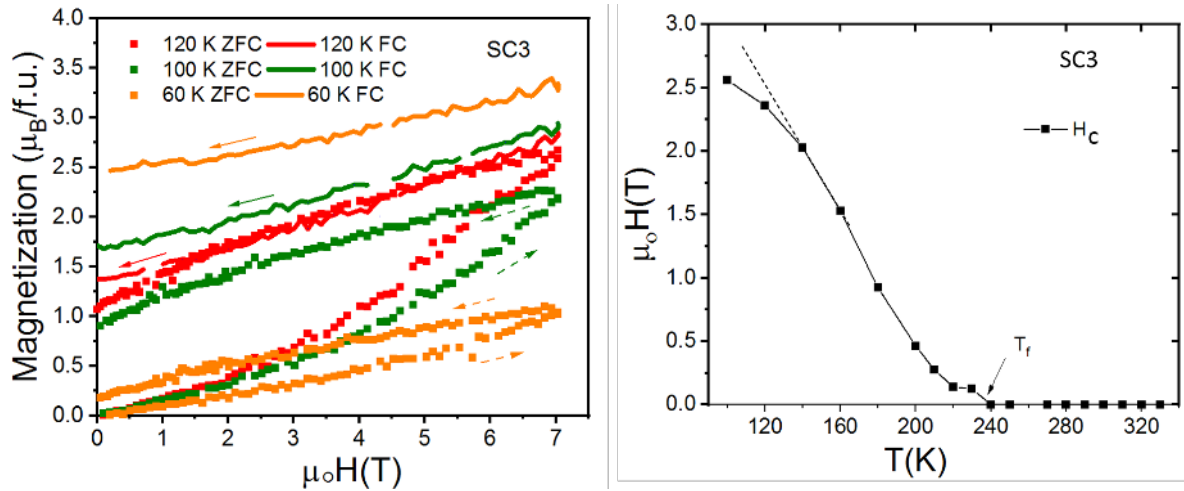


Figure 4.5: Left panel: $M(H)$ at temperatures below the freezing temperature. Solid lines were measured after cooling in a field of 7 T. Right panel: Temperature dependence of coercive field obtained at the negative field magnetization vanishes, the obtained values below 120 K can not be trusted since the $M(H)$ -loops doesn't reach the FC value for a maximum field of 7 T.

~ 60 K, a plateau behaviour can be seen. This is similar to what was observed in LuFe_2O_4 [11, 34, 47] and other systems [137, 138]. The explanation for this behaviour in LuFe_2O_4 [11] was in term of Kinetic arrest, in which the magnetic phase in the system is trapped in a metastable phase and the transition to a more thermodynamically stable phase by cooling in low field is prohibited by a barrier exceeding the thermal fluctuations. This can be seen in the drop of the TRM curve upon continuous warming at the freezing temperature around 60 K. However, the drop in magnetization is gradual and less sharp compared to LuFe_2O_4 due to the sample inhomogeneity. The TRM curves in $\text{Lu}_2\text{Fe}_3\text{O}_7$ reaches zero around 245 K. A significant difference in the magnetization at low temperature between the FC and the corresponding TRM can be seen. This difference is very large particularly after cooling in 7 T as compared to LuFe_2O_4 (see Fig. 4.6b). After cooling in the higher field, TRM exhibits $\sim 2.7\mu_B$ per formula unit which is very close to that for LuFe_2O_4 ($2.9\mu_B/\text{f.u.}$) [11]. This also was observed before in $\text{Lu}_2\text{Fe}_3\text{O}_7$ by [73]. The small difference could be due to the not well-established order in the bilayers. This observation is consistent with a similar spin arrangements in the bilayer to those in LuFe_2O_4 (see Sec. 4.5 for further discussion). The difference between FC and TRM at low temperature for 7 T is about 7 times larger than the value for 1 T, therefore, the net magnetic moment aligned in the field direction could be assumed to be purely induced by the magnetic field i.e. paramagnetic, thus, no contribution from the single layer for the TRM. This suggests that the additional $1\mu_B$ per formula unit in the FC of $\text{Lu}_2\text{Fe}_3\text{O}_7$ in 7 T at low temperature compared to LuFe_2O_4 is from the single layers. To extract the tentative bilayer contribution (see Fig. 4.6c) at low temperature, the single layer contribution (difference between FC and TRM) was calculated for the two measured fields and fitted using a paramagnetic model (linear behaviour), then subtracted from TRM.

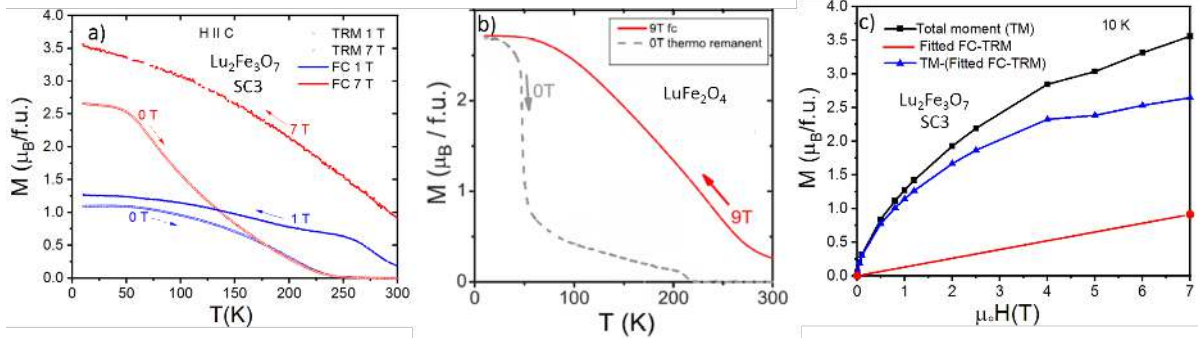


Figure 4.6: a) Temperature dependence of thermoremanent magnetization of $\text{Lu}_2\text{Fe}_3\text{O}_7$ after cooling in two different external fields with 2 K/m (symbols) and the corresponding field cooling curves (lines). b): TRM and FC curves of LuFe_2O_4 , taken from [11]. c) Total moment at low-temperature from the right panel of Fig. 4.2 and linear fitting (red line) of FC-TRM (red circles). The subtraction of the fitted FC-TRM from the total moment results in the tentative bilayer contribution (blue curve).

4.1.3 Magnetic phase diagram of $\text{Lu}_2\text{Fe}_3\text{O}_7$

The tentative magnetic "phase" diagram for $H \parallel c$ established from the DC magnetization measurements is presented in Fig. 4.7. The phase diagram consists of three different "phases": paramagnetic (PM), 2D-fM (ferrimagnetic), cluster glassy phase (CG) and the Kinetic arrested phase. The "phase boundary" between paramagnetic (PM) and ferrimagnetic (fM) is determined by the steepest (maximum) slope in the FC measurements (T_C) (left panel of Fig. 4.2). It is remarkably similar to that reported in LuFe_2O_4 [11, 47], however, in $\text{Lu}_2\text{Fe}_3\text{O}_7$, the ferrimagnetic state is not long range ordered in contrast to LuFe_2O_4 , and therefore strictly speaking not a thermodynamic phase. Switching between PM and fM can be achieved directly by cooling or warming in H because FC and FW are overlapped and no thermal hysteresis is present. Applying a magnetic field shifts the corresponding temperature to higher values. However, non-linear $M(H)$ measurements in the PM phase provided indications of internally ordered bilayers that are randomly stacked in light of similar evidence explained in LuFe_2O_4 [11].

The "phase boundary" between fM and the cluster glassy phase (CG) is determined by the maximum of the ZFC measurements (T_f) (right panel of Fig. 4.3). The fM region likely corresponds to be short-range magnetic order as is indicated by the absence of any sharp feature in FC curve in low- H . Thus, no long-range order is present and a freezing of the spins only occurs in the labeled CG phase. Upon further cooling to temperatures below ~ 60 K, the system appears to be kinetically arrested indicated by the blue area, the drop in thermoremanent data (left panel of Fig. 4.6) was taken as an approximate indication to which temperature occurs and extended, therefore, it is shown as blurred. The complex magnetic nature primarily is due to the complexity of the system. To obtain a more clear picture about the true nature of magnetic phases, investigations via microscopic studies are necessarily needed, these will be presented later on in Sec. 4.3 and 4.4.

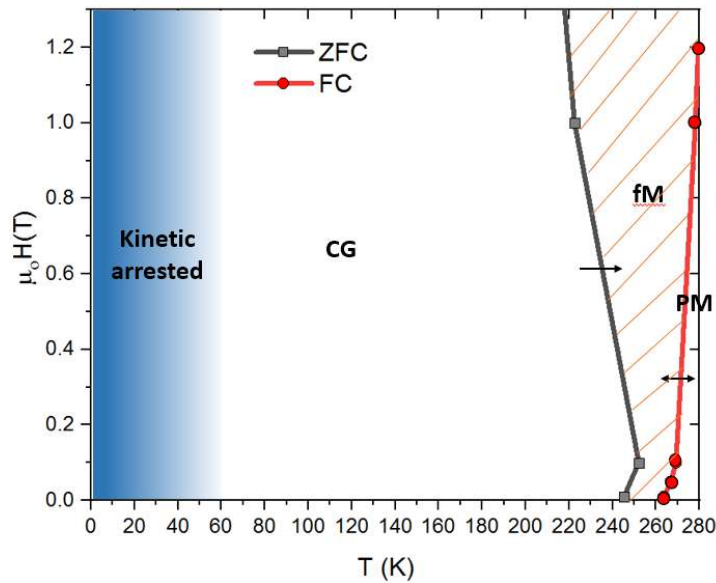


Figure 4.7: H-T "phase" diagram for SC3 of $\text{Lu}_2\text{Fe}_3\text{O}_7$ extracted from different DC measurements ($H \parallel$ to c). Three magnetic "phases" are labeled: PM, fM, CG, see text for labeling. The red circles were obtained from the FC measurements at different DC fields and the gray squares from ZFC measurements at different DC fields. Arrows indicate the direction T for which a feature accrue. The blurred blue area indicating the transition CG- fM is arrested below ~ 60 K.

4.2 Macroscopic magnetic properties of stoichiometric $\text{Lu}_3\text{Fe}_4\text{O}_{10}$

This section is focused on single crystal S2 of $\text{Lu}_3\text{Fe}_4\text{O}_{10}$ obtained from the crystal growth using $\text{CO}_2:\text{CO} = 85$ and assigned to be the most stoichiometric crystal as it exhibits a commensurate superstructure reflections by single crystal X-ray diffraction (Fig. 3.10c on P. 49). The magnetization measurements shown here are unique as they are the first to be reported at all for $\text{Lu}_3\text{Fe}_4\text{O}_{10}$.

4.2.1 Low field studies of $\text{Lu}_3\text{Fe}_4\text{O}_{10}$

The magnetization versus temperature curves measured on crystal S2 in 100 Oe are shown in Figure 4.8. As can be seen, this crystal exhibits an upturn around 240 K in the $M(T)$ curves under cooling in low magnetic field of 100 Oe. The upturn is quite sharp indicating that this temperature corresponds to a transition from the paramagnetic (PM) to the 3D ferrimagnetic phase (fM) similar to LuFe_2O_4 [11] and the isostructural YbFe_2O_4 [35]. The observed magnetization value is much lower than what is expected for a ferromagnetic spin arrangement. Upon further cooling, a drop in the magnetization around ~ 224 K indicates the entrance to antiferromagnetic (AFM) phase by at least a part of the sample, while some regions appear to remain in the fM phase. The drop is expected to go to lower magnetization values for better sample stoichiometry as observed in LuFe_2O_4 [11]. An overlap in the magnetization upon warming and cooling suggests the absence of thermal hysteresis. Moreover, there is no indication of the low-T phase transition associated with a structural distortion observed in

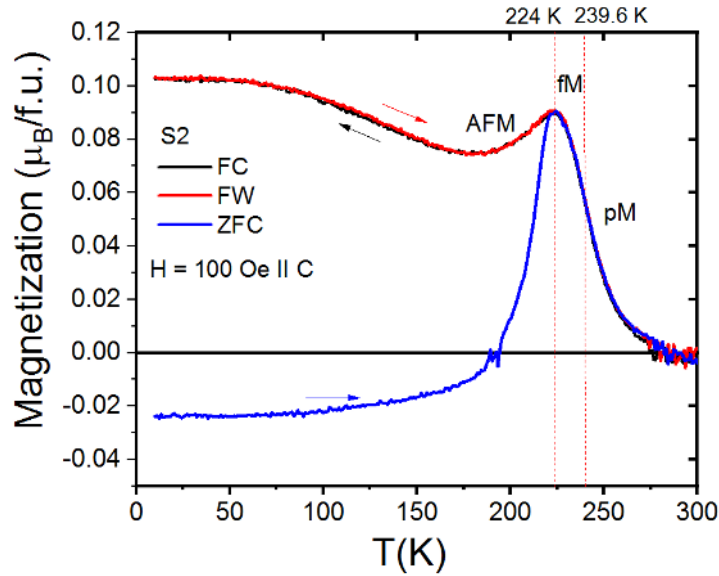


Figure 4.8: Magnetization measurements of $\text{Lu}_3\text{Fe}_4\text{O}_{10}$ single crystal as a function of temperature on field cooling, field warming and zero field cooling in 100 Oe. Lines separated different phases was determined by the steepest slope in the FC for transition from pM to fM and by the maximum of ZFC for fM to AFM transition. The negative magnetization values in ZFC below 200 K is an artifact due to the presence of some residual magnetic field.

LuFe_2O_4 [11], but not in $\text{Lu}_2\text{Fe}_3\text{O}_7$ (see Sec. 4.1). The large difference between the ZFC and the FC curves at low temperature indicates the presence of a glassy phase. A cluster glass is very likely to be formed as in LuFe_2O_4 [45, 47, 132] or as discussed for $\text{Lu}_2\text{Fe}_3\text{O}_7$ in the previous section.

4.2.2 High field studies of $\text{Lu}_3\text{Fe}_4\text{O}_{10}$

4.2.2.1 Isofield magnetization of $\text{Lu}_3\text{Fe}_4\text{O}_{10}$

Field cooling and field warming measurements performed in a few magnetic fields up to 0.45 T on $\text{Lu}_3\text{Fe}_4\text{O}_{10}$ (S2) crystal are shown in Fig. 4.9. A small bump can be observed around 275 K and interestingly the bump is more noticeable for the higher fields measurements up to 0.1 T, indicating the entrance into a proper 3D ferrimagnetic phase. The presence of a 3D ferrimagnetic phase is even supported by having a more pronounced feature around 224 K. This is surprising, as one would expect more pronounced features in the low-field measurements as observed in YbFe_2O_4 [35] and LuFe_2O_4 [11]. With increasing magnetic fields, $M(T)$ -curves below the transition temperature start to smear out into higher temperatures as expected for second order phase transitions to a ferrimagnetic phase. Moreover, at the lower side of the transition temperature, magnetization values increase with increasing applied field, indicating the growth of ferrimagnetic contributions. However, in analogy to LuFe_2O_4 [11] we expect a continuous increase in the magnetization for sufficiently high fields. The net moment at low temperature is extracted from the field-cooling curves consistent with a ferrimagnetic

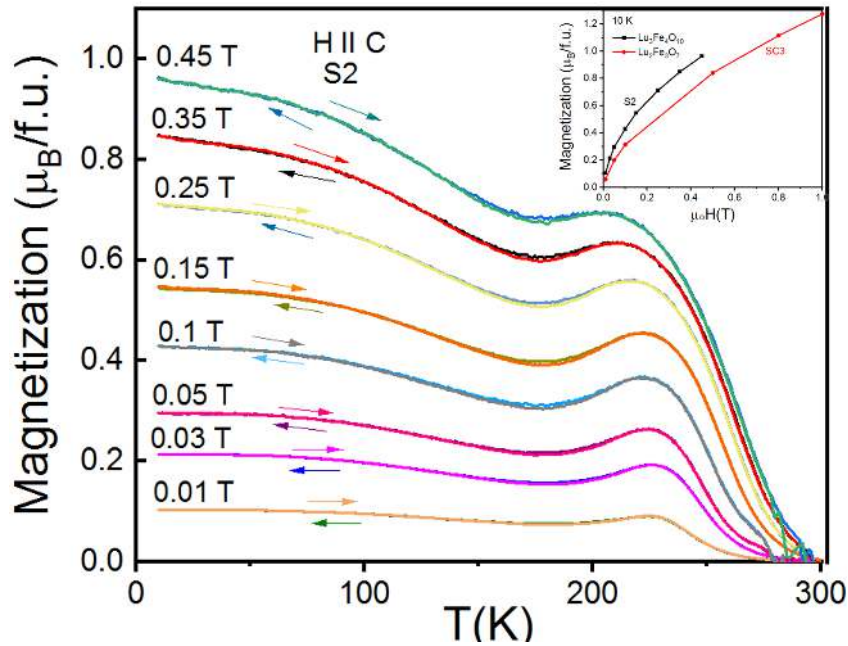


Figure 4.9: $M(T)$ in various $H||c$. FC and FW curves are both shown and indicated by arrow direction. Inset: Field dependent low-temperature magnetic moment for $\text{Lu}_3\text{Fe}_4\text{O}_{10}$ (black curve) and for $\text{Lu}_2\text{Fe}_3\text{O}_7$ (red curve).

order and it depends on the applied field (See inset of Fig. 4.9). The corresponding data for $\text{Lu}_2\text{Fe}_3\text{O}_7$ is also shown for comparison. The data are limited to below 0.5 T as no data is available for higher fields. Both compounds reveal a similar trend, however, the $\text{Lu}_3\text{Fe}_4\text{O}_{10}$ crystal exhibits a higher magnetization value for a corresponding field suggesting a better established spin order in the bilayer and/or in the single Fe^{3+} layers if ordered, or from the induced magnetic moment in the single layer if paramagnetic as $\text{Lu}_3\text{Fe}_4\text{O}_{10}$ contains one more single Fe^{3+} than present in $\text{Lu}_2\text{Fe}_3\text{O}_7$.

4.2.2.2 Isothermal magnetization of $\text{Lu}_3\text{Fe}_4\text{O}_{10}$

In contrast to $\text{Lu}_2\text{Fe}_3\text{O}_7$, but similar to LuFe_2O_4 [11], the isothermal magnetization $M(H)$ -loops measured below the transition temperature on $\text{Lu}_3\text{Fe}_4\text{O}_{10}$ (Fig. 4.10), reveal one feature that is indication for a first order metamagnetic transition between the low- H and high- H phase: The virgin curve obtained after the sample was cooled in zero field shown for 80 K in Fig. 4.10 is outside the loop. In the normal case meaning no meta-magnetic transition is present but only ferro-or ferrimagnetic phase, the virgin curves is inside the hysteresis loop as explained in the following: after cooling the sample without field the spins up and down are compensating each other resulting in no magnetic moment. Afterward, the virgin curve is measured with increasing the magnetic field ending up with all domains aligned up. Higher magnetization is expected for positive field compared to starting with all spin down leads the virgin curve to be inside the hysteresis [139] as observed previously in $\text{Lu}_2\text{Fe}_3\text{O}_7$ (see Sec. 4.1.2.2) but in contrary to $\text{Lu}_3\text{Fe}_4\text{O}_{10}$. First order metamagnetic transition means a hysteresis may exist in the phase

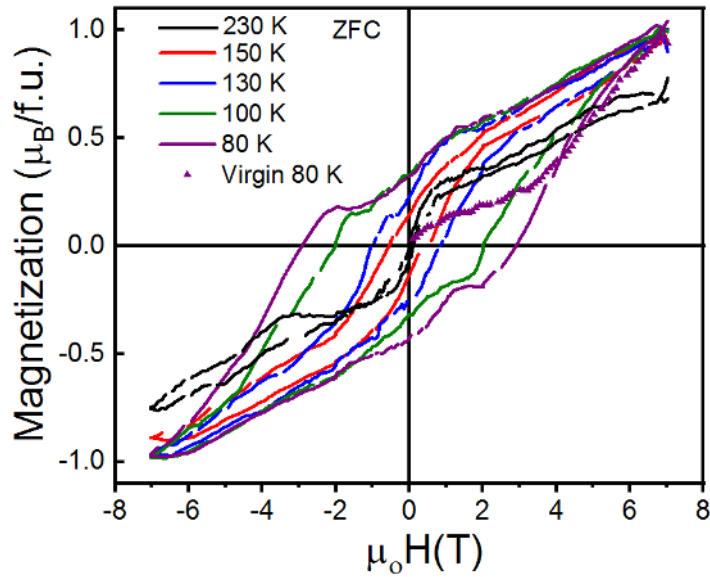


Figure 4.10: Smoothed magnetization M vs. field $\parallel c$ for temperatures lower than T_C . Smoothing was one using the adjacent-averaging method. Virgin curve measured after cooling in zero field at 80 K is also shown.

transition between the fM and AFM in which both can be stabilized in range of fields. Upon increasing H to values higher than the coercive field, a transition is triggered from AFM to fM. However, the process is reversible in our sample as at ~ 2 T in the 80 K loop, there is bump which is comparable to the one at 2 T in the virgin curve, meaning part of the sample is in the AFM phase. To maximize the AFM phase, the sample has to be heated above the transition temperature and afterwards cooled in zero-field. At 230 K, the magnetization reaches a $\sim 0.7 \mu_B/\text{f.u.}$ at maximum field of 7 T identical to LuFe_2O_4 [11] but in contrast to an observed value of $\sim 1.5 \mu_B/\text{f.u.}$ in $\text{Lu}_2\text{Fe}_3\text{O}_7$. With decreasing temperature to below the transition temperature, $M(H)$ -loops exhibit a typical shape for glassy phase as observed in $M(H)$ -loop at 60 K in LuFe_2O_4 [11] and the remanent magnetic moment increased upon decreasing the applied magnetic field meaning some parts of the sample are still in the ferrimagnetic phase exactly as observed in LuFe_2O_4 [11]. It is clear that all the measured $M(H)$ -loops are not closed, therefore, not saturated in fields up to 7 T not even the bilayer, whereas in $\text{Lu}_2\text{Fe}_3\text{O}_7$ as well in LuFe_2O_4 [11] 5 T was enough for at least bilayer saturation. Moreover, it is expected that significantly high field is needed to obtain a fully closed hysteresis loop as in $\text{Lu}_2\text{Fe}_3\text{O}_7$ (sec.4.1.2.2) and in LuFe_2O_4 [11]. It is difficult to discuss the $\text{Lu}_3\text{Fe}_4\text{O}_{10}$ bilayer vs Fe^{3+} single layers contribution as was previously done for $\text{Lu}_2\text{Fe}_3\text{O}_7$ in Sec .4.1.2.3 due to the scarcity of the available data. However, additional information can be obtained from the microscopic measurements, e.g. XMCD, which will be discussed later on in Sec. 4.4.2. Before heading to that, the polarized neutron measurements will be presented in the next section, which however was done only on $\text{Lu}_2\text{Fe}_3\text{O}_7$, but not $\text{Lu}_3\text{Fe}_4\text{O}_{10}$ as no crystals were obtained that are sufficiently large for neutron diffraction.

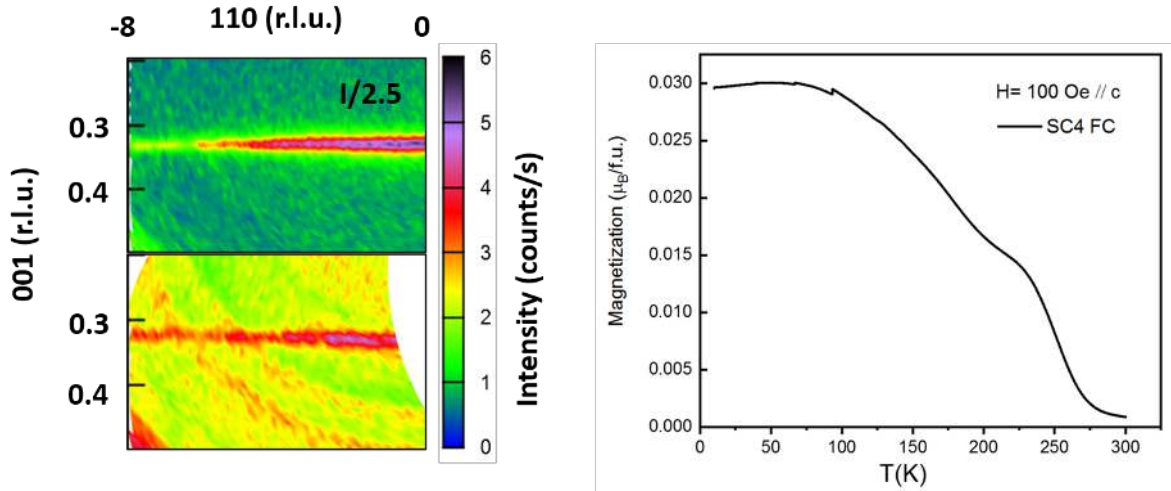


Figure 4.11: Left: Reciprocal space maps of the spin flip magnetic scattering measured with polarization parallel to \mathbf{Q} at ~ 4.2 K for two different crystals grown in (upper panel) $\text{CO}_2:\text{CO}=50$ (SC1) [counting time=24 s], (lower panel) $\text{CO}_2:\text{CO}=85$ (SC4) [counting time=55 s]. Right: FC curve of the SC4 measured in 100 Oe.

4.3 Diffuse magnetic scattering

The spin order in $\text{Lu}_2\text{Fe}_3\text{O}_7$ has been rarely studied by neutron scattering, with corresponding measurements having been done only on a non-stoichiometric single crystal by [74] and on non-stoichiometric polycrystalline material by [71]. In both studies diffuse magnetic rods along $(\frac{1}{3}\frac{1}{3}\ell)$ were observed from room temperature down to 7 K. The first polarized neutron scattering experiment was performed on $\text{Lu}_2\text{Fe}_3\text{O}_7$ single crystals on the DNS at the MLZ (for details on experimental setup and the polarization analysis, see Sec. 2.3.10 and Sec. 2.3.11). It was mainly carried out to explore the possible spin anisotropy as was done in non-intercalated rare earth ferrites [11, 57, 59] by using the polarization analysis.

The experiment was performed on two $\text{Lu}_2\text{Fe}_3\text{O}_7$ single crystals grown in different atmospheres: An off-stoichiometric single crystal (SC1) grown in $\text{CO}_2:\text{CO}=50$, exhibits frequency dependence in the AC susceptibility (see Fig. 3.7 for the macroscopic magnetic characterization) and a single crystal (SC4) grown in $\text{CO}_2:\text{CO}=85$, the gas ratio for which small crystals exhibiting long range CO were found from the same batch, the corresponding magnetization measurements are shown in the left panel of Fig. 4.11, which however looks similar in shape to the most stoichiometric crystal SC3 (c.f. Fig. 4.1).

To separate magnetic scattering from nuclear scattering, neutron polarization parallel to average \mathbf{Q} was used ($P \parallel x$). Only the component of the magnetization which is perpendicular to the scattering vector contributes to the scattering cross section. In this orientation, $\mathbf{M} \perp \mathbf{Q}$ is always perpendicular to the neutron polarization and thus all the magnetic scattering will involve a spin flip regardless of its orientation.

Figure 4.12 shows the mapped $h\ell$ plane of SC1 at 4.2 K for the different polarization directions. To separate magnetic scattering from nuclear scattering [100], a neutron polarization

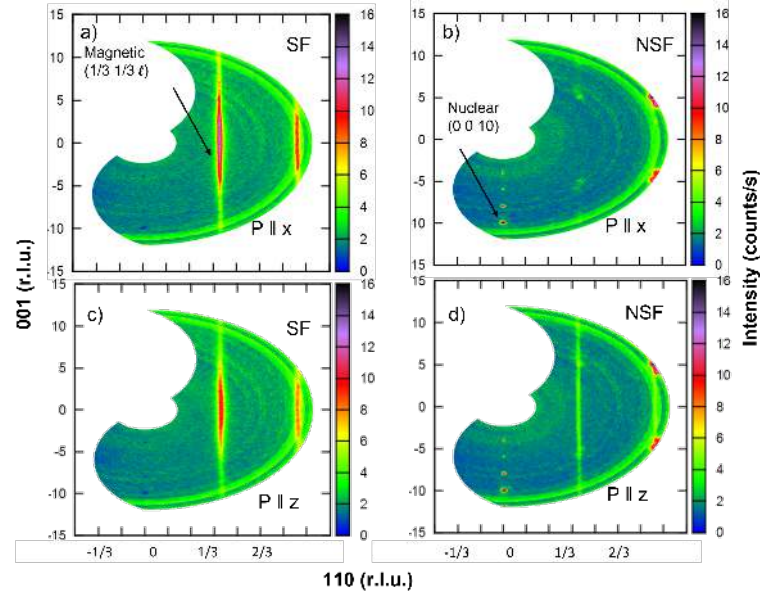


Figure 4.12: Reciprocal space map of $(hh\ell)$ -plane at 4.2 K in spin-flip (a,c) and non-spin-flip (b,d) with neutron polarization (a,b) parallel to \mathbf{Q} -direction and (c,d) perpendicular to scattering plane for five detector positions and counting time 24s each position (sample SC1). When the polarization of the neutrons is parallel to the scattering vector, both in-plane and out-of plane-components of the magnetic contribution are measured in the spin-flip (SF) channel and the full nuclear coherent contribution is measured in the non-spin-flip (NSF) channel i.e. structural reflections $(0\ 0\ \ell)$ with $\ell = 2n$.

parallel to the average \mathbf{Q} was used ($\mathbf{P} \parallel \mathbf{x}$), see panels a,b. In this orientation, all the magnetic scattering will involve a spin flip regardless of the moment orientation. The weak diffuse peak at $\sim (\frac{1}{3}\ \frac{1}{3} \pm 5.5)$ in the non-spin-flip channel for ($\mathbf{P} \parallel \mathbf{x}$) (Fig. 4.12b) must be of structural origin and may be due to medium range CO which appears more 3D than 2D (note that peaks at these positions were also observed in neutron diffraction of LuFe_2O_4 and attributed to CO [43]). The nature of peaks rather than the lines of diffuse scattering apparent in the spin-flip channel (Fig. 4.12a) suggests that there are significant correlations of CO between different bilayers.

Clearly, magnetic diffuse scattering is observed in the spin-flip scattering (Fig. 4.12a) that is relatively sharp in $hh0$ -direction but extended along ℓ , indicating that the spin correlations are mostly limited to the ab -plane with disorderly stacked bilayers. Since the distance of iron ions in different bilayers is much larger than the in-plane nearest neighbour distance (c.f. Fig. 1.8), in-plane correlations are much stronger than out-of-plane correlations. The appearance of only diffuse scattering suggests that the crystal is at least not stoichiometric enough to exhibit long-range order spin order, cluster glass like freezing.

To determine the orientation of the modulated spins, additional measurements with polarization perpendicular to the scattering plane ($\mathbf{P} \parallel \mathbf{z}$) were performed, see panels c,d. In this configuration, the spin-flip-channel is sensitive to the magnetic moment in the $(hh\ell)$ -scattering plane, while the moments perpendicular to the scattering plane give rise to magnetic scattering in the non-spin-flip channel. The additional intensity observed in the non-spin-flip channel for

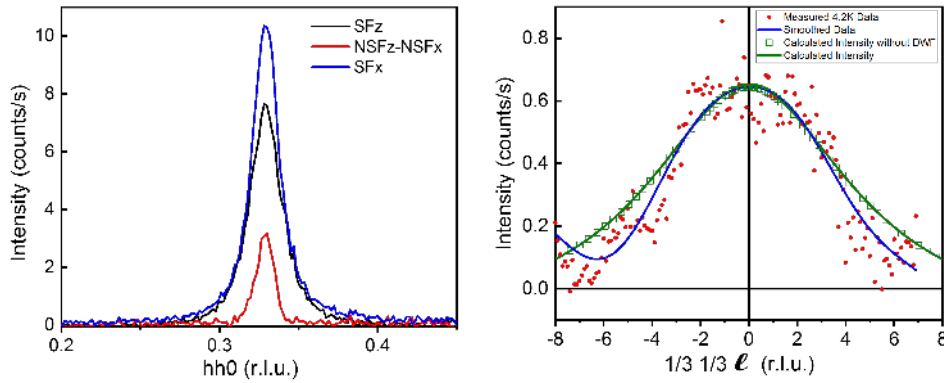


Figure 4.13: Left: The intensity of the diffuse scattering averaged along ℓ in the range $\ell = -5$ to $\ell = 5$ for $\text{SF} \parallel \mathbf{z}$, $\text{SF} \parallel \mathbf{x}$ and for the $\text{NSF} \parallel \mathbf{z}$ - $\text{NSF} \parallel \mathbf{x}$. Background is subtracted for SFz and SFx channel. Right: Diffuse magnetic scattering at the $(\frac{1}{3} \frac{1}{3} \ell)$ line (intensity averaged along $hh0$ from 0.25 to 0.4) in the spin flip channel for neutron polarization parallel to \mathbf{z} -direction at 4.2 K. The smoothed data (blue) and the intensity model for the random distribution of Fe^{2+} and Fe^{3+} (green line, squares: with, without Debye-Waller factor) are also shown. Background is subtracted for the measured data.

$\mathbf{P} \parallel \mathbf{z}$ (Fig. 4.12d) compared to $\mathbf{P} \parallel \mathbf{x}$ (Fig. 4.12b) indicates the presence of magnetic moments pointing out of the scattering plane, and thus perpendicular to the crystallographic c -axis of $\text{Lu}_2\text{Fe}_3\text{O}_7$.

To calculate the in-plane and out-of-plane modulated spin components for the Fe ions, the $\text{NSF} (\mathbf{P} \parallel \mathbf{x})$ was subtracted from $\text{NSF} (\mathbf{P} \parallel \mathbf{z})$. The subtraction is done to get rid off the nuclear scattering, which is present in both channels and to obtain the magnetic scattering from the modulated spin components perpendicular to the scattering plane i.e. in $\bar{1}10$ direction (this is only present in NSFz). Then, the intensity of the diffuse scattering was averaged along ℓ in the range $\ell = -5$ to $\ell = 5$ for NSFz after the subtraction and for the SFz channels and are shown in Fig. 4.13left. SFx is also shown, the SFx is supposed to be equal to $\text{SFz} + \text{NSFz}$ after subtraction. Finally, a numerical integration along the $hh0$ direction was performed on both SFz and NSFz channels resulting in intensity values of 0.0591 counts/s.r.l.u. for NSFz and 0.225 counts/s.r.l.u. for SFz . The ratio of the corresponding spin components (scaling with the square root of the intensities) of 001 ($\parallel c$) to $\bar{1}10$ directions is $0.47/0.24 \sim 2$. The macroscopic measurements in Fig. 4.2d indicated a similar SO in bilayer as in the non-intercalated compound, implying that both Fe^{2+} and Fe^{3+} spins in the bilayers point into the c -direction. The Fe^{2+} spins are aligned $\parallel c$ due to the crystal field and spin-orbit coupling and the bilayer Fe^{3+} spins are coaligned by the exchange interaction with the Fe^{2+} spins. The bilayer contains twice the spins that exist in the single layer and therefore the single layer contribution to the intensity would be expected to be half of the one in the bilayer, which coincides the obtained ratio of ~ 2 . Assuming the contribution to the moments is roughly proportional to the number of spins, this suggests that the single layer spins are modulated in-plane completely. With such an in-plane antiferromagnetic order, a not too large magnetic field applied out-of-plane is expected to

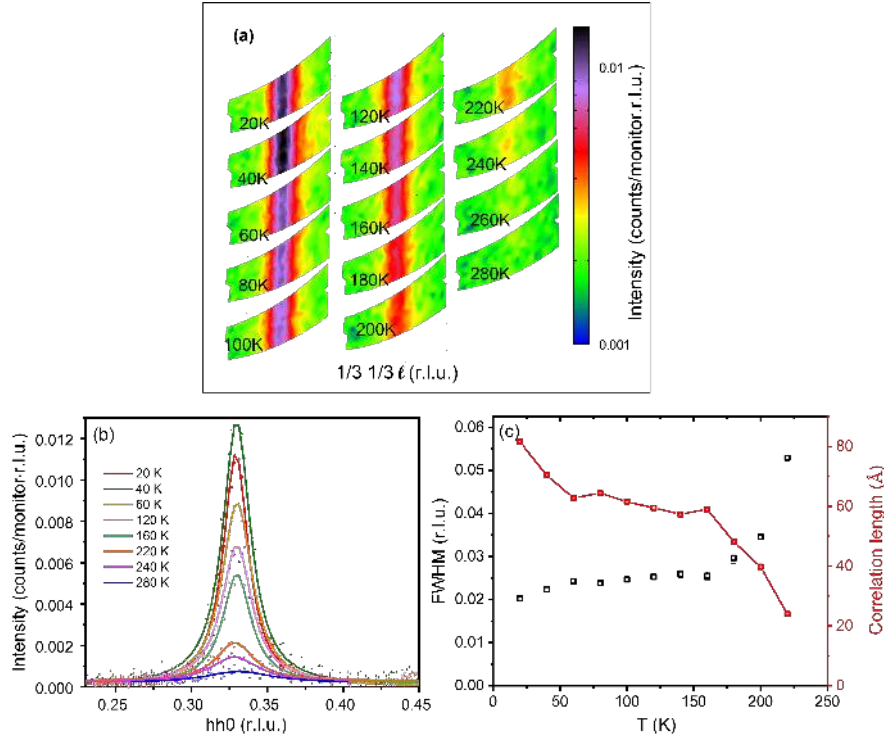


Figure 4.14: (a) Temperature dependence of part of the diffuse magnetic intensity (logarithmic scale) in the reciprocal $hh\ell$ plane in the spin-flip channel measured with $\mathbf{P} \parallel \mathbf{Q}_{\text{average}}$ at different temperatures. (b) Diffuse magnetic scattering averaged along the ℓ direction in the range $\ell = -5$ to $\ell = 5$ vs $hh0$ for selected temperatures from panel (a). The data were fitted with a Lorentzian (solid curves) and the background is subtracted for all curves. (c) Correlation length and Full Width Half Maxima extracted from the data fitting for various temperatures.

induce an out-of-plane net moment that is proportional to the field [140], consistent with our observations (Sec. 4.1.2.1). Furthermore, our deduced primarily in-plane orientation of the modulated single-layer spins is consistent with the conclusions from Mössbauer spectroscopy [46], in which single-layer spins pointing into a direction just 20° from the plane were found.

Fig. 4.13right shows the ℓ dependence of the intensity (averaged along $hh0$ from $h = 0.25$ to 0.4) of the diffuse magnetic scattering in the spin-flip channel ($\mathbf{P} \parallel \mathbf{z}$). The smoothed peak is extremely broad, demonstrating that the data is consistent with almost no spin correlations in c -direction. For comparison, the magnetic intensity is modeled for randomly distributed Fe^{2+} and Fe^{3+} spins with the Ising spins pointing along the c -axis according to

$$I_{\text{model}} = f_m^2 * P(\alpha)^2 * \text{DWF}^2, \quad (4.1)$$

where $P(\alpha) = \arccos(\alpha)$, α being the deviation angle of the scattering vector \mathbf{Q} from the magnetization \mathbf{M} , is the direction factor. The direction factor leads to a suppression of the measured intensity along ℓ , as does the magnetic form factor $f_m(\mathbf{Q})$. $\text{DWF} = \exp(-DW * \mathbf{Q}^2)$ is the Debye-Waller factor, with $DW = 0.006 \text{ \AA}^2$ according to the refinement of the crystal

structure at 100 K (no 4.2 K data are available) from X-ray diffraction. The modeled intensity was calculated twice: including and excluding the DWF and is shown in Fig. 4.13right. As can be seen, there is no significant influence of the DWF on the modeled intensity. The modeled intensity is slightly broader than the smoothed measured data, the reason behind this may be that the modeled intensity does not take into account any present correlation even within the bilayers besides instrumental resolution and mosaicity.

Upon warming, the intensity gradually decreases and the peak becomes wider in $hh0$ -direction as can be seen in Fig. 4.14a. The correlations are hardly observed in both $hh0$ and ℓ -directions around $T=240$ K. Fig. 4.14b shows the in-plane dependence of the intensity (averaged along ℓ from $\ell= -5$ to $\ell= 5$) of the diffuse magnetic scattering (spin-flip, $\mathbf{P} \parallel \mathbf{x}$) at different temperatures. These were fitted with a Lorentzian function and were corrected by subtracting the instrumental resolution (0.0066 r.l.u.) to obtain the Full Width Half Maxima that are shown in Fig. 4.14c. As can be seen, the intensity gradually decreases and the peak becomes wider in $hh0$ -direction. The correlations are even hardly observable around $T=240$ K. Furthermore, the FWHM is almost constant in the temperature range 60-168 K, and grows exponentially above $T= 168$ K. Interestingly, an anomaly around 60 K exists, anomalies around this temperature have been observed before in [72, 74] and were tentatively attributed to an ordering of Fe^{3+} spins in the single layers. The corresponding in-plane correlation lengths were obtained as $\xi= 2/\text{FWHM}$ and are shown in Fig. 4.14c. The estimated correlation length in $hh0$ -direction at 100 K is $\sim 18a$. This is larger than correlation length along ℓ . However, it is much smaller than the estimated correlation length for LuFe_2O_4 below T_N ($\sim 73a$ [11]), though slightly larger than the estimated correlation length above T_N ($\sim 13a$ at 260 K [11]).

4.4 X-ray magnetic circular dichroism

The X-ray magnetic circular dichroism (XMCD) measurements presented in this section were carried out at the High field chamber of the beamline UE46-PGM-1 at the BESSY synchrotron (see Sec. 2.5.1), to deduce the valence-resolved arrangement of spins. The first XMCD measurements in $\text{Lu}_2\text{Fe}_3\text{O}_7$ and $\text{Lu}_3\text{Fe}_4\text{O}_{10}$ in the same way previously done on LuFe_2O_4 [11, 36]. XMCD is defined as the difference of the absorption spectrum for left and right circularly polarized X-ray in the application of magnetic field (see theoretical background in Sec. 2.5). The X-ray absorption spectra were, therefore, measured as a function of the photon energy with left μ_+ and right μ_- circularly polarized X-rays at the Fe L_3 and L_2 edges in total electron yield (TEY) and treated with linear background subtraction (see Sec. 2.5.1 for details of the experiment and analysis of the raw data). The measurements were performed on stoichiometric $\text{Lu}_2\text{Fe}_3\text{O}_7$, off-stoichiometric $\text{Lu}_2\text{Fe}_3\text{O}_7$ and off-stoichiometric $\text{Lu}_3\text{Fe}_4\text{O}_{10}$ crystals in a magnetic field and incoming beam both parallel to the c -axis at the same temperature the LuFe_2O_4 measurements were performed for a comparison i.e. 120 K. This temperature was chosen for LuFe_2O_4 because it is the lowest temperature at which the sample was conductive enough for TEY, and at the same time avoiding the charging effect in the insulating phase [33].

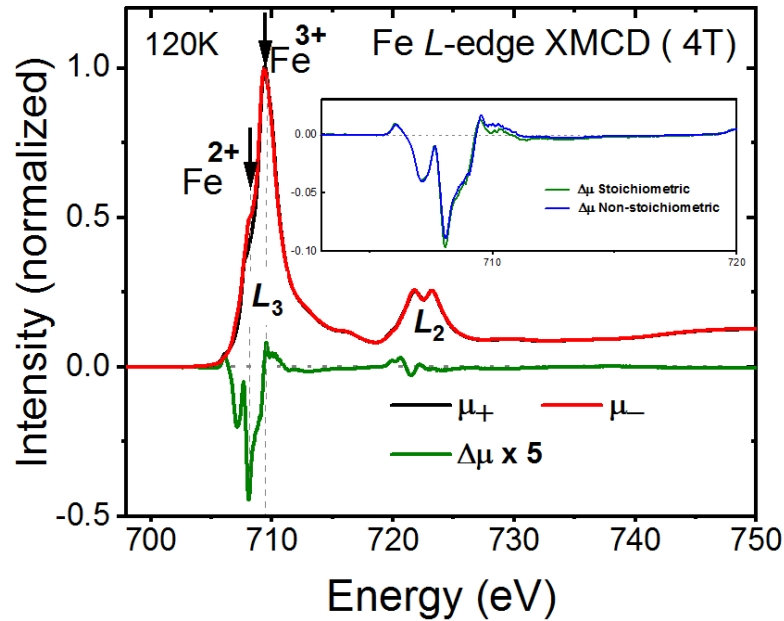


Figure 4.15: Normalized XAS spectra for left and right circularly polarized X-ray at the Fe L₂/L₃-edges and the XMCD signal of stoichiometric Lu₂Fe₃O₇ crystal (SC3) at 4 T. The XMCD signal $\Delta\mu$ is scaled by a factor of five for better visibility. Inset: XMCD signals for both stoichiometric (SC3) and non-stoichiometric Lu₂Fe₃O₇ (SC5) crystals.

4.4.1 X-ray magnetic circular dichroism on Lu₂Fe₃O₇

The main focus in this part is on the XMCD measurements performed on the stoichiometric single crystal Lu₂Fe₃O₇ (SC3), which exhibits a long-range charge order with magnetic characterization previously shown in Fig. 3.6 on p. 45. Additional measurements were performed on an off-stoichiometric crystal Lu₂Fe₃O₇ (SC5) as the crystal has larger size are presented as well. SC5 has an identical magnetic behaviour to crystal SC1 show in Fig. 3.6 on p. 45.

Figure 4.15 shows the normalized X-ray absorption spectra of SC3 at the Fe L₂/L₃-edges and the resulted XMCD. The inset shows the XMCD signals for both SC3 and SC4. SC4 was measured under the same conditions as for the stoichiometric crystal. Only small differences in the XMCD between the stoichiometric and the non-stoichiometric crystals can be seen. The differences may be due to the significant sample size difference (see left panel of Fig. 4.16), since in LuFe₂O₄ no variation in the XMCD was observed for different samples stoichiometry [21].

In Fig. 4.15, two peaks can be discerned in the XMCD at the L₃ edge refers to the Fe²⁺ and Fe³⁺, these peaks are determined and justified using the XMCD signal of LuFe₂O₄ (shown later in Fig. 4.17) and YbFe₂O₄ (discussed previously in Sec. 1.2.2), furthermore, using the XAS spectrum discussed below: a large downward peak at ~ 708 eV and a smaller upward peak at ~ 709.5 eV respectively are visible. A downward (upward) peak in the XMCD at the L₃ edge corresponds to a net magnetic moment pointing in (opposite to) the field direction. Thus, one can conclude that the net magnetic moment of the Fe²⁺ ions is in the field direction

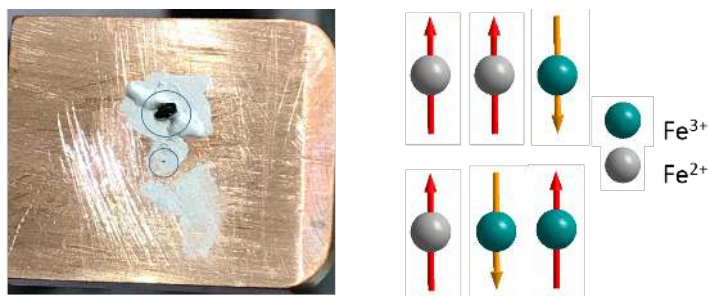


Figure 4.16: Left: Non-stoichiometric (upper) and stoichiometric (lower) $\text{Lu}_2\text{Fe}_3\text{O}_7$ crystals mounted using silver base on brass holder. Crystals are surrounded by circles, the very small stoichiometric crystal hardly can be seen. Right: possible spin model in the bilayer containing six resolved valences of Fe sites. Direction of spins are indicated by direction of arrows.

and the net magnetic moment of the Fe^{3+} ions opposite to the field direction. Moreover, the downward Fe^{2+} peak is much larger than the positive Fe^{3+} peak. Given that Fe^{2+} has a spin value of 2 while Fe^{3+} has a larger value of $5/2$ this implies that not all the Fe^{3+} spins point opposite to the field. In the XAS, the Fe^{2+} peak (more like a shoulder) has less height than the Fe^{3+} peak, similar to what was observed in LuFe_2O_4 (see upper panel of Fig. 4.17), which was explained as due to surface oxidation because TEY is surface sensitive [11, 36]. For in-situ cleaved crystals of LuFe_2O_4 , a $\text{Fe}^{2+}:\text{Fe}^{3+}$ ratio close to 1 : 1 was observed [44] (the crystals measured in this thesis and in [11] were not cleaved), the Fe^{2+} contribution is further reduced in $\text{Lu}_2\text{Fe}_3\text{O}_7$, because per formula unit, one Fe^{2+} ion of three Fe ions contribute to the XAS in $\text{Lu}_2\text{Fe}_3\text{O}_7$ whereas one Fe^{2+} ion of two Fe ions contribute for the XAS in LuFe_2O_4 .

The normalized X-ray absorption spectra (XAS) for the stoichiometric $\text{Lu}_2\text{Fe}_3\text{O}_7$ and LuFe_2O_4 are shown in the upper panel of Fig. 4.17. The corresponding XMCD signals are shown in the lower panel of Fig. 4.17. As discussed before, the two XAS curves look different, which is due to the existence of the additional Fe^{3+} single layer in $\text{Lu}_2\text{Fe}_3\text{O}_7$. However, both compounds exhibit a similar XMCD spectra shape. In the lower panel of Fig. 4.17, the XMCD signal of LuFe_2O_4 scaled through division by factor of 1.75 for comparison with $\text{Lu}_2\text{Fe}_3\text{O}_7$. This factor is chosen such that the negative Fe^{2+} of both compounds is the same. Both the XMCD and XAS signals are normalized with respect to the maximum of the XAS peak. The XAS maximum is proportional to the amount of Fe/f.u., hence, for $\text{Fe}^{3+}/\text{f.u.}$ but also for $\text{Fe}^{2+}/\text{f.u.}$. Neglecting the surface oxidation effect, per formula unit, LuFe_2O_4 contains 2 Fe ions (one Fe^{2+} and one Fe^{3+}), whereas, $\text{Lu}_2\text{Fe}_3\text{O}_7$ contains 3 Fe ions (one Fe^{2+} and two Fe^{3+}). Therefore, the XMCD is normalized with respect to the amount of Fe ions leading to a scaling factor of 1.5 ($\frac{1}{3}/\frac{1}{2}$) and with respect to Fe^{3+} ions leading to scaling factor of 2 ($\frac{1}{2}/1$). However, a scaling factor of 1.75 might indicate that not all Fe^{2+} ions contributes to the XAS maximum.

As discussed above, in $\text{Lu}_2\text{Fe}_3\text{O}_7$ the Fe^{3+} net moment is smaller than the Fe^{2+} net moment and is pointing in opposite direction (negative H-direction). We now consider the 1/3-type spin order similar to LuFe_2O_4 , which basically implies that three independent Fe^{2+} spins are present. This spin model has been discussed in Sec. 1.2.2, an example of the possible spin model in the bilayer is also shown in the right side of Fig. 4.16 [35]), as can be seen: all the Fe^{2+}

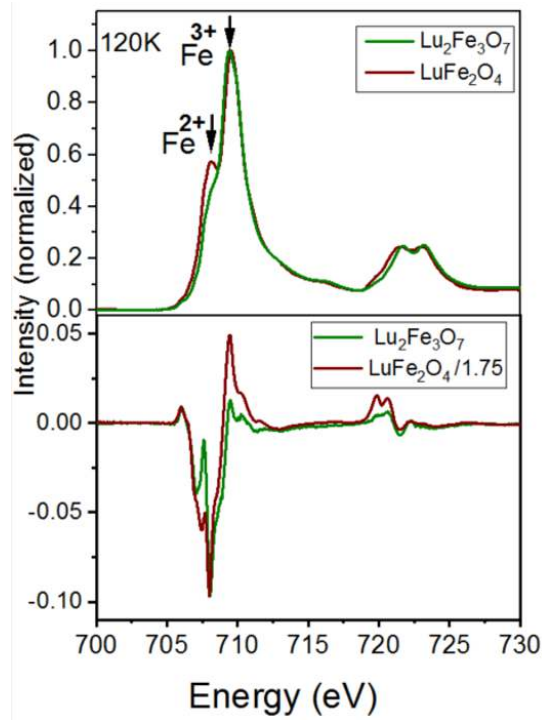


Figure 4.17: Upper panel: XAS spectrum of stoichiometric $\text{Lu}_2\text{Fe}_3\text{O}_7$ and LuFe_2O_4 crystals in the application of 4 T. XAS = $(\mu_- + \mu_+)/2$ and normalized to the peak maximum. Lower panel: the corresponding XMCD signals. LuFe_2O_4 XMCD signal was taken from [11] and scaled through division by 1.75.

and $\frac{1}{3}$ of the Fe^{3+} spins are aligned in the field direction and the $\frac{2}{3}$ of the Fe^{3+} spins are aligned opposite to the field direction. One can conclude that all Fe^{2+} are pointing in one direction since a scaling factor of 1.75 (close to 1.5) was used and leads to a comparable Fe^{2+} peak taking into account the XAS-normalization. In contrast, the Fe^{3+} net moment is clearly much smaller in $\text{Lu}_2\text{Fe}_3\text{O}_7$ compare to LuFe_2O_4 . In $\text{Lu}_2\text{Fe}_3\text{O}_7$, the Fe^{3+} negative net moment arise from two contributions: 1) the net moment from Fe^{3+} in the bilayer and 2) the net moment from Fe^{3+} in the single layer. Thus, the much smaller negative Fe^{3+} net moment might be due to a smaller negative bilayer- Fe^{3+} net moment or due to a positive net moment in the single layer or as a result of a combination of both the single and the bilayers. The most likely scenario is that bilayer arrangement is identical to LuFe_2O_4 [11, 36], and the smaller Fe^{3+} positive peak in XMCD is due to the single layer spins (partially) polarized in H-direction.

Using the fact that a similar spin order is expected to be realized in the bilayer, one can extract the magnetic moment in the single layer and the bilayer in a link between the macroscopic measurements and the XMCD as follows: From $M(T)$ measurements performed in [11] on LuFe_2O_4 , the magnetic moment at 120 K is reduced by $\sim 20\%$ from the low-T moment at 10 K. Meaning that Fe^{2+} and Fe^{3+} moments contributions are reduced by 20% as well, leading to $3.76 \mu_B/\text{Fe}^{2+}$ (including the orbital moment) and $-4/3 \mu_B/\text{Fe}^{3+}$. For $\text{Lu}_2\text{Fe}_3\text{O}_7$, the XMCD signal of is reduced by further 15% (Fig. 4.17) due to the less ordering in the bilayer, results in $\sim 3.2 \mu_B$ for Fe^{2+} and $\sim -1.13 \mu_B$ for Fe^{3+} in the bilayer and yielding a net $2.07 \mu_B/\text{f.u.}$ in the

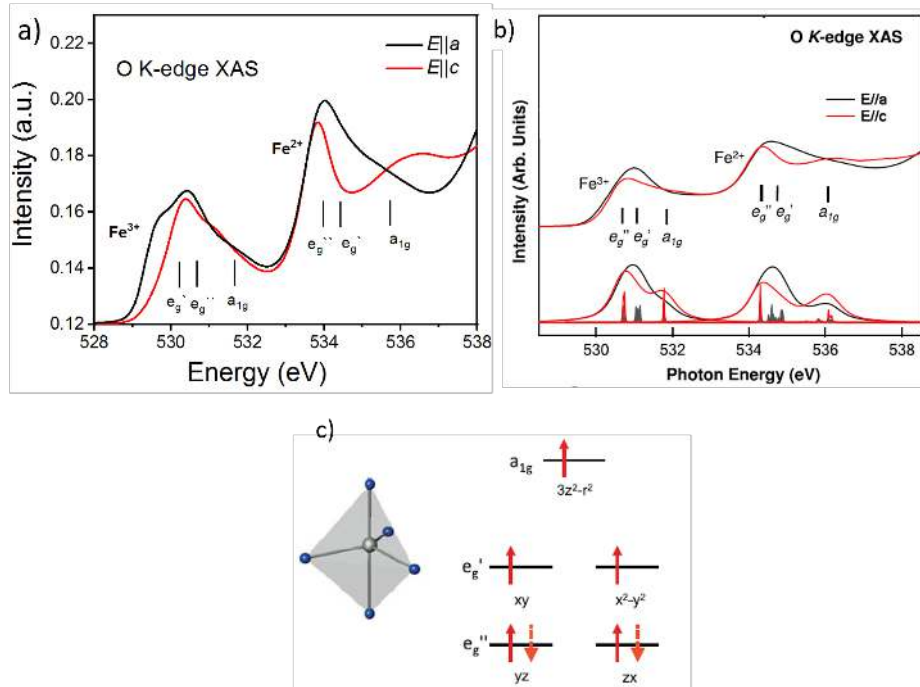


Figure 4.18: Linear X-ray absorption spectra at the O k-edge for different polarization directions at 120 K a) of $\text{Lu}_2\text{Fe}_3\text{O}_7$ b) of LuFe_2O_4 taken from [33]. Energy levels are labeled. c) (Left) Sketch of the trigonal-bipyramidal crystal field, (Right) the corresponding energy-splitting of the Fe 3d orbitals. For Fe^{3+} , each orbital is singly occupied, the extra-electron of Fe^{2+} can go to either of two e_g'' orbitals, taken from [21].

bilayer. Comparing with the magnetic moment extracted from $M(T)$ performed on $\text{Lu}_2\text{Fe}_3\text{O}_7$ (Fig. 4.2) of $2.345 \mu_B/\text{f.u.}$, results in a spin magnetic moment of $0.28 \mu_B/\text{f.u.}$ in the single layer. The orbital magnetic moment of Fe^{2+} ions will also be reduced in the same manner from $0.7 \mu_B/\text{f.u.}$ to $0.46 \mu_B/\text{f.u.}$ However, all the extracted values are only suggestive as the samples were not cleaved, and an oxidation of Fe^{2+} can occur, thus, the ratio of $\text{Fe}^{3+} : \text{Fe}^{2+}$ is not confirmed. Moreover, the measurements were performed in TEY mode which is a surface sensitive, and the used XMCD was normalized with respect to the XAS.

Fig. 4.18a shows the linear polarized X-ray absorption spectra (LXAS) measured on SC3 at 120 K at the O K-edge for polarization parallel to the ab-plane ($\mathbf{E} \parallel \mathbf{ab}$) and polarization parallel to c-direction ($\mathbf{E} \parallel \mathbf{c}$). This measurement was done to study the effect of the presence of Fe^{3+} single layer on the local iron environment and to determine the possible orbital moment values. In the FeO_5 trigonal bipyramidal crystal-field, the 3d Fe level split into two doublets, e_g'' , e_g' and a singlet a_{1g} , see Fig. 4.18c. A Fe^{3+} ion has five electrons which are single occupy the five orbitals, meaning no orbital degree of freedom. The Fe^{2+} ion has six electrons, with the extra electron goes to an orbital of the doubly-degenerate allowing an orbital magnetic moment of Fe^{2+} of up to $1\mu_B/\text{f.u.}$ [21]. In LuFe_2O_4 , the e_g'' level was found to be the lowest energy level according to polarized X-ray absorption spectroscopy at the O K-edge [33]. $\mathbf{E} \parallel$

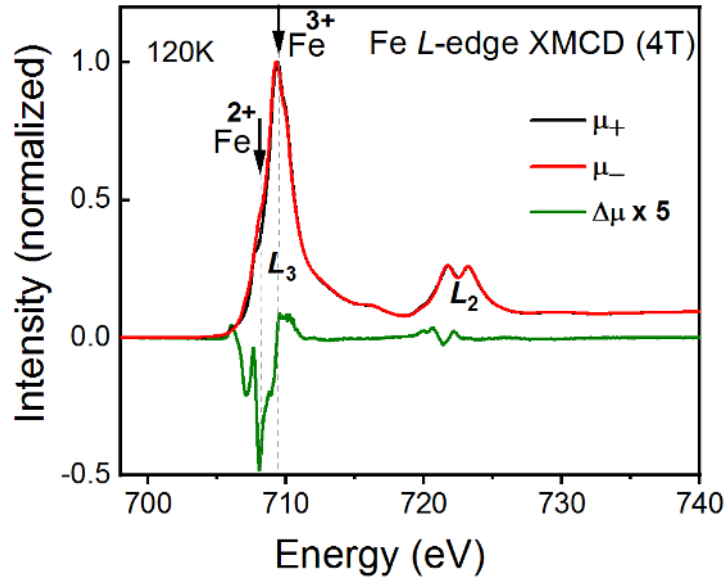


Figure 4.19: XAS spectra for left and right circularly polarized X-ray at the Fe L2/L3-edges and the XMCD signal of $\text{Lu}_3\text{Fe}_4\text{O}_{10}$ crystal at 4 T.

ab is sensitive to the orbital state in the e'_g while $\mathbf{E} \parallel \mathbf{c}$ for the orbital state in a_{1g} . For Fe^{3+} position in $\text{Lu}_2\text{Fe}_3\text{O}_7$, the spectra at Fe^{3+} position has a different structure than observed for LuFe_2O_4 in Fig. 4.18b, in which $\mathbf{E} \parallel \mathbf{ab}$ exhibit the maxima at higher energy than for $\mathbf{E} \parallel \mathbf{c}$ suggesting that the energy levels (e''_g and e'_g) are inverted, very likely in the single layer. For Fe^{2+} , the spectra looks exactly the same, which implies that there is no change in the energy levels, therefore, an orbital moment up to $1\mu_B/\text{f.u.}$ is possible similar to LuFe_2O_4 . These are indications that the local surrounding and the thus likely the super-exchange interactions are very similar in the bilayer to LuFe_2O_4 (as expected from the refined crystal structure, c.f. Sec. 5.2.3).

4.4.2 X-ray magnetic circular dichroism on $\text{Lu}_3\text{Fe}_4\text{O}_{10}$

The focus in this part is on the XMCD measurements performed on the off-stoichiometric single crystal $\text{Lu}_3\text{Fe}_4\text{O}_{10}$ (S1), has dimensions of $(0.13 \times 0.2 \times 0.09) \text{ mm}^3$ with magnetic characterization previously shown in Fig. 3.8 on p. 47. The more stoichiometric crystal (S2) was not measured because it was not yet found when the beam-time took place. The X-ray absorption spectra for both left μ_+ and right μ_- polarized light and the XMCD signal in 4 T are presented in Fig. 4.19. The XMCD signal $\Delta\mu$ is normalized to the XAS and scaled by a factor of five for better visibility. XMCD exhibits similar features to those observed in $\text{Lu}_2\text{Fe}_3\text{O}_7$ and LuFe_2O_4 . Moreover, a reduced Fe^{2+} peak is observed in the XAS similar to $\text{Lu}_2\text{Fe}_3\text{O}_7$ as an effect of surface oxidization, but also the presence of two additional Fe^{3+} single layers. A XMCD comparison of $\text{Lu}_3\text{Fe}_4\text{O}_{10}$ with LuFe_2O_4 and $\text{Lu}_2\text{Fe}_3\text{O}_7$ is shown in Fig. 4.20. LuFe_2O_4 scaled through division by a factor of 1.75 for comparison with $\text{Lu}_3\text{Fe}_4\text{O}_{10}$. Both the XAS and XMCD signal are normalized to the maximum of the XAS peak. Neglecting the surface oxidization

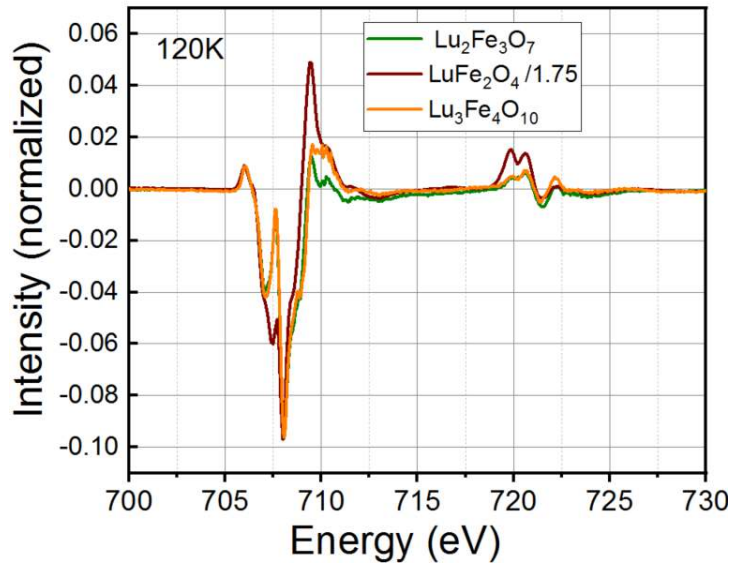


Figure 4.20: XMCD signal of stoichiometric $\text{Lu}_2\text{Fe}_3\text{O}_7$, LuFe_2O_4 and $\text{Lu}_3\text{Fe}_4\text{O}_{10}$ crystals in the application of 4 T. LuFe_2O_4 XMCD signal was taken from [11] and scaled through division by 1.75.

effect, a scaling factor between 2-3 is expected since per formula unit, $\text{Lu}_3\text{Fe}_4\text{O}_{10}$ contains four Fe ions: one Fe^{2+} and 3 Fe^{3+} (1 in bilayer, 2 in two single layers). In the same manner, to compare with $\text{Lu}_2\text{Fe}_3\text{O}_7$, a scaling factor between (1.3-1.5) is expected. However, no scaling was needed which suggests a better spin order in the bilayers of $\text{Lu}_3\text{Fe}_4\text{O}_{10}$ than in $\text{Lu}_2\text{Fe}_3\text{O}_7$.

As can be seen in the figure, the most clear difference is that $\text{Lu}_3\text{Fe}_4\text{O}_{10}$ exhibits a larger Fe^{3+} peak than $\text{Lu}_2\text{Fe}_3\text{O}_7$. This is unexpected, since $\text{Lu}_3\text{Fe}_4\text{O}_{10}$ contains more single Fe^{3+} layers which should lead to a more positive contribution and hence a reduction in the Fe^{3+} peak height in the XMCD. However, the growth of Fe^{3+} peak (negative net moment) may be due to a better order of Fe^{3+} in the bilayer and therefore, in the whole bilayer. This is consistent with lacking the scaling for $\text{Lu}_3\text{Fe}_4\text{O}_{10}$. The obtained results are tentative, since only a small off-stoichiometric crystal was measured, and more measurements are needed for further final conclusion. However, the shape of the XMCD signal is generally similar to LuFe_2O_4 , so likely same bilayer spin order is also present in $\text{Lu}_3\text{Fe}_4\text{O}_{10}$.

4.5 Discussion and conclusion

Generally, the studied $\text{Lu}_2\text{Fe}_3\text{O}_7$ crystals exhibit a magnetic behaviour that is similar to LuFe_2O_4 . Many common features are observed: 1) the Ising spin behaviour along the c -direction observed in the macroscopic magnetization measurements [43, 53]. 2) the temperature range where magnetic ordering or freezing occurs (~ 200 -250 K) [43, 53]. 3) the $\frac{1}{3}\frac{1}{3}$ in-plane propagation observed in diffuse magnetic scattering or Bragg peaks [45, 53]. 4) the presence of the thermoremanent (TRM) with the unusually high TRM starting to drop to lower values only upon warming above ~ 50 K, which may be accounted for by kinetic arrest [11]. 5) the deviations from paramagnetic linear behaviour in $M(H)$ above T_C [53]. 6) the shape of the

XMCD signal with large downward peak at the Fe^{2+} position and a smaller upward peak at the Fe^{3+} position, accounted for by all Fe^{2+} moments pointing in the field direction while two out of three bilayer Fe^{3+} moments point into the opposite direction [33, 36, 44].

However, the measured $\text{Lu}_2\text{Fe}_3\text{O}_7$ crystals appear not to be as well-ordered as the best crystals of LuFe_2O_4 . No sharp features in $M(T)$ curves are observed. Furthermore, only diffuse magnetic scattering was observed in the polarized neutron scattering study (although this study was not performed on the best crystal due to its small size). Furthermore, the SO appears to be more fragile than the CO in $\text{Lu}_2\text{Fe}_3\text{O}_7$ with respect to oxygen off-stoichiometry, as the most stoichiometric available sample exhibits 3D CO in single crystal X-ray diffraction which in $M(T)$ curves (Fig. 4.1) there are no sharp features characteristic of magnetic ordering in these materials [21, 35, 36]. In contrast to LuFe_2O_4 , where competing antiferromagnetic and ferrimagnetic phases are present that differ only in the stacking of the bilayer net magnetizations [53], $M(H)$ data (Fig. 4.4) suggests a preference for the ferrimagnetic phase to be stabilized in $\text{Lu}_2\text{Fe}_3\text{O}_7$ as a result of the modified magnetic interactions between neighboring bilayers. The feature observed in the ZFC curves below 60 K (Fig.S1 in supplemental material) in which an increase of the magnetization is observed is in disparity to LuFe_2O_4 . This feature could be due to the ordering of the iron moments in the single layer below 60 K as suggested based on Mössbauer spectroscopy studies [71, 73]. Such an ordering would be consistent with the increase of the $hh0$ -correlation length deduced from the polarized neutron scattering (Fig. 4.14c).

Because of the similar arrangement of atoms and correspondingly similar superexchange interactions in the bilayers of intercalated and non-intercalated compounds, the same spin order in each individual bilayer would be expected. This is indeed what our results from various experimental techniques indicate: 1) a net magnetic moment comparable to the saturation moment of LuFe_2O_4 is observed in the analysis of different macroscopic measurements $M(T)$, $M(H)$ and TRM. 2) the $\frac{1}{3}\frac{1}{3}$ in-plane propagation found in the polarized neutron study is consistent with the spin order determined in LuFe_2O_4 [36] and YbFe_2O_4 [35]. 3) the decomposition of the XMCD signal indicates the same larger Fe^{2+} net moment in field direction and smaller bilayer Fe^{3+} net moment opposite to the field as found in LuFe_2O_4 [33, 36, 44] and YbFe_2O_4 [35].

The principal difference of the magnetism between the intercalated and the non-intercalated compound is that in the former there is an additional contribution from the single layers. While the spins in the bilayers seem to behave as in LuFe_2O_4 , the spins in the single Fe-O layer have no analogue in LuFe_2O_4 . Our macroscopic magnetization and XMCD results indicate a net moment of these spins that is induced by a magnetic field, paramagnetic-like in first approximation even at low temperature. Our polarized neutron scattering results suggest that at 4.2 K, they are modulated with the same in-plane propagation as the bilayer spins, but with the modulated moment in-plane rather than out-of-plane. This is consistent with an out-of-plane net moment being easily induced by an out-of-plane magnetic field as well as with the results of Mössbauer spectroscopy studies [71, 73].

For $\text{Lu}_3\text{Fe}_4\text{O}_{10}$, although less data are available, macroscopic magnetization measurements $M(T)$ curves and $M(H)$ -loops are similar to in LuFe_2O_4 suggesting a first order meta-magnetic

phase transition between a high-field ferrimagnetic and a low-field AFM phase. In disparity, no additional low-T phase transitions have been observed. It is likely that this variation is related to the possible variations in oxygen content. Regarding the spin order in the bilayer, this is likely also similar to LuFe_2O_4 which mainly concluded from the XMCD signal, which however exhibits a better order than in $\text{Lu}_2\text{Fe}_3\text{O}_7$.

Returning to the iron ions in the bilayer of $\text{Lu}_2\text{Fe}_3\text{O}_7$, we note that the similar arrangement of atoms within the bilayers in intercalated and non-intercalated compounds should also lead to similar Coulomb-interactions driving charge ordering [21, 141, 142] and we would therefore expect not only the same spin but also the same charge order within each individual bilayer. The same CO is indeed suggested by the similar shape of the XMCD indicating the same spin-charge coupling within the bilayers [21, 35, 36]. Confirmation of this could be achieved by a successful solution and refinement of the charge-ordered crystal structure of $\text{Lu}_2\text{Fe}_3\text{O}_7$ which will be discussed in the next chapter.

5

Charge order studies and crystallographic refinement of $\text{Lu}_2\text{Fe}_3\text{O}_7$ and $\text{Lu}_3\text{Fe}_4\text{O}_{10}$

Does the intercalation render LuFe_2O_4 ferroelectric? Single crystals of both $\text{Lu}_2\text{Fe}_3\text{O}_7$ and $\text{Lu}_3\text{Fe}_4\text{O}_{10}$ sufficiently stoichiometric to exhibit superstructure reflections in X-ray diffraction attributable to charge ordering were successfully fabricated through the controlled growth via optical floating zone method as described in Sec. 2.1.2. The availability of these crystals opens the door to the refinement of CO crystal structure, which is the main focus of the thesis in whole and of this chapter in part.

The first part deals with $\text{Lu}_2\text{Fe}_3\text{O}_7$: a brief re-visit for the already introduced types of the CO realized in $\text{Lu}_2\text{Fe}_3\text{O}_7$ is followed by a discussion of the implications for the possible charge order configurations based on the symmetry analysis. Importantly, the refinement of the commensurately charge-ordered $\text{Lu}_2\text{Fe}_3\text{O}_7$ crystal structure in different examined symmetries for the both the average structure and the superstructure is presented afterward. The remaining part provides a limited overview for $\text{Lu}_3\text{Fe}_4\text{O}_{10}$: briefly the CO types, the analysis in term of symmetry, and the refinement for the average crystal structure at room temperature are shown and discussed. The chapter is finalized by a discussion of the causes and the obtained consequences "the realized CO and the possibility of the ferroelectricity scenario?".

5.1 Commensurate and incommensurate charge ordering in $\text{Lu}_2\text{Fe}_3\text{O}_7$

The observation of superstructure spots had been reported only from electron diffraction on small grains of polycrystalline $\text{Lu}_2\text{Fe}_3\text{O}_7$ [64, 75] (see also Sec. 1.3). These spots form an incommensurate zig-zag pattern around the $(\frac{1}{3}, \frac{1}{3}, \ell)$ line, consistent with a similar CO as in LuFe_2O_4 . This is similar to type 2 classified CO found at room temperature as introduced previously in Sec. 3.5.1.

In this type only one set of superstructure reflections exists near $(\frac{1}{3}, \frac{1}{3}, n)$, with n an integer rather than $(\frac{1}{3}, \frac{1}{3}, \frac{n}{2})$ observed in LuFe_2O_4 [29, 31], see Fig. 5.1a. However, as the $\text{Lu}_2\text{Fe}_3\text{O}_7$ unit cell contains two Fe-bilayers (see Fig. 1.8), an alternating CO as proposed for LuFe_2O_4 and YbFe_2O_4 [35] would not lead to a cell doubling, and instead of $(\frac{1}{3}, \frac{1}{3}, \frac{n}{2}), (\frac{1}{3}, \frac{1}{3}, n)$ reflections

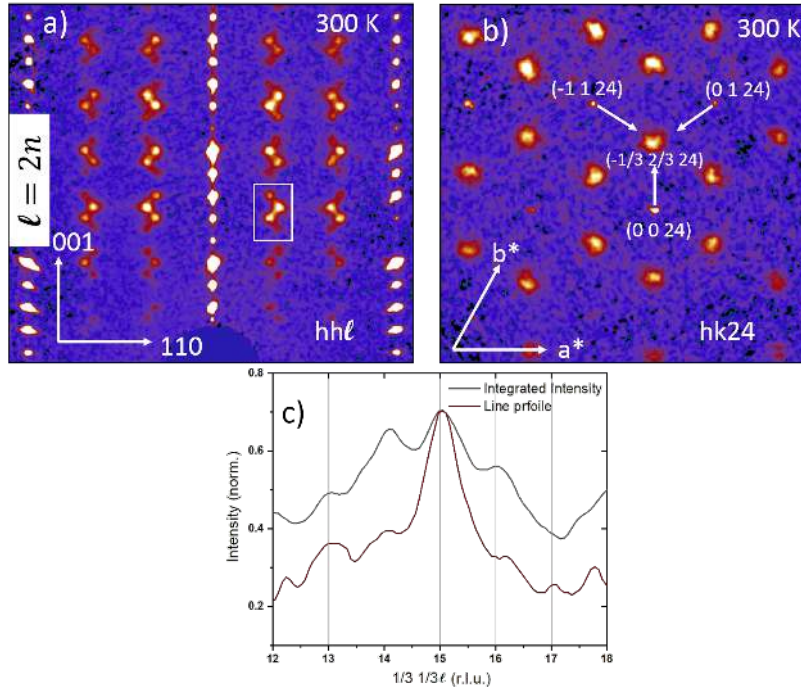


Figure 5.1: Precession images of the (a) hhl and (b) $hk24$ reciprocal space plane with (c) is the integrated intensity (gray line) in a small region perpendicular to the (hhl) for (a) of SC2 $\text{Lu}_2\text{Fe}_3\text{O}_7$ grown with a $\text{CO}_2/\text{CO}=85$ measured using supernova at RT. line profile through the center of one of the peaks highlighted by a white square (red line). (c) is from own work [64]

would be observed. Furthermore, an additional set of superstructure reflections near $(0,0, \frac{3n}{2})$ observed in LuFe_2O_4 [31] would be invisible as they would instead be located at $(0,0,0)$, which is the structural peaks position. Therefore, $(\frac{1}{3}, \frac{1}{3}, 0)$ -propagation suggesting a $\sqrt{3} \times \sqrt{3} \times 1$ CO cell rather than $\sqrt{3} \times \sqrt{3} \times 2$ in LuFe_2O_4 [36]. In fact, $(\frac{1}{3}, \frac{1}{3}, 0)$ propagation was introduced by [31] to index the 2D CO above T_{CO} in LuFe_2O_4 .

The intensity integrated in hh -direction around $hh = 1/3$ vs l is shown in Fig. 5.1c, also shown is a line profile through the center of one of the peaks (red line). The superstructure reflections in $\text{Lu}_2\text{Fe}_3\text{O}_7$ can be indexed with incommensurate propagation vector $(\frac{1}{3} - \delta, \frac{1}{3} - \delta, 0)$, and the symmetry-equivalent ones $(\frac{2}{3} + 2\delta, \frac{1}{3} - \delta, 0)$ and $(\frac{1}{3} - \delta, \frac{2}{3} + 2\delta, 0)$, with values of the incommensuration δ up to 0.025 ($\delta \sim 0.022$ for Fig. 5.1a). The incommensuration δ is comparable to what was observed in YbFe_2O_4 [35]. These different vectors are attributed to the 120° twinning around c -axis and the symmetry equivalent directions. An example of the superstructure reflections closed to $(\frac{1}{3}, \frac{2}{3}, 24)$ reached by three different structural reflections via the mentioned propagation vectors is shown in Fig. 5.1b. However, if the superstructure intensity can only be described by one propagation vector from one structural reflection without the contribution from any symmetry equivalent directions i.e. the 3-fold rotation is broken, then the sample is called mono-domain sample. The existence of a mono-domain sample will limit the structures to a corresponding propagation vector as will be discussed later in Sec. 5.2.2. Therefore, many crystals with incommensurate CO were screened for their

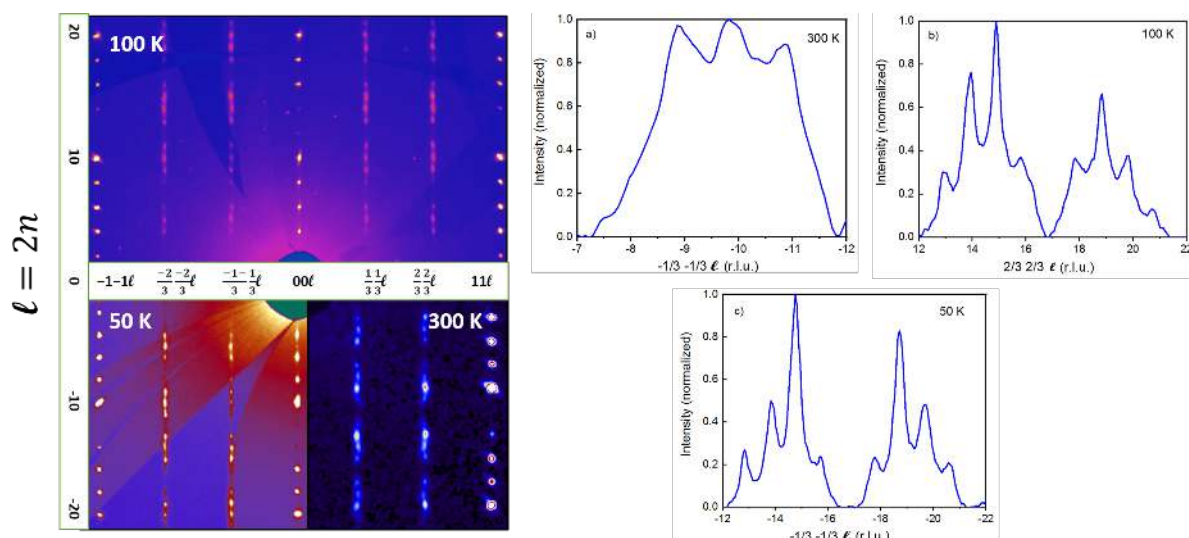


Figure 5.2: Composite precession images of the $hh\ell$ reciprocal space plane of SC3 $\text{Lu}_2\text{Fe}_3\text{O}_7$ grown with a $\text{CO}_2/\text{CO}=85$: upper measured at P24 at 100 K, left lower measured at P24 at 50 K, and right lower measured at supernova at RT. The integrated intensity in a small region perpendicular to the $(hh\ell)$ for the corresponding temperatures are shown in (a,b,c). All data were treated with linear background subtraction.

domain population, and no crystal with mono-domain was found, in contrast to LuFe_2O_4 [36]. The domains in the crystal shown in right panel of Fig. 5.1b appear pretty much equally populated. In fact, one would expect to see three reflections that are close to each other from the different domains, but due to the lack of resolution, a superposition of the reflections is observed. Moreover, the superposition spots look close to circular in shape rather than elongated shape indicating the presence of three reflections merged corresponding to three domains.

The most interesting and the new CO type is the apparently commensurate CO introduced previously in Sec. 3.5.1. Figure 5.2 shows a composite precession image of the $hh\ell$ planes for the commensurate CO type in sample SC3 at different temperatures. SC3 was studied by $M(T,H)$ measurements in Sec. 4.1 and XMCD in Sec. 4.4.1. The 300 K data set was measured in-house at the Supernova (another part of the precession image was also previously shown in Fig. 3.9c in different color scale) whereas the additional 100 K and 50 K data were measured at the P24 beam-line at the PETRA III synchrotron (Sec. 2.3.7). The latter was done to overcome the peak overlap problem observed for the supernova measurements. The intensity integrated in hh -direction around $hh = 1/3$ vs ℓ at RT, 100 K and 50 K are shown in Fig. 5.2a,b,c respectively. The peak widths for the data at 100 K and 50 K are narrower which is expected as the synchrotron has a better resolution and the effect of the Debye-Waller-factor is reduced. The commensurate CO is preserved down to 50 K, which is the lowest measured temperature. The commensurate CO type has not been reported before, not even in the non-intercalated LuFe_2O_4 . However, two reports on a commensurate pattern exists in YbFe_2O_4 below ~ 250 K [35, 40].

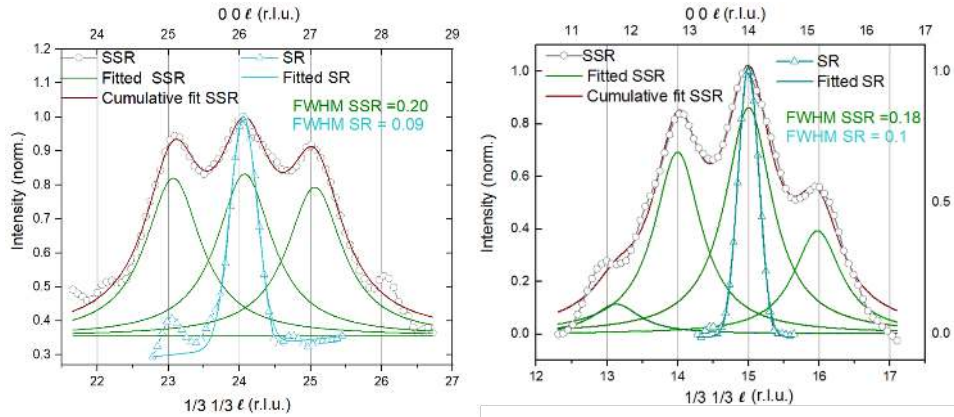


Figure 5.3: Intensity integrated perpendicular to l of: (left) $(0\ 0\ 26)$ structural reflection (SR), fitted SR intensity and super structural reflection (SSR) ($\frac{1}{3}\frac{1}{3}l = 23-25$) out of plane at room temperature from lower right panel of Fig. 5.2 for SC2. (Right): $(0\ 0\ 14)$ structural reflection (SR), fitted SR intensity and super structural reflection (SSR) ($\frac{1}{3}\frac{1}{3}l = 14-16$) out of plane at room temperature from Fig. 5.1a for SC3. Full widths at half maximum (FWHM) are given in Angstrom units. The SSR and SR were fitted with lorentzian and Gaussian profiles respectively. Linear background subtraction was done for both SR and SSR in right figure before fitting. Left figure is from own work [64]

To estimate the out-of-plane correlation lengths at room temperature for the commensurate CO for the data shown in Fig. 5.2, a comparison of the peak width of the super structural reflections (SSR) ($\frac{1}{3}\frac{1}{3}l = 24$) and the structural reflection (SR) ($0\ 0\ 26$) is shown in the left panel of Fig. 5.3. The SSR was fitted with a Lorentzian profile and the SR with a Gaussian profile. Afterward, the width of the SR was subtracted from the one of the SSR in order to approximately correct for the effect of instrumental resolution and mosaicity. This provides an estimated out-of-plane correlation length ($\xi_c = 2/\text{FWHM}$) of $18.2\ \text{\AA}$ (one bilayer: half unit cell roughly) for the incommensurate CO. In the same manner for the incommensurate CO in Fig. 5.1a, the comparison of the SSR ($\frac{1}{3}\frac{1}{3}l = 15$) and the structural reflection (SR) ($0\ 0\ 14$) as shown in the right panel of Fig. 5.3 providing a slightly larger estimated correlation length of $22.7\ \text{\AA}$ (two bilayers: one unit cell). These correlation lengths are significantly smaller than the correlation length reported in LuFe_2O_4 ($75\ \text{\AA}$ [52]), and also smaller than what observed in YFe_2O_4 ($550\ \text{\AA}$ [60]). Nevertheless, the correlations should be sufficient to deduce the CO pattern in principle. The focus on the out-of-plane correlations is because in reduced quality (off-stoichiometric) samples, the out-of-plane correlations are destroyed while the in-plane correlations are much less affected, therefore 2D CO is observed [11, 35, 57].

5.2 $\text{Lu}_2\text{Fe}_3\text{O}_7$ CO crystal structure at 100 K

As already outlined in Sec. 3.5.1, single crystal X-ray diffraction on $\text{Lu}_2\text{Fe}_3\text{O}_7$ crystals show distinct CO phases, which may be commensurate or incommensurate. Focusing on the newly discovered commensurate CO, the superstructural reflections were indexed by a propagation

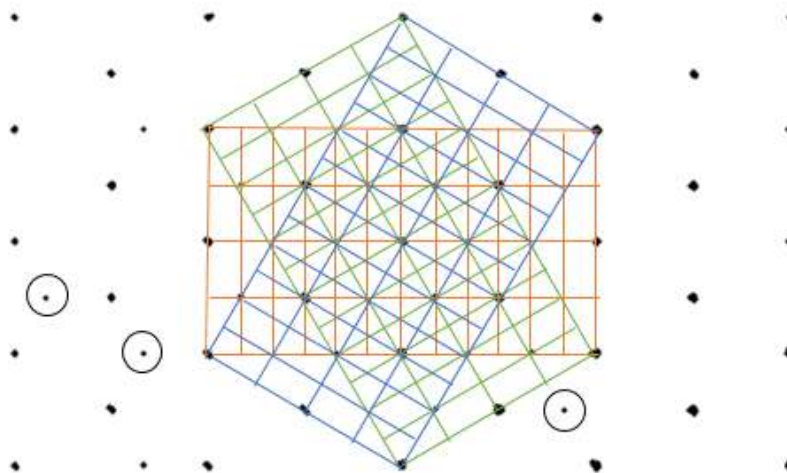


Figure 5.4: Observed reflections in reciprocal space along c_{hex} at 100 K indexed by the three domains rotated by 120° presented by a different colored cell. Larger size reflections are the structural reflections while the smaller ones are the superstructural reflections (some are surrounded by circle).

vector $(\frac{1}{3}, \frac{1}{3}, 0)$ and symmetry equivalents at 100 K. Fig. 5.4 shows the indexation of the reflections observed at 100 K, with three domains distinguished by color.

5.2.1 Indexing the pattern

The determination of the CO configuration requires the collection of a full data set of integrated intensities and structural refinement, as previously done for the non-intercalated compounds [11, 35]. However, the shorter correlation lengths in $\text{Lu}_2\text{Fe}_3\text{O}_7$ make this endeavor more difficult, as they contribute to significant peak overlap as can be seen in Fig. 5.2. This problem was ameliorated by improving the experimental resolution, and collecting the data set on the four-circle diffractometer at the P24 beam-line of PETRA III, DESY using a crystal with commensurate CO type (SC3). An extensive measurement was done at 100 K due to the more complex structure compared to the non-intercalated compounds. Optimal values of 0.5607 \AA for the wavelength and 120 mm for the crystal-to-detector distance were used to achieve better peaks separation.

a (\AA)	b (\AA)	c (\AA)	α ($^\circ$)	β ($^\circ$)	γ ($^\circ$)
5.9683(2)	5.9688(2)	28.4188(11)	90.001(3)	89.969(3)	120.042(4)

Table 5.1: Lattice parameters of the P1 cell at 100 K

All the observed reflections (11860) (see Sec. 2.4.1) can be indexed with a hexagonal supercell with lattice parameters as shown in table 5.1. This cell has a volume of $876.37(5) \text{ \AA}^3$, i.e. three times enlarged compared to the hexagonal ($P6_3/mmc$) cell of the basic structure of 292.3 \AA^3 . Before the integration process, a rejection mask was implemented to prevent the integration outside the detector area. The integration was done in the space group P1 testing different

integration mask sizes. Table 5.2 gives an overview of the internal residuals (see Sec. 2.4.1 for the definition) obtained with different integration mask sizes.

integration mask size	0.5	0.75	1.0	1.25	1.5	1.75	2	2.5
internal residual R_{int}	0.13	0.12	0.09	0.11	0.11	0.10	0.10	0.12

Table 5.2: Influence of different integration mask sizes (relative to the default) on the internal residual. Default mask size is 1.

The default mask size gave the lowest internal R-value and was therefore chosen for the final integration. The obtained reflections intensities are corrected for absorption empirically as discussed in Sec. 2.4.1 and the list of intensities is then exported in *hkl*-file format, which is directly imported in to Jana2006.

5.2.2 $\text{Lu}_2\text{Fe}_3\text{O}_7$ representation analysis

The presence of CO distorts the parent crystal structure $P6_3/mmc$ into a lower symmetry subgroup. As was previously done for LuFe_2O_4 [31] and YbFe_2O_4 [35], the Isodistort software [143, 144] was used to determine the possible solutions in terms of the symmetry modes of the irreducible representations (irreps). This analysis was done with the assumption that the Fe-valance modulation is the responsible for superstructure reflections appearance and that the distortion occurs due to CO only in the bilayers. As mentioned in Sec. 5.1, no mono-domain sample was found, therefore the possibility of having more than one of the symmetry-related propagation vectors involved in the distortion (so-called multi-k structures) was considered. Using the $(\frac{1}{3}, \frac{1}{3}, 0)$ propagation (the point of the Brillouin zone), results in four different irreps: K1, K4, K5 and K6. However, K1 and K4 were disregarded as they provide no distortion in the bilayer. All the possible solutions are obtained by K5 and K6 modes and summarized in table 5.3 with noting the possible CO type realized in each symmetry.

Out of all the presented structures, only four unique CO patterns are obtained (the rest are equivalent and provide no new symmetries): three orthorhombic ($Cmc2_1$, $Amm2$, $Cmcm$) and one monoclinic ($C2/m$) structure. (a, b) order parameters are enough to produce the different possibilities, moreover, with only a single-K mode. Combinations of different irreps were tried out, however, none of that induces any new symmetries. This is different than in YbFe_2O_4 [35], where the combination of Y1+Y2 modes led to a genuinely new symmetry, $P\bar{1}$, which could not be obtained with just single mode Y1 or Y2, both of which induce monoclinic symmetry.

Starting with the orthorhombic $Cmcm$ structure shown in the left panel of Fig. 5.5, which contains all others as subgroups provides a CO configuration that is not charge neutral (both the bilayers are Fe^{2+} majority in Fig. 5.5). This is rejected as physically not possible.

Considering now the only monoclinic ($C2/m$) structure with (0,0,0) origin, i.e. an inversion center located between the Fe-bilayers as shown in the right panel of Fig. 5.5. This structure yields charged rather than polar bilayers as well. However, in difference to $Cmcm$ the $C2/m$ structure is charge neutral as a whole due to the stacking of oppositely charged bilayers. However, it is physically unlikely as well, as the separation distances between the neighboring

Order parameter	SG	Basis	Origin	Remarks
K5 (0,0,0,a)	P $\bar{6}$ 2m	(2,1,0),(-1,1,0),(0,0,1)	(1/3,2/3,1/4)	overall charged
K5 (0,0,a,-a)	Cmcm	(3,0,0),(1,2,0),(0,0,1)	(0,0,0)	overall charged
K5 (0,a,0,b)	P $\bar{6}$	(2,1,0),(-1,1,0),(0,0,1)	(1/3,2/3,1/4)	overall charged
K5 (0,0,a,b)	Amm2	(0,0,1),(3,0,0),(1,2,0)	(0,0,1/4)	(anti)-polar
K5 (a,a,b,-b)	P2 ₁ /m	(-1,1,0),(0,0,1),(2,1,0)	(0,0,0)	overall charged
K5 (a,-a,b,-b)	Ama2	(0,0,1),(1,2,0),(-3,0,0)	(0,0,0)	overall charged
K5 (a,b,c,d)	Pm	(-1,1,0),(0,0,1),(2,1,0)	(0,0,1/4)	anti-polar
K6 (0,0,0,a)	P321	(2,1,0),(-1,1,0),(0,0,1)	(1/3,2/3,1/4)	overall charged
K6 (0,a,0,0)	P31m	(2,1,0),(-1,1,0),(0,0,1)	(1/3,2/3,0)	charged bilayer
K6 (0,0,a,a)	C222 ₁	(3,0,0),(1,2,0),(0,0,1)	(0,0,0)	overall charged
K6 (0,0,a,-a)	C2/c	(3,0,0),(1,2,0),(0,0,1)	(0,0,0)	overall charged
K6 (a,a,0,0)	C2/m	(1,2,0),(3,0,0),(0,0,-1)	(0,0,0)	charged bilayer
K6 (a,-a,0,0)	Cmc2 ₁	(3,0,0),(1,2,0),(0,0,1)	(0,0,0)	polar
K6 (0,a,0,b)	P3	(2,1,0),(-1,1,0),(0,0,1)	(1/3,2/3,0)	charged bilayer
K6 (0,0,a,b)	C2	(3,0,0),(1,2,0),(0,0,1)	(0,0,1/4)	anti-polar
K6 (a,b,0,0)	Cm	(1,2,0),(3,0,0),(0,0,-1)	(0,0,0)	(anti)-polar
K6 (a,a,b,b)	C2	(1,2,0),(3,0,0),(0,0,-1)	(0,0,0)	charged bilayer
K6 (a,-a,b,b)	P2 ₁	(-1,1,0),(0,0,1),(2,1,0)	(0,0,0)	(anti)-polar
K6 (a,a,b,-b)	P $\bar{1}$	(1,-1,0),(1,2,0),(0,0,1)	(0,0,0)	charged bilayer
K6 (a,-a,b,-b)	Cc	(3,0,0),(1,2,0),(0,0,1)	(0,0,0)	polar
K6 (a,b,c,d)	P1	(1,-1,0),(1,2,0),(0,0,1)	(0,0,0)	polar

Table 5.3: Structure solution for K5 and K6-modes based on $(\frac{1}{3}, \frac{1}{3}, 0)$ propagation from the Isodistort software [143, 144]. SG: space group. All the structures with polar bilayers are highlighted with green color. The various polar stacked structures have an actual symmetry of Cmc2₁, the anti-polar have an actual symmetry of Amm2, while those with charged bilayers have Cmcm symmetry.

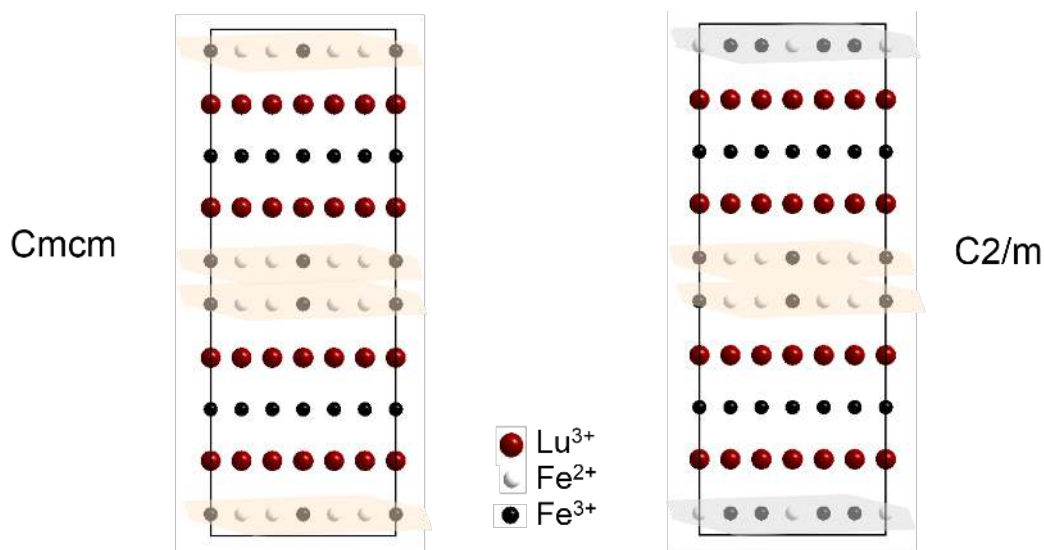


Figure 5.5: Structural representation of $Cmc2_1$ (left) and $C2/m$ (right). The layers are highlighted according to Fe-valance majority: orange for layer rich in Fe^{2+} and gray rich in Fe^{3+} .

bilayers are larger than 6 \AA , hampering the charge transfer between these bilayers to derive the CO. This latter structure was introduced before as one of the possible solutions for LuFe_2O_4 [36] using the $(\frac{1}{3}, \frac{1}{3}, \frac{2}{3})$ propagation. Moreover, as discussed in Sec. 1.2.1 it was the symmetry that was assumed to be realized in the refinement of LuFe_2O_4 [11] based on the commensurate approximation for incommensurate phase. This later on turned out to likely be not correct based on the refinement of actual commensurate CO in the isostructural YFe_2O_4 [35] in a lower symmetry of $P\bar{1}$ with the individual bilayers being polar. Another reason making the $C2/m$ unlikely is that the same CO within a single bilayer as in LuFe_2O_4 and YbFe_2O_4 can indeed be expected, given that intralayer Fe-Fe distance to bilayer thickness (1.426) is very close to what is found for these two compounds [21]. Moreover, the $C2/m$ refinement was considered for both the average structure (c.f. Sec. 5.2.3) and the superstructure (c.f. Sec. 5.2.4), therefore, very unlikely.

This leaves us with the two orthorhombic symmetries, $Cmc2_1$ and $Amm2$, as likely candidates: the first, the $Cmc2_1$ structure yields individually polar bilayers in which one of the layers has a majority of Fe^{2+} and the other a majority of Fe^{3+} , with polarization direction as shown in the left panel of Fig. 5.6, and a polar stacked bilayers. The second is the $Amm2$ structure with also polar bilayers with an alternatively stacking, leading to an anti-polar structure in terms of out-of-plane polarization (see middle panel of Fig. 5.6). However, due to the particular atom stacking in the basic $P6_3/mmc$ structure, the "anti-polar" configuration compensates only the c -component of the polarization of the bilayers, while an also existing (smaller) in-plane polarization is adding up, as indicated by the right panel of Fig. 5.6.

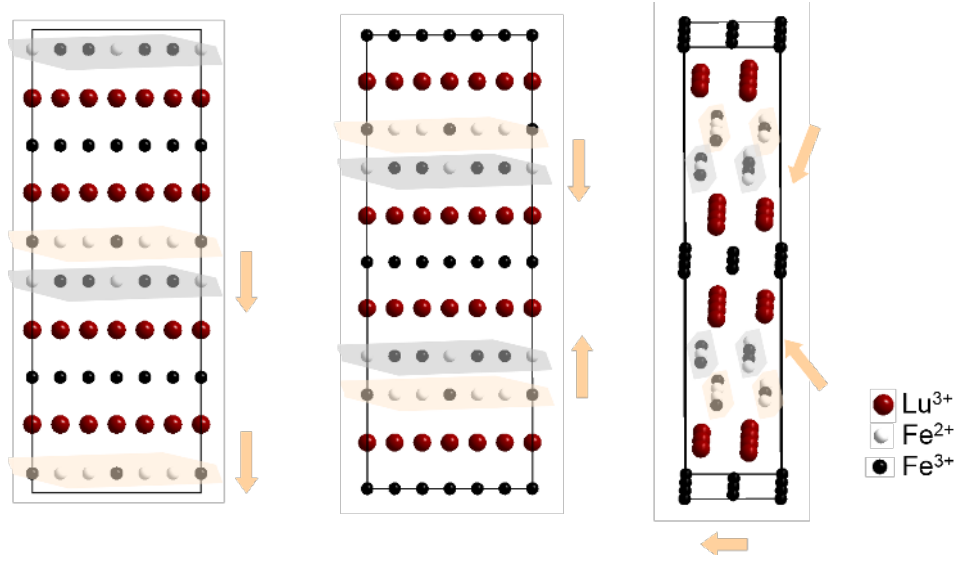


Figure 5.6: Structural representation of Cmc2₁ (left), Amm2 (right), and different viewing direction for Amm2. The layers are highlighted according to Fe-valence majority: layer rich in Fe²⁺ (orange) and rich in Fe³⁺ (gray). The arrows indicated the bilayer polarization direction.

The transformations between the P6₃/mmc structure and the structure of the above subgroups are described by the basis transformation matrices **A** and origin shifts **p** as follows:

$$\text{Cmcm, Cmc2}_1, : \quad \mathbf{A} = \begin{pmatrix} 3 & 0 & 0 \\ 1 & 2 & 0 \\ 0 & 0 & 1 \end{pmatrix} \text{ and } \mathbf{p} = \begin{pmatrix} 0 \\ 0 \\ 0 \end{pmatrix} \quad (5.1)$$

$$\text{Amm2} : \quad \mathbf{A} = \begin{pmatrix} 0 & 0 & 1 \\ 3 & 0 & 0 \\ 1 & 2 & 0 \end{pmatrix} \text{ and } \mathbf{p} = \begin{pmatrix} 0 \\ 0 \\ \frac{1}{4} \end{pmatrix} \quad (5.2)$$

$$\text{C2/m} : \quad \mathbf{A} = \begin{pmatrix} 1 & 2 & 0 \\ 3 & 0 & 0 \\ 0 & 0 & -1 \end{pmatrix} \text{ and } \mathbf{p} = \begin{pmatrix} 0 \\ 0 \\ 0 \end{pmatrix} \quad (5.3)$$

A linear transformation can bring the direct lattice vectors **a, b, c** into the new lattice vectors **a', b', c'** as follows:

$$\begin{pmatrix} \mathbf{a}' \\ \mathbf{b}' \\ \mathbf{c}' \end{pmatrix} = \mathbf{A} \cdot \begin{pmatrix} \mathbf{a} \\ \mathbf{b} \\ \mathbf{c} \end{pmatrix} \quad (5.4)$$

SG	point group	full point group	symmetry elements	TW
$P6_3/mmc$	$6/mmm$	$6/m2/m2/m$	24	-
$Cmcm$	mmm	$2/m2/m2/m$	$1, m \perp a, 2 \parallel a, m \perp b, 2 \parallel b, m \perp c, 2 \parallel c, \bar{1}$	3
$Cmc2_1, Amm2$	$mm2$	$mm2$	$1, m \perp a, m \perp b, 2 \parallel c$	6
$C2/m$	$2/m$	$2/m$	$1, m \perp b, 2 \parallel b, \bar{1}$	6

Table 5.4: Table of the structure solutions obtained by the isodistorted. Tabulated are the SG: space groups, their full point group, the present symmetry elements in each and the number of the twin laws (TW).

The new miller indices h', k', ℓ' in terms of the old:

$$\begin{pmatrix} h' \\ k' \\ \ell' \end{pmatrix} = \mathbf{A} \cdot \begin{pmatrix} h \\ k \\ \ell \end{pmatrix} \quad (5.5)$$

Note that the miller indices are transformed in the same way as the $\mathbf{a}, \mathbf{b}, \mathbf{c}$, therefore they are called covariant quantities.

The basis vectors of reciprocal space are $\mathbf{a}^*, \mathbf{b}^*, \mathbf{c}^*$ and their transformation is achieved by the matrix $[\mathbf{A}^{-1}]^t$, which stands for the transpose of the inverse of matrix \mathbf{A} :

$$\begin{pmatrix} \mathbf{a}^{*'} \\ \mathbf{b}^{*'} \\ \mathbf{c}^{*'} \end{pmatrix} = [\mathbf{A}^{-1}]^t \cdot \begin{pmatrix} \mathbf{a}^* \\ \mathbf{b}^* \\ \mathbf{c}^* \end{pmatrix} \quad (5.6)$$

A change of fractional coordinates in real space, x, y, z is described by the combination of the transformation matrix \mathbf{A} and the origin shift denoted by \mathbf{p} :

$$\begin{pmatrix} x' \\ y' \\ z' \end{pmatrix} = [\mathbf{A}^{-1}]^t \cdot \begin{pmatrix} x \\ y \\ z \end{pmatrix} - [\mathbf{A}^{-1}]^t \mathbf{p} \quad (5.7)$$

This transformation is also valid for directions in direct space (u, v, w).

Going from the hexagonal space group to one of these lower symmetry structural descriptions involves (by definition) losing some symmetry elements, which are considered as twin laws (c.f. [98]), for example the 3-fold rotation that relates the different domains to each other (see Sec. 5.1 and Fig. 5.4), upon symmetry lowering, this 3-fold axis is broken and corresponds to a twin law. Table 5.4 summarizes the different subgroups obtained from the isodistort, with their full point groups. The number of twin domains upon each transformation is also shown (obtained through the division of symmetry element number of the hexagonal by the symmetry element number of the subgroup).

The Miller indices of the subgroup cell transform between its different twins using the following equation:

$$\begin{pmatrix} h_t \\ k_t \\ \ell_t \end{pmatrix} = \mathbf{T}_i \cdot \begin{pmatrix} h \\ k \\ \ell \end{pmatrix} \quad (5.8)$$

with $i \in \{1, 2, 3, 4, 5, 6\}$ and \mathbf{T}_i being the twinning matrices obtained upon transformation from the hexagonal base to the related subgroup base and calculated by:

$$\mathbf{T}_i = \mathbf{A} \cdot \mathbf{R}_{\text{hex}} \cdot \mathbf{A}^{-1} \quad (5.9)$$

Starting the transformation from $P_{\frac{6_3}{m} \frac{2}{m} \frac{2}{c}}$ to the the maximal subgroup $Cmcm$, it is obvious that the 3-fold rotation corresponds to 120° rotation around \mathbf{c}_{hex} is lost. The application of equation (5.9) with substituting \mathbf{R}_{hex} with the rotational matrix \mathbf{R}_{120} given as:

$$\mathbf{R}_{120} = \begin{pmatrix} 0 & 1 & 0 \\ -1 & -1 & 0 \\ 0 & 0 & 1 \end{pmatrix} \quad (5.10)$$

yields the second twin matrix, the first one is the identity by default and the last is the 240° rotation around \mathbf{c}_{hex} . The obtained twin matrices are :

$$\mathbf{T}_1 = \begin{pmatrix} 1 & 0 & 0 \\ 0 & 1 & 0 \\ 0 & 0 & 1 \end{pmatrix} \quad \mathbf{T}_2^{120^\circ} = \begin{pmatrix} -\frac{1}{2} & \frac{3}{2} & 0 \\ -\frac{1}{2} & -\frac{1}{2} & 0 \\ 0 & 0 & 1 \end{pmatrix} \quad \mathbf{T}_3^{240^\circ} = \begin{pmatrix} -\frac{1}{2} & -\frac{3}{2} & 0 \\ \frac{1}{2} & -\frac{1}{2} & 0 \\ 0 & 0 & 1 \end{pmatrix} = \mathbf{T}_2^{-1} \quad (5.11)$$

As can be seen in the corresponding transformation matrix shown in 5.1, the $\mathbf{c}_{\text{hex}} \parallel \mathbf{c}_{\text{hex}}^* \parallel c_{Cmcm}$, therefore the 120° rotation around \mathbf{c}_{hex} is also a 120° rotation around c_{Cmcm}^* .

By equation (5.6), the indices of directions in direct space (0,0,1) remain the same.

With further lowering the symmetry to $Cmc2_1$, in addition to the already lost 3-fold rotation with 120° and 240° which occurs around $c_{Cmc2_1} \parallel \mathbf{c}_{\text{hex}}$, the inversion center is lost as well (fourth twin matrix); as it is a polar structural solution. Combining the inversion center with the second and third twinning matrices in 5.11 leads to the last fifth and sixth twin domains respectively. $\mathbf{T}_5 = \mathbf{T}_2 \cdot \mathbf{T}_4$ and $\mathbf{T}_6 = \mathbf{T}_4 \cdot \mathbf{T}_3$

$$\mathbf{T}_4 = \begin{pmatrix} -1 & 0 & 0 \\ 0 & -1 & 0 \\ 0 & 0 & -1 \end{pmatrix} \quad \mathbf{T}_5 = \begin{pmatrix} \frac{1}{2} & -\frac{3}{2} & 0 \\ \frac{1}{2} & \frac{1}{2} & 0 \\ 0 & 0 & -1 \end{pmatrix} \quad \mathbf{T}_6 = \begin{pmatrix} \frac{1}{2} & \frac{3}{2} & 0 \\ -\frac{1}{2} & \frac{1}{2} & 0 \\ 0 & 0 & -1 \end{pmatrix} \quad (5.12)$$

For $Amm2$, upon transformation from the hexagonal, the lost symmetry elements are similar to those lost in $Cmc2_1$. However, in difference, the indices of directions in direct space

in the hexagonal (0,0,1) transforms to (1,0,0) by equation (5.6), i.e. in the a-direction of the A_{m2} cell. The polar axis is $c_{A_{m2}}$ as shown in the right panel of Fig. 5.6 which is parallel to in-plane direction in the hexagonal settings (as expected from Fig. 5.6). The corresponding twin domains are obtained by the application of equation 5.9 and 5.10 using the corresponding transformation matrix. \mathbf{T}_2 , \mathbf{T}_3 are the 120° and 240° rotations around (1,0,0) respectively, \mathbf{T}_4 is the inversion, $\mathbf{T}_5 = \mathbf{T}_2 \cdot \mathbf{T}_4$ and $\mathbf{T}_6 = \mathbf{T}_4 \cdot \mathbf{T}_3$ shown as:

$$\mathbf{T}_1 = \begin{pmatrix} 1 & 0 & 0 \\ 0 & 1 & 0 \\ 0 & 0 & 1 \end{pmatrix} \quad \mathbf{T}_2^{120^\circ} = \begin{pmatrix} 1 & 0 & 0 \\ 0 & -\frac{1}{2} & \frac{3}{2} \\ 0 & -\frac{1}{2} & -\frac{1}{2} \end{pmatrix} \quad \mathbf{T}_3^{240^\circ} = \begin{pmatrix} 1 & 0 & 0 \\ 0 & -\frac{1}{2} & -\frac{3}{2} \\ 0 & \frac{1}{2} & -\frac{1}{2} \end{pmatrix} \quad (5.13)$$

$$\mathbf{T}_4 = \begin{pmatrix} -1 & 0 & 0 \\ 0 & -1 & 0 \\ 0 & 0 & -1 \end{pmatrix} \quad \mathbf{T}_5 = \begin{pmatrix} -1 & 0 & 0 \\ 0 & \frac{1}{2} & -\frac{3}{2} \\ 0 & \frac{1}{2} & \frac{1}{2} \end{pmatrix} \quad \mathbf{T}_6 = \begin{pmatrix} -1 & 0 & 0 \\ \frac{1}{2} & \frac{3}{2} & 0 \\ 0 & -\frac{1}{2} & \frac{1}{2} \end{pmatrix} \quad (5.14)$$

For the unpolar monoclinic $C2/m$ structure the inversion symmetry is not lost. However, a 2-fold rotation around $c_{\text{hex}} \parallel -c_{C2/m}$ is lost. With the combination of the lost symmetry elements results in the following twin laws, which are calculated in a similar manner as for the other subgroups using the related transformation matrix.

$$\mathbf{T}_1 = \begin{pmatrix} 1 & 0 & 0 \\ 0 & 1 & 0 \\ 0 & 0 & 1 \end{pmatrix} \quad \mathbf{T}_2^{120^\circ} = \begin{pmatrix} -\frac{1}{2} & -\frac{1}{2} & 0 \\ \frac{3}{2} & -\frac{1}{2} & 0 \\ 0 & 0 & 1 \end{pmatrix} \quad \mathbf{T}_3^{240^\circ} = \begin{pmatrix} -\frac{1}{2} & \frac{1}{2} & 0 \\ -\frac{3}{2} & -\frac{1}{2} & 0 \\ 0 & 0 & 1 \end{pmatrix} \quad (5.15)$$

$$\mathbf{T}_4^{180^\circ} = \begin{pmatrix} -1 & 0 & 0 \\ 0 & -1 & 0 \\ 0 & 0 & 1 \end{pmatrix} \quad \mathbf{T}_5 = \begin{pmatrix} \frac{1}{2} & \frac{1}{2} & 0 \\ -\frac{3}{2} & \frac{1}{2} & 0 \\ 0 & 0 & 1 \end{pmatrix} \quad \mathbf{T}_6 = \begin{pmatrix} \frac{1}{2} & -\frac{1}{2} & 0 \\ \frac{3}{2} & \frac{1}{2} & 0 \\ 0 & 0 & 1 \end{pmatrix} \quad (5.16)$$

5.2.3 Refinement of the average structure

In order to find the the possible structure solution in the large number of subgroups of the hexagonal $P6_3/mmc$, refinements were done at first ignoring the superstructure reflections and using only the structural reflections. The so obtained "average structure" corresponds to averaging the contents of three basic unit cells as the cell is enlarged three times by the modulation, see Fig. 5.15. This step will help to reduce the number of possibilities. Moreover, it is the fastest way to obtain structural information and an idea about the extent of the modulation as not the whole number of collected reflections are incorporated in the refinement. As the data was integrated using the super-cell, a transformation to the average structure was needed.

The used matrix to transform the P1 super-cell with defined lattice parameters in table 5.1 into the primitive hexagonal cell is:

$$\mathbf{T} = \begin{pmatrix} 1/3 & -1/3 & 0 \\ 1/3 & 2/3 & 0 \\ 0 & 0 & 1 \end{pmatrix} \quad (5.17)$$

At first, the average structure was refined based on the data collected at 100 K at P24 in the parent space group P6₃/mmc, the structural solution was obtained by the charge flipping method (c.f. Sec 2.4.2) using the software Superflip that can be called directly within Jana2006. Table 5.5 shows the refinement parameters before (B) and after (A) Lu-splitting.

Parameter	value
Spacegroup	P6 ₃ /mmc
a (Å)	3.4461
c (Å)	28.4180(5)
V (Å ³)	292.267(5)
R _{int} (obs/all)	10.60/10.62
R _{obs} /wR _{obs} ²	B: 26.08/51.34, A: 6.05/14.22
R _{all} /wR _{all} ²	B: 26.74/51.71, A: 6.61/14.37
GOF _{obs} /GOF _{all}	B: 16.18/15.32, A: 4.49/4.27
Num. of Reflections	904/1020
Num. of Parameters	25
Redundancy	30.33

Table 5.5: Refinement parameters of P6₃/mmc average structure at 100 K with a comparison for the residuals before (B) and after (A) Lu-splitting with refined occupancies. For details about the definition of different residuals (R) and the goodness of fit (GOF), see Sec.2.4.3

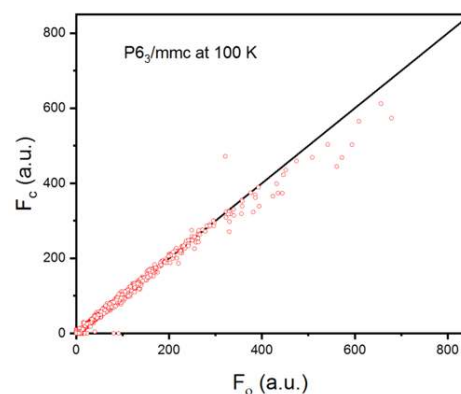
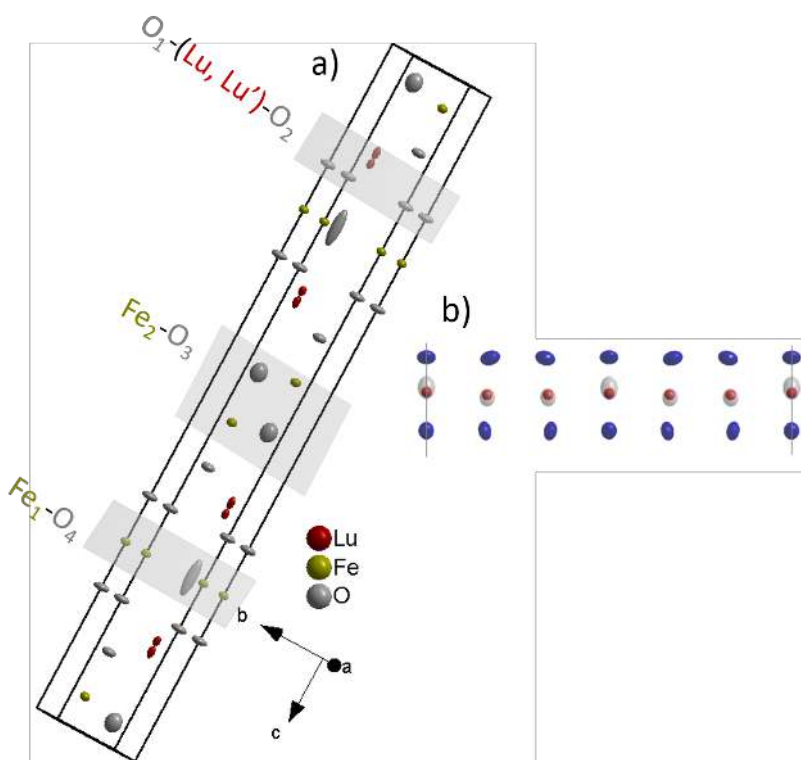


Figure 5.7: Plot of the calculated vs observed structure factors for the hexagonal (P6₃/mmc) average structure refinement (A) at 100 K, the black line indicates the ideal distribution.

The refinement R-values (A) are high and the agreement factors (GOF_{obs}/GOF_{all}) are far from the ideal value of one as no good match between the observed and the calculated structure factors could be obtained, as illustrated in Fig. 5.7. Upon refining atomic displacement parameters anisotropically (c.f. [145, 146]), an enormous elongation of the Lu atom thermal ellipsoids along c-direction is observed. Such thermal ellipsoid elongation of the Rare-earth element was observed before in the non-intercalated compounds: LuFe₂O₄ [11, 147], YbFe₂O₄ [35] and YFe₂O₄ [148]. However, the elongation of the rare earth element is very unlikely due to thermal motion (excited phonons), because it is the heaviest element, but may be due to static disorder [112], which means that one atom occupies two (or more) sites, and going through the structure which is occupied is random (hence "disorder"). One can resolve this by

Figure 5.8: a) The hexagonal $P6_3/mmc$ crystal structure at 100 K. The basic blocks of the unit cell are highlighted, and the atoms are presented with their refined thermal anisotropic displacement parameters. b) Lu (gray) and O (blue) atoms in $C2/m$ drawn as thermal ellipsoids in the projection along a at 210 K in LuFe_2O_4 . For comparison, the Lu positions at 350 K are displayed as orange spheres, taken from [36].



distributing the atoms with weights over two or more sites which refers to splitting. Therefore, the elongation of Lu in $\text{Lu}_2\text{Fe}_3\text{O}_7$ was remedied by splitting the Lu-position.

The refinement of the splitted Lu-position occupancies turned out to be close to 1:2 and a very drastic improvement of the refinement results is noted, validating that the splitting is necessary, see table 5.5. The better refinement upon splitting proving that is attributable to disorder and incompatible with harmonic potential expected for phonons i.e. across the entire crystal the atom is either at position 1 or at position 2, and randomly with the chance is proportional to the occupancy.

However, as the refinement in this section is done for the average of a modulated structure, it is very likely that the positions 1 and 2 are not randomly distributed, but rather according to the modulation, see Fig. 5.15 on p. 99. The full modulated structure is 3 times larger than the average structure, implying that in the average structure, 3 Lu-positions are averaged into one. Therefore, the 2:1 refined occupancies would refer then to two Lu positions are at site 1 and one Lu position at site 2. The splitting with 1:2 relative occupancies is similar to what was observed in LuFe_2O_4 [36], which corresponds to a modulation in the Lu-position for the superstructure as shown in Fig. 5.8b, similar to Fig. 5.15 on p. 99. In LuFe_2O_4 [36], the elongation was claimed to be connected to $\text{Fe}^{2+/3+}$ charge order [11]. The shift in the Lu-atoms position is correlated to different Fe valences i.e. CO, which favor unequal average bond lengths to the surrounding oxygen atoms [11, 115]. This explains the ADP elongation/splitting observed in $\text{Lu}_2\text{Fe}_3\text{O}_7$.

Table 5.6 shows the coordinates, occupancies and ADPs of the refined atoms with Lu-position splitting. The red coordinates are fixed by symmetry. Only the independent ADPs

(U_{11} and U_{33}) are shown, the rest are restricted by the hexagonal symmetry and are given in the following relations: $U_{22}=2U_{12}=U_{11}$, $U_{13}=U_{23}=0$. The refined crystal structure is depicted with their thermal ADPs in Fig. 5.8. As can be seen, in spite of the Lu-position splitting (before splitting U_{33} of Lu atom = 0.076), the splitted Lu atoms still exhibit relatively large ADPs along c_{hex} (see table. 5.6), which may indicate further unresolved disorder. Furthermore, almost all atoms, but particularly O4 (in the single Fe-layer) exhibit extremely unreasonable ADPs. The unreasonable ADPs for the atoms other than Lu, indicate that they are modulated as well, which is expected as the O atoms respond to the valance of the bonded Fe atoms. The Fe atoms have lower ADPs than the other atom types, suggesting that their positions are less strongly modulated. This is in line with the refinement of the full CO crystal structure in non-intercalated compounds [11, 35]. However, because they contribute less to the scattering than the heavier Lu, it is difficult to model them with split atoms, so the model is kept with just ADPs approximation for the non-Lu atoms. The CO reflected in the average structure by Lu-splitting breaks the point-group symmetry ($6/mmm$), therefore, a better refinement of the average structure should be obtained in the lower symmetry sub-groups of $P6_3/mmc$.

For this reason, all maximal sub-groups were tested and their refinement results are summarized in the upper part of table 5.8. As observed, going from $P6_3/mmc$ to a lower symmetry subgroup keeping the three-fold rotation leads to higher residuals and agreement factors than when it is broken, i.e. in $Cmcm$ symmetry. This strongly suggests the elimination of the hypothesis of having a multi-q structure (see Sec. 5.1), although there exist multi-q structures that nevertheless break 3-fold rotation. $Cmcm$ is one of suggested structural solutions by isodistort (and contains the others as subgroups, c.f. Sec. 5.2.2) and it is the most consistent model in the maximal subgroups as it has lowest wR_{all}^2 and GOF_{all} , however, the latter still far from the ideal value of one. The structure is shown in Fig. 5.9 right.

Site	ai	x	y	z	U11	U33
Lu ₁ (4f)	0.376(3)	1/3	2/3	0.13780(5)	0.00430(14)	0.0134(4)
Lu ₁ ' (4f)	0.624(3)	1/3	2/3	0.15428(3)	0.00431(11)	0.0089(2)
Fe ₁ (2b)	1	0	0	1/4	0.0088(2)	0.0054(3)
Fe ₂ (4f)	1	2/3	1/3	0.04369(3)	0.00918(17)	0.0063(2)
O ₁ (4f)	1	2/3	1/3	0.11088(15)	0.0171(11)	0.0061(12)
O ₂ (4e)	1	0	0	0.31831(15)	0.0225(13)	0.0051(11)
O ₃ (4f)	1	1/3	2/3	0.0318(3)	0.024(2)	0.034(4)
O ₄ (2c)	1	1/3	2/3	1/4	0.011(2)	0.128(16)

Table 5.6: Atomic positions and thermal displacement parameters of the refined average structure in $P6_3/mmc$ 100 K with Lu-position split

With further reduction of the symmetry, i.e. testing some of the subgroups of the $Cmcm$, no significant further improvement for the refinements results is observed (see the lower part of table 5.8). Focusing on the suggested solutions by Isodistort ($C2/m$, $Am2$ and $Cm2_1$). $Cm2_1$ seems to be the best in terms of the refinement values achievable for R_{obs} , wR_{all}^2 and in particular GOF_{all} , which is better than what obtained for the $Cmcm$ symmetry with a highest

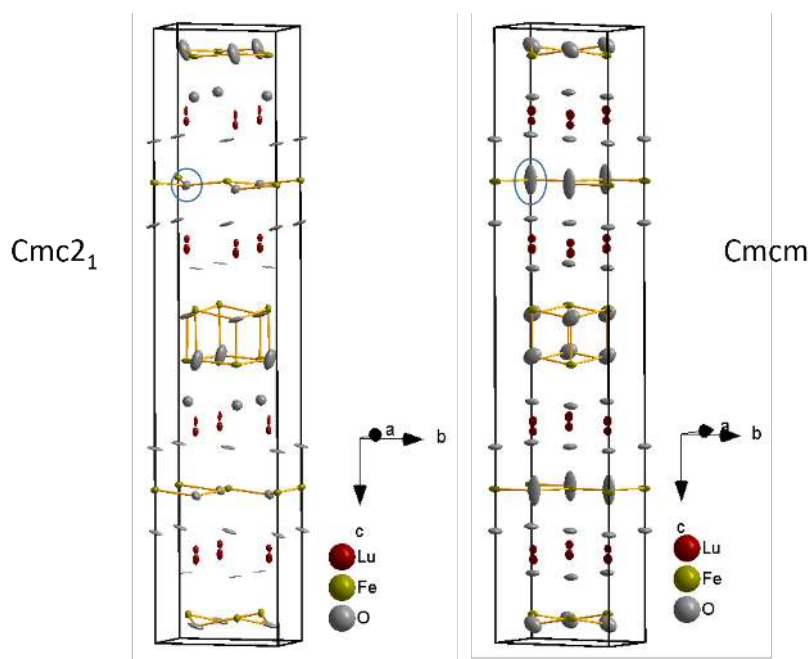


Figure 5.9: The average structure solution of $\text{Cmc}2_1$ (left) and $\text{Cmc}m$ (right) at 100 K. The bonded are the Fe-single and bilayers. Atoms are presented with their refined thermal anisotropic displacement parameters. Marked are the oxygen atom in the single layer.

number of reflections than the rest are included in the refinement for the $\text{Cmc}2_1$, it is shown in Fig. 5.9 left. Comparing the $\text{Cmc}m$ and $\text{Cmc}2_1$ structures in Fig. 5.9, at least smaller ADPs for some of the atoms are observed in $\text{Cmc}2_1$. Specifically, this is the case for the ADPs of the O atom in the single layer (encircled in Fig. 5.9), which is enlarged along z-direction in $\text{Cmc}m$ as can be clearly seen in Fig. 5.9 (also in $\text{P}6_3/\text{mmc}$, c.f. Fig. 5.8), but not in the $\text{Cmc}2_1$ structure. If the elongation is an effect of the modulation, then it should be kept with lowering the symmetry down to $\text{P}1$, but this is not the case. The likely explanation is that the presence of the mirror $\perp c_{\text{hex}}$ in $\text{Cmc}m$ leads to the elongation as illustrated in Fig. 5.10, this perfectly matches the observation in $\text{Cmc}m$, meaning a wrong symmetry is used. This clearly indicates that $\text{Cmc}2_1$ rather than $\text{Cmc}m$ is the correct symmetry and supports the conclusion from GOF, which for $\text{Cmc}2_1$ is significantly lower (higher $R_{\text{obs}}/wR_{\text{all}}^2$ values in $\text{Cmc}2_1$ are attributed to having twice number of reflections in the refinement in contrast to $\text{Cmc}m$). This leads to the tentative conclusion that the most likely solution is $\text{Cmc}2_1$. The refinement parameters for $\text{Cmc}m$ and $\text{Cmc}2_1$ are summarized in table 5.7 (See table A.2 and Fig. A.1 for the refinement parameters and structure plot of $\text{C}2/m$ and $\text{A}mm2$).

In all tested subgroups, the Lu position was splitted. As the refinement in the basic cell and disregarding the modulation vectors, one nevertheless has an average of the atomic positions, which corresponds to split positions, or in a worse approximation to enlarged ADPs.

Parameter	Cmcm	Cmc2 ₁
a (Å)	3.4461	3.4461
b (Å)	5.9688	5.9688
c (Å)	28.4180(5)	28.4180(5)
V (Å ³)	584.532(10)	584.532(10)
R _{int}	9.70/9.74	9.24/9.28
R _{obs} /wR _{obs} ²	5.48/12.63	5.76/12.64
R _{all} /wR _{all} ²	6.34/12.90	6.83/13.03
GOF _{obs} /GOF _{all}	3.12/2.81	2.80/2.48
N. of Reflections	3533/4524	6304/8482
Redundancy	7.433	3.964

Table 5.7: The refinement parameters of the average structure for both Cmcm and Cmc2₁ symmetries at 100 K

SG	GOF _{all}	R _{obs}	wR _{all} ²	Refls	Pars	Remarks (all Lu split)
P6 ₃ /mmc	4.27	6.05	14.37	904/1020	25	
P6̄2c	3.68	5.83	13.57	1410/1620	25	
P6̄m2	3.4	5.52	13.21	1651/2006	49	
P6̄ ₃ mc	3.58	5.88	13.57	1715/1984	45	
P6 ₃ 22	3.86	6.26	14.69	1345/1607	25	
P6 ₃ /m	3.87	6.18	14.68	1343/1609	25	
P3̄1c	3.67	5.82	13.57	1394/1606	25	
Cmcm	2.81	5.48	12.9	3533/4524	49	
P3̄m1	3.33	5.43	13.01	1635/1995	47	
Ama2	2.82	6.52	14.12	5232/6861	71	1 iso O
Amm2	2.80	6.22	14.06	5233/6895	89	3 iso O, incompl
Cmc2 ₁	2.48	5.76	13.03	6302/8482	90	1 iso O
C2 ₁ /m	3.6	5.31	16.46	3533/4524	73	no ext
C2/m	2.6	5.99	13.64	6294 /8469	93	
C2/c	2.61	6.03	13.69	6294/8436	72	
C2221	2.53	5.95	13.3	6283/8458	71	
C21	2.70	6.57	14.18	6304/8482	104	2 iso Lu

Table 5.8: Overview of refinements of the average structure. Extinction is present unless mentioned as (no ext.). Tabulated are the space group, Goodness of fit for all reflections, two residuals, number of merged reflections (Refls: observed/all) and parameters (Pars), and remarks. iso: isotropically refined, incompl: refinement incomplete (changes > 0.1 su)

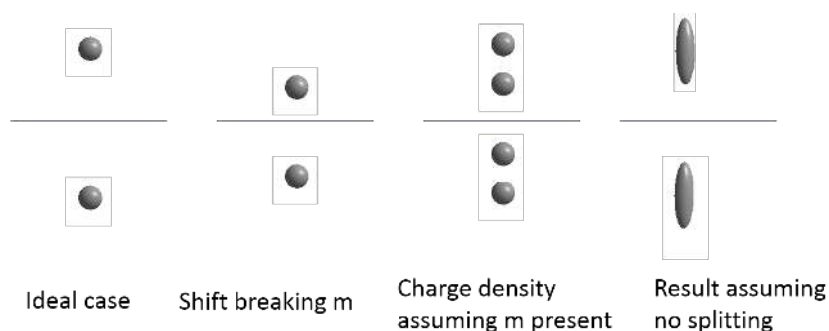


Figure 5.10: Sketch illustrating how the assumption of mirror plane (m) or inversion centre ($\bar{1}$) existence would lead to an elongation of electron density of atoms when modulation is dismissed

5.2.4 Super-cell refinement

Having reduced the likely subgroups to Cmcm and $\text{Cmc}2_1$, it is the time now to ascertain the structure by incorporating the superstructure reflections into the refinement. The presence of samples with incommensurate superstructure reflections (Fig. 5.1) makes it difficult to exclude the possibility of having a slight incommensuration in the apparently commensurate data, and the only description that works for the incommensurate case is the superspace approach. Moreover, if the space group of the average structure was determined, then the same space group will very likely also be the basis of the superspace group. For the mentioned reasons, the superspace approach was used in the refinement, which is based on a construction that moves artificially all superstructure reflections into the 4th dimension. For a detailed concept and description of the superspace approach see [149, 150]. In this approach, all the reflections are used, however, with maintaining the distinction between the structural and superstructure reflections. The structural reflections are indexed by the basic unit cell and the superstructure reflections by the use of the propagation vector to maximum order up to which the superstructure reflections should be processed ($hklm$) with $m=0$ for structural reflections, $m=\pm 1$ for first harmonics as (in our case) only the first harmonic reflections were used. $\mathbf{G} = h\mathbf{a}^* + k\mathbf{b}^* + l\mathbf{c}^* + m\mathbf{p}$, where \mathbf{p} is the propagation vector. In the hexagonal notation \mathbf{p} is $(\frac{1}{3}\frac{1}{3}0)_{\text{hex}}$, in Cmcm notation $(\frac{1}{3}10)_{\text{cmcm}}$.

As the average structure was ascertained to be likely either Cmcm or its subgroup $\text{Cmc}2_1$, a Cmcm basis was used as a starting model for the refinement of the super-cell; because the three-fold rotation is broken and it is the highest space group symmetry where this is the case. However, the superspace group may not keep all symmetry as basis and can turn out to be polar as we will see.

Cmcm symmetry combined with the observed propagation vector $(\frac{1}{3}\frac{1}{3}0)_{\text{hex}}$ has four different superspace groups: $\text{Cmcm}(\frac{1}{3}10)0ss$, $\text{Cmcm}(\frac{1}{3}10)000$, $\text{Cmcm}(\frac{1}{3}10)0s0$, $\text{Cmcm}(\frac{1}{3}10)00s$. Each of the super space group symbols above consists of three parts: Cmcm : C is the centering of the super space lattice and mcm applies to the 3D part of the space group. $(\frac{1}{3}10)$ is the modulation wave-vector, and s represents an intrinsic shift along the fourth dimension representing a shift of the modulation for the corresponding symmetry element by $\frac{1}{2}$ period. For exam-

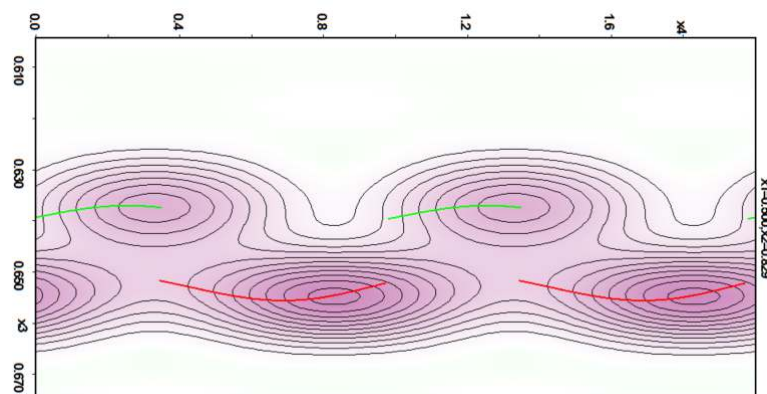


Figure 5.11: A contour map visualises the occupational modulation of the electron density as a function of x_3 (z -direction in 3D space) and x_4 (fourth dimension representing the modulation direction) of Lu atoms in the refined $\text{Cmcm}(\frac{1}{3}10)00s$. The occupational modulation shows a crenel function assures the alternation between the “Left,green” and “Right,red” configurations of Lu occupation.

ple: in the $0s0$ case, the first symmetry element in the space group mcm which is the mirror plane is not shifted, the c -glide is shifted by $\frac{1}{2}$ in the 4th direction, while the mirror plane in c -direction is not shifted. This means that the atom A which is connected by atom B by c -glide in the average structure, would be in-phase concerning the modulation for $\text{Cmcm}(\frac{1}{3}10)000$, but out-of-phase for $\text{Cmcm}(\frac{1}{3}10)0s0$. See table A.3 for reflection conditions of the different superspace groups of Cmcm .

The refinement was conducted in all superspace groups of the Cmcm incommensurately. For all four cases, occupational modulations of Lu atoms with a crenel function along the propagation direction (fourth dimension) are required i.e. the scattering density of one or more sites is modulated following a discontinuous function which defines an interval in x_4 where the corresponding atom exists [151, 152]. See the electron density map as a function of the atomic coordinates x_3 and x_4 of Lu atom at a fixed x_1 and x_2 coordinates in the refined $\text{Cmcm}(\frac{1}{3}10)00s$ in Fig. 5.11. The occupational modulation shows a crenel function, the Lu atom can be present at right site (red) or left site (green) i.e. along the modulation direction, the Lu atom changes its x_3 position discontinuously, therefore a sine function can not be used to describe the modulation. As observed, the Lu atoms are not exactly matching the electron density, which may suggest that the model is deficient.

The occupational modulation modeled by a crenel function implies the presence of higher harmonics [151] requiring the refinement commensurately as within the incommensurate approach, Jana2006 consider all the superstructure reflections ($hkl \pm 1$) as corresponding to only the intensity of first harmonic (as higher harmonics are supposed to be elsewhere), whereas no such intensity elsewhere was observed (if present there would be a position overlap within resolution). To treat the observed intensities as also including in the higher harmonics of the modulation, one has to switch to the commensurate case. Doing so, one has to fix the origin of the fourth dimension (t_0), with symmetry implications. The different possibilities listed in table 5.9, can equivalently be described by normal 3D space groups (different subgroups

of Cmc_m) with an enlarged cell. Corresponding refinements were carried out within these 3D space group. At least some of the Lu atoms had to be splitted in all the commensurately refined space groups.

Comparing the Cmc_m($\frac{1}{3}$ 10)0_{ss}, Cmc_m($\frac{1}{3}$ 10)000, Cmc_m($\frac{1}{3}$ 10)0_s0, Cmc_m($\frac{1}{3}$ 10)00_s, it is clear that Cmc_m($\frac{1}{3}$ 10)0_s0 and Cmc_m($\frac{1}{3}$ 10)000 can be excluded as solutions, as they exhibit higher R-factors ($R_{obs} = 16.98, 16.51$), ($wR_{all}^2 = 39.27, 37.94$) and the goodness of fit ($GOF_{all} = 5.94, 5.73$) is far from the ideal one. Another sign of inconsistency is the negative APDs of the Lu atoms in Cmc_m($\frac{1}{3}$ 10)0_s0. Moreover, looking at the second and the third blocks of table 5.9, the commensurate refinement of space groups headed by Cmc_m($\frac{1}{3}$ 10)0_s0 and Cmc_m($\frac{1}{3}$ 10)000 can be excluded as well due to the high achievable refinement agreement factors including the Cmc_mI/0 with the origin at (0, 0, 0), suggested by the Isodistort, is not a solution consist with our experimental data.

For the remaining commensurately refined space groups shown in table 5.9, headed by Cmc_m($\frac{1}{3}$ 10)0_{ss} and Cmc_m($\frac{1}{3}$ 10)00_s, there some obvious space groups to be excluded as well, those who has a higher refinement factors i.e. C2/m I/ $t_0 = 0$, C2/m II/ $t_0 = \frac{1}{6}$. The rest exhibit a quite close refinement parameters to each other. Focusing on Cmc2₁ as a solution suggested by Isodistort, relatively low R values are achieved with less refinement problems such as the negative ADPs or twin components, higher extinction parameter or unstable refinement. Two distinct structural solutions were tried: Cmc2₁ I/ $t_0 = \frac{1}{12}$ and Cmc2₁ II/ $t_0 = \frac{1}{4}$, they differ from each other by the choice of the center of the unit cell, although in the result seem to be functionally equivalent (see Fig. 5.14). In order to decide which is the right one, detailed refinements of both solutions are shown.

A comparison of the refinement parameters for the Cmc2₁ I/ $t_0 = \frac{1}{12}$ and Cmc2₁ II/ $t_0 = \frac{1}{4}$ is given in table 5.10. Both refinements exhibit comparable agreement factors but with GOF not close to the ideal one, see also the calculated vs. observed structure factors of the Cmc2₁ II/ $\frac{1}{4}$ in Fig. 5.10, where a deviation for some of the observed reflections from the calculated can be seen. Focusing first at the refinement that is not suggested by Isodistort, i.e. with the origin located at ($-\frac{1}{6}, 0, 0$), the refinement reveals several bad indications: the refinement was unstable, therefore incomplete. Moreover, the unreasonable ADPs for both O2 and O4 atoms, this was treated by splitting the corresponding position and afterward refining the ADP's isotropically, otherwise a non-positive definitive ADPs would appear, see the corresponding refinement result in table A.4. More crucially very anisotropic displacement parameters for some Lu (Lu3 and Lu4) atoms along the c_{hex} -direction are observed, therefore those Lu atoms were splitted. More than this, the non-positive definite ADPs of 2 Fe (Fe3, Fe4) and 3 O atoms (O11, O12, O14).

We come now to the refinement with the origin at (0, 0, 0), which is a representation by Isodistort corresponding to a polar stacked structure (see Fig. 5.6 left). Although the refinement was more stable and therefore completed, non-positive definite ADPs of 2 Fe (Fe5, Fe6) and 3 O atoms (O5, O6, O7) are observed as well, however, all atoms are refined ansiotropically. Similar to Cmc2₁ I/ $\frac{1}{12}$, two of the Lu-atoms (Lu2 and Lu3) exhibit very anisotropic displacement parameters and are therefore splitted. The refined coordinates and ADPs of all atomic sites are shown in table A.5. In general, this structural solution seems better, however due to the

mentioned problems, the first discussion "final conclusion" is premature at this stage. The twin component populations of both structures were reasonably refined, see table A.6. The twin components are ordered according to their definition in Eq. 5.11 and 5.12.

SG/ t_0	GOF _{all}	R _{obs}	wR _{all} ²	Refls	Pars	Remarks (all Lu crenel/split)
Cmcm(a10)0ss	2.68	6.85	17.64	13373	79	all anis, Lu crenel, all posmod
C222 ₁ I/ $\frac{1}{12}$	2.54	8.17	19.92	25343	177	2 O npd, all anis, incompl 0.26
C222 ₁ II/ $\frac{1}{4}$	2.54	8.14	19.85	25343	181	5 O npd, all anis
C2/m I/0	4.98	16.29	38.96	25319	136	4 Fe/3 O npd, Fe high iso, 2 Fe split, Lu & non-split Fe anis
C2/m II/ $\frac{1}{6}$	6.79	24.59	53.14	25319	97	3 Fe npd, Lu & 2 Fe anis, O common iso
C2/arb	2.39	8.66	20.34	35613	350	10 O npd, all anis, no ext 1 twf 0, incompl, v unstable
Cmcm(a10)000	5.73	16.51	37.94	13554	81	all anis, Lu crenel, all posmod
Cmcm I/0	4.65	12.89	30.72	13554	115	3 O npd, all anis
Cmcm II/ $\frac{1}{6}$	5.72	19.35	37.79	13554	105	1 O npd, all anis, ext >0.25
C2cm (Pma2)/arb	4.41	16.43	32.67	20627	185	1 Fe/8 O npd, all anis, 3 O split
Cmcm(a10)0s0	5.94	16.98	39.27	13555	83	Lu npd! all anis, Lu crenel, all posmod
C2 ₁ /m I/0	5.71	18.1	37.71	13555	130	2 O unreal. pos., 2 O >0.1, only Lu/Fe anis, 3 twf 0
C2 ₁ /m II/ $\frac{1}{6}$	4.38	11.88	28.92	13553	141	1 O split, only Lu/Fe anis
Cm2m I/ $\frac{1}{12}$	4.64	15.92	34.43	20668	156	1 Fe/3 O split pairs npd, 3 O split, only Lu/Fe anis, 1 twf 0
Cm2m II/ $\frac{1}{4}$	4.5	16.51	33.39	20655	92	1 O iso >0.15, 4 Fe npd, only Lu/Fe anis, 1 twf 0, incompl
Cm/arb	4.28	14.99	31.7	20647	194	6 Fe npd, 2 O large discs, only Lu/Fe/3 O anis, 2 twf 0, incompl
Cmcm(a10)00s/ic	3.06	7.37	20.12	13374	76	1 Lu npd, all anis, Lu crenel, Lu/O posmod, no ext
C2/c I/0	2.1	6.82	16.39	25279	199	2 O SPLIT, all anis exc split O, 2 twf 0, ext bit high
C2/c II/ $\frac{1}{6}$	2.6	6.71	20.32	25282	194	1 O iso >0.2, 1 Lu/3 O npd, all except 1 O anis, incompl
Cmcm I/ $\frac{1}{12}$	2.53	7.5	19.77	25368	202	2 Fe/3 O npd, 2 O SPLIT, all anis except split O, incompl
Cmcm II/ $\frac{1}{4}$	2.53	7.5	19.8	25368	205	2 Fe/3 O npd, all anis
Cc/arb	2.22	8.03	18.88	35594	374	3 Fe/11 O npd, all anis, incompl

Table 5.9: Overview of refinements based on Cmcm type superspace groups. Shown is incommensurate refinement (with extinction) followed by commensurate variants with different t_0 (refinement in commensurate supercell, no extinction unless mentioned). Tabulated are the space group and t_0 , Goodness of fit for all reflections, two residuals, number of reflections and parameters, and remarks. npd: not positive definite adp; neg: negative isotropic U; incompl: refinement incomplete (changes > 0.1 su); twf: twin fractions; anis: anisotropically refined; posmod: position modulated one harmonic.

Parameter	Cmc2 ₁ I/ $\frac{1}{12}$	Cmc2 ₁ II/ $\frac{1}{4}$
a (Å)	10.3395	10.3395
b (Å)	5.96830(10)	5.96830(10)
c (Å)	28.4180(5)	28.4180(5)
V (Å ³)	1753.65(4)	1753.65(4)
R _{int}	10.03/10.19	10.03/10.19
R _{obs} /wR _{obs} ²	7.50/17.94	7.50/17.95
R _{all} /wR _{all} ²	11.38/19.77	11.39/19.80
GOF _{obs} /GOF _{all}	3.07/2.53	3.07/2.53
Unique Reflections	25368	25368
Parameters	202	205

Table 5.10: Refinement parameters for both Cmc2₁ structures at 100 K

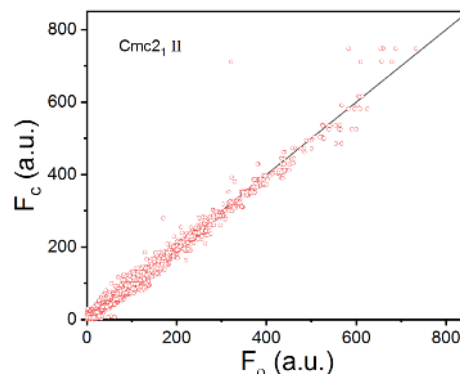


Figure 5.12: Calculated vs observed structure factors for Cmc2₁ II/ $\frac{1}{4}$ at 100 K, the black line indicates the ideal distribution

The main aim of the refinement is to ascertain the CO configuration as was done before for the non-intercalated compounds using the Bond-Valence-Sum method (BVS) [11, 35, 57], see also Sec. 2.4.4. Therefore, to determine the valence of Fe-ions and so deduce the CO pattern realized in each of the Cmc2₁ structures, the Bond-Valence-Sum method is applied (BVS), using equation 2.32 in Sec. 2.4.4. The used tabulated d_{0i} values to calculate the Fe²⁺ and Fe³⁺ in Cmc2₁ I/ $\frac{1}{12}$ and Cmc2₁ II/ $\frac{1}{4}$ are 1.734, 1.759 [115] respectively. The result from the BVS method, for the Fe sites from both Cmc2₁ structures are shown in the table 5.11 and illustrated by colors for different Fe sites in Fig. 5.14 and Fig. 5.13.

Site	Cmc2 ₁ I/ $\frac{1}{12}$	Cmc2 ₁ II/ $\frac{1}{4}$
Fe1	2.78(5) (3+)	2.71(5) (3+)
Fe2	2.81(3) (3+)	2.76(4) (3+)
Fe3	2.49(5) (2.5+)	2.42(4) (2.5+)
Fe4	2.83(8) (3+)	2.21(4) (2+)
Fe5	2.55(4) (2.5+)	2.43(4) (2.5+)
Fe6	2.21(4) (2+)	2.92(6) (3+)

Table 5.11: Calculated valences using the Bond-valence-sum analysis for each Fe-sites from both Cmc2₁ refined superstructures at 100 K.

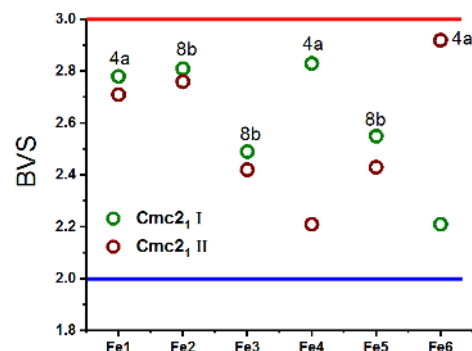


Figure 5.13: Plot of the Fe valences for the corresponding superstructures tabulated in table 5.11 and indicated in Fig. 5.14

In both structures, no full charge order of the Fe²⁺ and Fe³⁺ is obtained. Each symmetry has two Fe-sites with an intermediate valence (2.5+). Fe1 and Fe2 sites, located in the single layer, possess a 3+ valence as suggested previously by Mössbauer spectroscopy measurements in [46, 72]. The intermediate valence are the majority (8b) sites in the bilayers. The two struc-

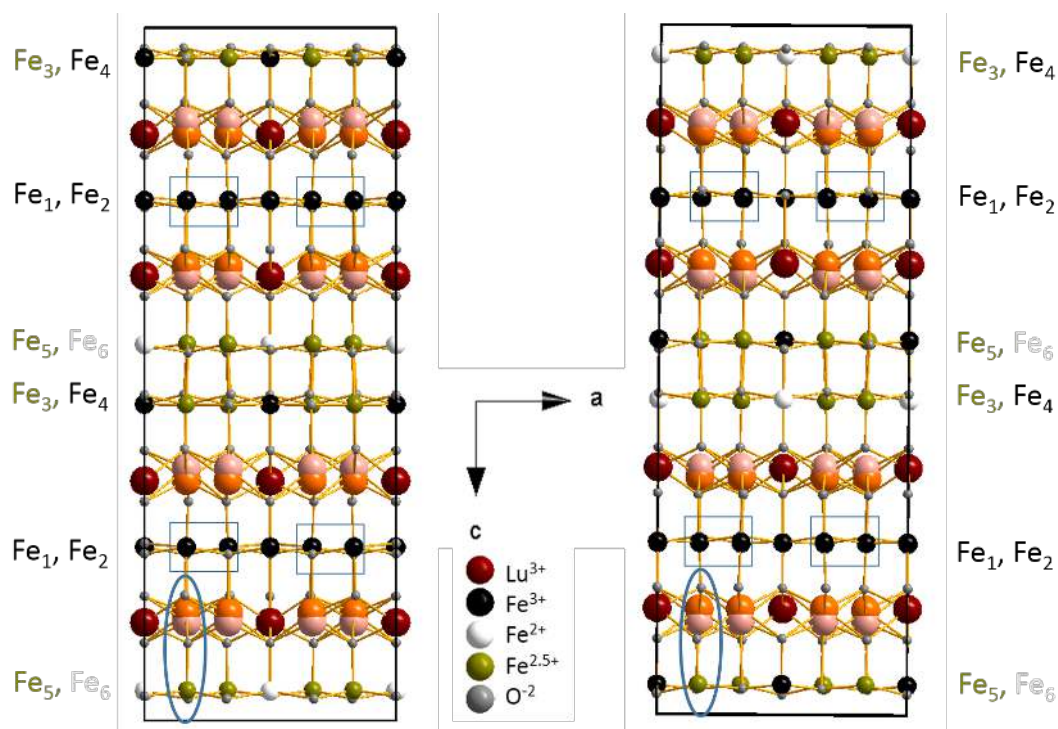


Figure 5.14: The $\text{Cmc}2_1$ I/ $\frac{1}{2}$ (left) and $\text{Cmc}2_1$ II/ $\frac{1}{4}$ (right) structure solutions. The different Fe valences found in both symmetries is represented by the colors. Fe2 atoms are surrounded by box. The splitted Lu atoms are differentiated by colors for the corresponding occupancy (orange for closer to $\frac{2}{3}$ and light pink for closer to $\frac{1}{3}$). The encircled splitted Lu-O-Fe atoms to point out when the Lu is splitted of having a 2.5+ average valance for the nearest Fe atom in the bilayer. The two solutions are not fundamentally distinct.

tures are extremely similar when are connected by $m(001)$ or inversion, which is not a space group symmetry, but a twin law (i.e. like two twins of the same thing), so do not look like fundamentally distinct solutions.

As can be seen in Fig. 5.14, along the propagation vector, every third Lu position is unsplit and the rest is split (typically with roughly 2:1 occupations), see the corresponding occupancies in table 5.12, in analogy to what is observed the average structure (see Sec. 5.2.3). Moreover, when the Lu position is splitted, the closest neighbouring Fe atoms in the bilayer has an intermediate valence (2.5+) (an example is marked for both structures by a circle in Fig. 5.14), while for the unsplit ones, the Fe has a valance of 2+ or 3+. The unsplit Lu has a shorter distance to the Fe^{2+} in the closest bilayer in contrast to Fe^{3+} present there exhibiting a larger distance. This is expected as the different Fe valance favors a different bond lengths to the surrounding oxygen atoms, therefore affect the distance to the Lu. This is the rare earth-modulation as was seen in non-intercalated LuFe_2O_4 [11] and YbFe_2O_4 [35], see Fig. 5.8 left. For the splitted Lu positions, less occupation is observed for the Lu-atoms that are closer to the bilayer, whereas more occupation for those are further away.

If the majority (8b) sites in $\text{Cmc}2_1$ II/ $\frac{1}{4}$ in Fig. 5.14 were assumed to have an opposite valance to the minority (4a) sites in the same layer, the yield CO configuration would then

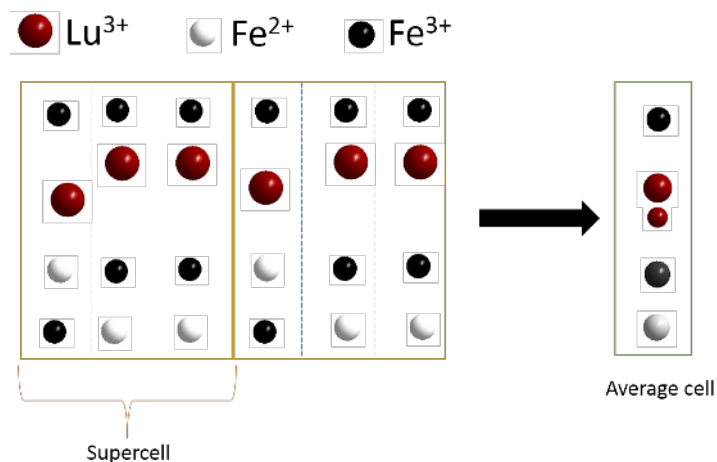


Figure 5.15: Illustration of the Lu-modulation surrounded by the closest single layer and bilayer, assuming a CO-pattern similar to isodistort $\text{Cmc}2_1$ solution. The left part shows 2 supercells, each supercell is averaged as it shown in right side. The averaged Fe atoms in the bilayer are shown in different gray shades.

correspond to the one suggested isodistort structure shown in Fig. 5.6 (left). The expected Lu-modulation in the Lu-O layer close to lower layer of the Fe-bilayer would look like illustrated in Fig. 5.15. The unresolved Fe-valences correspond to Lu-splitting in the superstructure shown in Fig. 5.14, however, no Lu-split is observed in Fig. 5.6 (left) where all Fe valences are resolved and, also not for the superstructure refinement in non-intercalated compounds e.g. YbFe_2O_4 [35]. Unlike the average structure, the modulation is accounted for in the superstructure refinement, moreover, it is not a wrong assumed symmetry element as discussed in Sec. 5.2.3 that causes the splitting because the splitting occurs along c -direction and there is no corresponding symmetry element left in $\text{Cmc}2_1$.

Atom (site)	$\text{Cmc}2_1$ I/ $\frac{1}{12}$	$\text{Cmc}2_1$ II/ $\frac{1}{4}$
Lu_1 (4a)	0.5	0.5
Lu_2 (8b)	0.421(3)	0.405(12)
Lu'_2 (8b)	0.579(3)	0.595(12)
Lu_3 (8b)	0.405(13)	0.421(3)
Lu'_3 (8b)	0.595(13)	0.579(3)
Lu_4 (4a)	0.5	0.5

Table 5.12: The occupancy of Lu atoms refined in both $\text{Cmc}2_1$ I/ $\frac{1}{12}$ and $\text{Cmc}2_1$ II/ $\frac{1}{4}$ at 100 K.

Before discussing the implications and the reason behind this unexpected result (Lu-splitting) that even exists in the refinement of the $\text{P}1$ space group (not shown), the $\text{Lu}_3\text{Fe}_4\text{O}_{10}$ compound - where also superstructural reflections are observed - will be presented at first in the next section.

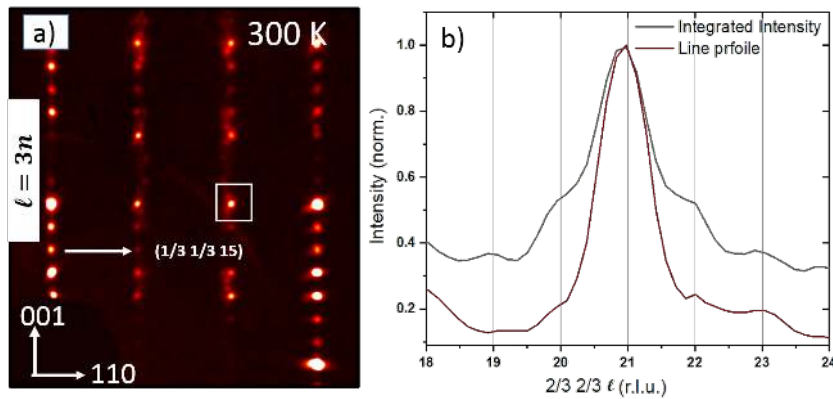


Figure 5.16: (a) Precession image of the hhl reciprocal space plane with (b) the integrated intensity (gray line) in a small region perpendicular to the (hhl) for (a) of S1 $\text{Lu}_3\text{Fe}_4\text{O}_{10}$ grown with a $\text{CO}_2/\text{CO}=85$ measured using supernova at RT. Line profile through the center of one of the peaks highlighted by a white square (red line) is also shown. (b) is from own work [64]

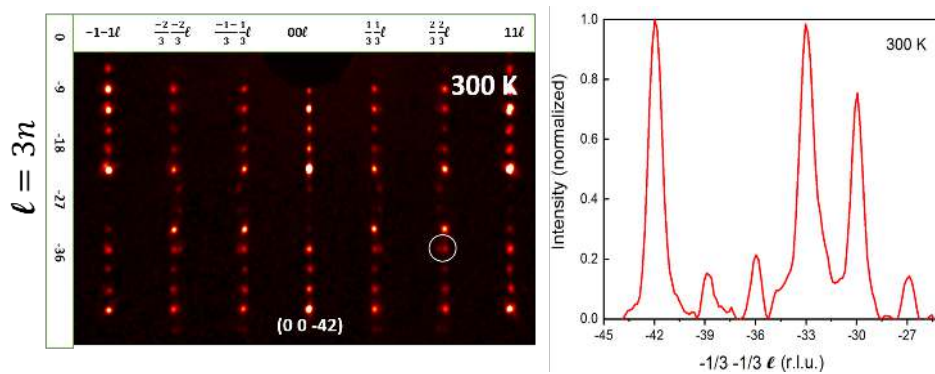


Figure 5.17: Precession image of the hhl reciprocal space plane of S1 $\text{Lu}_3\text{Fe}_4\text{O}_{10}$ grown with a $\text{CO}_2/\text{CO}=85$ measured at Supernova at RT. The integrated intensity in region perpendicular to the (hhl) for the corresponding temperatures are shown on the right side. Data was treated with line background subtraction.

5.3 Commensurate and incommensurate charge ordering in $\text{Lu}_3\text{Fe}_4\text{O}_{10}$

As discussed in Sec. 3.5.2, at room temperature for the first time sufficiently stoichiometric $\text{Lu}_3\text{Fe}_4\text{O}_{10}$ crystals exhibit CO types very similar to those realized in $\text{Lu}_2\text{Fe}_3\text{O}_7$, both commensurate and incommensurate. The incommensurate CO reflections are shown in Figure 5.16a. The superstructure reflections can be indexed with the incommensurate propagation vector $(\frac{1}{3} - \delta, \frac{1}{3} - \delta, 0)$ and symmetry-equivalent, with values of δ up to 0.019, (Fig. 5.16a, $\delta = 0.012$). The incommensuration δ is smaller than in $\text{Lu}_2\text{Fe}_3\text{O}_7$ and LuFe_2O_4 [35]. The intensity integrated in hh -direction around $hh=2/3$ vs l and the line profile along $(\frac{2}{3}, \frac{2}{3}, l)$ are also shown in Fig. 5.16b.

The commensurate CO ($\delta = 0$ within experimental resolution) at room temperature measured at the Supernova diffractometer is shown in Figure 5.17 with the intensity integrated in

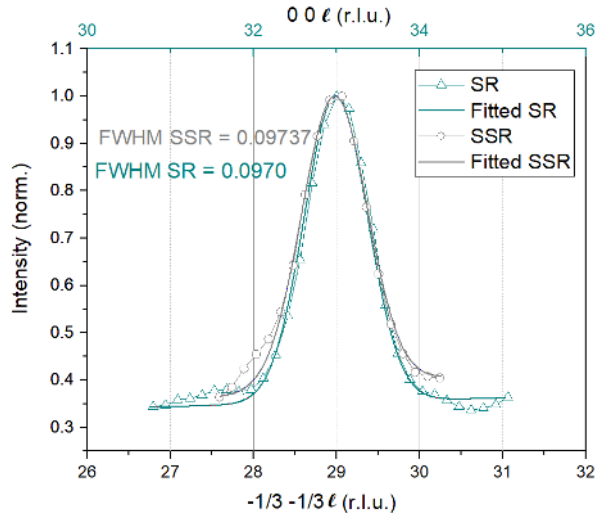


Figure 5.18: Intensity integrated perpendicular to l of: (0 0 33) structural reflection (SR), fitted SR intensity and super structural reflection (SSR) ($\frac{-1}{3} \frac{-1}{3} 29$) out of plane at room temperature. SSR and SR were fitted with a Lorentzian and Gaussian profiles respectively and linear background fitting for both. Full widths at half maximum (FWHM) are given in Angstrom units.

hh-direction vs l . However, a minor fraction of the sample exhibits incommensurate superstructural reflections, this explains the splitting that can be seen for example for the encircled reflection ($I_{\text{co}}/I_{\text{inco}} \sim 1.2$). The superstructure reflections are indexed with $(\frac{1}{3} \frac{1}{3} 0)$ propagation (the superstructural reflections are at integer l positions), and symmetry equivalents suggesting a $\sqrt{3} \times \sqrt{3} \times 1$ CO cell identical to $\text{Lu}_2\text{Fe}_3\text{O}_7$, but in contrast to LuFe_2O_4 [36].

Comparing with $\text{Lu}_2\text{Fe}_3\text{O}_7$, the commensurate CO in $\text{Lu}_3\text{Fe}_4\text{O}_{10}$ exhibits well-separated superstructure reflections despite of the larger c -axis in the unit-cell. This is due to the $-h + k + l = 3n$ reflection condition (no obverse/reverse twinning was observed for this sample). Moreover, as the superstructural peaks are at $l = 3n$ only, this indicates that it is a mono-domain sample, meaning the superstructural reflections are obtained by $s + (\frac{1}{3} \frac{1}{3} 0)$, with s being an allowed structural reflection and none by $s + (\frac{2}{3}, \frac{1}{3}, 0)$ or $s + (\frac{1}{3}, \frac{2}{3}, 0)$.

The out-of-plane correlation length for $\text{Lu}_3\text{Fe}_4\text{O}_{10}$ at RT is calculated in the same manner as for $\text{Lu}_2\text{Fe}_3\text{O}_7$ in Fig. 5.3, the estimated out-of-plane correlation length of 49 Å (less than one unit cell) for the incommensurate and 5405 Å (90 unit cells) for the commensurate CO, which is larger than in $\text{Lu}_2\text{Fe}_3\text{O}_7$, but also LuFe_2O_4 (75 Å [52]) and YFe_2O_4 (550 Å [60]). See Fig. 5.18 which shows the comparison of SR and SSR for the commensurate CO presented in Fig. 5.17. However, the width of the SR is very close to the width of the SSR, which necessarily leads to a very large uncertainty in the extracted correlation length.

5.3.1 $\text{Lu}_3\text{Fe}_4\text{O}_{10}$ representation analysis

The symmetry analysis with the use of the Isodistort software [143, 144] was performed as previously done in Sec. 5.2.2 for $\text{Lu}_2\text{Fe}_3\text{O}_7$, but this time starting from the rhombohedral $R\bar{3}m$ parent structure. After screening many crystals for their domain population, a mono-

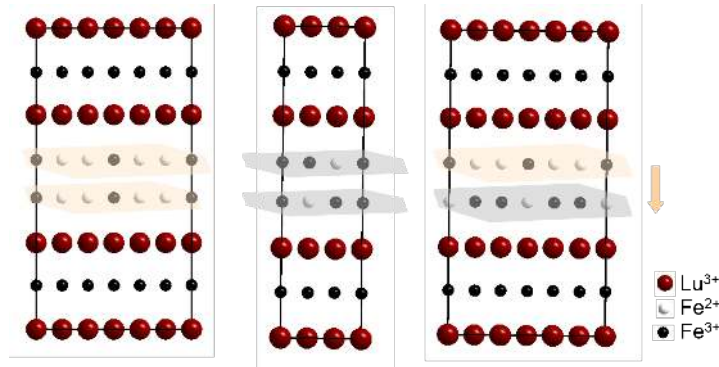


Figure 5.19: $C2/m$, $P\bar{1}$ and Cm structural representations respectively. Shown is only one bilayer, the other two are exactly the same due to $(\frac{1}{3}\frac{1}{3}0)$ propagation. The layers are highlighted according to Fe-charge majority: gray for layer rich in Fe^{3+} and orange rich in Fe^{2+} . The arrows indicated the bilayer polarization direction.

Order parameter	SG	Basis	Origin	Remarks
$\Sigma 1 (a,0;0,0;0,0)$	$C2/m$	$(-2,-1,0),(0,-3,0),(2/3,1/3,1/3)$	$(0,0,0)$	overall charged
$\Sigma 1 (a,b;0,0;0,0)$	$C2$	$(-2,-1,0),(0,-3,0),(2/3,1/3,1/3)$	$(0,0,0)$	overall charged
$\Sigma 2 (0,a;0,0;0,0)$	Cm	$(-2,-1,0),(0,-3,0),(2/3,1/3,1/3)$	$(0,0,0)$	polar
$\Sigma 2 (a,0;0,0;0,0)$	$P\bar{1}$	$(-2,-1,0),(-1,1,0),(-2/3,-1/3,-1/3)$	$(0,0,0)$	overall charged
$\Sigma 2 (a,b;0,0;0,0)$	$P1$	$(-2,-1,0),(-1,1,0),(-2/3,-1/3,-1/3)$	$(0,0,0)$	polar

Table 5.13: Structure solution for $\Sigma 1$ and $\Sigma 2$ -modes based on $(\frac{1}{3}\frac{1}{3}0)$ propagation from the ISODISTORT software [143, 144]. SG: space group. All the structures with polar bilayers are highlighted with green color.

domain sample was found as shown before in Sec. 5.3. The availability of this mono-domain sample reduces the possibilities as the three-fold rotation is clearly broken, therefore any space group with such symmetry element was not considered. A single propagation vector at the $\Sigma (a,a,0)$ point with $a=1/3$ provides various solutions that are summarized in Table. 5.13. Similar to $\text{Lu}_2\text{Fe}_3\text{O}_7$, all the solutions were obtained with a single mode either $\Sigma 1$ or $\Sigma 2$, and the combination of these two modes does not result in any new symmetries in contrast to YbFe_2O_4 [35]. The only feasible symmetries are Cm and $P1$, the rest are overall charged structures, which are not acceptable physically. See Fig. 5.19, in which $C2/m$ (left) for example is $2+$ charged while $P\bar{1}$ is $3+$ charged. However, the CO realized in $P1$ symmetry has an actual symmetry of Cm i.e. a mirror is still preserved in $P1$, meaning the Cm is a unique solution. Interestingly, this has a polar bilayer with overall polar stacking as shown in right panel of Fig. 5.19.

5.3.2 $\text{Lu}_3\text{Fe}_4\text{O}_{10}$ average structure at room temperature

The average crystal structure at room temperature for a $\text{Lu}_3\text{Fe}_4\text{O}_{10}$ crystal exhibiting an incommensurate CO was determined using MoK_α single crystal X-ray diffraction for the first

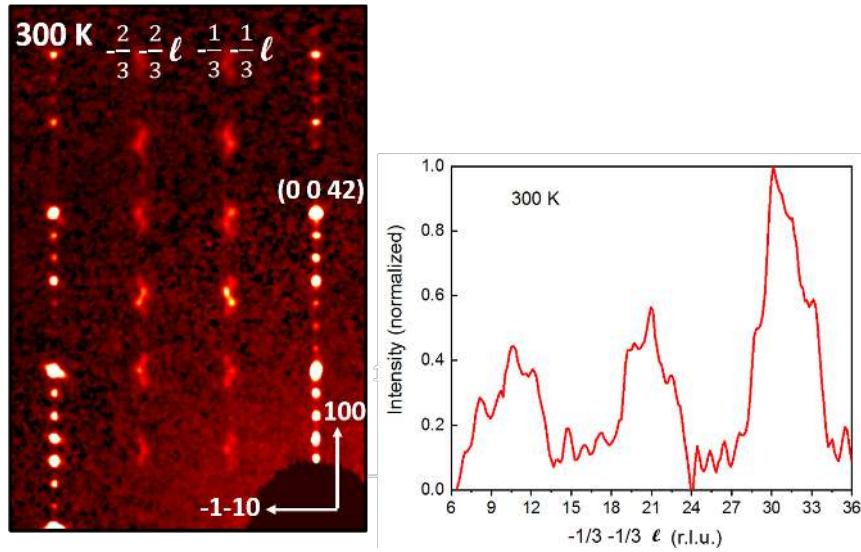


Figure 5.20: Left: Precession hhl plane of $\text{Lu}_3\text{Fe}_4\text{O}_{10}$ at 300 K. Right: 1-D line profile in hh -direction with 1 pixel. Data treated with linear background subtraction.

time. The average structure is not the same as the basic structure as seen for $\text{Lu}_2\text{Fe}_3\text{O}_7$ in Sec. 5.2.3, however, it still approximates the the ideal structure without CO.

The only X-ray refinement attempt for $\text{Lu}_3\text{Fe}_4\text{O}_{10}$ was reported in [62], which turned out to be unsuccessful due to the poor crystallization (the best R value was 0.27).

The lattice of $\text{Lu}_3\text{Fe}_4\text{O}_{10}$ was correctly identified by CrysAlice Software, as being rhombohedral as found in [61, 63] by powder X-ray diffraction. A precession image of the hhl plane is shown in the left panel of Fig. 5.20, besides the fundamental reflections referring to the $R\bar{3}m$ rhombohedral structure, weak incommensurate superstructure reflections with zigzag diffuse scattering along the $(\frac{1}{3} \frac{1}{3} \ell)$ can be observed. A line-profile in ℓ -direction for the $\frac{1}{3} \frac{1}{3} \ell$ is shown in the right panel of Fig. 5.20. The refinement of the average structure (c.f. Sec. 5.2.3) was done using Jana 2006 neglecting the super structural reflections for a data set of 3857 frames covering the full sphere with 66993 reflections merged into 1859 unique reflections with a high redundancy value of 36 allowing the application of empirical absorption correction with absorption coefficient of 41.517 mm^{-1} . A common twinning for rhombohedral space groups is so-called obverse/reverse twinning, in which a twofold axis parallel to the threefold axis constitutes the twin law described with the following matrix [153]:

Parameter	value
Spacegroup	$R\bar{3}m$
a (\AA)	3.4699
c (\AA)	60.6272(2)
V (\AA^3)	632.17(0)
R_{int}	7.95/9.28
$R_{\text{obs}}/wR_{\text{obs}}^2$	12.04/23.53
$R_{\text{all}}/wR_{\text{all}}^2$	15.32/24.29
$\text{GOF}_{\text{obs}}/\text{GOF}_{\text{all}}$	4.01/3.09
Num. of Reflections	642/1127
Num. of Parameters	37
ρ_{calc} (g/cm^3)	7.158

Table 5.14: Refinement parameters in $R\bar{3}m$ at 300 K

$$\mathbf{T}_{\text{obv/rev}} = \begin{pmatrix} -1 & 0 & 0 \\ 0 & -1 & 0 \\ 0 & 0 & 1 \end{pmatrix} \quad (5.18)$$

Considering the obverse reverse twinning, leads to a volume fraction of 0.062 for the second twin (i.e. essentially negligible). No extinction was applied, (otherwise a negative extinction would emerge). Table 5.14 summaries the refinement parameters at 300 K with the structure depicted in Fig. 5.21. The refinement R-values are high and the agreement factors are far from the ideal value of one. These values are however still better than in [62]. Moreover, in contrast to the refined $P6_3/mmc$ in $\text{Lu}_2\text{Fe}_3\text{O}_7$, for a comparable R_{int} value, the $\text{Lu}_3\text{Fe}_4\text{O}_{10}$ residuals are a bit better. Similar to $\text{Lu}_2\text{Fe}_3\text{O}_7$, an effect of the CO was seen in $\text{Lu}_3\text{Fe}_4\text{O}_{10}$ by the elongation of the Lu thermal ellipsoid along c-direction with unreasonable ADPs. Therefore, a splitting was performed for both Lu1 and Lu2 positions. This splitting change the special position of Lu1 (3a) to (6c). The observed refined occupancies of split Lu2 positions is $\sim 2:1$ similar to $\text{Lu}_2\text{Fe}_3\text{O}_7$ (see Sec. 5.2.3). Furthermore, two oxygen atom position (O1,O2) show unreasonable ADPs. The O1 position is splitted as it shows elongation in one direction. But it was difficult for O2, due to the elongation in more than one direction. It is not surprising that the residuals are high as the atoms are not reproduced correctly.

The coordinates, occupancies and ADPs of the refined atoms with Lu-position splitting are shown in table 5.15. Only the independent ADPs (U_{11} and U_{33}) are shown, the rest are restricted by the rhombohedral symmetry as follows: $U_{22}=U_{11}$, $U_{12}=1/2 U_{11}$, $U_{13}=0$, $U_{23}=0$. All the atoms are refined anisotropically. The $R\bar{3}m$ structure can not describe the fundamental structure due to the distortion by the CO and lower symmetry is needed. This is the first confirmation of the basic crystal structure of $\text{Lu}_3\text{Fe}_4\text{O}_{10}$ from a refinement. The refinement in lower symmetries necessarily requires a much larger set of reflections, moreover, $\text{Lu}_3\text{Fe}_4\text{O}_{10}$ has a larger cell than in $\text{Lu}_2\text{Fe}_3\text{O}_7$ enforcing having more parameters with more chance of correlations and double the number of twins exists due the obv/rev twinning. Therefore, the refinement in lower symmetries as was done for

Site	ai	z	U11	U33
Lu ₁ (6c)	0.5	0.00367(3)	0.0198(3)	0.0254(10)
Lu ₂ (6c)	0.64(2)	0.09296(12)	0.0208(4)	0.0299(19)
Lu ₂ ' (6c)	0.36(2)	0.1009(2)	0.0219(8)	0.029(3)
Fe ₁ (6c)	1	0.381523(51)	0.0240(7)	0.0234(11)
Fe ₂ (6c)	1	0.812827(68)	0.0289(9)	0.0357(17)
O ₁ (6c)	0.6(3)	0.9476(17)	0.049(18)	0.02(2)
O ₁ ' (6c)	0.4(3)	0.9545(18)	0.018(10)	0.02(3)
O ₂ (6c)	1	0.151(08)	0.087(16)	0.08(3)
O ₃ (6c)	1	0.78027(34)	0.037(6)	0.032(8)
O ₄ (6c)	1	0.41393(31)	0.038(5)	0.025(7)
O ₅ (6c)	1	0.34983(30)	0.037(5)	0.025(7)

Table 5.15: Atomic positions and thermal displacement parameters of the refined 300 K structure refined in $R\bar{3}m$. The wyckoff positions are shown in the standard setting 6c: (0,0,z)

$\text{Lu}_2\text{Fe}_3\text{O}_7$ is not shown. However, an attempt to refine the average structure in $C2/m$ symmetry was done though not completed but with splitted Lu and refined occupancies, a clear improvement in the refinement parameters is observed in particular $GOF_{\text{obs}}/GOF_{\text{all}}$ values, see Table A.7. Moreover, no refinement including the superstructure reflections were done, the reason of course encounters the much more number of reflections, parameters, correlations

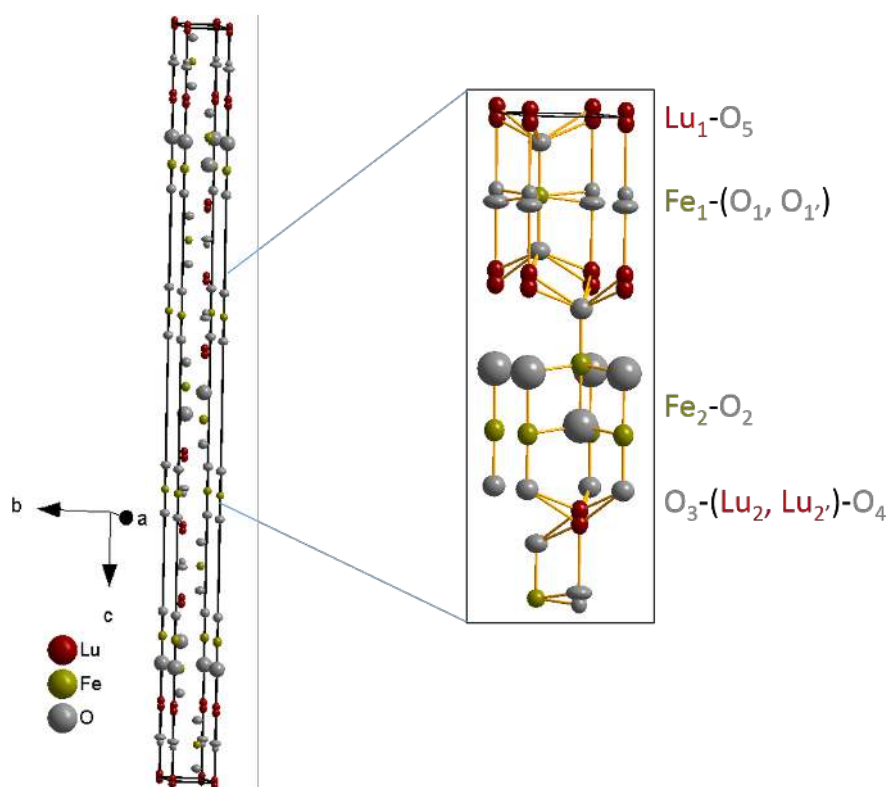


Figure 5.21: The $R\bar{3}m$ crystal structure at 300 K. The basic block of the unit cell is magnified consists of 3 layers of Lu/O, one Fe/O bilayer and two Fe/O single layers. The atoms are presented with their refined thermal anisotropic displacement parameters.

and twinning (even more complex than for the average structure) but also the very close superstructure reflections which makes the integration process for the refinement difficult and requires collecting the data at better resolution diffractometer at the synchrotron as was done for the $\text{Lu}_2\text{Fe}_3\text{O}_7$ (see Sec. 5.2.1).

5.4 Discussion

When we refined the average structure of $\text{Lu}_2\text{Fe}_3\text{O}_7$ in Sec. 5.2.3, large anisotropic displacement parameters for Lu atoms were observed, a problem that was remedied by the splitting of the Lu positions, with occupations refined to roughly 2:1, similar to what was observed in the non-intercalated LuFe_2O_4 [11] and YbFe_2O_4 [35]. The splitting in the average structure likely corresponds to a Lu positional modulation in the c_{hex} direction in the superstructure with 2 Lu-atoms sitting on site 1 and one Lu-atom on site 2 as discussed previously in Sec. 5.2.3. The split Lu position in the refinement of the superstructure implies a superposition of different CO which is basically the closest Fe-valances in the bilayer, as shown for example in Fig. 5.14, for the (Lu-Fe) surrounded by ellipsoid shape and discussed in Sec. 5.2.4. Such a superposition is involved in the twin domains, however, this superposition does not show up in splits when the refinement is done taking into account the twinning as was the case for refinements discussed within this thesis. Therefore, when refining the full superstructure in the large cell and including all reflections, one expects that like in YbFe_2O_4 [35], no Lu-position splitting remains.

The fact that splitting is still present in the refinement of the superstructures in $\text{Lu}_2\text{Fe}_3\text{O}_7$

taking into account twinning, implies that the CO configurations that are necessarily superimposed are therefore not related by a $P6_3/mmc$ symmetry element. Because all variants of a space group established through a structural transition are connected by lost symmetry elements (twin laws), this implies that there are superimposed CO configurations with *different* symmetries, i.e. different space groups (e.g. for $\text{Lu}_2\text{Fe}_3\text{O}_7$ one with $Cmc2_1$ symmetry and one with some subgroup of this such as e.g. Cm or Cc). This situation refers to the presence of polytypes, which is a subset of polymorphs [154]. Therefore, obviously one should refine the superstructure as polymorphs, which in principle can be done in Jana 2006 in which one first has to identify the space group candidates and then one could do a multi-phase refinement (each phase with its own twin laws). Very few examples of such polytype refinement exists, e.g. [155, 156] and in the present case it is a practically tough refinement due to the large number of atoms and twins and it is beyond the scope of this thesis. However, such polymorphism while yet to be elucidated in details, is firmly established as present in $\text{Lu}_2\text{Fe}_3\text{O}_7$.

One of the questions now is what leads such polymorphs to be established in $\text{Lu}_2\text{Fe}_3\text{O}_7$, but not in LuFe_2O_4 ? The insertion of the LuFeO_3 block consisting of Lu/O and Fe/O single layers between the Fe-bilayers upon intercalation unavoidably modifies the coupling between different bilayers to be weaker compared to in LuFe_2O_4 (see Sec. 1.3 explaining the relevant interactions for the establishment of full 3D CO), which increases not only the chance of no correlations (which would lead to diffuse lines), but also the chance of different relationships between bilayers (corresponding to different overall symmetry) of almost the same energy and thus the emergence of polytypes. The establishment of polymorph is quite common in layered structures [157, 158]. It is very likely that at least one of the present phases is polar, probably $Cmc2_1$, if the second present phase is a subgroup of the $Cmc2_1$ i.e. $P2_1$, Pm , Cm , Cc , $P1$, then the overall compound would be polar or anti-polar (See table.5.3). However, if one of the polytypes is indeed $Cmc2_1$ which is a polar structure due to the presence of c-glide and 2_1 screw a-axis, then the polytypes keeping either c-glide or 2_1 screw a-axis likely would also be polar.

Regarding $\text{Lu}_3\text{Fe}_4\text{O}_{10}$, the basic structure was experimentally verified by the average structure, however, the refinement of the superstructure requires collecting data at the synchrotron for better peaks separation and easier integration. $\text{Lu}_3\text{Fe}_4\text{O}_{10}$ basic structure has $R\bar{3}m$ symmetry as LuFe_2O_4 , with only one bilayer in the primitive cell in contrast to two in $\text{Lu}_2\text{Fe}_3\text{O}_7$. Furthermore, the $(\frac{1}{3}\frac{1}{3}0)$ -propagation rather than the $(\frac{1}{3}\frac{1}{3}\frac{3}{2})$ in LuFe_2O_4 implies that there is only one bilayer in the super cell as well. Therefore, any bimodel CO (2+, 3+ only) and excluding the overall charged asymmetries must have a polar CO. Each of the two layers in the bilayer has 3 Fe sites in the primitive cell of super cell: 2 should have one of the valances and one with opposite valance. This strongly indicates that, despite of the lack of a definitive refinement of the superstructure, the CO in $\text{Lu}_3\text{Fe}_4\text{O}_{10}$ is, like the one in $\text{Lu}_2\text{Fe}_3\text{O}_7$, indeed polar, validating the intercalation approach to producing ferroelectricity the CO in rare earth ferrites.

6

Summary and outlook

The research presented in this thesis is mainly devoted to uncover the charge order structure in $\text{Lu}_2\text{Fe}_3\text{O}_7$. The first tricky and difficult business was to successfully grow the layered $\text{Lu}_2\text{Fe}_3\text{O}_7$ single crystals, which was reported only once in the history of the intercalated compounds [74] due to the very complex structure. The second was to find the optimal conditions that produces a stoichiometric crystal to intrinsically establish long-range charge order and spin order as was done for the non-intercalated compounds [11, 35, 57]. With the floating zone method using the flow of different CO_2 : CO, distinct crystals in terms of oxygen stoichiometry are grown. Moreover, single crystals of $\text{Lu}_3\text{Fe}_4\text{O}_{10}$ were obtained for free due to small free energy difference between the intercalation layers. Getting the desired crystals was a very important part, which made all the analyses performed in this thesis possible.

A detailed analysis for the magnetic behaviour of the most stoichiometric $\text{Lu}_2\text{Fe}_3\text{O}_7$ crystal was presented in chapter 4 with a comparison to non-intercalated LuFe_2O_4 , furthermore, the magnetic phase diagram of this type is established. Macroscopic magnetization measurements performed on the stoichiometric crystal showed no sharp magnetic behavior, suggested a reduced magnetic correlations and the absence of an antiferromagnetic phase observed in LuFe_2O_4 . The main obtained results are: similar spin order in the bilayer as observed in LuFe_2O_4 with indications in the all measured techniques: In the macroscopic magnetization measurement, a comparable net magnetic moment to the saturation moment of the only contained bilayer LuFe_2O_4 is observed. In the polarized neutron scattering, the $\frac{1}{3} \frac{1}{3}$ in-plane propagation is observed and even more important is the similar shape of the XMCD signal with net magnetic moment of the Fe^{2+} approximately the same as LuFe_2O_4 , however, less well ordered. Furthermore, a spin-charge coupling was revealed by the XMCD measurements. In the single layers the magnetic moment is likely induced by the application of the magnetic field, paramagnetic-like in the first approximation. No stoichiometric large crystals of $\text{Lu}_2\text{Fe}_3\text{O}_7$ were obtained due to the complex crystal structure. Polarized neutron scattering performed on large crystals, exhibited a diffuse magnetic character suggested correlations that are limited to ab-plane in the bilayers which is still randomly stacked. This is supported by the frequency dependence observed in the ac-measurements. A 3D CO was observed but not 3D spin order (SO) in a $\text{Lu}_2\text{Fe}_3\text{O}_7$ crystal indicates that the SO is more fragile with respect to oxygen off-stoichiometry.

For $\text{Lu}_2\text{Fe}_3\text{O}_7$, of many analyzed crystals by in-house X-ray diffraction at room temperature, three types of CO in distinct types of crystals are observed as an influence of oxygen stoichiometry: i) diffuse scattering with 2D correlations, ii) incommensurate superstructure reflections indicating 3D CO, and for the first time iii) commensurate 3D CO. At room temperature, the indexation of the apparently commensurate CO with the propagation $(\frac{1}{3}\frac{1}{3}0)$, with the help of representation analysis leads to possible CO configurations similar as for LuFe_2O_4 : either charged bilayers with overall charge in Cmcm symmetry or no overall charge in C2/m symmetry or polar bilayers stacked with the same or alternating out-of-plane polarization, in Cmc2_1 or Amm2 , symmetry respectively. The latter has an in-plane net polarization. To determine the CO crystallographic structure, refinements were done using the data collected by single crystal X-ray diffraction and to determine the realized CO configuration, bond-valance-sum analysis was used. At first, the refinement of the average structure that is limited to the structural reflections and disregarding the modulation at 100 K manifests an expected symptom of the CO, i.e. the vertical elongation of the thermal ellipsoids of Lu as indication of the displacement due to CO and therefore, a splitting of Lu position following a similar occupational trend observed in LuFe_2O_4 for the average structure i.e. 1:2 and these seem to result from the positional modulation of Lu that accompanies the CO. However, the refinement of the superstructure still shows the elongation/split of Lu in all tested symmetries, with the best achievable refinement parameters in the polar Cmc2_1 symmetry. The refinement of likely Cmc2_1 with no origin shift showed an incomplete CO in the bilayer with $\sim 8 \text{Fe}^{2.5+}$ at the majority site (8b), 3 Fe^{2+} and 3 Fe^{2+} (Fe^{2+} and Fe^{3+} at the minority site 4a). This is not surprising as Lu splitting is required in the superstructure revealing the formation of structural polytypes hampering a full CO pattern. However, $\text{Lu}_2\text{Fe}_3\text{O}_7$ is very likely polar.

For $\text{Lu}_3\text{Fe}_4\text{O}_{10}$, similar types of CO as those in $\text{Lu}_2\text{Fe}_3\text{O}_7$ are observed in different crystals. The magnetic characterization shows somewhat enhanced correlations with similar behaviour to the non-intercalated LuFe_2O_4 : indications for a first order meta-magnetic phase transition are observed. From the XMCD measurements, an indication of similarity in the spin order in the bilayer was extracted. However, the information about the Fe-spin ordering in the bilayers and the single layers are limited. However, a similar phase diagram is expected to the LuFe_2O_4 . The refinement of the average structure in $\text{Lu}_3\text{Fe}_4\text{O}_{10}$ is achieved for the first time in rhombohedral $\text{R}\bar{3}\text{m}$ with similar indications for the CO effect as in $\text{Lu}_2\text{Fe}_3\text{O}_7$. The indexation of the commensurate superstructure reflections with the $(\frac{1}{3}\frac{1}{3}0)$ -propagation provided one solution that is polar Cm .

In summary, our results indicate strongly that both compounds are polar, validating the intercalation approach to producing ferroelectricity from CO in the rare earth ferrites as discussed in Sec. 1.3. We have recently performed pizoresponse force microscopy (PFM) on these compounds, and the preliminary observations indicated that $\text{Lu}_2\text{Fe}_3\text{O}_7$ is very likely to be ferroelectric with out-of-plane polarization direction consistent with Cmc2_1 symmetry being one of the phases and most likely the second (or more) phase/s will also be polar making a strong ferroelectric character for this material is likely. While there is no definitive conclusion in term of the refined CO structure, our results support the intercalation idea for achieving ferroelectricity by CO in the rare earth ferrites, adding another example to the magnetite that

this mechanism works. Therefore, it might be worthwhile to continue the research in this direction.

Bibliography

- [1] J. Bardeen, L. N. Cooper, and J. R. Schrieffer, "Theory of superconductivity", *Phys. Rev.* **108**, 1175 (1957) (cited on page 1).
- [2] M.-H. Phan and S.-C. Yu, "Review of the magnetocaloric effect in manganite materials", *J. Magn. Magn. Mater.* **308**, 325 (2007) (cited on page 1).
- [3] J. Volger, "Further experimental investigations on some ferromagnetic oxidic compounds of manganese with perovskite structure", *Physica* **20**, 49 (1954) (cited on page 1).
- [4] A. Haghiri-Gosnet and J. Renard, "CMR manganites: physics, thin films and devices", *J. Phys. D: Appl. Phys.* **36**, R127 (2003) (cited on page 1).
- [5] A. Ramirez, "Colossal magnetoresistance", *J. Phys.: Condens. Matter* **9**, 8171 (1997) (cited on page 1).
- [6] G. Barrera, J. Bruno, T. Barron, and N. Allan, "Negative thermal expansion", *J. Phys.: Condens. Matter* **17**, R217 (2005) (cited on page 1).
- [7] E. Verwey, "Electronic conduction of magnetite (Fe_3O_4) and its transition point at low temperatures", *Nature* **144**, 327 (1939) (cited on page 1).
- [8] W. Eerenstein, N. Mathur, and J. F. Scott, "Multiferroic and magnetoelectric materials", *Nature* **442**, 759 (2006) (cited on page 1).
- [9] M. Fiebig, "Revival of the magnetoelectric effect", *J. Phys. D: Appl. Phys.* **38**, R123 (2005) (cited on pages 1, 2).
- [10] M. Fiebig and N. A. Spaldin, "Current trends of the magnetoelectric effect", *Eur. Phys. J. B* **71**, 293 (2009) (cited on page 1).
- [11] J. de Groot, "Charge, spin and orbital order in the candidate multiferroic material LuFe_2O_4 ", PhD thesis (RWTH Aachen, 2012) (cited on pages 2, 5–7, 16, 25, 29, 34, 36, 39, 42, 44, 45, 47–49, 53–62, 66, 68, 69, 72, 78, 79, 82, 87–89, 97, 98, 105, 107).
- [12] C. Ederer and N. Spaldin, "Magnetoelectrics - A new route to magnetic ferroelectrics", *Nat. Mater.* **3**, 849 (2004) (cited on page 1).
- [13] M. Bibes and A. Barthelemy, "Multiferroics: Towards a magnetoelectric memory", *Nat. Mater.* **7**, 425 (2008) (cited on page 1).
- [14] N. A. Hill, "Why are there so few magnetic ferroelectrics?", *J. Phys. Chem. B* **104**, 6694 (2000) (cited on page 1).
- [15] R. N. P. Choudhary and S. K. Patri, "Multiferroics: An Introduction", in *AIP Conf. Proc.* Vol. 1063, edited by S. M. Bose, S. N. Behera, and B. K. Roul, 1 (2008), p. 263 (cited on page 1).
- [16] Y. Noda, Y. Fukuda, H. Kimura, I. Kagomiya, S. Matumoto, K. Kohn, T. Shobu, and N. Ikeda, "Review and prospect of ferroelectricity and magnetism in YMn_2O_5 ", *J. Korean Phys. Soc.* **42**, S1192 (2003) (cited on page 2).
- [17] S.-W. Cheong and M. Mostovoy, "Multiferroics: a magnetic twist for ferroelectricity", *Nat. Mater.* **6**, 13 (2007) (cited on page 2).

- [18] I. Dzyaloshinsky, "A thermodynamic theory of weak ferromagnetism of antiferromagnetics", *J. Phys. Chem. Solids* **4**, 241 (1958) (cited on page 2).
- [19] B. B. Van Aken, T. T. Palstra, A. Filippetti, and N. A. Spaldin, "The origin of ferroelectricity in magnetoelectric YMnO_3 ", *Nat. Mater.* **3**, 164 (2004) (cited on page 2).
- [20] C. J. Fennie and K. M. Rabe, "Ferroelectric transition in YMnO_3 from first principles", *Phys. Rev. B* **72**, 100103 (2005) (cited on page 2).
- [21] M. Angst, "Ferroelectricity from iron valence ordering in rare earth ferrites?", *Phys. Status Solidi RRL* **7**, 383 (2013) (cited on pages 3, 4, 8, 12, 13, 41, 42, 67, 70, 73, 74, 82).
- [22] M. S. Senn, J. P. Wright, and J. P. Attfield, "Charge order and three-site distortions in the Verwey structure of magnetite", *Nature* **481**, 173 (2012) (cited on page 3).
- [23] F. Schrettle, S. Krohns, P. Lunkenheimer, V. Brabers, and A. Loidl, "Relaxor ferroelectricity and the freezing of short-range polar order in magnetite", *Phys. Rev. B* **83**, 195109 (2011) (cited on page 3).
- [24] M. Angst, S. Adiga, S. Gorfman, M. Ziolkowski, J. Stempfer, C. Grams, M. Pietsch, and J. Hemberger, "Intrinsic ferroelectricity in charge-ordered magnetite", *Crystals* **9**, 546 (2019) (cited on page 3).
- [25] N. Ikeda, H. Ohsumi, K. Ohwada, K. Ishii, T. Inami, K. Kakurai, Y. Murakami, K. Yoshii, S. Mori, Y. Horibe, and H. Kito, "Ferroelectricity from iron valence ordering in the charge-frustrated system LuFe_2O_4 ", *Nature* **436**, 1136 (2005) (cited on pages 3–5).
- [26] N. Ikeda, K. Kohn, N. Myouga, E. Takahashi, H. Kitôh, and S. Takekawa, "Charge Frustration and Dielectric Dispersion in LuFe_2O_4 ", *J. Phys. Soc. Jpn.* **69**, 1526 (2000) (cited on page 3).
- [27] A. M. Mulders, S. M. Lawrence, U. Staub, M. Garcia-Fernandez, V. Scagnoli, C. Mazzoli, E. Pomjakushina, K. Conder, and Y. Wang, "Direct Observation of Charge Order and an Orbital Glass State in Multiferroic LuFe_2O_4 ", *Phys. Rev. Lett.* **103**, 077602 (2009) (cited on page 4).
- [28] N. Ikeda, Y. Yamada, S. Nohdo, T. Inami, and S. Katano, "Incommensurate charge ordering in mixed valence system LuFe_2O_4 ", *Physica B* **241**, 820 (1997) (cited on page 4).
- [29] Y. Yamada, S. Nohdo, and N. Ikeda, "Incommensurate charge ordering in charge-frustrated LuFe_2O_4 system", *J. Phys. Soc. Jpn.* **66**, 3733 (1997) (cited on pages 4, 75).
- [30] Y. Yamada, K. Kitsuda, S. Nohdo, and N. Ikeda, "Charge and spin ordering process in the mixed-valence system LuFe_2O_4 : Charge ordering", *Phys. Rev. B* **62**, 12167 (2000) (cited on pages 4, 8).
- [31] M. Angst, R. P. Hermann, A. D. Christianson, M. D. Lumsden, C. Lee, M. -. H. Whangbo, J. -. W. Kim, P. J. Ryan, S. E. Nagler, W. Tian, R. Jin, B. C. Sales, and D. Mandrus, "Charge Order in LuFe_2O_4 : Antiferroelectric Ground State and Coupling to Magnetism", *Phys. Rev. Lett.* **101**, 227601 (2008) (cited on pages 4–6, 75, 76, 80).
- [32] M. Tanaka, K. Siratori, and N. Kimizuka, "Mössbauer Study of RFe_2O_4 ", *J. Phys. Soc. Jpn.* **53**, 760 (1984) (cited on page 4).

- [33] K. T. Ko, H. J. Noh, J. Y. Kim, B. G. Park, J. H. Park, A. Tanaka, S. B. Kim, C. L. Zhang, and S. W. Cheong, "Electronic Origin of Giant Magnetic Anisotropy in Multiferroic LuFe_2O_4 ", *Phys. Rev. Lett.* **103**, 207202 (2009) (cited on pages 4, 6, 7, 36, 66, 70, 73).
- [34] X. S. Xu, M. Angst, T. V. Brinzari, R. P. Hermann, J. L. Musfeldt, A. D. Christianson, D. Mandrus, B. C. Sales, S. McGill, J. -. Kim, and Z. Islam, "Charge Order, Dynamics, and Magnetostructural Transition in Multiferroic LuFe_2O_4 ", *Phys. Rev. Lett.* **101**, 227602 (2008) (cited on pages 4, 7, 56).
- [35] H. Williamson, "Spin and Charge Order in the newly deemed antiferroelectric YbFe_2O_4 ", PhD thesis (RWTH Aachen university, 2019) (cited on pages 5–9, 13, 23, 25, 39, 41, 44, 49, 58, 59, 68, 73–80, 82, 87, 89, 97–100, 102, 105, 107).
- [36] J. de Groot, T. Mueller, R. A. Rosenberg, D. J. Keavney, Z. Islam, J.-W. Kim, and M. Angst, "Charge order in LuFe_2O_4 : an unlikely route to ferroelectricity", *Phys. Rev. Lett.* **108**, 187601 (2012) (cited on pages 5, 13, 23, 25, 66, 68, 69, 73, 74, 76, 77, 82, 88, 101).
- [37] D. Niermann, F. Waschkowski, J. de Groot, M. Angst, and J. Hemberger, "Dielectric properties of charge-ordered LuFe_2O_4 revisited: the apparent influence of contacts", English, *Phys. Rev. Lett.* **109**, 016405 (2012) (cited on pages 6, 12).
- [38] A. Ruff, S. Krohns, F. Schrettle, V. Tsurkan, P. Lunkenheimer, and A. Loidl, "Absence of polar order in LuFe_2O_4 ", *Eur. Phys. J. B* **85**, 290 (2012) (cited on pages 6, 12, 13).
- [39] S. Lafuerza, J. Garcia, G. Subias, J. Blasco, K. Conder, and E. Pomjakushina, "Intrinsic electrical properties of LuFe_2O_4 ", *Phys. Rev. B* **88**, 085130 (2013) (cited on pages 6, 12).
- [40] T. Nagata and N. Ikeda, "Modulation in charge ordering structure of ferroelectric YbFe_2O_4 by magnetic ordering", *AIP Adv.* **8**, 075312 (2018) (cited on pages 6, 49, 77).
- [41] I. Shindo, N. Kimizuka, and S. Kimura, "Growth of YFe_2O_4 single crystals by floating zone method", *Mater. Res. Bull.* **11**, 637 (1976) (cited on pages 6, 16).
- [42] T. Sekine and T. Katsura, "Phase equilibria in the system $\text{Fe}-\text{Fe}_2\text{O}_3-\text{Lu}_2\text{O}_3$ at 1200 °C", *J. Solid State Chem.* **17**, 49 (1976) (cited on pages 6, 9–11, 15, 40, 43).
- [43] A. D. Christianson, M. D. Lumsden, M. Angst, Z. Yamani, W. Tian, R. Jin, E. A. Payzant, S. E. Nagler, B. C. Sales, and D. Mandrus, "Three-Dimensional Magnetic Correlations in Multiferroic LuFe_2O_4 ", *Phys. Rev. Lett.* **100**, 107601 (2008) (cited on pages 6, 7, 16, 63, 72).
- [44] K. Kuepper, M. Raekers, C. Taubitz, M. Prinz, C. Derks, M. Neumann, A. V. Postnikov, F. M. F. de Groot, C. Piamonteze, D. Prabhakaran, and S. J. Blundell, "Charge order, enhanced orbital moment, and absence of magnetic frustration in layered multiferroic LuFe_2O_4 ", *Phys. Rev. B* **80**, 220409 (2009) (cited on pages 6, 7, 13, 36, 68, 73).
- [45] J. Iida, M. Tanaka, Y. Nakagawa, S. Funahashi, N. Kimizuka, and S. Takekawa, "Magnetization and spin correlation of 2-dimensional triangular antiferromagnet LuFe_2O_4 ", *J. Phys. Soc. Jpn.* **62**, 1723 (1993) (cited on pages 7, 13, 41, 45, 52, 59, 72).

- [46] M. Tanaka, "Mössbauer study of RFe_2O_4 family: a two-dimensional antiferromagnet on a triangular lattice", *Nucl. Instrum. Methods Phys. Res., Sect. B* **76**, 149 (1993) (cited on pages 7, 11, 65, 97).
- [47] M. Phan, N. Frey, M. Angst, J. De Groot, B. C. Sales, D. Mandrus, and H. Srikanth, "Complex magnetic phases in $LuFe_2O_4$ ", *Solid State Commun.* **150**, 341 (2010) (cited on pages 7, 13, 52, 55–57, 59).
- [48] J. Iida, Y. Nakagawa, S. Takekawa, and N. Kimizuka, "High-field magnetization of single-crystal $LuFe_2O_4$ ", *J. Phys. Soc. Jpn.* **56**, 3746 (1987) (cited on page 7).
- [49] I. J., S. Nakagawa, G. Kido, Y. Nakagawa, S. Takekawa, and N. Kimizuka, "High-field magnetization of single-crystals YFe_2O_4 , $YbFe_2O_4$ and $LuFe_2O_4$ ", *Physica B* **155**, 307 (1989) (cited on page 7).
- [50] W. Wu, V. Kiryukhin, H.-J. Noh, K.-T. Ko, J.-H. Park, W. Ratcliff, P. A. Sharma, N. Harrison, Y. J. Choi, Y. Horibe, S. Lee, S. Park, H. T. Yi, C. L. Zhang, and S.-W. Cheong, "Formation of Pancakelike Ising Domains and Giant Magnetic Coercivity in Ferrimagnetic $LuFe_2O_4$ ", *Phys. Rev. Lett.* **101**, 137203 (2008) (cited on pages 7, 52, 55).
- [51] S. Park, Y. Horibe, Y. J. Choi, C. L. Zhang, S. -. W. Cheong, and W. Wu, "Pancakelike ising domains and charge-ordered superlattice domains in $LuFe_2O_4$ ", *Phys. Rev. B* **79**, 180401 (2009) (cited on pages 7, 11).
- [52] J. Wen, G. Xu, G. Gu, and S. M. Shapiro, "Magnetic-field control of charge structures in the magnetically disordered phase of multiferroic $LuFe_2O_4$ ", *Phys. Rev. B* **80**, 020403 (2009) (cited on pages 7, 78, 101).
- [53] J. de Groot, K. Marty, M. D. Lumsden, A. D. Christianson, S. E. Nagler, S. Adiga, W. J. H. Borghols, K. Schmalzl, Z. Yamani, S. R. Bland, R. de Souza, U. Staub, W. Schweika, Y. Su, and M. Angst, "Competing Ferri- and Antiferromagnetic Phases in Geometrically Frustrated $LuFe_2O_4$ ", *Phys. Rev. Lett.* **108**, 037206 (2012) (cited on pages 7, 40, 41, 44, 54, 72, 73).
- [54] P. Wang and H. Xiang, "Room-temperature ferrimagnet with frustrated antiferroelectricity: promising candidate toward multiple-state memory", *Phys Rev X* **4**, 011035 (2014) (cited on page 8).
- [55] H. J. Xiang, E. J. Kan, S.-H. Wei, M.-H. Whangbo, and J. Yang, "Origin of the ising ferrimagnetism and spin-charge coupling in $LuFe_2O_4$ ", *Phys. Rev. B* **80**, 132408 (2009) (cited on page 8).
- [56] M. Naka, A. Nagano, and S. Ishihara, "Magnetodielectric phenomena in a charge- and spin-frustrated system of layered iron oxide", *Phys. Rev. B* **77**, 224441 (2008) (cited on page 8).
- [57] T. Mueller, "Order and disorder in the charge and spin structures of $YFe_2O_{4-\delta}$ and $Ni_{0.42}Mn_{0.58}TiO_3$ ", PhD thesis (RWTH Aachen university, 2018) (cited on pages 8, 9, 13, 23, 25, 29, 41, 44, 49, 62, 78, 97, 107).

- [58] H. J. Xiang and M. -. H. Whangbo, "Charge order and the origin of giant magnetocapacitance in LuFe_2O_4 ", *Phys. Rev. Lett.* **98**, 246403 (2007) (cited on page 8).
- [59] H. Williamson, T. Mueller, M. Angst, and G. Balakrishnan, "Growth of YbFe_2O_4 single crystals exhibiting long-range charge order via the optical floating zone method", *J. Cryst. Growth* **475**, 44 (2017) (cited on pages 9, 13, 15, 16, 23, 29, 40, 41, 44, 62).
- [60] T. Mueller, J. de Groot, J. Stremper, and M. Angst, "Stoichiometric $\text{YFe}_2\text{O}_{4-\delta}$ single crystals grown by the optical floating zone method", *J. Cryst. Growth*. **428**, 40 (2015) (cited on pages 9, 13, 15, 16, 23, 40, 41, 43, 44, 78, 101).
- [61] N. Kimizuka, K. Kato, I. Shindo, I. Kawada, and T. Katsura, "New compounds of $\text{Yb}_3\text{Fe}_4\text{O}_{10}$ and $\text{Yb}_4\text{Fe}_5\text{O}_{13}$ ", *Acta Crysta. B* **32**, 1620 (1976) (cited on pages 9, 12, 13, 103).
- [62] Y. Matsui, K. Kato, N. Kimizuka, and S. Horiuchi, "Structure image of $\text{Yb}_3\text{Fe}_4\text{O}_{10}$ by a 1 mv high-resolution electron microscope", *Acta Crysta. B* **35**, 561 (1979) (cited on pages 9, 103, 104).
- [63] Y. Matsui, "Extra electron reflections observed in YFe_2O_4 , YbFe_2O_4 , $\text{Yb}_2\text{Fe}_3\text{O}_7$ and $\text{Yb}_3\text{Fe}_4\text{O}_{10}$ ", *J. Appl. Cryst.* **13**, 395 (1980) (cited on pages 9, 12, 13, 43, 48, 49, 103).
- [64] S. Hammouda and M. Angst, "Growth of layered $\text{Lu}_2\text{Fe}_3\text{O}_7$ and $\text{Lu}_3\text{Fe}_4\text{O}_{10}$ single crystals exhibiting long-range charge order via the optical floating-zone method", *J. Cryst. Growth* (2019) (cited on pages 9, 17, 39, 40, 42, 43, 48, 49, 75, 76, 78, 100).
- [65] N. Kimizuka, A. Takenaka, Y. Sasada, and T. Katsura, "New compounds $\text{Yb}_2\text{Fe}_3\text{O}_7$ and $\text{Lu}_2\text{Fe}_3\text{O}_7$ ", *Solid State Commun.* **15**, 1199 (1974) (cited on pages 9, 10, 13, 51).
- [66] J. Iida, S. Takekawa, and N. Kimizuka, "Single crystal growth of LuFe_2O_4 , LuFeCOO_4 and YbFeMgO_4 by the floating zone method", *J. Cryst. Growth* **102**, 398 (1990) (cited on pages 9, 42).
- [67] N. Kimizuka and T. Katsura, "The standard free energy of formation of YbFe_2O_4 , $\text{Yb}_2\text{Fe}_3\text{O}_7$, YbFeO_3 , and $\text{Yb}_3\text{Fe}_4\text{O}_{10}$ at 1200 °C", *J. Solid State Chem.* **15**, 151 (1975) (cited on pages 9, 10).
- [68] K. Yoshii, N. Ikeda, R. Fukuyama, T. Nagata, T. Kambe, Y. Yoneda, T. Fukuda, and S. Mori, "Magnetic properties of $\text{R}_2\text{Fe}_3\text{O}_7$ (R= Yb and Lu)", *Solid State Commun* **173**, 34 (2013) (cited on pages 10, 11, 51).
- [69] K. Kato, I. Kawada, N. Kimizuka, I. Shindo, and T. Katsura, "Die kristallstruktur von $\text{Yb}_2\text{Fe}_3\text{O}_7$ ", *Z. Kristallogr. Cryst. Mater.* **143**, 278 (1976) (cited on pages 10, 11).
- [70] B. Malaman, O. Evrard, N. Tannieres, A. Courtois, and J. Protas, "Structure cristalline de la phase $\text{Yb}_2\text{Fe}_3\text{O}_7$ ", *Acta Crystallogr. B Struct. Cryst. Cryst. Chem* **32**, 749 (1976) (cited on pages 10, 11).
- [71] M. Tanaka, N. Kimizuka, J. Akimitsu, S. Funahashi, and K. Siratori, "Magnetic ordering in $\text{Lu}_2\text{Fe}_3\text{O}_7$ ", *J. Magn. Mater.* **31**, 769 (1983) (cited on pages 11, 51, 62, 73).

- [72] M. Tanaka and J. Iida, "Mössbauer study of $\text{Lu}_2\text{Fe}_3\text{O}_7$: a two-dimensional antiferromagnet on a triangular lattice", *Hyperfine Interact.* **84**, 217 (1994) (cited on pages 11, 51, 66, 97).
- [73] T. Sugihara, K. Siratori, N. Kimizuka, J. Iida, H. Hiroyoshi, and Y. Nakagawa, "Magnetic properties of $\text{Lu}_2\text{Fe}_3\text{O}_7$ ", *J. Phys. Soc. Jpn.* **54**, 1139 (1985) (cited on pages 11, 51, 56, 73).
- [74] J. Iida, M. Tanaka, and S. Funahashi, "Magnetic property of single crystal $\text{Lu}_2\text{Fe}_3\text{O}_7$ ", *J. Magn. Magn. Mater.* **104**, 827 (1992) (cited on pages 11, 16, 36, 44, 51, 62, 66, 107).
- [75] H. Yang, Y. Zhang, Y. Qin, C. Ma, H. Tian, and J. Li, "Electronic ferroelectricity, charge ordering and structural phase transitions in LuFe_2O_4 (LuFeO_3) $_n$ ($n=0$ and 1)", *Phys. Status Solidi (b)* **247**, 870 (2010) (cited on pages 12, 48, 51, 75).
- [76] Y. Qin, H. Yang, L. Wang, H. Tian, C. Ma, Y. Li, H. Shi, and J. Li, "Structure, charge ordering and physical properties of $\text{Yb}_2\text{Fe}_3\text{O}_7$ ", *Eur. Phys. J. B* **75**, 231 (2010) (cited on pages 12, 48).
- [77] Y. Qin, H. Yang, Y. Zhang, H. Tian, C. Ma, L. Zeng, and J. Li, "Suppression of the current leakage in charge ordered $\text{Lu}_2\text{Fe}_2\text{Fe}_{1-x}\text{Mn}_x\text{O}_7$ ($0 < x \leq 0.86$)", *Appl. Phys. Lett.* **95**, 072901 (2009) (cited on pages 12, 13, 48).
- [78] J. Scott, "Ferroelectrics go bananas", *J. Phys.: Condens. Matter* **20**, 021001 (2007) (cited on page 12).
- [79] Y. Chen, J. Dai, K. Au, K. Lam, Y. Qin, and H. Yang, "Temperature-dependent piezoelectric and dielectric properties of charge-ordered $\text{Lu}_2\text{Fe}_{2.1}\text{Mn}_{0.9}\text{O}_7$ ", *Mater. Lett.* **68**, 54 (2012) (cited on page 12).
- [80] Y. B. Qin, H. X. Yang, Y. Zhang, H. F. Tian, C. Ma, Y. G. Zhao, R. I. Walton, and J. Q. Li, "The effect of mg doping on the structural and physical properties of LuFe_2O_4 and $\text{Lu}_2\text{Fe}_3\text{O}_7$ ", *J. Condens. Matter Phys.* **21**, 015401 (2009) (cited on pages 12, 48).
- [81] J. A. Mundy, C. M. Brooks, M. E. Holtz, J. A. Moyer, H. Das, A. F. Rébola, J. T. Heron, J. D. Clarkson, S. M. Disseler, Z. Liu, et al., "Atomically engineered ferroic layers yield a room-temperature magnetoelectric multiferroic", *Nature* **537**, 523 (2016) (cited on page 12).
- [82] Y. Sun, Y. Liu, F. Ye, S. Chi, Y. Ren, T. Zou, F. Wang, and L. Yan, "A magnetoelectric multiglass state in multiferroic YbFe_2O_4 ", *J. Appl. Phys.* **111**, 07D902 (2012) (cited on page 13).
- [83] J. Bourgeois, G. André, S. Petit, J. Robert, M. Poienar, J. Rouquette, E. Elkaim, M. Hervieu, A. Maignan, C. Martin, and F. Damay, "Evidence of magnetic phase separation in LuFe_2O_4 ", *Phys. Rev. B* **86**, 024413 (2012) (cited on page 13).
- [84] M. Tanaka, H. Iwasaki, K. Siratori, and I. Shindo, "Mössbauer study on the magnetic structure of YbFe_2O_4 : a two-dimensional antiferromagnet on a triangular lattice", *J. Phys. Soc. Jpn.* **58**, 1433 (1989) (cited on page 13).

-
- [85] S. Nakamura, H. Kitô, and M. Tanaka, "An approach to specify the spin configuration in the RFe_2O_4 ($R=Y, Ho, Er, Tm, Yb, \text{ and } Lu$) family: ^{57}Fe Mössbauer study on a single crystal $LuFe_2O_4$ ", *J. Alloys Compd.* **275-277**, 574 (1998) (cited on page 13).
- [86] F. Lévy, "Single-crystal growth of layered crystals", *Il Nuovo Cimento B* (1971-1996) **38**, 359 (1977) (cited on page 16).
- [87] S. Hammouda, *Effect of rare earth ion size on ordering processes in rare earth ferrites RFe_2O_4 by $R=Lu_xY_{1-x}Fe_2O_4$ substitution study*, Master thesis, Al-Quds University, 2016 (cited on page 17).
- [88] "Physical Property Measurement System: Vibrating Sample Magnetometer (VSM) Option User's Manual" (Quantum Design 6325 Lusk Boulevard San Diego, CA 92121 USA, 2003) (cited on page 17).
- [89] "Magnetic Property Measurement System: SQUID VSM User's Manual" (Quantum Design 6325 Lusk Boulevard San Diego, CA 92121 USA, 2009) (cited on page 17).
- [90] "Magnetic Property Measurement System: DynaCool™ User's Manual" (Quantum Design 6325 Lusk Boulevard San Diego, CA 92121 USA, 2011) (cited on page 19).
- [91] D. Martien, "Introduction to AC susceptibility - AC magnetic measurements" (Quantum Design Application Notes) (cited on page 19).
- [92] P. J. Zakalek, "Magnetic interface effects in thin film heterostructures", PhD thesis (RWTH Aachen university, 2015) (cited on page 20).
- [93] M. Angst, "Material analysis by synchrotron radiation and neutrons", Lecture notes (RWTH Aachen, 2015) (cited on pages 21, 22).
- [94] D. W. Bennett, "Understanding Single-Crystal X-Ray Crystallography" (2010) (cited on page 22).
- [95] "Fundamentals of powder diffraction and structural characterization of materials" (Vitalij K. Pecharsky and Peter Y. Zavalij, 2005) (cited on page 23).
- [96] "Powder diffraction theory and practice" (Robert E. Dinnebier and Simon J. L. Billinge, 2008) (cited on page 23).
- [97] Rigaku Oxford Diffraction, (2015), CrysAlisPro Software system, version number 1.171.37.35, Rigaku Corporation, Oxford, UK (cited on page 24).
- [98] W. Clegg, A. J. Blake, J. M. Cole, J. S. O. Evans, P. Main, S. Parsons, and D. J. Watkin, "Crystal Structure Analysis: Principles and Practice", edited by W. Clegg (Oxford University Press, 2009) (cited on pages 25, 33, 84).
- [99] D. H. Perkins, "Introduction to high energy physics" (1982) (cited on page 26).
- [100] T. Brückel, S. Förster, G. Roth, and R. Zorn, eds., "Laboratory Course Neutron Scattering Lectures", Vol. 147 (Schriften des Forschungszentrums Jülich Reihe Schlüsseltechnologien, 2017) (cited on pages 27, 62).

- [101] D. L. Price, "Introduction to neutron scattering", in *Methods in experimental physics, neutron scattering*, Vol. 23, Part A, edited by D. L. Price and K. Sköld (Academic Press INC., 1987) Chap. 1, pp. 1–97 (cited on page 27).
- [102] S. Lovesey, "Theory of neutron scattering from condensed matter", Vol. 2, International series of monographs on physics (Clarendon Press Oxford, 1984) (cited on page 27).
- [103] H. A. Hauptman, "The phase problem of X-ray crystallography: overview", in *Electron crystallography* (Springer Netherlands, 1997), pp. 131–138 (cited on page 30).
- [104] V. Petříček, M. Dušek, and L. Palatinus, "Crystallographic computing system JANA2006: general features", *Z. Kristallogr.* **229**(5), 345 (2014) (cited on page 31).
- [105] T. Hahn, U. Shmueli, and J. W. Arthur, "International tables for crystallography", Vol. 1 (Reidel Dordrecht, 1983) (cited on page 31).
- [106] H. Shenk, "An introduction to direct methods. the most important phase relationships and their application in solving the phase problem", edited by C. A. Taylor, University College Cardiff Press Cardiff, Wales: International Union of Crystallography, 2001 (cited on page 32).
- [107] A. Altomare, G. Casciarano, C. Giacovazzo, A. Guagliardi, M. C. Burla, G. Polidori, and M. Camalli, "SIR92 – a program for automatic solution of crystal structures by direct methods", *J. Appl. Crystallogr.* **27**, 435 (1994) (cited on page 32).
- [108] G. Oszlányi and A. Sütö, "Ab initio structure solution by charge flipping", *Acta Cryst. A* **60**, 134 (2004) (cited on page 32).
- [109] L. Palatinus, "Ab initio determination of incommensurately modulated structures by charge flipping in superspace", *Acta Cryst. A* **60**, 604 (2004) (cited on page 32).
- [110] G. Oszlányi and A. Sütö, "The charge flipping algorithm", *Acta Crystallogr. A* **64**, 123 (2007) (cited on page 32).
- [111] L. Palatinus and G. Chapuis, "Superflip - a computer program for the solution of crystal structures by charge flipping in arbitrary dimensions.", *J. Appl. Cryst.* **40**, 786 (2007) (cited on page 32).
- [112] R. Herbst-Irmer, A. Spek, T. Schneider, and M. Sawaya, "Crystal structure refinement: a crystallographer's guide to shelx", Vol. 8 (Oxford University Press, 2006) (cited on pages 32, 33, 87).
- [113] M. Ladd and R. Palmer, "Structure determination by X-ray crystallography" (Springer US, 2013) (cited on page 32).
- [114] F. L. Hirshfeld, "Can X-ray data distinguish bonding effects from vibrational smearing?", *Acta Crystallogr. A* **32**, 239 (1976) (cited on page 33).
- [115] I. D. Brown and D. Altermatt, "Bond-valence parameters obtained from a systematic analysis of the Inorganic Crystal Structure Database", *Acta Cryst. B* **41**, 244 (1985) (cited on pages 34, 88, 97).

-
- [116] N. E. Brese and M. O’Keeffe, “Bond-valence parameters for solids”, *Acta Cryst. B* **47**, 192 (1991) (cited on page 34).
- [117] S. M. Kanowitz and G. J. Palenik, “Bond valence sums in coordination chemistry using oxidation-state-independent R_0 values. a simple method for calculating the oxidation state of iron in Fe-O complexes”, *Inorg. Chem.* **37**, 2086 (1998) (cited on page 34).
- [118] W. Liu and H. H. Thorp, “Bond valence sum analysis of metal-ligand bond lengths in metalloenzymes and model complexes. 2. Refined distances and other enzymes”, *Inorg. Chem.* **32**, 4102 (1993) (cited on page 34).
- [119] H. S. Bennett and E. A. Stern, “Faraday Effect in Solids”, *Phys. Rev.* **137**, A448 (1965) (cited on page 34).
- [120] F. Baudelet, C. Giorgetti, S. Pizzini, C. Brouder, E. Dartyge, A. Fontaine, J. Kappler, and G. Krill, “Study of 5d magnetism in rare-earth-transition-metal (Fe, Co) intermetallic compounds by magnetic circular X-ray dichroism”, *J. Electron. Spectrosc. Relat. Phenom.* **62**, 153 (1993) (cited on page 34).
- [121] C. Kapusta, P. Fischer, and G. Schütz, “Magnetic X-ray absorption spectroscopy”, *J. Alloys Compd.* **286**, 37 (1999) (cited on pages 34, 36).
- [122] P. A. van Aken and B. Liebscher, “Quantification of ferrous/ferric ratios in minerals: new evaluation schemes of Fe L_{23} electron energy-loss near-edge spectra”, *English, Phys. Chem. Minerals* **29**, 188 (2002) (cited on page 34).
- [123] G. van der Laan and A. I. Figueroa, “X-ray magnetic circular dichroism—a versatile tool to study magnetism”, *Coord. Chem. Rev.* **277-278**, 95 (2014) (cited on page 35).
- [124] A. Rogalev, F. Wilhelm, N. Jaouen, J. Goulon, and J.-P. Kappler, “X-ray magnetic circular dichroism: historical perspective and recent highlights”, in *Magnetism: a synchrotron radiation approach*, Vol. 697, edited by E. Beaurepaire, H. Bulou, F. Scheurer, and J.-P. Kappler, *Lect. Notes Phys.* (Springer-Verlag, Berlin Heidelberg, 2006), pp. 71–93 (cited on page 35).
- [125] W. Kuch, “X-ray magnetic circular dichroism for quantitative element-resolved magnetic microscopy”, *Phys. Scr* **2004**, 89 (2004) (cited on page 35).
- [126] S. W. Lovesey and S. P. Collins, “X-ray scattering and absorption by magnetic materials” (Clarendon Press Oxford, 1996) (cited on page 36).
- [127] B. T. Thole, P. Carra, F. Sette, and G. van der Laan, “X-ray circular dichroism as a probe of orbital magnetization”, *Phys. Rev. Lett.* **68**, 1943 (1992) (cited on page 36).
- [128] P. Carra, B. T. Thole, M. Altarelli, and X. Wang, “X-ray circular dichroism and local magnetic fields”, *Phys. Rev. Lett.* **70**, 694 (1993) (cited on page 36).
- [129] T. Funk, A. Deb, S. J. George, H. Wang, and S. P. Cramer, “X-ray magnetic circular dichroism—a high energy probe of magnetic properties”, *Coord. Chem. Rev.* **249**, 3 (2005) (cited on page 36).
- [130] E. Weschke and E. Schierle, “The UE46 PGM-1 beamline at bessy II”, *JLSRF* **4**, 127 (2018) (cited on page 38).

- [131] S. Blundell, "Magnetism in Condensed Matter" (American Association of Physics Teachers, 2003) (cited on pages 41, 52).
- [132] F. Wang, J. Kim, Y.-J. Kim, and G. D. Gu, "Spin-glass behavior in $\text{LuFe}_2\text{O}_{4+\delta}$ ", *Phys. Rev. B* **80**, 024419 (2009) (cited on pages 41, 45, 52, 59).
- [133] N. Kimizuka and T. Katsura, "Standard free energy of formation of YFeO_3 , $\text{Y}_3\text{Fe}_5\text{O}_{12}$, and a new compound YFe_2O_4 in the $\text{Fe}-\text{Fe}_2\text{O}_3-\text{Y}_2\text{O}_3$ system at 1200 °C", *J. Solid State Chem.* **13**, 176 (1975) (cited on page 43).
- [134] K. Kitayama, M. Sakaguchi, Y. Takahara, H. Endo, and H. Ueki, "Phase equilibrium in the system $\text{Y}-\text{Fe}-\text{O}$ at 1100 °C", *J. Solid State Chem.* **177**, 1933 (2004), (Fig 4.2 Reprinted with permission from Elsevier) (cited on page 43).
- [135] K. Yoshii, N. Ikeda, Y. Nishihata, D. Maeda, R. Fukuyama, T. Nagata, J. Kano, T. Kambe, Y. Horibe, and S. Mori, "Exchange bias in multiferroic RFe_2O_4 ($\text{R} = \text{Y}, \text{Er}, \text{Tm}, \text{Yb}, \text{Lu}$, and In)", *English, J. Phys. Soc. Jpn.* **81**, 033704 (2012) (cited on page 52).
- [136] M. Angst, "Complex magnetic phase diagram of highly stoichiometric LuFe_2O_4 " (cited on page 53).
- [137] M. Chattopadhyay, S. Roy, and P. Chaddah, "Kinetic arrest of the first-order ferromagnetic-to-antiferromagnetic transition in $\text{Ce}(\text{Fe}_{0.96}\text{Ru}_{0.04})_2$: formation of a magnetic glass", *Phys. Rev. B* **72**, 180401 (2005) (cited on page 56).
- [138] J. Moore, G. Perkins, K. Morrison, L. Ghivelder, M. Chattopadhyay, S. Roy, P. Chaddah, K. Gschneidner Jr, V. Pecharsky, and L. Cohen, "Local probing of arrested kinetics in Gd_5Ge_4 ", *J. Phys.: Condens. Matter* **20**, 465212 (2008) (cited on page 56).
- [139] S. Hammouda, "Effect of rare earth ion size on ordering processes in rare earth ferrites RFe_2O_4 by $\text{R}=\text{Lu}_x\text{Y}_{1-x}\text{Fe}_2\text{O}_4$ substitution study", MA thesis (Al-Quds university, 2013) (cited on page 60).
- [140] S. Blundell, "Magnetism in condensed matter" (OUP Oxford, 2001) (cited on page 65).
- [141] Y. Yamada, K. Kitsuda, S. Nohdo, and N. Ikeda, "Charge and spin ordering process in the mixed-valence system LuFe_2O_4 : charge ordering", *Physical Review B* **62**, 12167 (2000) (cited on page 74).
- [142] A. B. Harris and T. Yildirim, "Charge and spin ordering in the mixed-valence compound LuFe_2O_4 ", *Physical Review B* **81**, 134417 (2010) (cited on page 74).
- [143] B. J. Campbell, H. T. Stokes, D. E. Tanner, and D. M. Hatch, "ISODISPLACE: a web-based tool for exploring structural distortions", *J. Appl. Crystallogr.* **39**, 607 (2006) (cited on pages 80, 81, 101, 102).
- [144] "ISOTROPY software suite iso.byu.edu" (cited on pages 80, 81, 101, 102).
- [145] K. Trueblood, H.-B. Bürgi, H. Burzlaff, J. Dunitz, C. Gramaccioli, H. Schulz, U. Shmueli, and S. Abrahams, "Atomic displacement parameter nomenclature. report of a subcommittee on atomic displacement parameter nomenclature", *Acta Crystallogr., Sect. A: Found. Crystallogr.* **52**, 770 (1996) (cited on page 87).

-
- [146] R. W. Grosse-Kunstleve and P. D. Adams, "On the handling of atomic anisotropic displacement parameters", *J. Appl. Crystallogr* **35**, 477 (2002) (cited on page 87).
- [147] M. A. Subramanian, T. He, J. Chen, N. S. Rogado, T. G. Calvarese, and A. W. Sleight, "Giant room-temperature magnetodielectric response in the electronic ferroelectric LuFe_2O_4 ", *J. Adv. Mater.* **18**, 1737 (2006) (cited on page 87).
- [148] Y. Horibe, N. Ikeda, K. Yoshii, and S. Mori, "Direct observation of low-temperature superstructure in spin- and charge-frustrated ferrite $\text{YFe}_2\text{O}_{4-\delta}$ ", *Phys. Rev. B* **82**, 184119 (2010) (cited on page 87).
- [149] T. Wagner and A. Schönleber, "A non-mathematical introduction to the superspace description of modulated structures", *Acta Crystallogr., Sect. B: Struct. Sci* **65**, 249 (2009) (cited on page 92).
- [150] S. Van Smaalen, "Incommensurate crystallography", Vol. 21 (Oxford University Press, 2007) (cited on page 92).
- [151] V. Petříček, A. Van der Lee, and M. Evain, "On the use of crenel functions for occupationally modulated structures", *Acta Crystallogr., Sect. A: Found. Crystallogr.* **51**, 529 (1995) (cited on page 93).
- [152] M. Evain and V. Petricek, "Crenel functions and aperiodic structure determinations", *Ferroelectrics* **305**, 43 (2004) (cited on page 93).
- [153] R. Herbst-Irmer and G. M. Sheldrick, "Refinement of obverse/reverse twins", *Acta Crystallogr. B Struct. Sci.* **58**, 477 (2002) (cited on page 103).
- [154] A. Guinier, G. Bokij, K. Boll-Dornberger, J. Cowley, S. Āurovič, H. Jagodzinski, P. Krishna, P. De Wolff, B. Zvyagin, D. Cox, et al., "Nomenclature of polytype structures. report of the international union of crystallography ad hoc committee on the nomenclature of disordered, modulated and polytype structures", *Acta Crystallogr., Sect. A: Found. Crystallogr.* **40**, 399 (1984) (cited on page 106).
- [155] K. Friese, O. Jarchow, K. Kato, and Y. Kanke, "Verschiedene aspekte der kristallstrukturen von YbV_4O_8 . III. domänenstruktur aus parallel verwachsenen bereichen der α -und β -phasen und gruppentheoretische betrachtung ihrer symmetrie", *Kristallogr. Cryst. Mater* **212**, 859 (1997) (cited on page 106).
- [156] K. Friese, A. Hönnerscheid, and M. Jansen, "Crystal structure determination of systematically intergrown compounds: $\text{Li}_5(\text{OH})_2\text{Br}_3$ and $\text{Li}_2(\text{OH})\text{Br}$ ", *Z. Kristallogr. Cryst. Mater* **218**, 536 (2003) (cited on page 106).
- [157] N. Barrier, J. M. Rueff, M. B. Lepetit, J. Contreras-Garcia, S. Malo, and B. Raveau, "A new polymorph with a layered structure $\epsilon\text{-CaTe}_2\text{O}_5$ ", *Solid State Sci.* **11**, 289 (2009) (cited on page 106).
- [158] B.-I. Lee, H. Jeong, J.-s. Bae, and S.-H. Byeon, "A layered polymorph of rare earth hydroxides", *ChemComm* **49**, 6051 (2013) (cited on page 106).

A

Appendix

Scan number	Type	2θ	ω	κ	ϕ
1	ϕ	0	90	0	0
2	ϕ	0	90	0	0
3	ϕ	35	90	0	0
4	θ	35	-35	60	0
5	θ	35	-35	60	30
6	θ	35	-35	60	60
7	θ	35	-35	60	90
8	θ	35	-35	60	120
9	θ	35	-35	60	150
10	θ	35	-35	60	-180
11	θ	35	-35	60	-150
12	θ	35	-35	60	-120
13	θ	35	-35	60	-90
14	θ	35	-35	60	-60
15	θ	35	-35	60	-30
16	θ	55	-35	60	0
17	θ	55	-35	60	60
18	θ	55	-35	60	120
19	θ	55	-35	60	-180
20	θ	55	-35	60	-120
21	θ	55	-35	60	-60
22	ϕ	55	90	0	0

Table A.1: Different ascans performed on Kappa-diffractometer at EH1. Angles are given in Eulerian and the scan step size is 0.8

Parameter	C2/m	Amm2
a (Å)	3.4461	28.4180(5)
b (Å)	5.9688	3.4461
c (Å)	28.4180(5)	5.9688
V (Å ³)	584.532(10)	584.532(10)
R _{int}	8.75/8.79	9.36/9.40
R _{obs} /wR _{obs}	5.99/13.27	6.22/13.74
R _{all} / wR _{all}	7.03/13.64	7.16/14.06
GOF _{obs} / GOF _{all}	2.93/2.60	3.15/2.80
N. of Reflections	6294/8469	5233/6895
Redundancy	3.99	4.90

Table A.2: The refinement parameters of the average structure for both C2/m and Amm2 symmetries at 100 K

Parameter	Cmcm($\frac{1}{3}$ 10)000	Cmcm($\frac{1}{3}$ 10)0s0	Cmcm($\frac{1}{3}$ 10)00s	Cmcm($\frac{1}{3}$ 10)0ss
(h, k, l, m)	$h + k = 2n$			
(h, k, l, -k)	$l = 2n$	$k + l = 2n$	$l = 2n$	$k + l = 2n$
(h, k, l, -k)	$h + k + l = 2n$	$h + l = 2n$	$h + k + l = 2n$	$h + l = 2n$
(h, k, 0, m)	$h + k = 2n$	$h + k = 2n$	$m = 2n$	$h + k + m = 2n$
(h, k, 0, m)	-	-	$h + k + m = 2n$	$m = 2n$
(h, k, 0, -k)	$h + k = 2n$	$h = 2n$	$h = 2n$	$h + k = 2n$
(h, k, 0, -k)	-	$k = 2n$	$k = 2n$	-
(0, k, l, 0)	$k = 2n$	$k = 2n$	$k = 2n$	$k = 2n$
(0, k, 0, 0)	$k = 2n$	$k = 2n$	$k = 2n$	$k = 2n$
(0, 0, l, 0)	$l = 2n$	$l = 2n$	$l = 2n$	$l = 2n$

Table A.3: The reflection conditions for different supergroup of Cmcm symmetry

Site	x	y	z	U11	U22	U33	U12	U13	U23
Lu ₁ (4a)	0	0.83113(16)	0.65401(4)	0.0033(3)	0.0046(2)	0.00939(14)	0	0	0.0000(2)
Lu ₂ (8b)	0.66634(15)	0.83129(18)	0.63555	0.0019(4)	0.0029(3)	0.0042(3)	0.0001(3)	-0.0004(5)	-0.0003(3)
Lu' ₂ (8b)	0.33247(12)	0.83288(17)	0.65325(3)	0.0055(3)	0.0041(2)	0.0106(3)	0.0003(4)	-0.0005(5)	-0.0001(3)
Lu ₃ (8b)	0.66736(3)	0.8339(4)	0.8575(3)	0.0084(5)	0.0018(4)	0.034(2)	-0.0002(5)	0.0071(10)	0.0017(7)
Lu' ₃ (8b)	0.33426(14)	0.8316(2)	0.84426(8)	0.0014(3)	0.0014(2)	0.0103(4)	-0.0001(3)	-0.0009(5)	0.0000(3)
Lu ₄ (4a)	0	0.83327(19)	0.85810(5)	0.0034(3)	0.0021(3)	0.0462(5)	0	0	-0.0005(4)
Fe ₁ (4a)	0	0.4988(7)	0.74930(8)	0.0094(12)	0.0087(15)	0.0041(9)	0	0	0.0007(5)
Fe ₂ (8b)	0.33327(3)	0.4988(4)	0.74924(5)	0.0077(6)	0.0075(7)	0.0044(4)	-0.0006(8)	0.0000(2)	0.0008(5)
Fe ₃ (8b)	-0.16559(2)	0.6680(3)	0.54337(5)	0.0070(7)	0.0069(6)	-0.00219(18)	-0.0007(5)	-0.0001(4)	-0.0003(3)
Fe ₄ (4a)	1/2	0.66411	0.54334	0.0053(8)	0.0056(7)	-0.0008(3)	0	0	-0.0003(5)
Fe ₅ (8b)	-0.16929(3)	0.6645(4)	0.95590(7)	0.0082(9)	0.0077(8)	0.0236(6)	0.0003(7)	0.0010(8)	-0.0008(7)
Fe ₆ (4a)	1/2	0.6733(6)	0.95696(10)	0.0079(11)	0.0157(13)	0.0209(8)	0	0	-0.0024(12)
O ₁ (4a)	0	0.844(4)	0.5300(5)	0.036(10)	0.015(7)	0.011(4)	0	0	-0.006(5)
O ₂ (8b)	0.34328(4)	0.821(6)	0.5298(9)	0.024(3)	0.024(3)	0.024(3)	0	0	0
O' ₂ (8b)	0.33721(3)	0.825(5)	0.5443(7)	0.024(3)	0.024(3)	0.024(3)	0	0	0
O ₃ (8b)	-0.16703(10)	0.337(2)	0.75962(19)	0.013(3)	0.012(3)	0.0052(16)	0.001(2)	-0.001(2)	-0.003(2)
O ₄ (4a)	1/2	0.331(6)	0.7438(5)	0.0061(17)	0.0061(17)	0.0061(17)	0	0	0
O' ₄ (4a)	1/2	0.346(4)	0.7590(5)	0.0061(17)	0.0061(17)	0.0061(17)	0	0	0
O ₅ (4a)	0	0.5161(17)	0.8201(5)	0.012(4)	0.001(3)	0.007(4)	0	0	0.002(2)
O ₆ (8b)	0.34012(8)	0.4919(13)	0.8191(2)	0.007(2)	0.010(3)	0.0029(18)	-0.0022(17)	-0.0026(14)	0.0022(17)
O ₇ (8b)	-0.15985(15)	0.661(2)	0.6084(3)	0.013(5)	0.026(5)	0.019(3)	-0.005(5)	0.004(3)	-0.007(4)
O ₈ (4a)	1/2	0.643(3)	0.6099(4)	0.032(8)	0.006(4)	0.011(3)	0	0.000(3)	
O ₉ (8b)	0.67349(13)	0.846(2)	0.9683(4)	0.014(4)	0.011(4)	0.019(3)	-0.002(2)	-0.006(3)	0.002(3)
O ₁₀ (4a)	0	0.828(4)	0.9644(6)	0.014(6)	0.020(7)	0.021(5)	0	0	0.004(7)
O ₁₁ (8b)	0.67475(10)	0.516(2)	0.6834(3)	0.025(5)	0.040(6)	0.002(2)	-0.018(4)	0.001(2)	-0.012(3)
O ₁₂ (4a)	0	0.494(3)	0.6837(5)	0.046(11)	0.029(8)	-0.001(3)	0	0	-0.004(3)
O ₁₃ (8b)	0.82742(12)	0.665(2)	0.88772(18)	0.011(3)	0.013(3)	0.0014(12)	-0.001(3)	0.000(2)	0.000(2)
O ₁₄ (4a)	1/2	0.676(2)	0.8872(2)	0.008(4)	0.007(4)	-0.0014(13)	0	0	0.000(2)

Table A.4: Refined atomic positions: position and thermal displacement parameters in Cmc2₁I/ $\frac{1}{12}$ symmetry at 100 K. Atoms marked by prime are produced by splitting.

Appendix A. Appendix

Site	x	y	z	U11	U22	U33	U12	U13	U23
Lu ₁ (4a)	1/2	0.83326(19)	0.641905	0.0006(3)	0.0012(3)	0.0011(5)	0	0	0.0001(4)
Lu ₂ (8b)	0.83265(3)	0.8339(4)	0.6425(3)	0.0015(5)	0.0010(4)	0.0008(19)	0.0001(5)	0.0005(10)	-0.0002(7)
Lu' ₂ (8b)	0.16574(14)	0.8315(2)	0.65574(9)	0.0002(3)	0.0008(2)	0.0003(4)	0.0000(3)	-0.0001(5)	0.0000(3)
Lu ₃ (8b)	0.83370(15)	0.83131(19)	0.86445(5)	0.0004(4)	0.0016(3)	0.0001(3)	0.0000(3)	0.0000(5)	0.0000(3)
Lu' ₃ (8b)	0.16754(13)	0.83284(17)	0.84675(6)	0.0010(3)	0.0022(3)	0.0003(3)	-0.0001(4)	0.0000(5)	0.0000(3)
Lu ₄ (4a)	1/2	0.83118(16)	0.84599(4)	0.0006(3)	0.0025(2)	0.00023(14)	0	0	0.0000(2)
Fe ₁ (4a)	1/2	0.4988(7)	0.75073(8)	0.0016(14)	0.0047(14)	0.0001(9)	0	0	-0.0001(5)
Fe ₂ (8b)	0.1667(4)	0.4989(4)	0.75079(6)	0.0015(7)	0.0043(7)	0.0001(5)	0.0002(7)	0.0000(2)	-0.0001(5)
Fe ₃ (8b)	0.3307(3)	0.6646(4)	0.54416(8)	0.0014(9)	0.0042(8)	0.0006(6)	0.0001(7)	-0.0001(8)	0.0001(7)
Fe ₄ (4a)	0	0.6732(7)	0.54309(9)	0.0014(12)	0.0089(13)	0.0005(8)	0	0	0.0003(12)
Fe ₅ (8b)	0.3344(2)	0.6681(3)	0.95667(5)	0.0013(7)	0.0038(6)	-0.00006(18)	-0.0002(6)	0.0000(4)	0.0000(3)
Fe ₆ (4a)	0	0.6641(5)	0.95669(7)	0.0011(8)	0.0032(8)	0.0000(3)	0	0	0.0000(5)
O ₁ (4a)	1/2	0.831(4)	0.5347(6)	0.003(7)	0.009(6)	0.000(4)	0	0	0.000(6)
O ₂ (8b)	0.17209(12)	0.846(2)	0.5316(4)	0.003(5)	0.006(4)	0.001(3)	-0.001(2)	0.000(3)	0.000(4)
O ₃ (8b)	0.3335(9)	0.33667(19)	0.74068(19)	0.002(3)	0.005(3)	0.0002(15)	0.000(2)	0.000(2)	0.000(2)
O ₄ (4a)	0	0.339(5)	0.7476(5)	0.004(10)	0.008(8)	0.002(15)	0	0	-0.002(9)
O ₅ (4a)	1/2	0.496(3)	0.8164(5)	0.008(11)	0.018(8)	0.000(3)	0	0	0.001(3)
O ₆ (8b)	0.1744(11)	0.5164(19)	0.8167(3)	0.005(5)	0.022(6)	0.000(2)	-0.006(4)	0.000(2)	0.001(3)
O ₇ (8b)	0.3273(11)	0.665(2)	0.61234(18)	0.002(3)	0.007(3)	0.0000(11)	0.000(3)	0.0000(19)	0.000(2)
O ₈ (4a)	0	0.676(2)	0.6127(2)	0.001(4)	0.004(4)	0.0000(12)	0	0	0.000(2)
O ₉ (8b)	0.84215(15)	0.821(3)	0.9628(6)	0.002(4)	0.018(6)	0.002(9)	0.006(4)	0.001(7)	-0.001(9)
O ₁₀ (4a)	1/2	0.843(4)	0.9703(5)	0.006(11)	0.011(8)	0.000(3)	0	0	0.001(6)
O ₁₁ (8b)	0.84024(9)	0.4922(13)	0.6808(2)	0.001(2)	0.005(3)	0.0001(18)	-0.0007(17)	0.0002(15)	-0.0003(17)
O ₁₂ (4a)	1/2	0.5163(17)	0.6797(5)	0.002(4)	0.000(3)	0.000(4)	0	0	0.000(2)
O ₁₃ (8b)	0.34008(14)	0.662(2)	0.8916(3)	0.003(5)	0.015(5)	0.000(3)	-0.002(5)	0.000(3)	0.001(4)
O ₁₄ (4a)	0	0.642(3)	0.8903(4)	0.006(8)	0.004(4)	0.000(3)	0	0	0.000(3)

Table A.5: Refined atomic positions: position and thermal displacement parameters in Cmc2₁ II/ $\frac{1}{4}$ symmetry at 100 K. Atoms marked by prime are produced by splitting.

Twin	Cmc2 ₁ I/ $\frac{1}{12}$	Cmc2 ₁ II/ $\frac{1}{4}$
1	0.27(9)	0.30(10)
2	0.13(4)	0.08(4)
3	0.06(4)	0.15(4)
4	0.31(4)	0.28(4)
5	0.09(4)	0.13(4)
6	0.14(4)	0.05(4)

Table A.6: The domain population of the 6-twin components refined in both Cmc2₁ I/ $\frac{1}{12}$ and Cmc2₁ II/ $\frac{1}{4}$ at 100 K.

Parameter	C2/m
a (Å)	6.0100
b (Å)	3.4699
c (Å)	20.3081(1)
V (Å ³)	421.44
R _{obs} /wR _{obs}	11.38/22.67
R _{all} /wR _{all}	22.20/26.14
GOF _{obs} /GOF _{all}	2.57/1.62
N. of Reflections	2535/8570

Table A.7: The refinement parameters of the average structure refinement of Lu₃Fe₄O₁₀ for C2/m symmetry including Lu-splitting and occupation refinement at 300 K

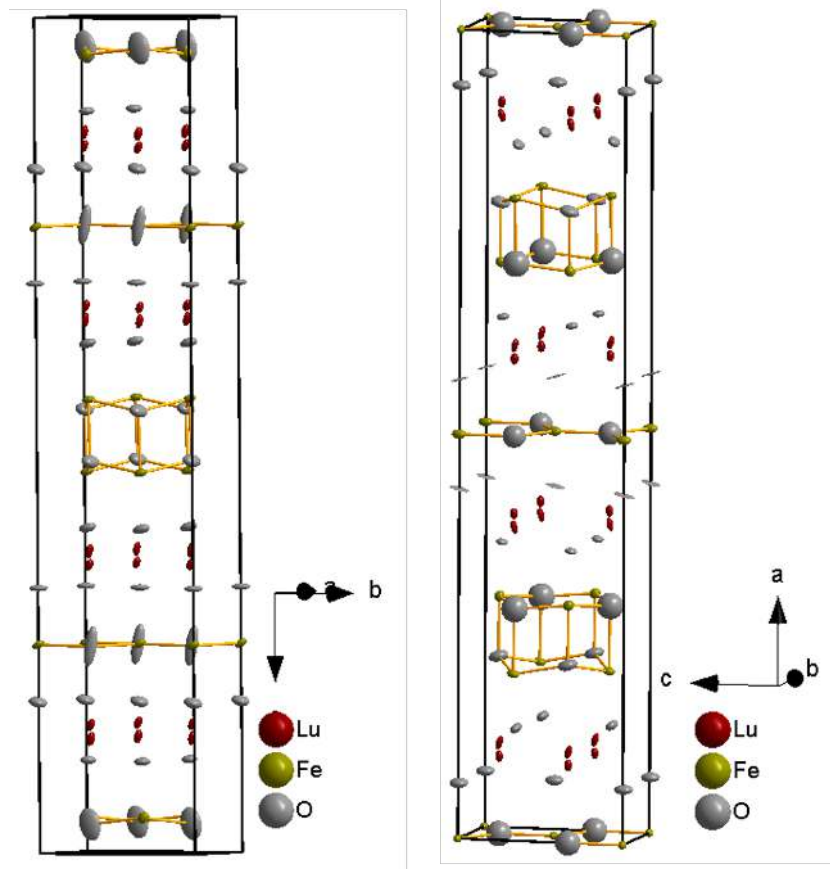


Figure A.1: The average structure solution of C2/m (left) and Amm2 (right) at 100 K. The bonded are the Fe-single and bilayers. Atoms are presented with their refined thermal anisotropic displacement parameters.

List of Figures

1.1	Diagram of overlapped two ferroic orders. The ferroelectricity (left) with the polarization P is switchable with the application of electric field E and the ferromagnetism (right) with the magnetisation M is switchable with the application of magnetic field H . In the overlapped area (Magnetoelectric multiferroics), switching process is reversed i.e. H for the electric polarization and E for magnetisation. Concept from [11] and adapted.	2
1.2	Charge order model for single Fe-bilayer as proposed by [25, 26] with polarization direction indicated by arrow.	3
1.3	Structural solution representation obtained from the representation analysis for two different propagation vectors. Arrows indicated the bilayer polarization direction. Taken from [21].	4
1.4	Composite image of the hkl -plane of highly stoichiometric LuFe_2O_4 crystal. Left: incommensurate CO at room temperature with circles surrounded the reflections type neglected in the refinement. Right: diffuse scattering replacing the 3D-CO above T_{co} . Taken from [11] and adapted by [35].	5
1.5	XMCD spectra for both LuFe_2O_4 at 4 T and YbFe_2O_4 at 6 T across the Fe $L_{2/3}$ with total electron yield. Taken from [35].	6
1.6	The combined CO with $\text{SO } P\bar{1}$ superstructure cell for the ferrimagnetic phase in YbFe_2O_4 . Taken from [35].	7
1.7	Minimum set of interactions $U_1 \dots U_4$ leading to 3D charge ordering. Geometrical frustration is indicated by blue triangle. Taken from [21].	8
1.8	Sketch of the layer stacking of a) LuFe_2O_4 , b) $\text{Lu}_2\text{Fe}_3\text{O}_7$ containing one LuFeO_3 block, c) $\text{Lu}_3\text{Fe}_4\text{O}_{10}$ containing two LuFeO_3 blocks (Oxygen ions are omitted). Taken from [64].	9
1.9	Phase diagram of the $\text{Fe-Fe}_2\text{O}_3\text{-Lu}_2\text{O}_3$ at 1200 $^\circ\text{C}$ with the use of different CO_2/H_2 . The regions where $\text{Lu}_2\text{Fe}_3\text{O}_7$ are stable are marked in blue and LuFe_2O_4 in pink. $\text{Lu}_3\text{Fe}_4\text{O}_{10}$ and higher intercalated compounds are not present in this phase diagram, which may be only stable at higher temperatures. Redrawn from [42].	10
1.10	The change of lattice parameters of polycrystalline $\text{Lu}_2\text{Fe}_3\text{O}_{7-\delta}$ for different oxygen stoichiometry. Figure plotted based on data from [42].	11
1.11	The hexagonal crystal structure of $\text{Yb}_2\text{Fe}_3\text{O}_7$ at room temperature drawn based on [69, 70].	11
1.12	Electron diffraction image shows the (left) incommensurate superstructure reflections of $\text{Lu}_2\text{Fe}_3\text{O}_7$, taken from [75] (middle) diffuse scattering of $\text{Yb}_2\text{Fe}_3\text{O}_7$, taken from [76] (right) intergrowth of different Yb-intercalated compounds, taken from [61].	12
1.13	The P-E hysteresis loops of (a) $\text{Lu}_2\text{Fe}_3\text{O}_7$ [38] (b) $\text{Lu}_2\text{Fe}_2\text{Fe}_{0.14}\text{Mn}_{0.86}\text{O}_7$ [38] and (c) LuFe_2O_4 [77].	13

1.14	The rare-earth ion radius R^{3+} effect on the cell volume from and the ratio of the intralayer Fe-Fe distance a_{hex} to bilayer thickness d_b . Figure from [21] and adapted, data based on [44, 45, 47, 65, 82–85].	13
2.1	$\text{Lu}_2\text{Fe}_3\text{O}_7$ prepared as loose powder, white color indicated impurities of Lu_2O_3 and the used tube furnace.	16
2.2	a) An image of the used optical mirror furnace with inset of a real molting zone b) Crystal boule grown in gas flow of $\text{CO}_2/\text{CO} = 33$ and (001) facets c) Sketch of the floating zone setup with four mirrors. b) taken from [64].	17
2.3	Illustration of the SQUID set up and it's response curve.	18
2.4	Illustrations of scattering geometry, taken from [92].	20
2.5	Illustration for Bragg's law and the Ewald sphere construction.	21
2.6	In-house supernova diffractometer.	24
2.7	Kappa-diffractometer at EH1.	25
2.8	Line profile along ℓ for data measured at Supernova (Cu, Mo)- $\text{K}\alpha$ and at P24 (0.49 Å).	26
2.9	The magnetic field line configuration for M perpendicular (left) and parallel (right).	28
2.10	Schematic setup for DNS: Z-field means a field perpendicular to the horizontal scattering plane. The x-direction is facing the end of the detector array and is parallel to the average \mathbf{Q} . The y-axis is perpendicular to x and z.	29
2.11	(left) Laue image along c-direction, (right) Single crystal of $\text{Lu}_2\text{Fe}_3\text{O}_7$ mounted on Al-holder in which $(1\bar{1}0)$ axis is perpendicular to the scattering plane.	30
2.12	Atomic X-ray form factor for all elements in $\text{Lu}_2\text{Fe}_3\text{O}_7$ including the different valances of Fe ions, taken from [11].	34
2.13	Schematic representation of absorption process in the case of $2P \rightarrow 3d$ transitions at the $L_{2/3}$ edges.	35
2.14	Figure illustrates the steps used to analysis the data: a) Twelve raw absorption spectra: six μ_+ for left and six μ_- right circularly polarized X-ray. b) Averaged absorption spectra of μ_+ and μ_- (the inset shows the offset in the pre-and post-edges). c) Constant background subtraction for XAS. d) Normalized XMCD signal.	37
3.1	Powder X-ray diffractogram of polycrystalline pellets of $\text{Lu}_2\text{Fe}_3\text{O}_7$ calcined under different CO_2 and $\text{Ar}(96\%):\text{H}_2(4\%)$ ratios. The flow of $\text{Ar}(96%):\text{H}_2(4\%)$ is fixed to 30 ml/min and the flow of CO_2 varied. Impurities of LuFe_2O_4 & LuFeO_3 are indicated by arrows. Taken from own work [64] and adapted.	40
3.2	Field cooled magnetization measured in $H=100$ Oe on five different pellets synthesized in different CO_2 and $\text{Ar}(96%):\text{H}_2(4\%)$ ratios. Zero field cooling curve for P39:30 is shown as well. Dashed lines indicate the freezing temperature for each pellet, and was determined by the steepest slope of FC curves.	41

3.3	X-ray powder diffractograms of powdered parts of the grown boules (see text) grown with selected different gas flow of CO ₂ /CO, and of pure Lu ₂ Fe ₃ O ₇ and Lu ₃ Fe ₄ O ₁₀ crystals (extracted from single crystal X-ray diffraction). The present phases in each diffractogram marked with small lines. Taken from own work [64].	42
3.4	Main phases obtained for some of the crystal growth attempts at different gas flow of CO ₂ /CO. The ticks at the bottom indicate the concrete gas ratios used in the various crystal growths. Taken from own work [64].	43
3.5	Field cooled magnetization measured on SC1 in a magnetic field of 100 Oe along two different orientations parallel and perpendicular to the field.	44
3.6	Temperature dependence magnetization measured with 100 Oe applied field parallel to c-direction for different Lu ₂ Fe ₃ O ₇ single crystals, the inset shows the (0.4×0.2×0.05) mm ³ measured SC2 mounted on holder for single crystal X-ray diffraction	45
3.7	Temperature dependence of the magnetization (upper panel) and AC susceptibility obtained with different frequencies as labeled and 10 Oe applied AC magnetic field. The real and imaginary parts of the susceptibility are shown in the middle and lower panels. All are performed using the non-stoichiometric Lu ₂ Fe ₃ O ₇ SC1.	46
3.8	Field cooled magnetization measured in a magnetic field of 100 Oe on two Lu ₃ Fe ₄ O ₁₀ crystals grown with gas ratio = 85, the inset shows the (0.4×0.2×0.05) mm ³ measured S2 mounted on holder for single crystal X-ray diffraction.	47
3.9	Precession images of the (hhl) reciprocal space plane of Lu ₂ Fe ₃ O ₇ crystals grown with CO ₂ /CO = 83 for a and 85 for b (SC2) and c (SC3), measured at room temperature. From own work [64]	48
3.10	Precession images of the (hhl) reciprocal space plane of a Lu ₃ Fe ₄ O ₁₀ crystals grown with CO ₂ /CO = 90 for a and 85 for b (S1) and c (S2), measured at room temperature. Figure (a,b) from own work [64]	49
4.1	Magnetization on Lu ₂ Fe ₃ O ₇ during field cooling, field warming and zero field cooling at 100 Oe. T _C assigned by the steepest slope in FC curve, while T _f by the maximum of ZFC curve.	52
4.2	Left: Temperature dependent magnetization during field cooling and followed by field warming at different magnetic fields. FC and FW are perfectly overlapped for all used fields. Right: Field dependent low-temperature magnetic moment for Lu ₂ Fe ₃ O ₇ (black curve) and for LuFe ₂ O ₄ (red curve). LuFe ₂ O ₄ data were extracted from Fig. 4 in [136].	53
4.3	Left: Zero-field-cooling and field-cooling measurements for SC3. Right: Zero-field-cooling and field-cooling measurements for SC1.	54

-
- 4.4 a) Magnetization M vs. $H \parallel$ to c loops measured on $\text{Lu}_2\text{Fe}_3\text{O}_7$ at different temperatures. b): hysteresis loop including the virgin curve which was measured after cooling in zero field at 160 K. c) The slopes and the intercepts of the fitted hysteresis in field region of 5-7 T. The dotted line indicated the expected behaviour. 55
- 4.5 Left panel: $M(H)$ at temperatures below the freezing temperature. Solid lines were measured after cooling in a field of 7 T. Right panel: Temperature dependence of coercive field obtained at the negative field magnetization vanishes, the obtained values below 120 K can not be trusted since the $M(H)$ -loops doesn't reach the FC value for a maximum field of 7 T. 56
- 4.6 a) Temperature dependence of thermoremanent magnetization of $\text{Lu}_2\text{Fe}_3\text{O}_7$ after cooling in two different external fields with 2 K/m (symbols) and the corresponding field cooling curves (lines). b): TRM and FC curves of LuFe_2O_4 , taken from [11]. c) Total moment at low-temperature from the right panel of Fig. 4.2 and linear fitting (red line) of FC-TRM (red circles). The subtraction of the fitted FC-TRM from the total moment results in the tentative bilayer contribution (blue curve). 57
- 4.7 H-T "phase" diagram for SC3 of $\text{Lu}_2\text{Fe}_3\text{O}_7$ extracted from different DC measurements ($H \parallel$ to c). Three magnetic "phases" are labeled: PM, fM, CG, see text for labeling. The red circles were obtained from the FC measurements at different DC fields and the gray squares from ZFC measurements at different DC fields. Arrows indicate the direction T for which a feature accrue. The blurred blue area indicating the transition CG- fM is arrested below ~ 60 K. 58
- 4.8 Magnetization measurements of $\text{Lu}_3\text{Fe}_4\text{O}_{10}$ single crystal as a function of temperature on field cooling, field warming and zero field cooling in 100 Oe. Lines separated different phases was determined by the steepest slope in the FC for transition from pM to fM and by the maximum of ZFC for fM to AFM transition. The negative magnetization values in ZFC below 200 K is an artifact due to the presence of some residual magnetic field. 59
- 4.9 $M(T)$ in various $H \parallel c$. FC and FW curves are both shown and indicated by arrow direction. Inset: Field dependent low-temperature magnetic moment for $\text{Lu}_3\text{Fe}_4\text{O}_{10}$ (black curve) and for $\text{Lu}_2\text{Fe}_3\text{O}_7$ (red curve). 60
- 4.10 Smoothed magnetization M vs. field $\parallel c$ for temperatures lower than T_C . Smoothing was one using the adjacent-averaging method. Virgin curve measured after cooling in zero field at 80 K is also shown. 61
- 4.11 Left: Reciprocal space maps of the spin flip magnetic scattering measured with polarization parallel to \mathbf{Q} at ~ 4.2 K for two different crystals grow in (upper panel) $\text{CO}_2:\text{CO}=50$ (SC1) [counting time=24 s], (lower panel) $\text{CO}_2:\text{CO}=85$ (SC4) [counting time=55 s]. Right: FC curve of the SC4 measured in 100 Oe. 62

- 4.12 Reciprocal space map of (hh ℓ)-plane at 4.2 K in spin-flip (a,c) and non-spin-flip (b,d) with neutron polarization (a,b) parallel to \mathbf{Q} -direction and (c,d) perpendicular to scattering plane for five detector positions and counting time 24s each position (sample SC1). When the polarization of the neutrons is parallel to the scattering vector, both in-plane and out-of plane-components of the magnetic contribution are measured in the spin-flip (SF) channel and the full nuclear coherent contribution is measured in the non-spin-flip (NSF) channel i.e. structural reflections (0 0 ℓ) with $\ell = 2n$ 63
- 4.13 Left: The intensity of the diffuse scattering averaged along ℓ in the range $\ell = -5$ to $\ell = 5$ for SF $\parallel \mathbf{z}$, SF $\parallel \mathbf{x}$ and for the NSF $\parallel \mathbf{z}$ - NSF $\parallel \mathbf{x}$. Background is subtracted for SFz and SFx channel. Right: Diffuse magnetic scattering at the ($\frac{1}{3} \frac{1}{3} \ell$) line (intensity averaged along hh0 from 0.25 to 0.4) in the spin flip channel for neutron polarization parallel to z-direction at 4.2 K. The smoothed data (blue) and the intensity model for the random distribution of Fe²⁺ and Fe³⁺ (green line, squares: with, without Debye-Waller factor) are also shown. Background is subtracted for the measured data. 64
- 4.14 (a) Temperature dependence of part of the diffuse magnetic intensity (logarithmic scale) in the reciprocal hh ℓ plane in the spin-flip channel measured with $\mathbf{P} \parallel \mathbf{Q}_{\text{average}}$ at different temperatures. (b) Diffuse magnetic scattering averaged along the ℓ direction in the range $\ell = -5$ to $\ell = 5$ vs hh0 for selected temperatures from panel (a). The data were fitted with a Lorentzian (solid curves) and the background is subtracted for all curves. (c) Correlation length and Full Width Half Maxima extracted from the data fitting for various temperatures. 65
- 4.15 Normalized XAS spectra for left and right circularly polarized X-ray at the Fe L2/L3-edges and the XMCD signal of stoichiometric Lu₂Fe₃O₇ crystal (SC3) at 4 T. The XMCD signal $\Delta\mu$ is scaled by a factor of five for better visibility. Inset: XMCD signals for both stoichiometric (SC3) and non-stoichiometric Lu₂Fe₃O₇ (SC5) crystals. 67
- 4.16 Left: Non-stoichiometric (upper) and stoichiometric (lower) Lu₂Fe₃O₇ crystals mounted using silver base on brass holder. Crystals are surrounded by circles, the very small stoichiometric crystal hardly can be seen. Right: possible spin model in the bilayer containing six resolved valances of Fe sites. Direction of spins are indicated by direction of arrows. 68
- 4.17 Upper panel: XAS spectrum of stoichiometric Lu₂Fe₃O₇ and LuFe₂O₄ crystals in the application of 4 T. XAS = $(\mu_{-} + \mu_{+})/2$ and normalized to the peak maximum. Lower panel: the corresponding XMCD signals. LuFe₂O₄ XMCD signal was taken from [11] and scaled through division by 1.75. 69

4.18	Linear X-ray absorption spectra at the O k-edge for different polarization directions at 120 K a) of $\text{Lu}_2\text{Fe}_3\text{O}_7$ b) of LuFe_2O_4 taken from [33]. Energy levels are labeled. c) (Left) Sketch of the trigonal-bipyramidal crystal field, (Right) the corresponding energy-splitting of the Fe 3d orbitals. For Fe^{3+} , each orbital is singly occupied, the extra-electron of Fe^{2+} can go to either of two e_g'' orbitals, taken from [21].	70
4.19	XAS spectra for left and right circularly polarized X-ray at the Fe L2/L3-edges and the XMCD signal of $\text{Lu}_3\text{Fe}_4\text{O}_{10}$ crystal at 4 T.	71
4.20	XMCD signal of stoichiometric $\text{Lu}_2\text{Fe}_3\text{O}_7$, LuFe_2O_4 and $\text{Lu}_3\text{Fe}_4\text{O}_{10}$ crystals in the application of 4 T. LuFe_2O_4 XMCD signal was taken from [11] and scaled through division by 1.75.	72
5.1	Precession images of the (a) hhl and (b) $hk24$ reciprocal space plane with (c) is the integrated intensity (gray line) in a small region perpendicular to the (hhl) for (a) of SC2 $\text{Lu}_2\text{Fe}_3\text{O}_7$ grown with a $\text{CO}_2/\text{CO}=85$ measured using supernova at RT. line profile through the center of one of the peaks highlighted by a white square (red line). (c) is from own work [64]	76
5.2	Composite precession images of the hhl reciprocal space plane of SC3 $\text{Lu}_2\text{Fe}_3\text{O}_7$ grown with a $\text{CO}_2/\text{CO}=85$: upper measured at P24 at 100 K, left lower measured at P24 at 50 K, and right lower measured at supernova at RT. The integrated intensity in a small region perpendicular to the (hhl) for the corresponding temperatures are shown in (a,b,c). All data were treated with linear background subtraction.	77
5.3	Intensity integrated perpendicular to ℓ of: (left) (0 0 26) structural reflection (SR), fitted SR intensity and super structural reflection (SSR) ($\frac{1}{3}\frac{1}{3}\ell = 23-25$) out of plane at room temperature from lower right panel of Fig. 5.2 for SC2. (Right): (0 0 14) structural reflection (SR), fitted SR intensity and super structural reflection (SSR) ($\frac{1}{3}\frac{1}{3}\ell = 14-16$) out of plane at room temperature from Fig. 5.1a for SC3. Full widths at half maximum (FWHM) are given in Angstrom units. The SSR and SR were fitted with lorentzian and Gaussian profiles respectively. Linear background subtraction was done for both SR and SSR in right figure before fitting. Left figure is from own work [64]	78
5.4	Observed reflections in reciprocal space along c_{hex} at 100 K indexed by the three domains rotated by 120° presented by a different colored cell. Larger size reflections are the structural reflections while the smaller ones are the superstructural reflections (some are surrounded by circle).	79
5.5	Structural representation of $Cmcm$ (left) and $C2/m$ (right). The layers are highlighted according to Fe-valance majority: orange for layer rich in Fe^{2+} and gray rich in Fe^{3+}	82

5.6	Structural representation of $Cmc2_1$ (left), $Amm2$ (right), and different viewing direction for $Amm2$. The layers are highlighted according to Fe-valance majority: layer rich in Fe^{2+} (orange) and rich in Fe^{3+} (gray). The arrows indicated the bilayer polarization direction.	83
5.7	Plot of the calculated vs observed structure factors for the hexagonal ($P6_3/mmc$) average structure refinement (A) at 100 K, the black line indicates the ideal distribution.	87
5.8	a) The hexagonal $P6_3/mmc$ crystal structure at 100 K. The basic blocks of the unit cell are highlighted, and the atoms are presented with their refined thermal anisotropic displacement parameters. b) Lu (gray) and O (blue) atoms in $C2/m$ drawn as thermal ellipsoids in the projection along a at 210 K in $LuFe_2O_4$. For comparison, the Lu positions at 350 K are displayed as orange spheres, taken from [36].	88
5.9	The average structure solution of $Cmc2_1$ (left) and $Cmcm$ (right) at 100 K. The bonded are the Fe-single and bilayers. Atoms are presented with their refined thermal anisotropic displacement parameters. Marked are the oxygen atom in the single layer.	90
5.10	Sketch illustrating how the assumption of mirror plane (m) or inversion centre ($\bar{1}$) existence would leads to an elongation of electron density of atoms when modulation is dismissed	92
5.11	A contour map visualises the occupational modulation of the electron density as a function of x_3 (z-direction in 3D space) and x_4 (fourth dimension representing the modulation direction) of Lu atoms in the refined $Cmcm(\frac{1}{3}10)00s$. The occupational modulation shows a crenel function assures the alternation between the "Left,green" and "Right,red" configurations of Lu occupation.	93
5.12	Calculated vs observed structure factors for $Cmc2_1$ $II/\frac{1}{4}$ at 100 K, the black line indicates the ideal distribution	97
5.13	Plot of the Fe valances for the corresponding superstructures tabulated in table 5.11 and indicated in Fig. 5.14	97
5.14	The $Cmc2_1$ $I/\frac{1}{12}$ (left) and $Cmc2_1$ $II/\frac{1}{4}$ (right) structure solutions. The different Fe valances found in both symmetries is represented by the colors. Fe2 atoms are surrounded by box. The splitted Lu atoms are differentiated by colors for the corresponding occupancy (orange for closer to $\frac{2}{3}$ and light pink for closer to $\frac{1}{3}$). The encircled splitted Lu-O-Fe atoms to point out when the Lu is splitted of having a 2.5+ average valance for the nearest Fe atom in the bilayer. The two solutions are not fundamentally distinct.	98
5.15	Illustration of the Lu-modulation surrounded by the closest single layer and bilayer, assuming a CO-pattern similar to isodistort $Cmc2_1$ solution. The left part shows 2 supercells, each supercell is averaged as it shown in right side. The averaged Fe atoms in the bilayer are shown in different gray shades.	99

5.16	(a) Precession image of the $hh\ell$ reciprocal space plane with (b) the integrated intensity (gray line) in a small region perpendicular to the $(hh\ell)$ for (a) of S1 $\text{Lu}_3\text{Fe}_4\text{O}_{10}$ grown with a $\text{CO}_2/\text{CO}=85$ measured using supernova at RT. Line profile through the center of one of the peaks highlighted by a white square (red line) is also shown. (b) is from own work [64]	100
5.17	Precession image of the $hh\ell$ reciprocal space plane of S1 $\text{Lu}_3\text{Fe}_4\text{O}_{10}$ grown with a $\text{CO}_2/\text{CO}=85$ measured at Supernova at RT. The integrated intensity in region perpendicular to the $(hh\ell)$ for the corresponding temperatures are shown on the right side. Data was treated with line background subtraction.	100
5.18	Intensity integrated perpendicular to ℓ of: $(0\ 0\ 33)$ structural reflection (SR), fitted SR intensity and super structural reflection (SSR) $(\frac{-1}{3}\ \frac{-1}{3}\ 29)$ out of plane at room temperature. SSR and SR were fitted with a Lorentzian and Gaussian profiles respectively and linear background fitting for both. Full widths at half maximum (FWHM) are given in Angstrom units.	101
5.19	$C2/m$, $P\bar{1}$ and Cm structural representations respectively. Shown is only one bilayer, the other two are exactly the same due to $(\frac{1}{3}\ \frac{1}{3}\ 0)$ propagation. The layers are highlighted according to Fe-valance majority: gray for layer rich in Fe^{3+} and orange rich in Fe^{2+} . The arrows indicated the bilayer polarization direction.	102
5.20	Left: Precession $hh\ell$ plane of $\text{Lu}_3\text{Fe}_4\text{O}_{10}$ at 300 K. Right: 1-D line profile in hh -direction with 1 pixel. Data treated with linear background subtraction.	103
5.21	The $R\bar{3}m$ crystal structure at 300 K. The basic block of the unit cell is magnified consists of 3 layers of Lu/O, one Fe/O bilayer and two Fe/O single layers. The atoms are presented with their refined thermal anisotropic displacement parameters.	105
A.1	The average structure solution of $C2/m$ (left) and $Amm2$ (right) at 100 K. The bonded are the Fe-single and bilayers. Atoms are presented with their refined thermal anisotropic displacement parameters.	127

List of Tables

1.1	Published $\text{Lu}_2\text{Fe}_3\text{O}_7$ Lattice parameters	10
2.1	Characteristic bond lengths d_{0i} of Fe^{2+} , Fe^{3+} taken from published crystal data in [115, 117, 118].	34
3.1	Overview of the whole prepared pellets with the use of different mixtures of CO_2 and $\text{Ar}(96\%):\text{H}_2(4\%)$ flows.	39
5.1	Lattice parameters of the P1 cell at 100 K	79
5.2	Influence of different integration mask sizes (relative to the default) on the internal residual. Default mask size is 1.	80
5.3	Structure solution for K5 and K6-modes based on $(\frac{1}{3}, \frac{1}{3}, 0)$ propagation from the Isodistort software [143, 144]. SG: space group. All the structures with polar bilayers are highlighted with green color. The various polar stacked structures have an actual symmetry of $\text{Cmc}2_1$, the anti-polar have an actual symmetry of $\text{Amm}2$, while those with charged bilayers have Cmcm symmetry.	81
5.4	Table of the structure solutions obtained by the isodistorted. Tabulated are the SG: space groups, their full point group, the present symmetry elements in each and the number of the twin laws (TW).	84
5.5	Refinement parameters of $\text{P}6_3/\text{mmc}$ average structure at 100 K with a comparison for the residuals before (B) and after (A) Lu-splitting with refined occupancies. For details about the definition of different residuals (R) and the goodness of fit (GOF), see Sec.2.4.3	87
5.6	Atomic positions and thermal displacement parameters of the refined average structure in $\text{P}6_3/\text{mmc}$ 100 K with Lu-position split	89
5.7	The refinement parameters of the average structure for both Cmcm and $\text{Cmc}2_1$ symmetries at 100 K.	91
5.8	Overview of refinements of the average structure. Extinction is present unless mentioned as (no ext.). Tabulated are the space group, Goodness of fit for all reflections, two residuals, number of merged reflections (Refls: observed/all) and parameters (Pars), and remarks. iso: isotropically refined, incompl: refinement incomplete (changes $> 0.1\text{su}$)	91
5.9	Overview of refinements based on Cmcm type superspace groups. Shown is incommensurate refinement (with extinction) followed by commensurate variants with different t_0 (refinement in commensurate supercell, no extinction unless mentioned). Tabulated are the space group and t_0 , Goodness of fit for all reflections, two residuals, number of reflections and parameters, and remarks. npd: not positive definite adp; neg: negative isotropic U; incompl: refinement incomplete (changes $> 0.1\text{su}$); twf: twin fractions; anis: anisotropically refined; posmod: position modulated one harmonic.	96
5.10	Refinement parameters for both $\text{Cmc}2_1$ structures at 100 K	97

5.11	Calculated valences using the Bond-valence-sum analysis for each Fe-sites from both $Cmc2_1$ refined superstructures at 100 K.	97
5.12	The occupancy of Lu atoms refined in both $Cmc2_1$ I/ $\frac{1}{12}$ and $Cmc2_1$ II/ $\frac{1}{4}$ at 100 K.	99
5.13	Structure solution for $\Sigma 1$ and $\Sigma 2$ -modes based on $(\frac{1}{3}\frac{1}{3}0)$ propagation from the ISODISTORT software [143, 144]. SG: space group. All the structures with polar bilayers are highlighted with green color.	102
5.14	Refinement parameters in $R\bar{3}m$ at 300 K	103
5.15	Atomic positions and thermal displacement parameters of the refined 300 K structure refined in $R\bar{3}m$. The wyckoff positions are shown in the standard setting 6c: (0,0,z)	104
A.1	Different ascans performed on Kappa-diffractometer at EH1. Angles are given in Eulerian and the scan step size is 0.8	123
A.2	The refinement parameters of the average structure for both $C2/m$ and $Amm2$ symmetries at 100 K.	124
A.3	The reflection conditions for different supergroup of $Cmcm$ symmetry	124
A.4	Refined atomic positions: position and thermal displacement parameters in $Cmc2_1$ I/ $\frac{1}{12}$ symmetry at 100 K. Atoms marked by prime are produced by splitting.	125
A.5	Refined atomic positions: position and thermal displacement parameters in $Cmc2_1$ II/ $\frac{1}{4}$ symmetry at 100 K. Atoms marked by prime are produced by splitting.	126
A.6	The domain population of the 6-twin components refined in both $Cmc2_1$ I/ $\frac{1}{12}$ and $Cmc2_1$ II/ $\frac{1}{4}$ at 100 K.	127
A.7	The refinement parameters of the average structure refinement of $Lu_3Fe_4O_{10}$ for $C2/m$ symmetry including Lu-splitting and occupation refinement at 300 K	127

Acknowledgments

First and foremost, I am grateful to Allah for giving me the strength to complete this work. Thanks for everyone who supported me through the difficult time in performing this challenging project. I would like to express my sincere gratitude to:

Prof. Manuel Angst for being a great supervisor. He has provided insightful discussions. His immense knowledge and guidance helped me in all the time of the research.

Prof. Thomas Brückel for the opportunity to conduct the research at his institute. I was lucky to be a part of the wonderful JCNS-2.

The **brain gain** for funding one year of my PhD project.

Dr. Karen Friese for the help in the refinement of crystallographic CO structure and the time she and **Dr. Andrzej Grzechnik** gave me from their experiment on P24 beamline.

Dr. Thomas mueller for the assistance during the DNS measurements at FRM II. Additionally he was always willing to assist in anyway he could throughout this research.

Dr. Carsten Paulmann for the assistance during the P24 PETRA III beamline at DESY and his help in answering any question regarding the data reduction.

Dr. Eugen Weschke for the assistance during the XMCD measurements on the high field chamber at BESSY.

Dr. Kirill Nemkowski for the assistance during the DNS beamtime at MLZ.

Barbara Daeger for her steady support in all administrative matters.

Jörg Perßon for his consultation regarding the crystal growth.

Berthold Schmitz, Frank Gossen and Micha Hölzle for technical support whenever it is needed.

Dr. Pankaj Thakuria and **Dr. Hailey Williamson**, the former members of my group for the help and the discussion.

Dr. Oleg Petracic, Dr. Emmanuel Kentzinger, Dr. Paul Zakalek, Dr. Markus Herrmann and Mohammed Ait Haddouch for the help and discussion each in its field.

I would like to thank the amazing **staff of JCNS-2** (too many to list here but you know who you are!) for being so helpful and friendly. I enjoyed working with your environment gorgeous people.

Annika Stelhorn I admire her positive outlook that she tried to transfer to me, I have enjoyed running with you too much.

Abdulrahman (Abu-Zaid), my friends **Malgo. Janczara** and **Asma Qdemat** for the care, the help, and the nice hospitality.

My Friends from the Palestinian-German science bridge **PGSB** for the cherished time spent together and the adventures.

Last but not the least, I heartily pay my gratitude to my mom, dad (I wish you have stayed a bit longer to see this), and my extended family for their love and continuous care. I would not have made it this far without them.